



POLITECNICO DI MILANO
DEPARTMENT OF AEROSPACE SCIENCE AND TECHNOLOGY
DOCTORAL PROGRAMME IN AEROSPACE ENGINEERING

MOMENT METHODS FOR NON-EQUILIBRIUM
LOW-TEMPERATURE PLASMAS WITH
APPLICATION TO ELECTRIC PROPULSION

Doctoral Dissertation of:
Stefano Boccelli

Supervisor:

Prof. Aldo Frezzotti

External Supervisor:

Prof. Thierry E. Magin

Tutor:

Prof. Luigi Vigevano

The Chair of the Doctoral Program:

Prof. Pierangelo Masarati

Year 2021 – Cycle XXXIII

*“If you can’t solve a problem,
then there is an easier problem you can’t solve: find it.”*

G. Pólya.

Acknowledgements

First, I would like to thank Prof. Aldo Frezzotti. Under your supervision, I could enjoy all the freedom that I wanted, yet you have been always available for discussing with me, and, if needed, for bringing me back on track from my constant wandering among various unrelated engineering topics. What I perhaps appreciated most of your supervision is your ability to X-ray any problem, and identify the ultimate issues. Thank you for all the time that you dedicated to teaching me, and for the patience of sometimes repeating over and over the same concepts (be they complex or trivial) until I could finally get a grasp of them.

The first idea for this thesis work comes from Prof. Thierry E. Magin, who originally proposed me to model Hall thruster discharges using moment methods. Since I first came to VKI for working at my MSc thesis, back in the spring of 2016, I have learned so much from you, virtually about any side of research. I am also very grateful for the numerous research and collaboration opportunities that you have offered to me, over the years. The research group and the expertise that you have built are truly amazing, and made all the time spent at VKI absolutely unique and a constant learning experience.

At the beginning of this PhD, Hall thrusters were quite a new topic for me. I would like to thank Dr. Anne Bourdon, for all the precious insights into Hall thrusters and plasma physics in general, and for the very interesting meetings with her research group at the Laboratoire de Physique des Plasmas (LPP). I am also very grateful to Prof. James G. McDonald, at the University of Ottawa, for hosting me to learn about maximum-entropy moment methods. The experience in your research group was a turning point into my PhD research. Also, I would like to thank all members of my PhD committee for their helpful feedback.

I have learned so much from all professors, and probably equally as much from so many colleagues and friends. Federico and Bruno, although our research interests somehow diverged after the end of the Research Master, your friendship and scientific input was like a fixed-point inside the nonlinearity of a PhD. You guys set the standard that I try hard to follow in my work. Thank you.

To all VKI colleagues, friends, professors and staff members goes my profound gratitude. Every single one of you contributes making VKI such a special place. My PhD was characterized by a good amount of roaming around, spending time here and there. But despite this, VKI always felt like home. Thanks Isa for all the nice times in the CC office, and all our talks in front of a nice cup of coffee. Thanks to Maria, Claudia, Anabel, who also helped so much in organizing the 3rd PLS, Bogdan, Yunus, George, and thanks to all the office mates that I met over these years (and that I probably unintentionally annoyed by constantly chewing my pen). Pietro, Giuseppe, Lorenzo and Alfonso, I was so lucky to have the chance of mentoring your RM or MSc thesis work. I have learned a lot from you. The energy and amazing ingenuity that you put into research gave me the extra fuel for keeping working at the PhD, when the simulations were not converging or when my moment code was running even slower than the full kinetic simulations (now it is faster, I promise!)

Sahadeo, Mahdieh, I am very happy that we had the chance to collaborate on blackout and steering needles. A big shout-out to all PoliMi colleagues, sharing the office / open space / ex-library / aquarium / whatever it is. I could meet a lot of talent in that room, and wish to all you folks the very best. Karthik, I had a lot of fun working together at the EP-trajectory optimization coupling. I wish to address my special thanks also to Luca Zioni, the best secretary that a department could ever hope for, and to Prof. Maurizio Boffadossi, for the many stimulating conversations about aerodynamics, experimentation and various other topics. You made the department a very lively place.

Moving to the Paris area, I would like to thank all people from the low-temperature plasmas group, at LPP, in particular Alejandro, Thomas and Prof. Pascal Chabert. Your insights into plasma physics were so precious, and I am glad that we are keeping the collaboration active. I met so many passionate and dedicated researchers in my short time in Paris. Among all, I would like to thank particularly Bo, Hanen and Pedro for the interesting discussions and for the fun time besides work.

During the winter of 2019, I had the opportunity to spend some months at the University of Ottawa. I wish to thank the whole research group of Prof. McDonald, in particular Fabien and Willem, with whom I had the chance to collaborate more directly. Thanks for all the knowledge that you have shared with me about the maximum-entropy method. Also, I would like to thank my office mates, Ramki, Farzane, Kevin, Aliou. And Hongxia: your dedication to research is amazing and is a great source of motivation for all who stand beside you. Keep up the great work! Thank you also to Prof. Clinton P. T. Groth, at the University of Toronto Institute for Aerospace Studies, and to his team. Finally, besides the research, thanks a lot James and Lani for your amazing hospitality. The kindness of your family made my stay unforgettable.

Un ringraziamento speciale va alla mia famiglia. Grazie a mamma e papà, per essere sempre presenti, da vicino o da lontano, alla nonna ed a mio fratello Riccardo per le stimolanti discussioni sui neutroni, la meccanica quantistica e tutte le cose a me incomprensibili che studi tu. Inoltre, un ringraziamento ingegneristico va a papà per aver accolto il mio disordinato “laboratorio”, dopo il trasloco. Ho imparato tanto sui plasmi “giocando” in garage, quanto in vari mesi di simulazioni. Grazie a tutti gli amici, nuovi o di lunga data, Gale, Marti, Sara, Luca, Chiara, Kamila... ed ai colleghi della PLS Milan Penguins Division: Darione, i “Davidi” DB e DDCB, ed il grande Maik.

L’ultimo ringraziamento va ad Elena. Grazie per la tua vicinanza incondizionata, per la tua pazienza nei momenti più bui e per la tua allegria in quelli felici. La tua presenza è stata un regalo meraviglioso, che non posso adeguatamente esprimere in poche righe.

Finally, this PhD thesis would undoubtedly be much much worse had Alexandra Elbakyan never created Sci-Hub.

Summary

LOW-TEMPERATURE plasmas frequently show non-equilibrium features, due to the low collisionality and to the effect of the electric and magnetic fields. An accurate modeling of such situations requires to employ kinetic descriptions (such as the Boltzmann or Vlasov equations), that describe the evolution in phase space of the particle velocity distribution function (VDF). This is the case, for example, for Hall thruster electric propulsion devices, where non-equilibrium characterizes both neutrals and charged species. Fluid methods (such as the Euler or the Navier-Stokes-Fourier hydrodynamic approaches) cannot reproduce such situations accurately, and often mispredict transport processes. Moreover, such methods cannot reproduce kinetic instabilities, commonly observed in Hall thruster devices. Nonetheless, such methods are widely employed, due to their favorable computational cost, if compared to the much more expensive kinetic simulations.

A promising strategy for extending fluid descriptions towards non-equilibrium is offered by moment methods. Such methods solve for an enlarged set of equations, including higher-order moments with respect to the commonly employed mass, momentum and energy balances. This work aims at investigating the accuracy of moment and fluid methods for modeling kinetic plasmas. Particular emphasis is put on a selection of the kinetic features appearing in Hall thrusters. Among the possible moment methods, order-4 maximum-entropy methods will be considered, as they show a superior robustness and the ability to represent strongly non-Maxwellian distribution functions. In particular, the 5 and 14-moment systems will be studied. These formulations are able to retrieve important VDFs, commonly appearing in plasma physics, such as the Druyvesteyn distribution, as well as ring-like and anisotropic VDFs, and reproduce the Maxwellian as a limiting case.

This work starts with an analysis of the maximum-entropy methods in low-collisional situations, that are often encountered in low-temperature plasmas and particularly in Hall thrusters. Then, the methods are extended to the simulation of plasmas, by formulating electromagnetic source terms and investigating the dispersion relation of electrostatic plasma waves.

The 5 and 14-moment systems are then applied to the simulation of the axial and azimuthal ion dynamics in a Hall thruster channel, and to the dynamics of electrons. The latter are magnetized and drift in the $\mathbf{E} \times \mathbf{B}$ direction, and their distribution function is known to settle to non-equilibrium steady states, also due to the presence of a weak collisionality with background neutrals. For all cases, a kinetic reference solution is obtained, either numerically (with the use of particle or deterministic solvers) or analytically, and the accuracy of the maximum-entropy systems is investigated, and additionally compared to the solution of the Euler equations of gas dynamics. The maximum-entropy systems demonstrate strong improvements for all the considered conditions, and often reach the same accuracy as kinetic methods, in terms of the tracked moments. This comes at the price of a higher computational cost with respect to the Euler equations, but still lower than kinetic methods. Finally, the last chapter of this work is devoted to the study of the propellant dynamics, and an alternative gas feed configuration is proposed, aimed at increasing the mass utilization efficiency of the thruster through a maximisation of the residence time of neutral particles in the ionization region.

From the analysis performed in this work, the order-4 maximum-entropy methods appear completely suitable for the task of describing a number of kinetic features in Hall thruster plasmas. The computational cost is clearly higher than for the Euler equations, but still advantageous with respect to fully kinetic formulations. Additional developments of this method, building upon this work and suggested as future work activities, will pave the way to further applications of the methods to different plasma applications.

Sommario

IPLASMI a bassa temperatura sono spesso caratterizzati da non-equilibrio termodinamico, per effetto della bassa collisionalità e dei campi elettrici e magnetici. Una modellazione accurata di tale situazione richiede l'uso di descrizioni cinetiche (quali per esempio le equazioni di Boltzmann o Vlasov), che descrivono l'evoluzione della funzione di distribuzione delle velocità nello spazio delle fasi. I propulsori spaziali di tipo Hall sono un esempio di tale non-equilibrio, che caratterizza sia le specie cariche che le specie neutrali presenti nel plasma. La descrizione del problema tramite un approccio di tipo “fluido” (quali le equazioni inviscide di Eulero o l'approccio idrodinamico di Navier-Stokes-Fourier) non permette di riprodurre accuratamente le situazioni di non-equilibrio menzionate, e spesso predice in modo fallimentare i processi di trasporto. Inoltre, i metodi fluidi non permettono di predirre le instabilità di natura cinetica spesso osservate nei propulsori di tipo Hall. Malgrado tali limitazioni, i metodi di tipo fluido sono frequentemente utilizzati per via del loro basso costo computazionale, che li rende favorevoli rispetto alle molto più impegnative simulazioni cinematiche.

Una strategia promettente per estendere le descrizioni fluide verso situazioni di non-equilibrio consiste nei “metodi dei momenti”. Tali metodi risolvono un sistema allargato di equazioni, che include momenti di ordine superiore rispetto ai soli bilanci di massa, momento ed energia. L’obiettivo di questo lavoro consiste nell’investigare l’accuratezza di metodi dei momenti e di metodi fluidi, per l’applicazione a plasmi cinematici. Tra i possibili metodi dei momenti, saranno considerati metodi della massima entropia, che mostrano un ottimo grado di robustezza e la capacità di rappresentare funzioni di distribuzione fortemente non-Maxwelliane. In particolare, saranno studiati sistemi di 5 e 14 momenti, membri di ordine 4 della famiglia dei metodi della massima entropia. Tali formulazioni perme-

ttono di riprodurre importanti funzioni di distribuzione, comuni nella fisica dei plasmi, quali la distribuzione di Druyvesteyn, funzioni di distribuzione “ad anello” ed anisotrope, ed includono la distribuzione Maxwelliana come caso limite.

Questo lavoro parte dall’analisi dei sistemi della massima entropia in condizioni scarsamente collisionali, caratteristiche dei plasmi a bassa temperatura, e dei propulsori di tipo Hall. I metodi sono poi applicati alla simulazione di plasmi, tramite la formulazione dei termini di sorgente elettromagnetici, e l’analisi della relazione di dispersione per onde elettrostatiche. I sistemi di 5 e 14 momenti sono poi applicati allo studio dell’evoluzione assiale ed azimutale degli ioni nel canale di un propulsore di tipo Hall, e successivamente allo studio della dinamica degli elettroni. Gli elettroni in particolare sono magnetizzati, ed hanno una componente di velocità di drift nella direzione $\mathbf{E} \times \mathbf{B}$. La loro funzione di distribuzione è nota essere fuori equilibrio anche nello stato stazionario, per l’effetto dei campi elettromagnetici e della collisionalità con gli atomi neutrali. Per tutti i casi considerati, una soluzione cinetica è ottenuta numericalmente (tramite metodi alle particelle o solutori deterministici) oppure analiticamente, ed è successivamente confrontata con i metodi della massima entropia e con la soluzione delle equazioni di Eulero. I metodi della massima entropia mostrano forti miglioramenti rispetto ai classici approcci fluidi, ed in molti casi mostrano un’accuratezza analoga ai metodi cinetici. Infine, l’ultimo capitolo di questo lavoro è dedicato allo studio della dinamica del propellente neutrale, dall’iniezione all’espansione fuori dal canale, ed una configurazione alternativa di iniezione viene proposta ed investigata. Tale configurazione ha l’obiettivo di migliorare l’efficienza del propulsore, tramite la massimizzazione del tempo di residenza delle particelle neutrali nella regione di ionizzazione.

Dalle analisi eseguite in questo lavoro, il metodo della massima entropia di ordine 4 (sistemi di 5 e 14 momenti) appare completamente applicabile all’obiettivo di modellare il non-equilibrio nei propulsori di tipo Hall. Il costo computazionale di questi metodi appare notevolmente superiore ad una soluzione delle equazioni di Eulero, ma in ogni caso vantaggioso rispetto a formulazioni completamente cinetiche. Ulteriori sviluppi del metodo sono suggeriti come lavoro futuro, e permetteranno l’applicazione dei metodi della massima entropia a differenti tipologie di plasmi.

Contents

Summary	VII
Sommario	IX
1 Introduction	1
1.1 Plasmas for space propulsion: the Hall thruster	1
1.2 Modeling of low-temperature plasmas	4
1.3 Objectives and structure of the thesis	7
1.3.1 Motivation	7
1.3.2 Aims of this work	8
1.3.3 Structure of this manuscript	9
2 Kinetic and fluid modeling of gases and plasmas	11
2.1 Kinetic theory	13
2.2 The dimensionless kinetic equation: operating regime for electrons, ions and neutrals	15
2.3 Fluid formulations: moments of the kinetic equation	20
2.3.1 Moments of the distribution function	20
2.3.2 The generalized moment equation	23
2.3.3 Pressureless gas, Euler equations and moment methods	24
2.4 The maximum-entropy closure	28
2.4.1 Order-4 maximum-entropy method: 14-moment system	30
2.4.2 Order-4 maximum-entropy method: 5-moment system	33
2.5 Conclusions	34

Contents

3 Overview of the numerical methods	37
3.1 Particle-based solutions of the kinetic equation	37
3.2 The finite volume method	39
3.2.1 Formulation	39
3.2.2 Numerical fluxes for fluid and moment systems	41
3.2.3 Time integration	43
3.2.4 Boundary conditions	44
3.2.5 Finite volume solution of the kinetic equation	45
3.3 Units for low-density numerical simulations	47
4 Application of the maximum-entropy closure to rarefied gases and plasmas	49
4.1 The rarefied Sod shock tube problem	50
4.1.1 Kinetic solution	52
4.1.2 Solution of the 5-moment system	54
4.1.3 Comparison of the HLL and Rusanov fluxes	57
4.2 Approximated wave speeds	60
4.2.1 Approximated wave speeds for the 5-moment system	61
4.2.2 Extending the approximation to the 6-moment system	63
4.2.3 Extending the approximation to the 14-moment system	66
4.3 Computational efficiency and minimum allowed σ	70
4.4 2-dimensional test case: rarefied crossing jets	73
4.4.1 Kinetic solution	74
4.4.2 14-moment and Euler solutions	77
4.5 Electromagnetic source terms	81
4.6 Plasma dispersion relations	85
4.6.1 Electron waves	87
4.6.2 Ion acoustic waves	90
4.7 Conclusions	94
5 Collisionless ions in Hall thrusters: an analytical axial model and a simple fluid closure	95
5.1 Genesis of the axial VDF	96
5.2 Analytical axial VDF	98
5.2.1 Moments of the analytical VDF	101
5.2.2 Comparison with 2D PIC simulations	102
5.2.3 Comparison with experimental results	105
5.2.4 Notes: beyond monoenergetic ion birth	107
5.3 A fluid model with ad hoc heat flux closure	109
5.3.1 Derivation of the fluid equations	109

5.3.2 Heat flux closure	110
5.3.3 Comparison with PIC simulations	115
5.4 Conclusions	117
6 Maximum-entropy modeling of ions	119
6.1 Order-4 maximum-entropy systems for collisionless and un-magnetized ions	120
6.1.1 Governing equations for ions: 5-moment system	120
6.1.2 Governing equations for ions: 14-moment system	122
6.2 Axial ion acceleration in a Hall thruster channel	122
6.3 Tonks-Langmuir sheath	124
6.3.1 Description of the case	124
6.3.2 Kinetic solution	125
6.3.3 5-moment maximum-entropy solution	126
6.3.4 Euler system solution	127
6.4 Ions in a stationary wave	128
6.4.1 Description of the case	129
6.4.2 Kinetic solution	129
6.4.3 5-moment and Euler solutions	132
6.5 Ions in a travelling wave	137
6.6 Ions in axial-azimuthal 2D plane	141
6.6.1 Description of the case	141
6.6.2 Kinetic solution	143
6.6.3 Fluid simulations	144
6.6.4 Comparison of the results	145
6.7 Conclusions	146
7 Maximum-entropy modeling of electrons	149
7.1 Overview of non-equilibrium effects for electrons in Hall thrusters	150
7.2 14-moment formulation against analytical VDFs	151
7.2.1 Preliminary considerations	151
7.2.2 Analytical and maximum-entropy VDFs	152
7.3 BGK-like source terms for electron-neutral collisions	156
7.3.1 A simple Maxwellian-relaxation collision model	158
7.3.2 Collision model for large mass disparity	159
7.3.3 Elastic collisions with energy loss	161
7.3.4 Excitation and ionization reactions	163
7.3.5 Collision frequency and non-equilibrium	163
7.4 Application: homogeneous relaxation towards non-equilibrium	165

Contents

7.5 Application: a one-dimensional test case	168
7.6 Conclusions	171
8 DSMC and TPMC analysis of the neutral gas injection: an alternative gas feed configuration	175
8.1 Preliminary considerations	176
8.2 Direct and reversed injection: a simplified analysis	177
8.3 DSMC simulations	178
8.4 Test-particle Monte Carlo simulations: the method	182
8.5 Test-particle Monte Carlo simulations: results	187
8.5.1 Preliminary analysis in the free-molecular limit	187
8.5.2 Collisional case and residence time in the ionization region	189
8.5.3 Estimation of the mass utilization efficiency	190
8.6 Conclusions	192
Conclusions and future work	195
A Notes on the GPU implementation	201
B Time integration error for accelerated gases	207
C Wave speeds approximation via Artificial Neural Networks	211
D Implementation of the 14-moment wave speeds	223
Bibliography	225
List of publications	239

CHAPTER **1**

Introduction

Starting at the beginning of the last century, with the development of the vacuum tube diode [1], which marked the dawn of electronics, plasmas have quickly become a fundamental branch of human technology. Nowadays, plasmas are employed in a huge variety of industrial and medical applications, and in a large number of research fields. We shall cite, for example, the surface processing of semiconductors [2], X-rays generation [3], novel compact particle accelerator designs [4], nuclear fusion research [5], Solar physics and space weather prediction [6].

This work focuses on low-temperature plasmas, where the heavy species (background neutrals and ions) are typically at a much lower temperature than electrons. Particular emphasis will be put to the plasma conditions encountered in Hall thruster electric propulsion devices.

1.1 Plasmas for space propulsion: the Hall thruster

Since the early days of rocket propulsion research, it was recognized that electric fields have the potential to accelerate ions to very high velocities, drastically increasing the specific impulse I_{sp} of classical chemical rockets [7, 8]. As the power input is typically limited by solar cells, this form of

space propulsion is characterized by low thrust, often in the sub-Newton range, depending on the size of the thruster. Therefore, these devices are not able to lift a spacecraft from the ground to orbit, but still require an initial kick to orbital speed by use of traditional chemical boosters.

However, electrical propulsion has a number of important advantages. To start off, the low thrust happens to be finely tunable through a selection of the mass flow rate and the power input, making electric thrusters very accurate devices for tasks such as satellite maneuvering and station keeping, and the high specific impulse additionally reduces the amount of required fuel, increasing the possible mission time or the payload [9, 10].

The latter point happens to be crucial for what concerns Solar System exploration. Indeed, considering the Tsiolkovskii equation [11], one can easily see that the low specific impulse of chemical rockets implies the need for extremely high amounts of fuel [12]. For example, it can be estimated that a mission to Mars could easily require that 85% of the space-craft mass is composed by fuel, and the situation drastically worsens for other planets (for instance, the percentage is roughly 90% for Venus, 98% for Mercury etc.) [13], making gravity assist absolutely necessary. From this perspective, the high specific impulse of electric propulsion is a game changer. Also, in terms of trajectory design, the possibility to keep the thrusters active for long amounts of time introduces new degrees of freedom, and combinations of the classical ballistic trajectory and thrust arcs can be employed, optimizing the fuel efficiency or the travel time [14, 15].

A large number of different electric thruster designs have been proposed over the years [16, 17]. As a quick review, we shall cite, among others, the pulsed plasma thruster (PPT) [18], the pulsed inductive thruster [19], the magnetoplasmadynamic thruster (MPD) [20] and the helicon thruster [21]. More advanced concepts have also been presented in the past and are currently being investigated, such as fusion-based propulsion (see for example [22, 23]). Finally, we shall cite the two most widely studied (and employed) designs: the gridded ion thruster and the Hall thruster [24]. Each configuration comes with its own advantages in terms of reliability, specific impulse and attainable thrust levels.

In this work, particular attention is put on plasma modeling for the conditions encountered in Hall thrusters. However, a number of the results could be easily extended to different configurations.

The Hall thruster

In Hall thrusters, the potential drop that accelerates ions is obtained by limiting the longitudinal electron mobility by effect of a radial magnetic

1.1. Plasmas for space propulsion: the Hall thruster

field \mathbf{B} [25, 26]. The resulting electric field \mathbf{E} is mostly axial, and this results in a crossed electric and magnetic fields configuration, that makes electrons drift in the $\mathbf{E} \times \mathbf{B}$ direction.¹

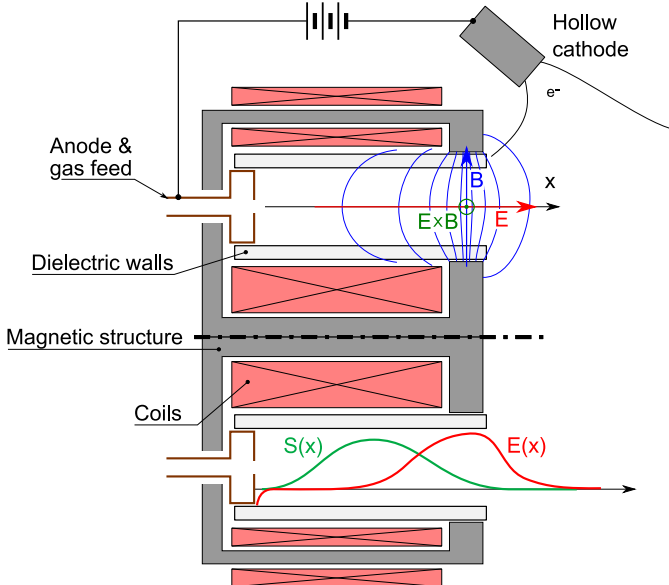


Figure 1.1: Schematic of a magnetic layer Hall thruster (SPT). $S(x)$ and $E(x)$ indicate the ionization and electric field profiles.

The structure of a simple Hall thruster² is shown in Fig. 1.1. The propellant (typically xenon) is injected from the anode and is confined among insulating walls, while electrons are injected at the cathode, located outside of the channel. A fraction of electrons manages to enter the channel walls, and eventually reaches the anode, overcoming the magnetic field barrier by effect of (i) collisions with neutral particles (ii) wall collisions and (iii) by effect of oscillations.³ Inside the channel, the neutrals are ionized in a region that often precedes the exit plane and the regions of maximum electric and magnetic fields. Such region is denoted as the ionization region, and is followed by the acceleration region, where ions are accelerated electrostatically to velocities in the order of 15 – 20 km/s. Finally, part of the electrons emitted by the cathode neutralize the plume, preventing a gradual charging-up of the spacecraft.

A number of different Hall thruster designs have been investigated over the years. For example, double-stage Hall thrusters have been proposed,

¹For this reason, Hall thrusters are referred to as “closed drift” devices.

²Of magnetic layer type.

³These effects are responsible for the anomalous transport observed in experiments.

allowing for a separate control between thrust and specific impulse by separating the ionization and acceleration stages [27]. Various magnetic configurations have also been proposed, with the aim of optimizing the plasma profile, or reducing wall erosion⁴ (see the magnetically shielded thrusters, [29, 30]).

The choice of the walls material proves to be crucial in a Hall thruster, as it dictates the temperature of wall-emitted electrons, and thus their diffusion across the magnetic field lines [25, 31]. An important variation of the insulating-walls design is obtained by employing conductive walls [32] instead of the frequently used boron nitride ceramic walls. In such conducting-wall thrusters, a part of the channel becomes electrically equipotential, and most of the acceleration happens in a thin region near the anode (thruster with anode layer, TAL). Wall-less configurations have also been investigated [33], aiming at directly solving the problem of wall erosion.

In this work, we will only consider the simple configuration of Fig. 1.1, often referred to as “magnetic layer Hall thruster”, or “Stationary Plasma Thruster” (SPT). Unless otherwise specified, all mentions to “Hall thrusters” in this work will refer to such configuration.

1.2 Modeling of low-temperature plasmas

The modeling of low-temperature plasmas encountered in electric propulsion devices can be tackled at different levels of accuracy. In the following, we shall give a brief introduction to some of the possible models, and highlight their range of validity and computational complexity. Most of the attention will be put on transport modeling, while a number of important topics (such as the detailed treatment of collisions, instabilities and particle-wall interactions [34, 35]) will not be discussed in detail, as to reflect the aim and focus of the present work.

At the simplest level, when collisions dominate the dynamics of each species, one can consider drift-diffusion models, that have proven effective for a range of problems for Torr-level discharges [36]. Such models solve for the density equations of the different charged species, assuming a simple diffusion-type relation between the drift velocity and the applied fields. The drift-diffusion model typically has a low computational effort, although the equations are parabolic, due to the presence of diffusion terms.⁵

For situations of lower collisionality, the diffusion laws become ques-

⁴See for example [28].

⁵This requires to satisfy the von Neumann condition on finite grids (see [37]), which is sub-optimal with respect to hyperbolic equations, that only need to respect the CFL conditions.

tionable, and drift-diffusion models can be replaced by multi-fluid formulations, where a larger set of equations is solved for each species [38], and the coupling happens through the electromagnetic fields and the inter-species collisional sources.⁶ The choice for the set of equations to be solved depends on the considered species and the operating conditions, a common choice being the set of mass, momentum and energy equations. This results in the so-called “fluid models”, typically consisting in the Euler equations of gas dynamics (one set of equations for each species) if the conduction and viscous terms are neglected, or the Navier-Stokes-Fourier (NSF) equations in the “hydrodynamic approach”.

Multi-fluid models based on the Euler/NSF equations are valid when the assumption of local thermodynamic equilibrium is satisfied, namely when the considered species have a (quasi-) Maxwellian distribution of particle velocities [39]. A first extension of such methods, commonly employed in plasma physics whenever magnetic fields are present, consists in including temperature anisotropy between the parallel and perpendicular directions [40]. However, as will also be discussed in this work, Hall thrusters happen to show further deviations from equilibrium [41]. Indeed, ions appear to be low-collisional, and strongly affected by the electric field. On the other hand, electrons are both magnetized and collisional [42, 43], resulting in skewed and asymmetric velocity distribution functions (VDF) [44].⁷ Non-equilibrium directly affects transport quantities, as the Euler/NSF convective fluxes may no longer be accurate due to the breaking apart of the closure assumptions. Moreover, Hall thrusters are known to show a wide range of plasma instabilities, whose origin and characteristics are kinetic in nature (see for example [47, 48]), and are known to heavily influence the electron cross-field transport [49].

In principle, all such kinetic effects could be described by solving the Boltzmann, Fokker-Planck or Vlasov kinetic equations, but at the price of a very high computational cost [50]. This ultimately reflects the high dimensionality of the kinetic equation (in case of a deterministic numerical solution [51, 52]), or the need to keep the statistical noise to an acceptable level (for Particle-in-Cell (PIC) methods [53]). Additionally, such methods are often time-explicit, and thus need to resolve the plasma frequency, forcing a rather small time step, and the Debye length, imposing tiny cell sizes. Various strategies have been proposed for reducing the computational cost of kinetic methods, such as scaling the thruster geometry [54, 55] or arti-

⁶Other possible coupling phenomena such as radiation will not be considered in this work.

⁷In this regard, Hall thrusters share a number of similarities with magnetron sputtering devices [45, 46], except that they typically operate at a much lower background pressure.

ficially modifying the vacuum permittivity [56], while preserving certain crucial plasma properties. However, such models in general do not guarantee that all kinetic features are properly preserved. Despite the high computational cost, kinetic methods are often employed for obtaining a deep understanding of selected features, often in reduced dimensionalities, as to reduce the computational complexity [57–59].

The hybrid fluid-PIC method is a commonly employed approach for speeding-up the calculations, while retaining some kinetic information [60, 61]. This approach is based on the observation that the electron dynamics is so fast that a quasi-steady state is reached at the ion time scales. In these models, one simulates ions (slow and low-collisional) as particles, while the electron population (more collisional due to the higher temperature and lower mass, and faster) is described by the Euler or NSF equations. These approaches simplify significantly the fast electron dynamics, still retaining a kinetic description for ions. However, of course, such methods assume that electrons have reached conditions close to local thermodynamic equilibrium, which is not necessarily the case in low-collisional $\mathbf{E} \times \mathbf{B}$ configurations.

Non-equilibrium fluid-like models: moment methods

In order to extend the validity of fluid models towards non-equilibrium, an option consists in enlarging the set of governing equations, as to include additional thermodynamic fields such as the heat flux vector, up to the desired order [40, 62]. Such formulations are commonly referred to as “moment methods”, and promise to increase the range of validity of fluid systems, while retaining affordable computational costs.

Among all possible formulations, we shall cite the Grad [63] and maximum-entropy [64, 65] families of moment methods. In both cases, one starts by assuming a shape for the distribution function, that can reproduce non-Maxwellian shapes. An equation is then written for each parameter appearing in the assumed distribution function, resulting in a set of moment equations, that include but extend the mass-momentum-energy description.

The Grad method has the strong advantage of providing a direct link between the shape of the VDF and its moments, but also has a series of drawbacks. For example, it does not guarantee that the VDF is positive. On the other hand, the maximum-entropy formulation is typically more robust, guarantees a positive VDF by construction, and is hyperbolic. Among its drawbacks, it should be mentioned that such formulation was shown unable to reproduce some states that would otherwise be physically realiz-

able [66]. Moreover, in this formulation, the link between the moments and the distribution function is not known analytically, and would require an entropy-maximisation problem to be solved at every occurrence during the simulations. The latter problem can however be mitigated through the use of approximated solutions [67], which make the maximum-entropy methods much more computationally affordable. For this reason, and in view of its robustness (even in non-equilibrium conditions), the maximum-entropy method will be the method of choice for this work. More details about its formulation and on the mentioned issues will be given in Chapter 2.

1.3 Objectives and structure of the thesis

1.3.1 Motivation

As discussed, moment methods are obtained by extending the fluid formulation, including additional equations for the higher order moments. These additional governing equations allow us to reproduce accurately a range of non-equilibrium states. Moreover, this is done at a computational cost that can be comparable to fluid methods, and is often much lower than the cost of a kinetic solution. Also, being based on PDEs, moment methods are not subject to the statistical noise that affects particle-based kinetic methods, and are suitable for the application of a broad range of optimization strategies.⁸ Methods that are at the same time computationally efficient and accurate in non-equilibrium situations will provide in the next future a useful tool for the design of Hall thrusters and low-temperature plasma devices in general.

Besides this specific application, one should consider that non-equilibrium situations are virtually ubiquitous in plasma physics. Many different moment formulations for plasma applications are actively being investigated [68–71] and are likely to become a broadly employed approach for the study of many plasma problems and for obtaining engineering predictions. Among all possibilities, we choose to investigate the maximum-entropy family of moment methods. Such methods have been studied in a range of conditions and for different problems, but their systematic application to plasmas is still missing in the literature. The accuracy of these methods, as well as their computational advantage over full kinetic approaches, are still to be investigated for most plasma problems, including Hall thrusters.

⁸Such as, for instance, adjoint optimization methods.

1.3.2 Aims of this work

This thesis aims at investigating the applicability of moment methods to the accurate description of the non-equilibrium conditions that characterize Hall thrusters. Particular emphasis will be put on the order-4 maximum-entropy moment methods. The thesis is centered around two tasks:

- After a theoretical introduction, the first part deals with developing the order-4 maximum-entropy moment method, that has been previously applied to rarefied and multiphase flows, but never to completely collisionless and charged gases, and in presence of electrical and magnetic fields;
- The second part is then devoted to the applications to Hall thrusters-like conditions. Different test cases are investigated, and the accuracy and computational cost of the maximum-entropy method are discussed, comparing it to kinetic solutions and to simpler moment methods.

Throughout the work, a number of heavy simplifications have been made. For instance, the collision operator will be often simplified with a BGK approximation, if not completely neglected. Even more drastically, all analysis of this work consider individual species and never couple them. Ions are studied independently from electrons, and the electric field (the only coupling element, if we neglect charge-charge collisions) is externally imposed. Of course, the coupling is a crucial feature of any real plasma.

However, in terms of the present work, the coupling constitutes an unnecessary complexity. Keeping in mind our goal of describing the problem using moment methods, aiming at retrieving as many kinetic features as possible, one can identify three sources of error: (i) the higher order closing moments appearing in the fluxes (ii) electro-magnetic source terms and (iii) the computation of collisional sources.⁹ The first two points reflect how accurately the moment method can represent the streaming of the distribution function in physical space (Point i) and velocity (Point ii). Point (iii) on the other hand reflects the collision operator and chemical production. Prior to considering full and coupled systems, it is here reputed that investigating the accuracy of the said points, individually, has priority. For this reason, rather than providing a full description of the plasma, the aim of the work is instead to give an accurate comparison of the methods in very controlled conditions.

⁹These points will be discussed in detail in the next sections.

Clearly, a number of further issues may arise when the coupling will be enabled, and additional careful studies will thus be required. Among other topics, this will be indeed one of the suggested future work activities.

1.3.3 Structure of this manuscript

This manuscript is structured as follows.

The Chapters 2 and 3 are introductory, and outline the theoretical foundations and numerical methods upon which this work is built. In particular, **Chapter 2** discusses some of the theoretical models that allow us to describe rarefied gases and plasmas. The chapter starts from kinetic theory and describes all sets of moment equations that will be employed in this work, including the Euler equations and the 5-moment and 14-moment (order-4) maximum-entropy systems. **Chapter 3** briefly discusses how the governing equations can be solved numerically.

The kinetic equation and the Euler equations are readily applied to rarefied gases and plasmas, and have been discussed in a broad literature both theoretically and numerically. On the other hand, the maximum-entropy systems have been covered only partially. **Chapter 4** discusses the further ingredients required in order to solve the maximum-entropy system in the required conditions, in terms of numerical solution (approximating the eigenvalues, identifying the proper numerical schemes) and modeling of the electromagnetic terms and their resulting dispersion relation.

All other chapters discuss applications to Hall thruster-like configurations. First, ions are considered: **Chapter 5** constitutes a first attempt at analyzing the problem. By considering the thruster channel as 1-dimensional, some analytical results are obtained for the axial velocity distribution function, and a simple moment method is developed. These results are compared to 2-dimensional kinetic simulations and experiments, and give both qualitative and quantitative information over the kinetic features to be expected.

Then, the ion description using the maximum-entropy systems is investigated in **Chapter 6**. The same test cases of the previous chapter is considered, together with other cases relevant for plasma physics and to Hall thrusters. In particular, a Tonks-Langmuir sheath is studied, together with ions in stationary and moving waves, in one and two dimensions. All along, a comparison between kinetic results, moments and the Euler equations is given.

Chapter 7 then tackles electrons modeling. As mentioned, electrons are magnetized, and this includes additional complexity to the problem.

Chapter 1. Introduction

The maximum-entropy description is first compared to analytical solutions from the literature, for 0-dimensional test cases. This is followed by the formulation of electron-neutral collisional terms, and the study of space homogeneous relaxation problems, and finally by the analysis of 1-dimensional problems, where electrons evolve along a thruster-like channel, in presence of a magnetic field barrier. This chapter completes the work on moment methods.

Chapter 8 considers a quite different problem, and discusses the neutral species injection and expansion into the Hall thruster channel. The analysis focuses on the residence time of neutral particles inside an imposed ionization region, and the corresponding ionization probability, resulting in the engine efficiency, is studied. An alternative injection configuration is then proposed: the propellant is injected from a slit located on the inner wall, close to the exit plane, and is directed towards the anode. The numerical analysis suggest that this configuration is associated to an increased mass utilization efficiency.

Finally, a concluding chapter is devoted to summarize the work, highlighting the main achievements and weaknesses, and some possible future developments are suggested.

CHAPTER 2

Kinetic and fluid modeling of gases and plasmas

This chapter introduces the governing equations for the description of rarefied gases and low-temperature plasmas. The numerical solution of such equations and the application to Hall thrusters configurations will be discussed in the next chapters.

The starting point for studying the behavior of a rarefied gas or plasma consists in analyzing the individual behavior of its particles. Only electrons and monoatomic species will be considered, since most often electric propulsion operates on noble gases.¹ In most electric propulsion applications, the particle energy is rather low (the electron energy is in the range of 1 – 100 eV, while heavy particles are slower and have a temperature roughly in the 1000 K range) and a non-relativistic description can be profitably employed. In this work, the internal (electronic) structure of atomic species will not be considered, hence all particles are considered as classi-

¹A notable exception consists in iodine-fed thrusters, currently being tested both in the lab and in orbit [72].

cal points evolving following the Newton's equations:

$$\begin{cases} \frac{d\mathbf{x}_i}{dt} = \mathbf{v}_i, \\ \frac{d\mathbf{v}_i}{dt} = \frac{\mathbf{F}_i}{m_i}, \end{cases} \quad (2.1)$$

where \mathbf{x}_i and \mathbf{v}_i are the position and velocity of the i -th particle, m_i its mass and \mathbf{F}_i all forces acting on it, including inter-particle interactions and external forces of electromagnetic nature. Inter-particle interactions depend on the considered species and divide in three categories: neutral-neutral, neutral-charged and charged-charged (Coulomb) interactions.

For macroscopic systems, one does not solve these equations directly, due to the large number of particles involved. Instead, a statistical formulation is introduced. Different strategies are possible at this point: one possibility consists in writing the equations using the Hamiltonian formalism, deriving the Liouville equation for the N-particles distribution function, and then expanding it in the BBGKY hierarchy and neglecting correlations [39, 73, 74]. This is the preferred approach in gas dynamics. Another strategy, common in plasma physics, consists in deriving the Klimontovich equation for the microscopic distribution function, and then applying an average operator to it [75–77]. In either case, one ends up with an equation for the one-particle distribution function f , discussed in the following.

This chapter is structured as follows. Section 2.1 introduces the kinetic equation (Boltzmann/Vlasov/BGK), that governs the evolution of the distribution function f . A non-dimensionalization of such equations allows one to extract dimensionless parameters, that can be profitably employed for understanding the operating regimes. This is done in Section 2.2, where the operating conditions of typical Hall thrusters are analyzed for electrons, ions and neutrals. In Section 2.3, the statistical microscopic formulation is connected to macroscopic thermodynamics through the definition of the moments of the distribution function. A generalized moment equation for the evolution of a given moment is discussed, and is employed to derive the pressureless gas approximation and the Euler equations of gas dynamics. Moment methods are also introduced as a generalization of the said systems. Section 2.4 then considers the maximum-entropy moment method, that will be employed in this work, discussing the governing equations and specifying the shape of the closing moments.

2.1 Kinetic theory

By “kinetic equation” we refer to an evolution equation for the one-particle velocity distribution function (VDF) $f_a(\mathbf{x}, \mathbf{v}, t)$:

$$\frac{\partial f_a}{\partial t} + \mathbf{v} \cdot \frac{\partial f_a}{\partial \mathbf{x}} + \frac{\mathbf{F}_a}{m_a} \cdot \frac{\partial f_a}{\partial \mathbf{v}} = \mathcal{C}_a, \quad (2.2)$$

where the subscript a specifies which species is being described, either electrons, ions or neutrals. The vector \mathbf{F}_a introduces external forces,² that accelerate the VDF along the velocity axes. The only forces considered here have electromagnetic nature and are described by the Lorentz force, $\mathbf{F}_a = q_a(\mathbf{E} + \mathbf{v} \times \mathbf{B})$, with \mathbf{E} and \mathbf{B} the electric and magnetic fields.³ These fields include the externally imposed fields and the self-consistent ones arising from space-charge distributions (Coulomb long-range interactions) and currents. These fields may be obtained through the Maxwell equations, or simply the Poisson equation in the electrostatic case.

In the general case, the VDF is defined in three physical space and three velocity dimensions, constituting the 6-dimensional phase space. This case will be denoted in the following chapters by 3D3V. Analogously, 1D1V refers to a 1-dimensional approximation both in space and velocity and corresponds to a gas of particles with only one velocity component, that evolves in one physical direction only.

The collision operator \mathcal{C}_a lumps the effect of all collisions, that are short-range interactions in the case of neutral-neutral and charged-neutral interactions, and only include the effect of short-range charged interactions.

The Boltzmann equation

Boltzmann derived the homonymous equation in the assumptions that

- Only binary collisions are accounted for (the gas is dilute);
- Correlations vanish in time and can be neglected (this is the “molecular chaos” assumption, that introduces irreversibility and leads to the H-theorem);
- Spatial variations of the distribution function are neglected for the sake of collisions (the problem must be sufficiently uniform).

²In Eq. (2.2), the forcing term was written out of the velocity gradient: this is correct for the Lorenz force, and whenever the forces do not depend on the particle velocity.

³Note that the velocity \mathbf{v} that multiplies the magnetic field \mathbf{B} is the velocity coordinate in the phase space, as different points in the phase space experience a different magnetic force.

In such cases, and for multi-species mixtures, the collision operator can be written as a sum of the contributions for each species in the mixture, denoted by c subscript in the following [39, 78]

$$\mathcal{C}_a = \sum_c \mathcal{C}_{ac} = \int (f'_a f'_c - f_a f_c) |\mathbf{v} - \mathbf{v}_c| b db d\epsilon d\mathbf{v}_c, \quad (2.3)$$

where f'_a and f'_c are evaluated using the inverse collision, b is the impact parameter and ϵ the angle of the collision cylinder. The collision operator can be rewritten as to let the collision cross-section emerge. In case of Coulomb collisions, the long-range nature of the forces introduces either the need to crop the integral at the Debye length, or to rewrite it as to obtain the Landau collision operator [79]. This will not be discussed further, as charge-charge collisions turn out to be unimportant for the conditions of this work (see Section 2.2).

A major consequence of the Boltzmann equation is the H-theorem, showing that a colliding gas eventually settles to the Maxwellian equilibrium distribution function,

$$\mathcal{M}_a = n_a \left(\frac{m_a}{2\pi k_B T_a} \right)^{3/2} \exp \left[-\frac{m_a (\mathbf{v} - \mathbf{u}_a)^2}{2k_B T_a} \right], \quad (2.4)$$

with n_a the gas number density, m_a the particle mass, k_B the Boltzmann constant, T_a the gas temperature, and \mathbf{u}_a the average velocity. Note that for particles having a single translational degree of freedom (such as in the case of a 1D1V description), the equilibrium Maxwellian takes an exponent of 1/2 in place of 3/2,

$$\mathcal{M}_a^{(1V)} = n_a \left(\frac{m_a}{2\pi k_B T_a} \right)^{1/2} \exp \left[-\frac{m_a (v - u_a)^2}{2k_B T_a} \right], \quad (2.5)$$

The Boltzmann operator results in an integro-differential kinetic equation, whose analytical solution is known only in a limited set of cases. A number of further simplifications are possible. We shall mention only a few here.

The BGK kinetic equation

A simplified form of the collision operator was proposed by Bhatnagar, Gross and Krook [80], where the VDF is assumed to relax towards a local Maxwellian. For a simple gas, the relaxation happens at a given rate, equal to the inverse of the collision frequency, $\tau = 1/\nu$, and we have:

$$\mathcal{C}_a = -\frac{f_a - \mathcal{M}_a}{\tau}. \quad (2.6)$$

2.2. The dimensionless kinetic equation: operating regime for electrons, ions and neutrals

This results in the BGK kinetic equation.⁴ This model automatically retrieves the H-theorem and is simple enough to allow for obtaining analytical solutions. However, its simplicity also brings a number of drawbacks. For example, besides resulting in the same relaxation rate for all moments of the distribution function, this model is known to reproduce a wrong Prandlt number of 1, in place of the value 2/3 that one may expect for monatomic gases (see for example [81, 82]).

Nonetheless, in view of its great simplicity, the BGK model has been applied to multiple different conditions, including multi-species gases with internal degrees of freedom [83–85]. Moreover, while the original model uses a macroscopic collision frequency, the model has been extended to include the dependence of the particles velocity [86, 87].

The Vlasov equation

Finally, plasmas (especially when fully ionized) may be substantially collisionless, when the density is low enough and the electric and magnetic fields dominate the dynamics. In such case, the collision operator is $\mathcal{C}_a = 0$ and one obtains the Vlasov equation,

$$\frac{\partial f_a}{\partial t} + \mathbf{v} \cdot \frac{\partial f_a}{\partial \mathbf{x}} + \frac{\mathbf{F}_a}{m_a} \cdot \frac{\partial f_a}{\partial \mathbf{v}} = 0. \quad (2.7)$$

2.2 The dimensionless kinetic equation: operating regime for electrons, ions and neutrals

In this section, we introduce a non-dimensionalization of the kinetic equation (2.2), and apply it to Hall thruster plasmas. This will allow us to compute the dimensionless numbers for electrons, ions and neutrals, and will thus give an insight on the operating regimes. This analysis is preliminary to the formulation of a simplified model, and allows us to understand what terms can be safely neglected.

Non-dimensionalisation is performed by first introducing a characteristic quantity for all variables, and then collecting them as to form dimensionless groups [73], resulting in the dimensionless kinetic equation,

⁴This choice for the collision operator leads to the “relaxation time approximation”, commonly employed in plasma physics

$$\left(\frac{L_0}{V_a t_0} \right) \frac{\partial \tilde{f}_a}{\partial \tilde{t}} + \tilde{\mathbf{v}} \cdot \frac{\partial \tilde{f}_a}{\partial \tilde{\mathbf{x}}} + \left(\frac{q_a E_0}{m_a V_a^2 / L_0} \right) \tilde{\mathbf{E}} \cdot \frac{\partial \tilde{f}_a}{\partial \tilde{\mathbf{v}}} \\ + \left(\frac{q_a B_0 V_a}{m_a V_a^2 / L_0} \right) (\tilde{\mathbf{v}} \times \tilde{\mathbf{B}}) \cdot \frac{\partial \tilde{f}_a}{\partial \tilde{\mathbf{v}}} = \left(\frac{\nu_a}{V_a / L_0} \right) \tilde{\mathcal{J}}_a + \left(\frac{\nu_{a,r}}{V_a / L_0} \right) \tilde{\mathcal{R}}_a \quad (2.8)$$

where dimensionless quantities are denoted by $\tilde{\bullet}$, the subscript 0 is a characteristic quantity common to all species (such as the thruster geometry) and characteristic quantities with subscript a are species-specific. The collision operator at the right hand side was splitted into non-reactive ($\tilde{\mathcal{J}}_a$) and reactive ($\tilde{\mathcal{R}}_a$) collisions. For the sake of the present simplified analysis, we will not detail further the effect of different inelastic collisional processes, and we will neglect recombination reactions.⁵ The terms inside the parentheses are respectively, from left to right:

- The Strouhal number, expressing the time scale for the considered species, with respect to the reference time t_0 ;
- The inverse of the Froude numbers for the electric and magnetic fields, ratio of the inertia and the electromagnetic forces;
- At the right hand side, the inverse of the Knudsen number, where $1/\text{Kn} \rightarrow 0$ gives collisionless conditions.

The relative importance of these terms gives an estimation of the regime of the various species. An accurate value for the reference dimensions and fields is not needed, and an estimate correct within an order of magnitude is sufficient. The values employed here are based on the SPT-100 thruster [88–90], $L_0 = 0.025$ m, $E_0 = 50\,000$ V/m, $B_0 = 0.02$ T. Other reference quantities are species-specific. The plasma density is taken as $n_e = n_i = 10^{18}$ m⁻³, and the neutral density is $n_n = 5 \times 10^{19}$ m⁻³. For electrons, we assume a temperature of $T_e = 80$ eV. Electrons are typically subsonic, therefore we take their characteristic velocity equal to the thermal velocity: $V_e \approx 6 \times 10^6$ m/s. Xenon singly charged ions are considered, whose mass is $m_i = 2.18 \times 10^{-25}$ kg, and with a temperature $T_i = 10\,000$ K. Since ions are typically supersonic, their characteristic velocity is taken as the bulk velocity, $V_i = 15\,000$ m/s. Neutrals are colder and slower. We assume $T_n = 500$ K and $V_n = 300$ m/s.

⁵Gas-phase recombination, being a three-body reaction, can be expected to be less important than ionization in the considered low-pressure and high temperature regimes.

Collision frequencies are computed as follows. First, the notation ν_{ab} denotes the collision frequency for a test particle of species a inside a population of species b . For neutral-neutral collisions, we assume a cross-section $\sigma_{nn} = 5.6 \times 10^{-19} \text{ m}^2$ (see [91]). The collision frequency is $\nu_{nn} = n_n \sigma_{nn} v_n^{th} \approx 8000 \text{ s}^{-1}$, with v_n^{th} the neutral thermal velocity. Elastic ion-neutral collisions would require to consider the induced dipole [92], but in terms of a rough estimate, we simply consider $\sigma_{in} = \sigma_{ni} \equiv \sigma_{nn}$. Therefore, $\nu_{ni} = n_i \sigma_{ni} V_i \approx 8400 \text{ s}^{-1}$, while $\nu_{in} = n_n \sigma_{in} V_i \approx 4.2 \times 10^5 \text{ s}^{-1}$. Particular care should be taken in formulating this assumption in case of charge-exchange collisions, where the cross-section could increase significantly [34]. For electron-neutral collisions, given the electron temperature, we consider the approximated value $\sigma_{en} = 10^{-19} \text{ m}^2$ [93, 94]. This gives $\nu_{en} = n_n \sigma_{en} V_e \approx 3 \times 10^7 \text{ s}^{-1}$ and will turn to be the leading collisional process in Hall thruster plasmas. Following this derivation, one would also write $\nu_{ne} = n_e \sigma_{en} V_e \approx 6 \times 10^5 \text{ s}^{-1}$. Part of this large collision frequency is responsible for ionization processes (and is thus crucial in terms of ion balance). However, elastic electron-neutral collisions have a small effect in the neutral momentum and energy, in view of the large mass ratio $m_e/m_n \approx 5 \times 10^{-6}$. For this reason, when considering the neutral kinetic equation, it is more meaningful to consider an effective collision frequency for momentum transfer, by weighted the original collision frequency by the mass ratio. We will use: $\nu_{ne}^{(mom)} = n_e \sigma_{en} V_e m_e / m_n \approx 2.5 \text{ s}^{-1}$.

Charge-charge collisions require to consider the plasma parameter Λ and the Coulomb logarithm [95, 96],

$$\Lambda = \frac{4\pi \varepsilon_0^{3/2}}{3e^3 \sqrt{n}} (k_B T_e)^{3/2} \implies \ln(\Lambda) \approx 14, \quad (2.9)$$

with $n = n_e = n_i$ the plasma density and T_e measured in [K]. The collision frequency of a test electron with other electrons (ν_{ee}) or with ions (ν_{ei}) is then estimated by

$$\nu_{ee} \approx \nu_{ei} \approx \frac{n_e e^4 \ln \Lambda}{\varepsilon_0^2 \sqrt{m_e} (k_B T_e)^{3/2}} \approx 2 \times 10^6 \text{ s}^{-1}, \quad (2.10)$$

while the ion-ion collision frequency is obtained as $\nu_{ii} \approx \nu_{ei} \sqrt{m_e/m_i} \approx 4000 \text{ s}^{-1}$. As mentioned for the neutral-electron collisions, the large mass ratio is such that electron-heavy collisions are inefficient in terms of momentum and energy exchange. Therefore, also for ion-electron collisions, we weight the collision frequency by the mass ratio, and write:

$$\nu_{ie}^{(mom)} = \nu_{ei} m_e / m_i \approx 10 \text{ s}^{-1}. \quad (2.11)$$

Finally, the characteristic time t_0 is arbitrary, and is here taken from the transit time of ions, $t_0 = L_0/V_i = 1.67 \mu\text{s}$.

Electrons

Considering the specified quantities, the dimensionless numbers for electrons become

$$(0.002) \frac{\partial \tilde{f}_e}{\partial \tilde{t}} + \tilde{\mathbf{v}} \cdot \frac{\partial \tilde{f}_e}{\partial \tilde{\mathbf{x}}} + (6.1) \tilde{\mathbf{E}} \cdot \frac{\partial \tilde{f}_e}{\partial \tilde{\mathbf{v}}} + (14.6) (\tilde{\mathbf{v}} \times \tilde{\mathbf{B}}) \cdot \frac{\partial \tilde{f}_e}{\partial \tilde{\mathbf{v}}} = \\ (0.008) \tilde{\mathcal{J}}_{ee} + (0.008) \tilde{\mathcal{J}}_{ei} + (0.125) \tilde{\mathcal{J}}_{en} + (1/\text{Kn}_{e,r}) \tilde{\mathcal{R}}_e. \quad (2.12)$$

Electrons are obviously seen to be much faster than ions (small Strouhal number), and this justifies the often employed steady state assumption, when only the ion or neutral time scales are of interest. This is due to their much higher velocity, associated to their small mass. Both the electric and the magnetic fields appear to be important. The magnetic field in particular will cause a rotation in the electrons velocities, such that a simple single-velocity 1V model is not applicable. Regarding the right hand side, collisions appear to have a much smaller effect, in particular Coulomb collisions are mostly negligible. Electron-neutral collisions are relatively dim, but they are the leading collisional term and as such they need to be retained. In particular, in a completely collisionless model, electrons would have no mechanism to cross the magnetic field lines, and the magnetic field would create a perfect confinement.⁶ On the other hand, in a real thruster, electrons crossing the magnetic field are crucial for the creation of an ionization region, and ultimately for the working of the Hall thruster.

Note that the magnitude of the chemical production source term (inverse of the Knudsen number for reactive collisions) was not specified in the previous equation. Indeed, whatever its magnitude, this term must be retained, as it is needed to balance out the ion charges produced in the ionization region, and ultimately to obtain a consistent simulation.

Ions

The magnitude for the dimensionless quantities for ions reads

$$(1) \frac{\partial \tilde{f}_i}{\partial \tilde{t}} + \tilde{\mathbf{v}} \cdot \frac{\partial \tilde{f}_i}{\partial \tilde{\mathbf{x}}} + (4.1) \tilde{\mathbf{E}} \cdot \frac{\partial \tilde{f}_i}{\partial \tilde{\mathbf{v}}} + (0.025) (\tilde{\mathbf{v}} \times \tilde{\mathbf{B}}) \cdot \frac{\partial \tilde{f}_i}{\partial \tilde{\mathbf{v}}} = \\ (10^{-5}) \tilde{\mathcal{J}}_{ie} + (0.007) \tilde{\mathcal{J}}_{ii} + (0.7) \tilde{\mathcal{J}}_{in} + (1/\text{Kn}_{i,r}) \tilde{\mathcal{R}}_i, \quad (2.13)$$

⁶If one neglects oscillations and instabilities.

where $\nu_{ie}^{(\text{mom})}$ was used in place of ν_{ie} , as previously discussed. The Strouhal number is unitary, due to our choice of the characteristic time. The Froude numbers show that ions are affected by the electric field but are substantially unmagnetized (as discussed in Chapter 1). In the following simulations, the magnetic field will be indeed completely neglected. Coulomb collisions also appear to be negligible, while, as for the electron population, collisions with background neutrals are not predominant (with respect to the electric field), but are not completely negligible either. Note that in the electron case, it was crucial to retain some collisional mechanism in order to have a non-zero cross-field mobility. For ions on the other hand, the magnetic field is negligible, and therefore collisions are not crucial. In the remaining of this work, ions will be treated as completely collisionless for simplicity, as often done in the Hall thrusters literature [27, 97–100]. Nonetheless, this assumption should be kept in mind and relaxed whenever possible. Also, it is important to stress that this assumption would become questionable if higher mass flow rates were employed, and would anyway completely lose its validity in the plume region, where the electric field rapidly decays to zero and ion-neutral collisions soon dominate the dynamics.

Finally, as done for the electrons, the reactive collision source has not been detailed. Indeed, whatever its value, this term is crucial for ions to build up inside the thruster.

Neutrals

For the neutral population, the kinetic equation is obviously simpler. Using the collision frequency $\nu_{ne}^{(\text{mom})}$ for the neutral-electrons collision in place of ν_{ne} , one has

$$(50) \quad \frac{\partial \tilde{f}_n}{\partial \tilde{t}} + \tilde{\mathbf{v}} \cdot \frac{\partial \tilde{f}_n}{\partial \tilde{\mathbf{x}}} = (10^{-4}) \tilde{\mathcal{J}}_{ne} + (0.7) \tilde{\mathcal{J}}_{ni} \\ + (0.66) \tilde{\mathcal{J}}_{nn} + (10 - 50) \tilde{\mathcal{R}}_n. \quad (2.14)$$

The relatively large value of the Strouhal number reflects the slower evolution of neutrals along the channel, with respect to the ions. In absence of the electric and magnetic terms, collisions become an important effect. The dimensionless numbers show that collisions may play a non-negligible role, somehow comparable to the convection itself. In particular, neutral-ion collisions (either momentum or charge exchange ones) are known to increase the average neutral velocity beyond the value $V_n = 300$ m/s considered here. Note that the value of the Knudsen number for such collisions

is slightly larger than one, meaning that the flow is significantly rarefied. In such conditions, gas-surface interactions are likely to play an equally important role, depending on the surface-to-volume ratio.⁷

Differently than for electrons and ions, the value of the Knudsen number for neutral ionization has been also given in the previous equation, based on the ionization frequency $\nu_{iz} = n_e \sigma_{iz} V_e \approx 6 \times 10^5 \text{ s}^{-1}$. Using the whole channel length results in an inverse Knudsen number of 50, while a more reasonable estimate would consider that ionization happens mostly inside the ionization region, whose length is approximately 5 mm [90]. This gives a somewhat lower estimate of 10. These high values are expected, as they confirm that the thruster is indeed effectively ionizing the propellant.

2.3 Fluid formulations: moments of the kinetic equation

As discussed, the kinetic equation is, in its most general case, 6-dimensional. Numerical solvers must therefore deal with memory and computational requirements that are often excessive for present day simulations. Moreover, the information contained in the kinetic equation may be sometimes unnecessarily detailed, and a much coarser description could be enough. These observations motivate the derivation of fluid models, where only few statistical moments of the distribution function are described. In this section, the subscript “ a ” will be dropped for simplicity.

2.3.1 Moments of the distribution function

All macroscopic fields that compose the classical fluid dynamic descriptions (such as the Navier-Stokes equations or the MHD formulations) are statistical moments of the distribution function and are obtained by integrating the VDF over the velocity space [39]. This removes the dependence of the VDF on the particle velocity variable, and results in a quantity that depends on space and time. From the definition of the VDF, the number density reads

$$n(\mathbf{x}, t) = \iiint_{-\infty}^{+\infty} f(\mathbf{x}, \mathbf{v}, t) \, dv_x \, dv_y \, dv_z. \quad (2.15)$$

The integrals range from $-\infty$ to $+\infty$, spanning all velocity space. In other words, all particles contributing to the VDF are accounted for. The

⁷Since surfaces are introduced into the model as boundary conditions of the kinetic equation, this effect does not appear automatically in this analysis.

mass density is $\rho = mn$. The (average) momentum is obtained by weighting the VDF by the particle momentum,

$$\rho(\mathbf{x}, t) u_i(\mathbf{x}, t) = \iiint_{-\infty}^{+\infty} m v_i f(\mathbf{x}, \mathbf{v}, t) dv_x dv_y dv_z. \quad (2.16)$$

By computing moments of the distribution function about the average velocity u_i , one obtains central moments. These moments do not depend anymore on the velocity, but instead describe the purely thermodynamic state of the gas, and allow us to identify non-equilibrium. The pressure tensor components are second order central moments, defined as

$$P_{ij}(\mathbf{x}, t) = \iiint_{-\infty}^{+\infty} m(v_i - u_i)(v_j - u_j) f(\mathbf{x}, \mathbf{v}, t) dv_x dv_y dv_z. \quad (2.17)$$

Where the hydrostatic pressure is $P = (P_{xx} + P_{yy} + P_{zz})/3$. In this work, we will consider perfect gases, such that $P = n k_B T$. Note that a separate temperature can be defined for each axis, such that $P_{xx} \equiv P_x = n k_B T_x$, and the same for the y and z components. From the kinetic definition, it is clear that the temperatures give an indication of the width of the distribution function along the three velocity axes. Using the same notation, the energy of a particle with three translational degrees of freedom would read

$$\rho(\mathbf{x}, t) E(\mathbf{x}, t) = \frac{\rho u^2}{2} + \frac{3}{2} n k_B T = \iiint_{-\infty}^{+\infty} \frac{m v^2}{2} f(\mathbf{x}, \mathbf{v}, t) dv_x dv_y dv_z. \quad (2.18)$$

The heat flux vector is an order-3 central moment and is here defined as

$$q_i(\mathbf{x}, t) = \iiint_{-\infty}^{+\infty} m c^2 c_i f(\mathbf{x}, \mathbf{v}, t) dv_x dv_y dv_z. \quad (2.19)$$

where the peculiar velocity $c_i = v_i - u_i$ was defined. Note that in much of the literature, the heat flux definition embeds a factor $1/2$. Unless specified otherwise, in this work we employ the definition of Eq. (2.19) to be consistent with the definitions that will follow. Being an odd-order central moment, the heat flux indicates the skewness of the VDF, and being proportional to the cube of the peculiar velocity, it is particularly sensitive to the tails of the VDF. The mentioned moments are employed in most fluid dynamic descriptions. However, there is no limit in the number of moments that can be computed. In particular, in the present work we will need moments up to an order 5 of the velocity, that we define in the following.

After having defined the heat flux vector, a heat flux tensor can also be introduced,

$$Q_{ijk}(\mathbf{x}, t) = \iiint_{-\infty}^{+\infty} m c_i c_j c_k f(\mathbf{x}, \mathbf{v}, t) dv_x dv_y dv_z. \quad (2.20)$$

Clearly, q_i can be obtained from the contractions of Q_{ijk} . Denoting a summation by repeated indices, we use the notation:

$$q_i = Q_i \equiv Q_{iij}. \quad (2.21)$$

A rank 2 tensor is then defined for the order-4 moment, R_{ijkk} ,

$$R_{ijkk}(\mathbf{x}, t) = \iiint_{-\infty}^{+\infty} m c_i c_j c^2 f(\mathbf{x}, \mathbf{v}, t) dv_x dv_y dv_z, \quad (2.22)$$

and its contraction $R_{iijj} = R_{xxkk} + R_{yykk} + R_{zzkk}$,

$$R_{iijj}(\mathbf{x}, t) = \iiint_{-\infty}^{+\infty} m c^4 f(\mathbf{x}, \mathbf{v}, t) dv_x dv_y dv_z, \quad (2.23)$$

At equilibrium, when the VDF is Maxwellian, this moment can be shown to take the value $R_{iijj} = 15P^2/\rho$. This moment is connected to the kurtosis of the VDF. Finally, a vector containing order-5 moments is also defined as

$$S_{ijjk}(\mathbf{x}, t) = \iiint_{-\infty}^{+\infty} m c_i c^4 f(\mathbf{x}, \mathbf{v}, t) dv_x dv_y dv_z. \quad (2.24)$$

The moments described in the previous equations are a total of 29 independent scalar quantities: the density, 3 velocity components, 6 entries for the pressure tensor, 10 for Q_{ijk} , 6 for R_{ijkk} and 3 for S_{ijjk} . No further moments will be needed in the present work, except for their contractions. It should be noted that all odd-order central moments are zero for symmetric VDFs.

Moments of the 1V distribution function

In case the kinetic equation is formulated as to describe one only component of the particle velocity (“1-dimensional physics”), the moments of the 1V VDF are obtained as a single integral. The 29 independent moments reduce to a small set of 5 moments, defined as

$$\rho = \int_{-\infty}^{+\infty} m f(v) dv, \quad (2.25a)$$

$$\rho u = \int_{-\infty}^{+\infty} m v f(v) dv, \quad (2.25b)$$

$$P = \int_{-\infty}^{+\infty} m(v-u)^2 f(v) dv, \quad (2.25c)$$

$$Q = \int_{-\infty}^{+\infty} m(v-u)^3 f(v) dv, \quad (2.25d)$$

$$r = \int_{-\infty}^{+\infty} m(v-u)^4 f(v) dv, \quad (2.25e)$$

$$s = \int_{-\infty}^{+\infty} m(v-u)^5 f(v) dv. \quad (2.25f)$$

Dimensionless moments

As seen, all moments are proportional to the particle mass and to an increasing power of the velocity. An effective adimensionalization can thus be performed by dividing the moments by ρ and by a power of the quantity $\sqrt{P/\rho}$, that is fundamentally a thermal velocity. By doing this non-dimensionalization on the density, momentum and hydrostatic pressure, we find

$$\rho^* = 1, \quad u_i^* = u_i / \sqrt{P/\rho}, \quad P^* = 1, \quad (2.26)$$

while the dimensionless central moments read

$$P_{ij}^* = P_{ij} / \left[\rho (P/\rho)^{2/2} \right], \quad (2.27a)$$

$$Q_{ijk}^* = Q_{ijk} / \left[\rho (P/\rho)^{3/2} \right], \quad (2.27b)$$

$$R_{ijkk}^* = R_{ijkk} / \left[\rho (P/\rho)^{4/2} \right], \quad (2.27c)$$

$$S_{ijjkk}^* = S_{ijjkk} / \left[\rho (P/\rho)^{5/2} \right], \quad (2.27d)$$

The contractions q_i^* and R_{iijj}^* are obtained in the same way.

2.3.2 The generalized moment equation

The moments definition can be generalized by denoting the particle quantities by ψ , and computing the moment of the VDF weighted by ψ as

$$M_\psi = \iiint_{-\infty}^{+\infty} \psi(\mathbf{v}) f(\mathbf{x}, \mathbf{v}, t) d\mathbf{v} \equiv \langle \psi(\mathbf{v}) \rangle. \quad (2.28)$$

Considering that $f(\mathbf{x}, \mathbf{v}, t) = n g(\mathbf{x}, \mathbf{v}, t)$, with n the number density and g the normalized distribution function, the moment M_ψ represents the averaged value of $\psi(\mathbf{v})$ over the normalized distribution of particle velocities, further scaled by the number density. For example, the choice $\psi = m$ would result in the mass density, while $\psi = mv_x$ would result in the average momentum along x . By multiplying by ψ the whole kinetic equation

and then applying the average operator, one obtains a governing equation for the moment M_ψ , reading [39]

$$\frac{\partial \langle \psi \rangle}{\partial t} + \frac{\partial}{\partial \mathbf{x}} \cdot \langle \mathbf{v} \psi \rangle = \frac{q}{m} \left\langle (\mathbf{E} + \mathbf{v} \times \mathbf{B}) \cdot \frac{\partial \psi}{\partial \mathbf{v}} \right\rangle + \iiint \psi \mathcal{C} d\mathbf{v}. \quad (2.29)$$

This equation has an important characteristic: while writing it for a moment $M_\psi = \langle \psi \rangle$ of a given order n , the convective fluxes $\langle \mathbf{v} \psi \rangle$ introduce a moment of order $n + 1$ in the velocity. This requires that one also writes an equation for the moment $n + 1$, that in turn will require the moment of order $n + 2$. The resulting system is not closed, and an infinite number of moment equations would be required to recover the kinetic equation. Practically speaking, one truncates the series at a certain point, or following certain assumptions. The set of equations resulting from such choice will be denoted by “moment method” and in conservative form are written as

$$\frac{\partial \mathbf{U}}{\partial t} + \frac{\partial}{\partial \mathbf{x}} \cdot [\mathbf{F}_x, \mathbf{F}_y, \mathbf{F}_z] = \mathbf{G}_{\text{EB}} + \mathbf{G}_c, \quad (2.30)$$

where \mathbf{U} is the vector of moments, \mathbf{F}_i are the vectors of convective fluxes, with $i = x, y, z$ and \mathbf{G}_{EB} and \mathbf{G}_c the electromagnetic and collisional source terms respectively.

2.3.3 Pressureless gas, Euler equations and moment methods

As seen in the previous section, the choice of a set of particle quantities ψ results in a set of governing equations for the respective moments, that can be closed by formulating some assumption. We shall illustrate here two noteworthy examples, namely the pressureless gas system and the Euler equations. More general strategies will be then introduced.

The pressureless gas formulation

The simplest formulation can be obtained by writing a governing equation for the particle mass, choosing $\psi = m$, and three equations for the particle momentum, obtained from $\psi = mv_i$. The higher order moments (that require a closure) are the pressure terms P_{ij} . In the limiting case of a gas where the convective fluxes are much larger than the thermal ones, one may decide to neglect these contributions.⁸ The resulting system is known as the pressureless gas formulation (sometimes called “cold gas”), and correspond to prescribing that the VDF is a Dirac delta in velocity space, centered on

⁸This can be an effective choice in some situations, but results in discontinuities known as δ -shocks.

the bulk velocity. The set of equations (2.30) is defined by

$$\mathbf{U} = \begin{pmatrix} \rho \\ \rho u_x \\ \rho u_y \\ \rho u_z \end{pmatrix}, \quad \mathbf{F}_i = \begin{pmatrix} \rho u_i \\ \rho u_i u_x \\ \rho u_i u_y \\ \rho u_i u_z \end{pmatrix}, \quad \mathbf{G}_{\text{EB}} = \frac{\rho q}{m} \begin{pmatrix} 0 \\ E_x + u_y B_z - u_z B_y \\ E_y + u_z B_x - u_x B_z \\ E_z + u_x B_y - u_y B_x \end{pmatrix}, \quad (2.31)$$

where the x,y and z convective fluxes are obtained by choosing $i = x, y, z$. The formulation of the collisional source term \mathbf{G}_c depends on the specific case and the type of collisions to be considered. The pressureless gas system will be employed for the description of ions in Section 6.6.

The Euler equations of gas dynamics

The choice $\psi = m(1, v_i, v^2/2)$ extends the previous description, by also considering the energy of the particle. This results in the Euler equations of gas dynamics, where the chosen closure consists in assuming that higher order moments are zero (the heat flux q_i in this case) and that the pressure tensor is isotropic. The equations read

$$\mathbf{U} = \begin{pmatrix} \rho \\ \rho u_x \\ \rho u_y \\ \rho u_z \\ \frac{1}{2}\rho u^2 + \frac{1}{\gamma-1}P \end{pmatrix}, \quad \mathbf{F}_i = \begin{pmatrix} \rho u_i \\ \rho u_i u_x + P\delta_{xi} \\ \rho u_i u_y + P\delta_{yi} \\ \rho u_i u_z + P\delta_{zi} \\ \frac{1}{2}\rho u^2 u_i + \frac{\gamma}{\gamma-1}P u_i \end{pmatrix}, \quad (2.32)$$

where δ_{ij} is the Kronecker delta, and γ is the specific heats ratio (adiabatic constant), with $N/2 = 1/(\gamma - 1)$, where N is the number of degrees of freedom (DOF) for the considered species. Particles that show only three DOFs (no internal energy) have $N = 3$, and therefore $\gamma = 5/3$. In the case of a gas described by one single degree of freedom, only a single component of velocity should be retained (say, v_x) and the other moments are to be discarded. The adiabatic constant is then obtained from the choice $N = 1$, resulting in $\gamma = 3$.

The electromagnetic source term for the Euler equations is easily ob-

tained as

$$\mathbf{G}_{\text{EB}} = \frac{\rho q}{m} \begin{pmatrix} 0 \\ E_x + u_y B_z - u_z B_y \\ E_y + u_z B_x - u_x B_z \\ E_z + u_x B_y - u_y B_x \\ E_x u_x + E_y u_y + E_z u_z \end{pmatrix}. \quad (2.33)$$

Also in this case, the collision terms \mathbf{G}_c depend on the process and species to be considered and will not be detailed here.

At a kinetic level, the aforementioned closure assumptions correspond to prescribing that the VDF is symmetric. The Maxwellian is a particular case of a symmetric VDF, that further results in a zero collisional source term, for what concerns collisions between particles of the same species. Other collisions terms may still be non-zero.⁹

Moment methods, the Chapman-Enskog expansion and the Grad closure

Strictly speaking, the term “moment methods” refers to modeling the problem by a system of moment equations, closed by some assumption.¹⁰ The pressureless gas system and the Euler systems are two simple examples of (rather low order) moment methods, and they were obtained by an intuitive choice of the particle quantities ψ . A number of general formulations have been proposed in the years, with varying degree of success and generality, and we shall discuss here some of them.

The Chapman-Enskog expansion [101] is a common strategy to find a closure to the moment equations, and consists in expanding the VDF in powers of a small parameter ϵ (proportional to the inverse of the Knudsen number),

$$f = f^{(0)} + \epsilon f^{(1)} + \epsilon^2 f^{(2)} + \dots, \quad (2.34)$$

where $f^{(0)}$ is the local Maxwellian and the other terms are corrections of progressively higher order. The choice of the maximum order of ϵ to be retained results in a set of governing equations of increasing complexity. For a Maximum order ϵ^0 , one retrieves the Euler equations. At the order ϵ^1 on the other hand, the Navier-Stokes-Fourier equations are retrieved. At a higher order, one obtains the Burnett [102] and super-Burnett systems, that are however unstable to certain wavelengths [62] and are not well behaved in terms of entropy production [103]. Various corrections to these problems have been proposed through the years (see for example [104]). Also,

⁹For example, electron collisions with background neutrals.

¹⁰Traditionally, in the fluid dynamic community, moment methods are refer to systems at least one order higher than the Euler/NSF equations, thus writing governing equations for moments of higher order than the energy.

detailed studies have been performed on the Chapman-Enskog method, extending it towards multi-component plasmas, and including multiscale analyses of the streaming and collision terms [105]. However, the behavior of the Burnett and super-Burnett systems shows that the Chapman-Enskog closure works well only for moderate deviations from equilibrium, and a different formulation is in order if one wishes to reach higher orders.

Another general approach towards obtaining a closed set of moment equations is the Grad method [63], that consists in expanding the VDF in a series of N-dimensional Hermite polynomials of the velocity $\mathcal{H}^{(n)}(\mathbf{v})$, weighted by a set of coefficients $a^{(n)}$,

$$f = f_0 \left(1 + a_i^{(1)} \mathcal{H}_i^{(1)} + \frac{1}{2} a_{ij}^{(2)} \mathcal{H}_{ij}^{(2)} + \dots + \frac{1}{N!} a_{ij\dots q}^{(N)} \mathcal{H}_{ij\dots q}^{(N)} \right) \quad (2.35)$$

where f_0 is again the local Maxwellian. The moment equations are closed by truncating such series, putting all coefficients $a^{(n)}$ above a certain order equal to zero. This formulation has been broadly employed in plasma physics, see for example the classical works of Zhdanov [40], Balescu [106] and Braginskii [107], where the 13, 21 and 29-moment approximations are discussed. The Grad formulation has an important advantage, namely the moments of the distribution function f are directly mapped to the coefficients $a^{(n)}$. In terms of its drawbacks, it is important to notice that in order to retrieve strong non-equilibrium conditions, it has been shown that the number of required moments may be rather large [108, 109], with a significant increase in the computational complexity. Also, the Grad closure is known to suffer from a limited region of hyperbolicity [110], such that the eigenvalues of the fluxes Jacobian may develop an imaginary part. Finally, for strong non-equilibrium situations, the Grad method does not guarantee that the VDF remain positive, and the method may generate unphysical subshocks beyond a certain Mach number [62], thus requiring a regularization [111, 112].

A number of other formulations have been developed in the years (see for example the Quadrature Moments [113, 114] or the Pearson Distribution [68, 115] formulations). Among all possible formulations, we shall focus on the “maximum-entropy” family of moment methods, whose order-4 member will be investigated in this work.

2.4 The maximum-entropy closure

This section introduces the maximum-entropy family of moment methods, that will be central in this work. For a complete introduction to the method, the reader is referred to [64, 65, 116], and for an application to different problems including microfluidics and radiation transport, [117–122].

The idea behind the maximum-entropy method is the following: for a given state of the gas, described by a finite set of moments \mathbf{U} , an infinite number of possible distribution functions exist; among these, the maximum-entropy method considers the distribution that maximises the entropy of the system, $\sigma = f \log f$. In a statistical sense, this corresponds to selecting the most probable distribution, given the limited amount of information about its moments \mathbf{U} . The resulting VDF takes the form of an exponential of a polynomial of the particle velocity,

$$f = \exp [\boldsymbol{\alpha}^T \Psi(\mathbf{v})] , \quad (2.36)$$

where Ψ is a vector of monomials of the particle velocity \mathbf{v} (where the maximum power of \mathbf{v} defines the order of the approximation), while $\boldsymbol{\alpha}$ is the vector of the corresponding weights. Provided that the order of the highest-power velocity monomial inside Ψ is even, and that the respective coefficient is negative, the maximum-entropy VDF is bounded. Also, it is always positive (since the exponential of a real number is positive), which is a strong advantage over the Grad system, especially if strong non-equilibrium conditions are targeted. Moreover, the resulting system of governing equations for the moments can be shown to be hyperbolic whenever the underlying entropy maximisation problem is solvable.

In order to ensure that the moments of the distribution function f are equal to \mathbf{U} , one writes the condition:

$$\mathbf{U} - \iiint_{-\infty}^{+\infty} \Psi \exp [\boldsymbol{\alpha}^T \Psi] d\mathbf{v} = 0 . \quad (2.37)$$

Since the maximum-entropy distribution has been employed, this is known as the “entropy-maximisation problem”, where one aims at finding the vector of coefficients $\boldsymbol{\alpha}$ that realize such condition. Practically speaking, one often solves a slightly different problem: after the vector Ψ has been defined, the functional J is maximised for a set of target moments \mathbf{U} , where J is defined as

$$J = \iiint_{-\infty}^{+\infty} \exp [\boldsymbol{\alpha}^T \Psi] d\mathbf{v} - \boldsymbol{\alpha}^T \mathbf{U} , \quad (2.38)$$

where the condition of zero gradient $\partial J/\partial \boldsymbol{\alpha} = 0$ retrieves Eq. (2.37). After this problem is solved, the maximum-entropy distribution f is fully defined, and the closing moments appearing in the moment equations can be obtained by integration.

Besides the mentioned advantages, this method also has a number of drawbacks. In particular, the entropy maximisation problem proves to be non-trivial for the methods above order 2. This requires to employ computationally expensive numerical solutions. Also, for orders above 2, the maximum-entropy method happens to embed a region of non-realizability in the moment space, referred to as the Junk subspace [66, 123], such that some states that would be physically realizable (as defined from the solution to the Hamburger problem [124]) cannot be properly reproduced by a VDF in the form of Eq. (2.36). This region, associated to a singularity in the fluxes, reaches the equilibrium point. As will be discussed in Section 4.2, the wave speeds may grow unbounded as the singularity is approached, and some additional care is required in the numerical solution.

Order-2 maximum-entropy method: the Euler equations

As a first example, we shall analyze the choice $\Psi = (1, v_i, v^2)$, with $i = x, y, z$. This gives an order-2 method, from the maximum power appearing in Ψ . The corresponding maximum-entropy VDF happens to be a Maxwellian, that is thus a particular case of this formulation,

$$f = \exp(\alpha_0 + \alpha_i v_i + \alpha_2 v^2) \equiv A \exp[B(v_i - u_i)^2]. \quad (2.39)$$

For this system, the entropy maximisation problem of Eq. (2.37) is trivial. Indeed the coefficients $\alpha_0, \alpha_i, \alpha_2$ are easily mapped to the moments of the Maxwellian VDF, observing that $A = n(m/2\pi k_B T)^{3/2}$ and $B = -m/2k_B T$, and the α coefficients are therefore obtained. All closing moments will be zero, since this VDF is symmetric, and one finally obtains the Euler equations of gas dynamics.

Order-2 maximum-entropy method: the anisotropic Euler equations

The Maxwellian case is not the only order-2 member of the family of maximum-entropy methods. A more general choice would be $\Psi = (1, v_i, v_i v_j)$, that has 10 independent entries. The resulting maximum-entropy VDF is

$$f = \exp(\alpha_0 + \alpha_i v_i + \alpha_{ij} v_i v_j) \equiv A \exp\left[\sum_i B_i (v_i - u_i)^2\right], \quad (2.40)$$

that is an anisotropic Gaussian. Also for this system, the vector of coefficients α is easily mapped to the moments of the VDF. This choice results in a system composed by 10 governing equations, that can represent temperature anisotropy, but still assume a symmetric VDF, thus resulting in a zero heat flux.

2.4.1 Order-4 maximum-entropy method: 14-moment system

The next level after the order-2 methods, are the order-4 maximum-entropy systems.¹¹ A number of different choices are possible for the vector Ψ , but the simplest is [64]

$$\Psi = (1, v_i, v_i v_j, v_i v^2, v^4) , \quad (2.41)$$

that has 14 different entries and will result in a 14-moment system. The maximum-entropy VDF reads

$$f_{14} = \exp(\alpha_0 + \alpha_i v_i + \alpha_{ij} v_i v_j + \alpha_{i,3} v_i v^2 + \alpha_4 v^4) . \quad (2.42)$$

Despite being the simplest member of the order-4 maximum-entropy methods, this VDF is very flexible. For example, this VDF includes as liming cases the Maxwellian and the Gaussian distributions. Moreover, if all coefficients except α_4 are zero, it can be seen to retrieve the Druyvestein distribution [2, 125]. This VDF can be both asymmetrical (thus allowing for an heat flux) and anisotropic, and by effect of α_4 it can reproduce ring-like distributions. The resulting system of moment equations reads, in index form,

$$\frac{\partial}{\partial t} \rho + \frac{\partial}{\partial x_i} (\rho u_i) = G_1 , \quad (2.43a)$$

$$\frac{\partial}{\partial t} (\rho u_i) + \frac{\partial}{\partial x_j} (\rho u_i u_j + P_{ij}) = G_{2,3,4} , \quad (2.43b)$$

$$\begin{aligned} \frac{\partial}{\partial t} (\rho u_i u_j + P_{ij}) + \frac{\partial}{\partial x_k} (\rho u_i u_j u_k + u_i P_{jk} + u_j P_{ik} \\ + u_k P_{ij} + Q_{ijk}) = G_{5-10} , \end{aligned} \quad (2.43c)$$

$$\begin{aligned} \frac{\partial}{\partial t} (\rho u_i u_j u_k + u_i P_{jj} + 2u_j P_{ij} + Q_{ijj}) \\ + \frac{\partial}{\partial x_k} (\rho u_i u_k u_j + u_i u_k P_{jj} + 2u_i u_j P_{jk} + 2u_j u_k P_{ij} + u_j u_k P_{ik} \\ + u_i Q_{kjj} + u_k Q_{ijj} + 2u_j Q_{ijk} + R_{ikjj}) = G_{11,12,13} , \end{aligned} \quad (2.43d)$$

¹¹As mentioned, no order-3 closure exist, as this would generate an unbounded maximum-entropy VDF.

$$\begin{aligned} & \frac{\partial}{\partial t} (\rho u_i u_i u_j u_j + 2u_i u_i P_{jj} + 4u_i u_j P_{ij} + 4u_i Q_{ijj} + R_{iijj}) \\ & + \frac{\partial}{\partial x_k} (\rho u_k u_i u_i u_j u_j + 2u_k u_i u_i P_{jj} + 4u_i u_i u_j P_{jk} + 4u_i u_j u_k P_{ij} + 2u_i u_i Q_{kjj} \\ & + 4u_i u_k Q_{ijj} + 4u_i u_j Q_{ijk} + 4u_i R_{ikjj} + u_k R_{iijj} + S_{kijj}) = G_{14}, \quad (2.43e) \end{aligned}$$

where the heat flux vector is denoted by Q_{ijj} , and represents the contraction over Q_{ijk} terms. The source terms G at the right hand side include both electromagnetic and collisional contributions. The collisional sources depend on the considered species (for a single species BGK collision operator, the reader is referred to [67, 126]). The electromagnetic sources will be developed in Section 4.5.

A solution of this system requires to specify the closing moments Q_{ijk} , R_{iikk} and S_{ijjkk} . These moments could be computed from the VDF, that in turn is obtained by solving the entropy-maximisation problem. Unfortunately, this problem happens to be rather complex for the 14-moment formulation, and no algebraic solution is known. Therefore, in order to find the f_{14} VDF from a set of target moments (and therefore, to compute the closing terms of the moment system), one has to solve the problem numerically, often done by employing iterative methods. During a simulation, such procedure needs to be done at each time step and for each cell in the domain, dramatically increasing the computational time, up to the point that the method may be no longer convenient with respect to a fully kinetic method.

Luckily, some interpolative approximations to the entropy maximisation problem have been developed for the 14-moment system, allowing for affordable CFD computations [67]. These formulations bypass the entropy maximisation problem and directly give the closing moments as a function of the moments \mathbf{U} . For all details, the reader is referred to the original paper, and only the main ingredients will be illustrated here. The closure starts from the definition of a parabolic mapping of moment space, introducing a parameter σ that assumes a value $\sigma \rightarrow 0$ in correspondence of the Junk subspace (and thus, also the equilibrium point) and $\sigma = 1$ at the physical realizability boundary:

$$\begin{aligned} \sigma = \frac{1}{4P_{ij}P_{ji}} & \left[2P_{ij}P_{ji} + P_{ii}P_{jj} - \rho R_{iijj} \right. \\ & \left. + \sqrt{(2P_{ij}P_{ji} + P_{ii}P_{jj} - \rho R_{iijj})^2 + 8\rho P_{mn}P_{nm}Q_{kii}(P^{-1})_{kl}Q_{ljj}} \right]. \quad (2.44) \end{aligned}$$

The closing moments are then written as

$$R_{ijkk} = \frac{1}{\sigma} Q_{ijl} (P^{-1})_{lm} Q_{mkk} + \frac{2(1-\sigma)P_{ik}P_{kj} + P_{ij}P_{kk}}{\rho}, \quad (2.45)$$

with the elements of the heat flux tensor defined by

$$Q_{ijk} = K_{ijkm} Q_{mnn}, \quad (2.46)$$

where the matrix K_{ijkm} is defined as

$$K_{ijkm} = [2P_{il}(P^2)_{jk} + 2P_{kl}(P^2)_{ij} + 2P_{jl}(P^2)_{ik}] B_{lm}^{-1}, \quad (2.47)$$

and with the matrix B_{lm} defined as

$$B_{lm} = 2P_{lm}(P^2)_{\alpha\alpha} + 4(P^3)_{lm}. \quad (2.48)$$

The remaining moments S_{ijjkk} read

$$S_{ijjkk} = \frac{1}{\sigma^2} P_{kn}^{-1} P_{lm}^{-1} Q_{npp} Q_{mjj} Q_{ikl} + 2\sigma^{1/2} \frac{P_{jj}Q_{ikk}}{\rho} + (1-\sigma^{1/2}) W_{im} Q_{mnn}, \quad (2.49)$$

Note that in this expression a power of σ equal to $1/2$ is used, differently from the original paper where a coefficient $3/5$ was employed, as it has been later shown to provide better results. The matrix W_{im} appearing in the expression is defined as

$$W_{im} = \frac{1}{\rho} [2P_{il}(P_{\alpha\alpha})^3 + 12P_{il}(P^3)_{\alpha\alpha} + 14(P^2)_{\alpha\alpha}(P^2)_{il} + 20P_{\alpha\alpha}(P^3)_{il} + 20(P^4)_{il} - 2(P^2)_{\alpha\alpha}P_{\beta\beta}P_{il} - 6(P_{\alpha\alpha})^2(P^2)_{il}] B_{lm}^{-1}. \quad (2.50)$$

It is important to notice that the presented interpolative closure is not entirely hyperbolic, and the eigenvalues may show some slight imaginary part in some regions of the moment space (see Appendix C). This does not bring particular issues into the computation. Also, it should be noted that different interpolative closures have been developed in other references (see [127]), providing an interpolation of increased accuracy in certain regions of the moment space. These will not be considered in the present work.

Finally, we shall report here the expressions of the physical realizability boundary and of the Junk subspace. The former is obtained by the solution of the Hamburger problem and reads

$$R_{iijj} \geq (Q_{kii} (P^{-1})_{kl} Q_{ljj} + P_{ii}P_{jj}) / \rho, \quad (2.51)$$

and this is retrieved by $\sigma = 1$ in the parabolic mapping. On the other hand, for $\sigma \rightarrow 0$ the mapping retrieves the Junk subspace, whose moments cannot be described by the assumed shape of the VDF. The Junk subspace reads

$$Q_i = 0 \quad \text{and} \quad R_{iijj} > (2P_{ji}P_{ij} + P_{ii}P_{jj}) / \rho. \quad (2.52)$$

In the discussion of the 5-moment system, these boundaries will simplify, and a graphical interpretation will be shown. Since the Junk subspace is associated to a singularity, where the wave speeds grow unbounded, a lower limiting value is imposed to σ in numerical calculations. This value is often in the range of $\sigma_{\min} \approx 10^{-3} - 10^{-5}$, and will be discussed further in Section 4.3.

2.4.2 Order-4 maximum-entropy method: 5-moment system

A special case of the 14-moment system can be obtained in the limit of “1D thermodynamics”, where the particle motion is constrained along one single axis. This corresponds to the 1V kinetics considered in Section 2.1. Considering that particles have a single translational degree of freedom, the 14-moment formulation simplifies to a system of 5 equations. Denoting by v the only nonzero velocity component, the 5-moment description is obtained by the choice $\Psi = m(1, v, v^2, v^3, v^4)$. Notice that this description is still of order 4. The resulting 1V distribution function is

$$f_5 = \exp(\alpha_0 + \alpha_1 v + \alpha_2 v^2 + \alpha_3 v^3 + \alpha_4 v^4). \quad (2.53)$$

Also in this case, the VDF is seen to be always positive, and is bounded provided that $\alpha_4 < 0$. The resulting moment system reads

$$\frac{\partial \rho}{\partial t} + \frac{\partial}{\partial x} (\rho u) = G_1, \quad (2.54a)$$

$$\frac{\partial}{\partial t} (\rho u) + \frac{\partial}{\partial x} (\rho u^2 + P) = G_2, \quad (2.54b)$$

$$\frac{\partial}{\partial t} (\rho u^2 + P) + \frac{\partial}{\partial x} (\rho u^3 + 3uP + Q) = G_3, \quad (2.54c)$$

$$\frac{\partial}{\partial t} (\rho u^3 + 3uP + Q) + \frac{\partial}{\partial x} (\rho u^4 + 6u^2P + 4uQ + r) = G_4, \quad (2.54d)$$

$$\begin{aligned} \frac{\partial}{\partial t} (\rho u^4 + 6u^2P + 4uQ + r) + \frac{\partial}{\partial x} (\rho u^5 + 10u^3P + 10u^2Q \\ + 5ur + s) = G_5. \end{aligned} \quad (2.54e)$$

As for the 14-moment case, the collisional source terms depend on the species considered and will be covered in the relevant sections, while the electromagnetic sources will be developed in Section 4.5. Note that the 5-moment formulation could also be obtained from the 14-moment system, in the limit of a zero temperature and zero bulk velocity in two out of the three space directions.

The 5-moment system has the same issues of the 14-moment system in terms of absence of an algebraic solution to the entropy maximisation problem. Clearly, as the system is much smaller, a numerical solution will be much less demanding. Nonetheless, in this work we will employ the interpolative closure developed in [67]. The first step consists in non-dimensionalizing the variables, scaling them by ρ and a power of the thermal velocity $\sqrt{P/\rho}$, as done in Section 2.3.1 (subscript \star). The parameter σ is then defined as

$$\sigma = \frac{3 - r_\star + \sqrt{(3 - r_\star)^2 + 8Q_\star^2}}{4}. \quad (2.55)$$

and the only required closing moment is

$$s_\star = \frac{Q_\star^3}{\sigma^2} + (10 - 8\sigma^{1/2})Q_\star. \quad (2.56)$$

The expression for the physical realizability boundary and the Junk subspace are much simpler for the 5-moment problem. Physical realizability is satisfied by

$$r_\star \geq Q_\star^2 + 1 \quad (2.57)$$

while the Junk subspace corresponds to the line

$$Q_\star = 0 \quad \text{and} \quad r_\star > 3, \quad (2.58)$$

where $(q_\star, r_\star) = (0, 3)$ represents equilibrium, that happens to be located at one extreme of the Junk line. These boundaries are represented in Fig. 2.1. In this work, the solution to the 5-moment system will often be represented in the (Q_\star, r_\star) plane, that will simply be referred to as “moment space”. This is indeed a convenient way to graphically represent how the solution evolves with respect to equilibrium.

2.5 Conclusions

This chapter has introduced some common governing equations that allows to model rarefied gases and plasmas from the kinetic to the continuum regime, together with the assumptions upon which they are built. The

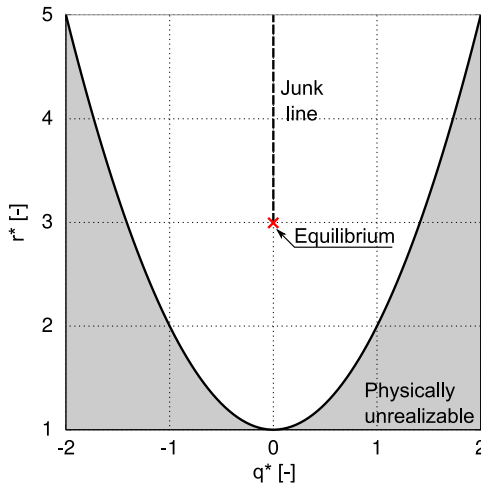


Figure 2.1: Physical realizability boundary, equilibrium and Junk line in moment space for the 5-moment system. Variables q^* and r^* represent the dimensionless heat flux and dimensionless order-4 moment respectively.

equations are to be written for each species separately, and coupling among them will happen through collisions and electromagnetic source terms. For a complete treatment of plasmas, one cannot leave aside the Maxwell (or Poisson's) equations that govern the dynamics of electromagnetic fields. However, their treatment goes beyond the scope of this work, where we are only interested in developing the governing equations and comparing them for different conditions.

In the next chapter, the numerical schemes required to solve these equations are discussed.

CHAPTER 3

Overview of the numerical methods

This chapter introduces the numerical methods used for solving the governing equations discussed in Chapter 2. Section 3.1 considers a particle-based solution of the kinetic equations, discussing the PIC and DSMC approaches. Section 3.2 then introduces the finite volume method (FV), that allows one to efficiently integrate a system of PDEs. Besides the classical application to the solution of the fluid and moment equations, the finite volume method is applied to the direct solution of the 1D1V kinetic equation, in Section 3.2.5. Finally, Section 3.3 discusses a set of scaled units, that will improve the numerical conditioning for situations of low density.

3.1 Particle-based solutions of the kinetic equation

As seen in Chapter 2, the kinetic equation is 6-dimensional in its most general form.¹ This high dimensionality, with respect to standard 3-dimensional fluid dynamic simulations, causes large memory requirements, that often happen to be overwhelming if the required cell size is small. For example, in plasma physics the cell size is frequently governed by the Debye length, often much smaller than the characteristic size of the problem. For

¹Considering electrons or atomic species without internal degrees of freedom.

this reason, one often gives up with the hope of discretizing directly the 6-dimensional kinetic equation with standard numerical methods (such as finite differences/volumes/elements), and uses Monte Carlo-type methods instead, based on simulating a limited set of particles [128]. For a comprehensive description of particle methods for gases and plasmas, the reader is referred to the following classical references: for the simulation of charged particles using the Particle-in-Cell (PIC) method, Birdsall & Langdon [53]; for the simulation of neutral gases, Bird [129]; and for a treatment of additional problems, Hockney & Eastwood [130]. Only a succinct review of the key concepts is given in the following.

The idea underlying particle methods consists in approximating the distribution function in phase space by a finite set of macro-particles (just denoted as “particles” in the following), each describing a (usually large) amount of real particles. The ratio of real-to-simulated particles plays an important role and is defined as $W = N_{\text{real}}/N_{\text{sim}}$. An operator splitting is then applied to the kinetic equation under the assumptions that the gas is dilute, separating the particle advection from the gas-phase collisions, and the two steps are performed successively. In case a charged gas is considered, an additional step is included, where electromagnetic fields are computed from the charges density and velocity.

For classical particles, the advection operation is performed by integrating Newton’s equations, and common integrators include the Leapfrog and Boris particle pushers [131] when electric and magnetic fields are present, or a simpler first order Euler ballistic advection for neutral particles. The value of the electric and magnetic fields at the particle location are often found by linear interpolation [132].

After particles are advected in space and velocity, collisions are performed. Different formulations are possible, according to the type of collisions and the considered problem. A common strategy in the simulation of low-temperature plasmas consists in Monte Carlo Collisions (MCC) [133], where the tracked species collide with a prescribed background gas. Various strategies have been formulated for describing the Boltzmann collision operator, such as the Direct Simulation Monte Carlo (DSMC) method [129, 134]. Such strategy groups particles within a spatial cell and lets them collide, sampling the collision pairs according to the Boltzmann collision rate probability density. A number of phenomenological models have been formulated for describing the interaction potential, the most commonly used being the hard-sphere (HS), the variable hard-sphere (VHS) and the variable-soft-sphere (VSS) models (see [129, 135]). The collision step typically imposes strong limitations to explicit particle simulations, limiting

the time step to a fraction of the mean collision time, and for the DSMC method an additional limitation is imposed to the grid size, that should properly resolve the mean free path.

Particle-surface collisions are often performed with the Maxwell model [136], assuming a partial or full accommodation of the particle to the wall temperature, described by an accommodation coefficient α , but more detailed approaches are possible [137–139].

For simulating charged particles, the external and self-consistent electromagnetic fields need to be computed. This is done by assigning the particles charge and velocity to grid points, employing some uniform, linear or bell-shaped weighting based on the distance between the particle and the grid point [132]. After the charges and velocities are deposited, the Maxwell equations (or simply the Poisson’s equation in case of an electrostatic simulation) are solved. An important requirement to avoid numerical heating is that the grid size in PIC simulation needs to properly resolve the local Debye length.

3.2 The finite volume method

The finite volume method allows us to solve a set of PDEs in a deterministic fashion, and is particularly suited to hyperbolic systems of governing equations. In this work, the finite volume method will be used to solve the fluid equations and in some occasions the Boltzmann equation.² For a thorough discussion of the method, the reader can refer to [37, 140, 141]. Only a brief recap will be given in the following.

3.2.1 Formulation

We consider a system described by the state vector \mathbf{U} , and write a system of governing equations in conservative form,

$$\frac{\partial \mathbf{U}}{\partial t} + \frac{\partial \mathbf{F}_k}{\partial x_k} = \mathbf{G}, \quad (3.1)$$

where \mathbf{F}_k are the fluxes vectors along direction k and \mathbf{G} is a vector of source terms. The domain is divided into a set of cells, that are separated from the other cells via interfaces, as shown in Fig. 3.1 for a 1-dimensional domain, where x_{\min} and x_{\max} are the borders of the domain and the cell i has interfaces denoted by $i \pm 1/2$. One or more ghost cells are placed outside the domain, allowing us to apply the boundary conditions.

²No solution of the Poisson’s equation will be discussed, as it is beyond the scope of this work.

Chapter 3. Overview of the numerical methods

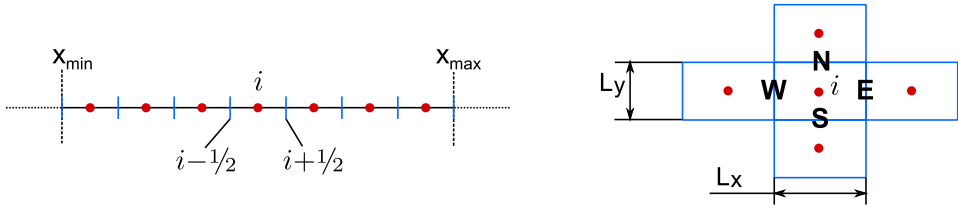


Figure 3.1: Left: discretization of a 1D domain into finite volume cells and their interfaces. Right: labels for a 2D Cartesian cell.

The governing equation is then integrated over the individual cells, giving

$$\frac{d}{dt} \int_{\Omega_i} \mathbf{U} d\Omega + \oint_{\partial\Omega_i} \mathbf{F} \cdot \hat{\mathbf{n}} d\Sigma = \int_{\Omega_i} \mathbf{G} d\Omega, \quad (3.2)$$

where the Gauss' theorem was employed to recast the volume integral into a surface integral, and $\hat{\mathbf{n}}$ is the normal to the surface. The cell quantity Ω_i is the cell volume in a 3-dimensional description, the cell surface in a 2D description and the cell length in case of a 1D description. The cell surface $\partial\Omega_i$ is an actual surface in 3D, a line delimiting the cell in 2D or simply the left and right cell extremes in a 1D description. Denoting by \mathbf{U}_i and \mathbf{G}_i the average value of the solution and of the source vector over the cell,

$$\mathbf{U}_i \equiv \frac{1}{\Omega_i} \int_{\Omega_i} \mathbf{U} d\Omega, \quad \mathbf{G}_i \equiv \frac{1}{\Omega_i} \int_{\Omega_i} \mathbf{G} d\Omega, \quad (3.3)$$

one ultimately obtains the space-discretized form of the governing equation. In one dimension, this reads

$$\frac{d\mathbf{U}_i}{dt} + \frac{1}{L_i} [\mathbf{F}_{i+1/2} - \mathbf{F}_{i-1/2}] = \mathbf{G}_i, \quad (3.4)$$

where the numerical fluxes $\mathbf{F}_{i\pm1/2}$ are taken only in the considered direction, and are still to be defined. In two dimensions, for a Cartesian grid aligned with the x and y axes, one has

$$\frac{d\mathbf{U}_i}{dt} + \frac{1}{L_{ix}} [\mathbf{F}_E - \mathbf{F}_W] + \frac{1}{L_{iy}} [\mathbf{F}_N - \mathbf{F}_S] = \mathbf{G}_i, \quad (3.5)$$

where L_{ix} and L_{iy} are the cell length along the x and y directions respectively and the subscripts N (north), S (south), W (west) and E (east) are used to identify the interfaces, following Fig. 3.1. With this notation, \mathbf{F}_E and \mathbf{F}_W are x -fluxes, while \mathbf{F}_N and \mathbf{F}_S are y -fluxes. Note that more advanced stencils could be employed,³ for better accuracies. The simple formulation reported here will be sufficient for the present work.

³For example, including neighboring cells in the source terms definition.

3.2.2 Numerical fluxes for fluid and moment systems

The choice for the numerical fluxes proves to be crucial for the performance of a finite volume method. A number of different formulations have been developed in the years (for a review of the main methods, see Toro [142]). Rather than being completely general, a number of such methods have been developed with a specific target system in mind. This is the case for the Roe scheme [143], the AUSM family of schemes [144] and the kinetic schemes [145, 146] to cite a few, that specifically target the Euler or Navier-Stokes equations. This is an issue for certain moment methods, as these schemes would need either a very detailed knowledge of the eigenstructure of the system [119], or at least to be reformulated and extended.

Central schemes such as Lax-Friedrichs' are general enough to be directly applied to the moment equations, but are known to be very diffusive. This happens to be a major issue for moment methods, where the wave speeds may exceed by orders of magnitude the wave speeds of the Euler system for some non-equilibrium conditions, as will be discussed in Section 4.2. This magnifies the undesirable numerical diffusion of the Lax-Friedrichs scheme. Higher order central schemes that mitigate such issue have also been developed, as in the case of the Nessyahu-Tadmor [147] and the Kurganov-Tadmor schemes [148], the latter requiring as an additional information the maximum wave speed of the system.

When the maximum and minimum wave speeds of the system are known, a classical and robust choice consists in the HLL (Harten, Lax & van Leer) scheme [149]. Although not optimal for low-velocity flows such as boundary layers or contact discontinuities (its HLLC extension would improve the situation), the scheme has been proficiently employed in the solution of moment systems due to its simplicity. However, it will be shown in Section 4.1.3 that, despite working well for moderate departures from equilibrium, the method shows some oscillations in the higher moments, when applied to strong non-equilibrium conditions. This may be due to numerical reasons, or may be caused by the scheme generating a non-realizable flux. For additional discussion on possible methods for the maximum-entropy system, the reader can refer to [150]. Finally, in case the full entropy maximisation problem is being solved at every iteration (as opposed to employing the interpolative closure), another option consists in employing kinetic fluxes [151].

The preferred scheme of the present work will be the Rusanov scheme (also known as “local Lax-Friedrichs”) [142]. Such scheme is slightly more

diffusive than the HLL scheme,⁴ but this is easily fixed by going second order in space, as discussed in the following. With the Rusanov scheme, the interface flux \mathbf{F}_{int} is obtained from the left and right states and fluxes (subscripts L and R) and the maximum wave speed S_{\max} (maximum absolute value among the left and right cells),

$$\mathbf{F}_{\text{int}} = \frac{1}{2} (\mathbf{F}_R + \mathbf{F}_L) - \frac{S_{\max}}{2} (\mathbf{U}_R - \mathbf{U}_L). \quad (3.6)$$

MUSCL scheme for second order spatial accuracy

If the left and right states of Eq. (3.6) are taken directly from the left and right cells, the resulting spatial discretization is first order in space. The van Leer's MUSCL scheme [152] allows us to retrieve a second order solution in space, by employing a linear reconstruction of the solution, where the slope is limited to achieve TVD properties. With marginal modifications, one could also reach third order in space [153], however this was not investigated in the present work.

For systems of conservation equations, reconstruction is conveniently performed in primitive variables, that we define by Q . Using primitive variables appears to be crucial for maximum-entropy simulations in presence of strong non-equilibrium.⁵ The left and right states of the interface $i + 1/2$ are obtained as

$$Q_{i+1/2}^L = Q_i + \frac{x_{i+1/2} - x_i}{x_i - x_{i-1}} (Q_i - Q_{i-1}) \Phi(\theta_i), \quad (3.7a)$$

$$Q_{i+1/2}^R = Q_{i+1} - \frac{x_{i+1} - x_{i+1/2}}{x_{i+2} - x_{i+1}} (Q_{i+2} - Q_{i+1}) \Phi(1/\theta_{i+1}), \quad (3.7b)$$

where $\theta_i = (Q_{i+1} - Q_i)/(Q_i - Q_{i-1})$ is the ratio of consecutive gradients, and Φ is a slope limiter function. The symmetric van Albada's limiter is selected in this work, $\Phi(\theta) = (\theta^2 + \theta)/(\theta^2 + 1)$.

The MUSCL approach, together with van Albada's slope limiter and Rusanov fluxes, has been seen to work smoothly for both the 5 and 14-moment simulations for most conditions. However, for some test cases (such as the crossing jets cases of Section 4.4), second order appears to stall the simulation at certain simulated times. Employing different TVD slope limiters did not appear to improve the situation significantly. On the other hand, simply disabling the possibility to employ a linear reconstruction based on

⁴This may be the reason why the mentioned oscillations do not appear.

⁵Reconstruction in conserved variables may create large inconsistencies unless a dimensionless formulation is employed. Indeed, conserved moments include increasing powers of the velocity: and a linear reconstruction for the momentum ρu would be inconsistent with a linear reconstruction of, say, the order-4 moment $\rho u^4 + \dots$.

a large stencil would result in an overly diffusing simulation and the need to use a very large number of cells to reach spatial convergence. Therefore, an intermediate approach was applied in such cases, artificially limiting the slope by a further factor $\beta = 0.5$ or $\beta = 0.75$. For a uniform grid, this modification reads

$$Q_{i+1/2}^L = Q_i + \beta \Phi(\theta_i) \frac{Q_i - Q_{i-1}}{2}, \quad (3.8a)$$

$$Q_{i+1/2}^R = Q_{i+1} - \beta \Phi(1/\theta_{i+1}) \frac{Q_{i+2} - Q_{i+1}}{2}. \quad (3.8b)$$

This further limiting causes the approach to depart from the second-order TVD region (as defined in [140]). Nonetheless, it allows us to significantly reduce the numerical diffusion of the Rusanov scheme, while still retaining a robust method.

3.2.3 Time integration

Once the equations are discretized in space, a time integrator is selected. The simplest choice consists in the explicit forward Euler scheme,

$$\mathbf{U}_i^{n+1} = \mathbf{U}_i^n - \frac{\Delta t}{L_{ix}} [\mathbf{F}_E^n - \mathbf{F}_W^n] - \frac{\Delta t}{L_{iy}} [\mathbf{F}_N^n - \mathbf{F}_S^n] + \Delta t \mathbf{G}_i^n, \quad (3.9)$$

where the superscript n denotes the current time and Δt the time step. The scheme has first order accuracy, and is only stable for Courant numbers lower than one. More importantly, for charged gas simulations, the forward Euler scheme may produce excessive numerical cooling (or heating) and may numerically drive the temperature to zero, when conserved variables are employed. This effect is important mostly in the study of the long-time behavior of closed systems (see for example the test cases of Sections 6.4 and 6.5), when the external input of work in the system is negligible and the self-consistent fields dominate. On the other hand, for open systems, where the fluid is constantly being refreshed, this issue may very well be negligible.

The reason for this to occur is that the Euler method does not integrate exactly *both* the momentum and the total energy. Employing higher order schemes (such as the ubiquitous order-4 Runge-Kutta method) surely improves the situation, but does not solve it. The problem will be considered in more detail in Appendix B, where it will be shown that the Midpoint Euler method, a simple 2nd order Runge-Kutta formulation, allows one to integrate exactly both the momentum and the total energy for simple test

cases and uniform forces, thus solving the issue. For this reason, the Mid-point Euler scheme is the reference method for the present work.

First, the method performs a half-step, and computes an intermediate solution as:

$$\mathbf{U}_i^{n+1/2} = \mathbf{U}_i^n - \frac{\Delta t}{2 L_{ix}} [\mathbf{F}_E^n - \mathbf{F}_W^n] - \frac{\Delta t}{2 L_{iy}} [\mathbf{F}_N^n - \mathbf{F}_S^n] + \frac{\Delta t}{2} \mathbf{G}_i^n, \quad (3.10)$$

this solution is then used to compute both the fluxes and the source terms at the step $n + 1/2$, denoted as $\mathbf{F}^{n+1/2} = \mathbf{F}(\mathbf{U}^{n+1/2})$ and the same for the sources. The actual step is then performed from n to $n + 1$, but using *only* the fluxes and sources at the intermediate step:

$$\begin{aligned} \mathbf{U}_i^{n+1} = & \mathbf{U}_i^n - \frac{\Delta t}{L_{ix}} \left[\mathbf{F}_E^{n+1/2} - \mathbf{F}_W^{n+1/2} \right] \\ & - \frac{\Delta t}{L_{iy}} \left[\mathbf{F}_N^{n+1/2} - \mathbf{F}_S^{n+1/2} \right] + \Delta t \mathbf{G}_i^{n+1/2}, \end{aligned} \quad (3.11)$$

In this work, collisions or fields were never so strong as to cause an overwhelming stiffness, and thus to require an implicit formulation, and the explicit Midpoint Euler method proved to work just fine. In the case of stiffer problems, point-implicit formulations could be employed.

3.2.4 Boundary conditions

In the presence of solid walls, the choice of a proper set of boundary conditions (BCs) may not be trivial in the case of moment equations. In particular, for wall-bounded gases, one may expect Knudsen layers to form (see [119, 154] for an implementation of the BCs for such conditions). The simulation of plasmas shares analogous issues, as one may need to consider for example secondary electron emission at walls, due to electron impact, or the emission of electrons by ion impact at the electrodes. These problems are respectively important for instance for modeling the near wall conductivity [31] and for DC gas discharges [36].

In the present work, we do not need to consider such problems in great detail, and simple BCs are sufficient. All simulations will be either periodic or will have open-boundaries, and BCs are implemented through ghost cells. In the periodic case, the value at the ghost cells is updated in time as to match the corresponding periodic neighbor cell. In open-boundary simulations, the ghost cells are assigned a large velocity and small density, such that all characteristic waves will leave the domain. This is rigorous for su-

personics flows,⁶ but more care shall be taken for subsonic ones. It should be noticed that the electrode-bounded plasmas considered in this work fall in the category of open-boundaries, due to the assumption of full recombination at the electrodes.

3.2.5 Finite volume solution of the kinetic equation

Instead of using particle methods, the kinetic equation can be solved by direct discretization of the phase space. Various approaches are possible (see for example [155–157]). In this section we will discuss how to solve the equations using the finite volume method [51]. In the general case, this would require to consider 6-dimensional finite volume cells and is therefore not trivial, but the situation changes dramatically if one only needs to solve the simpler 1D1V case. In such case, the finite volume description is 2-dimensional in total, one axis representing the physical position and the other represents the velocity. The first step consists in rewriting the kinetic equation in the form of Eq. (3.1),

$$\frac{\partial f}{\partial t} + \frac{\partial F_x}{\partial x} + \frac{\partial F_v}{\partial v} = G, \quad (3.12)$$

with $F_x = vf$, $F_v = fqE/m$, with q and E the electric charge and electric field respectively, and f is the 1V distribution function. No magnetic field can be considered in the 1D1V formulation, as it would rotate the VDF and thus break the 1D1V assumptions. The source term G is case-dependent, and can include both collisions and production of species. To discretize the equation, a 2-dimensional grid in phase space is employed, as shown in Fig. 3.2

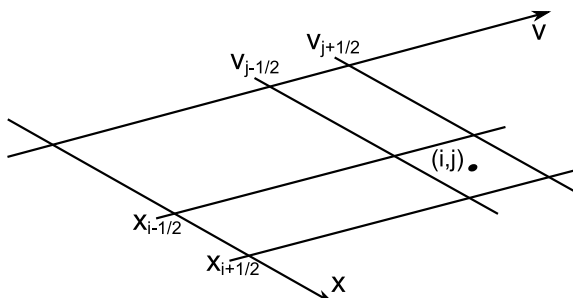


Figure 3.2: Finite volume discretization of the phase space for solving the 1D1V kinetic equation.

⁶Here, supersonic refers to the fastest wave speed of the system, that may be much larger than the speed of sound for moment systems.

Two indices i, j are used to identify the cells, and a Cartesian grid is employed, as to simplify the fluxes. The final discretized equation reads

$$\frac{\partial f_{ij}}{\partial t} + \frac{1}{L_x} [F_{x,i+1/2} - F_{x,i-1/2}] + \frac{1}{L_v} [F_{v,j+1/2} - F_{v,j-1/2}] = S_{ij} \quad (3.13)$$

Regarding the numerical fluxes, an upwinded formulation is easily written from the following principle: the physical space axis x is to be advected towards the positive or negative directions based on the value of the local velocity, while the velocity axis v follows the local acceleration qE/m . By adapting the second order upwinded formulation of Mieussens [51], the numerical fluxes read

$$F_{x,i+1/2} = \frac{1}{2} [v_j f_{i,j} + v_j f_{i+1,j} - |v_j| (f_{i+1,j} - f_{i,j} - \Psi_{x,i+1/2})] \quad (3.14a)$$

$$F_{v,j+1/2} = \frac{1}{2} \left[\frac{qE_i}{m} f_{i,j} + \frac{qE_i}{m} f_{i,j+1} - \left| \frac{qE_i}{m} \right| (f_{i,j+1} - f_{i,j} - \Psi_{v,j+1/2}) \right] \quad (3.14b)$$

where E_i is the value of the electric field in the i -th cell. The choice $\Psi = 0$ results in a first order solution (no reconstruction, pure upwinding), while for second order accuracy we can chose a minmod limited reconstruction,

$$\Psi_{x,i+1/2} = \text{minmod} ((f_{i,j} - f_{i-1,j}), (f_{i+1,j} - f_{i,j}), (f_{i+2,j} - f_{i+1,j})) \quad (3.15a)$$

$$\Psi_{v,j+1/2} = \text{minmod} ((f_{i,j} - f_{i,j-1}), (f_{i,j+1} - f_{i,j}), (f_{i,j+2} - f_{i,j+1})) \quad (3.15b)$$

Where the `minmod()` function is implemented as:

$$\text{minmod}(a, b, c) = \begin{cases} \min(a, b, c) & \text{if } (a \geq 0 \ \& \ b \geq 0 \ \& \ c \geq 0) \\ -\min(|a|, |b|, |c|) & \text{if } (a < 0 \ \& \ b < 0 \ \& \ c < 0) \\ 0 & \text{otherwise} \end{cases} \quad (3.16)$$

A set of ghost cells is employed around the domain, and their value is kept fixed at the desired boundary conditions during the simulation, or may be varied following the desired time-evolution law. In the present work, a simple forward Euler time integration scheme will be employed for the 1D1V kinetic solution. An open source numerical implementation of this solver, with OpenMP parallelization, was prepared during this work and is available at [158].

3.3 Units for low-density numerical simulations

The low number density of charged particles in low-temperature plasmas results in a particularly low numerical value of the electron mass density, in view of their small mass. For example, considering an electron number density of $n_e = 10^{17} \text{ m}^{-3}$, reasonable for Hall thruster simulations, the resulting mass density is $\rho_e \approx 10^{-13} \text{ kg/m}^3$. This poses some issues in the numerical solution of the maximum-entropy systems. In particular, a direct application of the interpolative closure to such densities results in difficulties in inverting the closure matrix B_{lm} . The same problem may appear for ions, if even lower number densities are considered.

Three strategies are possible to overcome this issue. A classical approach would consist in non-dimensionalizing the equations (or at least, non-dimensionalizing the fluid quantities when they are initialized in the code). Such approach is elegant and well suited to classical fluid simulations, but requires some extra care in writing the electrical and chemical source terms.

Another approach would consist in non-dimensionalizing selectively some (but not all) variables. For example, in the present problem the density is the variable that causes most issues. Therefore, one can re-write the set of equations, consistently dividing each term by a reference density.

In this work, we consider a different approach: a slightly different set of units is employed, maintaining the structure of the SI system, but measuring the mass in picograms instead of kilograms. This introduces a scaling of 10^{15} in the mass, strongly increasing the numerical value for the density. With such definition, the numeric implementations are kept untouched (including the source terms) and only the initialization and the definition of numerical constants (kept separated, in the code) are affected.

Clearly, changing the mass units affects not only the density, but also other fluid and electric quantities. For example, with this change, the electric potential and related quantities would be measured in fV. However, it is here preferred to transform also the electric current by the same factor of 10^{15} , measuring it in fA, thus keeping untouched the units of V and correspondingly the electric and magnetic fields, and only charge units turn into fC. All other fundamental units (m, s, K, ...) are kept unchanged. With this choice, the full list of units required in the simulations reads

Mass $[m] = \text{pg}$

Electrical charge $[q] = \text{fC}$

Density $[\rho] = \text{pg/m}^3$

Chapter 3. Overview of the numerical methods

Pressure $[P] = \text{fPa}$

Higher order moments $[q_i, Q_{ijk}, R_{iijj}, S_{iijjk}] = \text{pg} \times \left(\frac{\text{m}}{\text{s}}\right)^n \times \text{m}^{-6} = \text{f}(...)$

Velocities $[u] = \text{m/s} - \text{unchanged}$

Boltzmann constant $[k_B] = \text{fJ/K}$

Electric potential $[\phi] = \text{V} - \text{unchanged}$

Electric field $[E] = \text{V/m} - \text{unchanged}$

Magnetic field $[B] = \text{T} - \text{unchanged}$

Vacuum permittivity $[\varepsilon_0] = \text{F/m} - \text{unchanged}$

Note that all conserved fluid quantities ($\rho, \rho u + P, \dots$) are proportional to the density (which is scaled) and to a power of the thermal velocity (whose units are “m/s” and is therefore unchanged by our new variables). Therefore all conserved quantities will simply be scaled by 10^{15} . This scaling has shown to work robustly for all simulations shown in the present work.

CHAPTER 4

Application of the maximum-entropy closure to rarefied gases and plasmas

In order to apply the maximum-entropy method to the low-temperature plasma conditions considered in this work, some further analysis and developments are necessary.

The first part of this chapter will focus on investigating the method in low-collisional situations. First, in Section 4.1 we introduce the Sod shock test case, and consider free-molecular, transitional and continuum conditions, solving both the kinetic equation and the 1D1V 5-moment system. This test case will offer a first verification of the 5-moment system for varying degrees of non-equilibrium, and will serve as a basis for the further sections. For this problem, Section 4.1.3 compares the HLL and Rusanov numerical fluxes and identifies the most suitable one.

As can be seen from an analysis of the Sod shock tube problem, the wave speeds of the maximum-entropy system differ greatly from the speed of sound, when non-equilibrium situations are considered. Their analytical expression is not known, and computing them numerically during CFD simulations is very expensive. In this regard, Section 4.2 is devoted to the development of approximated wave speeds for the 14-moment system.

The resulting expressions empirically extend some previous results available for the 5-moment system. Due to the CFL condition, computational efficiency is strictly connected to the wave speeds. This point is analyzed in Section 4.3, where the computational efficiency of the maximum-entropy method is compared to the Euler equations. Finally, a 2-dimensional test case is considered, analyzing two crossing jets in free molecular conditions (Section 4.4).

The second part of the chapter extends the method towards plasmas: Section 4.5 derives the electromagnetic source terms for the 5 and 14-moment systems, and Section 4.6 discusses the dispersion relation for simple electrostatic longitudinal electron and ion waves. After the analysis and developments presented in this chapter, the method will be ready for the applications to Hall thruster-like configurations, discussed in the following chapters.

4.1 The rarefied Sod shock tube problem

The solution of the 5-moment maximum-entropy system has been investigated on different Riemann problems in the literature, see for example [159]. In this section, we consider the solution of the 5-moment system with interpolative closure, for the classical Sod shock tube problem [160]. This configuration is a Riemann problem where the initial density is discontinuous across the origin, while the temperature is uniform and the velocity is initially zero everywhere. The solution is assumed to be in equilibrium on both sides of the initial discontinuity, and the gas state is thus represented by a Maxwellian distribution function.

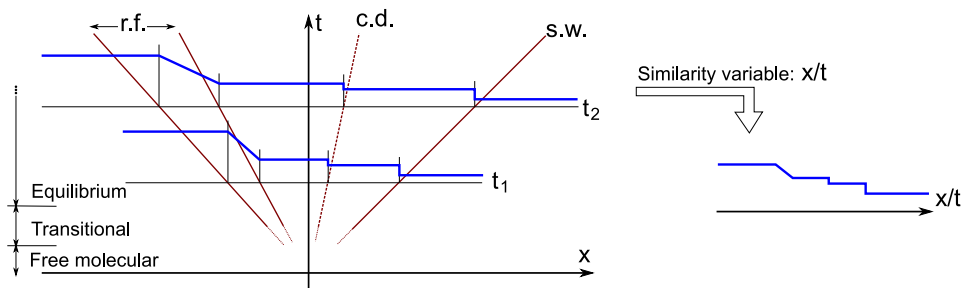


Figure 4.1: Solution of the Sod shock tube problem: self-similar profile expanding in the time-space plane.

The solution of the Sod shock tube problem in the continuum regime is widely known to be composed by a fast-moving shock wave, a slower

contact discontinuity and a rarefaction fan travelling in the opposite direction [161–163]. The solution shows similarity if scaled with the variable $\xi = x/t$, with x the space position and t the time, since the waves travel at a constant speed. This is shown in Fig. 4.1. However, these results gradually break apart as one considers the transitional regime, up to the point that no shock wave or discontinuity appears at all in the free-molecular regime. These regimes are realized in the very first instants of the Riemann problem, for times that are lower than the mean collision time. The absolute value of such times depends on the considered density, and may be as ridiculously low as some picoseconds in high-pressure laboratory tests¹ or may reach much higher values in rarefied high atmosphere conditions.² For the small-time rarefied solution, a scaled variable $\xi = x/t$ can still be profitably employed, and allows one to compare profiles obtained from the same simulation at successive times, and similarity is established naturally after a few mean collision times.

Whatever the density, the very same dimensionless profiles are obtained when the same Knudsen number is simulated. In this section we arbitrarily choose the left and right initial states (subscripts L, R) as $u_{L,0} = u_{R,0} = 0$, a discontinuous density $\rho_{L,0} = 4 \text{ kg/m}^3$ and $\rho_{R,0} = 1 \text{ kg/m}^3$, and a uniform temperature $T_{L,0} = T_{R,0} = 480 \text{ K}$.³ An Argon gas is simulated, with mass $m_{\text{Ar}} = 6.6337 \times 10^{-26} \text{ kg}$. The collision cross section is set to $\sigma = 5.463 \times 10^{-19} \text{ m}^2$. Then, the simulation is run for a certain time, until the expanding shock structure reaches a desired given extent L_{sim} .

A definition of the Knudsen number for this problem is not trivial. The spatially varying conditions would in principle require that one considers local gradients for defining the Knudsen number [165]. Instead, we would like here to consider the Knudsen number as a global indicator of how much the solution has progressed with respect to the collisionality. In particular, we define $\text{Kn} = \lambda/L_{\text{sim}}$, ratio of the mean free path to the simulated domain, where the mean free path is fixed for simplicity to the left-state value, $\lambda = 1/(n_L \sigma) = 3.041 \times 10^{-8} \text{ m}$. Since the actual density changes locally and reaches the value $\rho_R = 1 \text{ kg/m}^3$, this choice results in a slight underestimation of Kn , by at most a factor 4.

For $\text{Kn} \rightarrow 0$, the solution has plenty of time to equilibrate, and we expect to retrieve the classical “(shock) / (contact discontinuity) / (rarefaction fan)” structure. For larger values, rarefaction becomes progressively more

¹Clearly, this condition is idealized, as the opening time of laboratory shock tubes already exceeds many mean collision times.

²For instance at an altitude of 100 km, the number density is roughly $n \approx 10^{19} \text{ m}^{-3}$ and the mean collision time is $\tau \approx 0.3 \text{ ms}$ [164].

³For Argon, this gives the pressures $P_{L,0} = 400\,000 \text{ Pa}$ and $P_{R,0} = 100\,000 \text{ Pa}$.

important, until for $\text{Kn} \rightarrow \infty$, we expect the solution to be composed by a smooth profile that connects the left and right states. Considering the intermediate case of $\text{Kn} = 0.1$, the mean free path is $1/10$ of the simulated domain L_{sim} . Practically speaking, all solutions for $\text{Kn} \geq 1$ appear almost identical in terms of the lower order moments (density, velocity and pressure), and differ only when higher order moments are considered.

We consider here a 1D1V problem, where particles are assumed to have only one translational degree of freedom. This may appear to be an excessive simplification, since the physical realm of a 1V shock is debatable at best. However, this allows us to keep the difficulty at a minimum, and to employ the simple deterministic solver developed in Chapter 3 in place of the particle-based solver, allowing us to obtain noise-free estimations for the higher order moments. The kinetic equation describing the 1D1V BGK gas is

$$\frac{\partial f}{\partial t} + v \frac{\partial f}{\partial x} = -\nu(f - \mathcal{M}), \quad (4.1)$$

where \mathcal{M} is the 1V Maxwellian at the local conditions (see Eq. (2.5)) and the velocity independent collision frequency ν is computed in every cell from the local values,

$$\nu = nv^{th}\sigma = \sigma \frac{\rho}{m} \sqrt{\frac{8P}{\pi\rho}}. \quad (4.2)$$

The 5-moment system corresponding to this case is reported in Eq. 2.54, and its BGK collision sources read [67]

$$\mathbf{G}^{(5)} = \begin{pmatrix} 0 \\ 0 \\ 0 \\ -\nu Q \\ -\nu(4uQ + R - 3P^2/\rho) \end{pmatrix}. \quad (4.3)$$

These terms do not affect the density, momentum and total energy, and only drive the heat flux Q towards zero, and the order-4 moment R towards the equilibrium value $3P^2/\rho$.

4.1.1 Kinetic solution

A solution to the kinetic equation was computed for the three mentioned conditions with the deterministic solver outlined in Section 3.2.5, using a grid composed by 1000×1000 cells in physical space and velocity. A

number of 15 000 time steps proved sufficiently fine for reproducing the results with negligible numerical diffusion. The value of the time step is chosen as to reach the required simulation time. The kinetic solution is shown in Fig. 4.2. The effect of collisions is clearly dim at these conditions, and the resulting distribution function is a combination of the left and right families of particles (two Maxwellian at different densities).

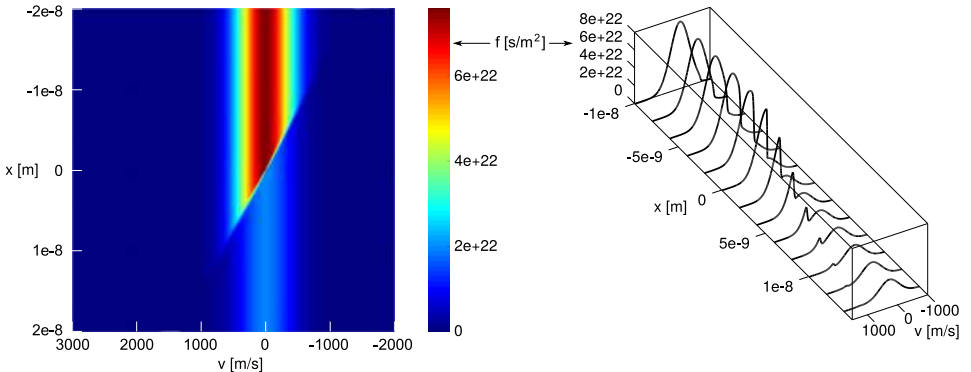


Figure 4.2: Kinetic solution in phase space for a time comparable to the mean collision time ($\text{Kn} = 1$). Test case a).

Solutions at lower values of the Knudsen number are qualitatively similar, except that the distribution is smoother in velocity, but obviously starts to show discontinuities in space as the continuum regime is approached [166–168]. The moments of the kinetic solution are shown in Fig. 4.3. The considered cases correspond to the following conditions:

- a) $\text{Kn} = 1, T_{\text{sim}} = 10^{-11} \text{ s};$
- b) $\text{Kn} = 0.1, T_{\text{sim}} = 10^{-10} \text{ s};$
- c) $\text{Kn} = 0.01, T_{\text{sim}} = 10^{-9} \text{ s};$
- d) $\text{Kn} = 0.001, T_{\text{sim}} = 10^{-8} \text{ s};$
- e) $\text{Kn} = 0.0001, T_{\text{sim}} = 10^{-7} \text{ s};$

For increasing simulated times, the solution is progressively more spread in space: the different profiles are superimposed by rescaling the spatial coordinate by the simulated time. As to allow for a comparison with the maximum-entropy system, a plot of the solution in moment space is also shown, together with the Junk subspace of the 5-moment system⁴ and the physical realizability boundary. In Fig. 4.3, equilibrium is represented by $(q^*, r^*) = (0, 3)$.

⁴Clearly, the kinetic solution can cross freely the Junk subspace.

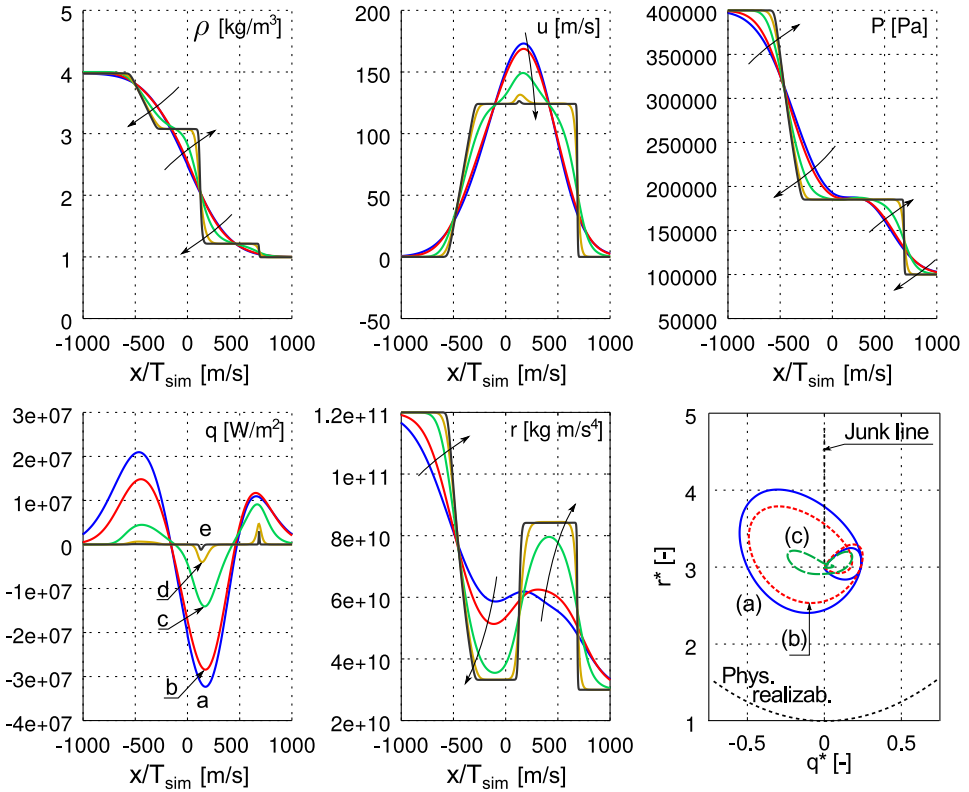


Figure 4.3: Moments from the solution of the BGK kinetic equation. Cases (a) to (e) are obtained from different simulations, with increasing simulation times and domain size.

4.1.2 Solution of the 5-moment system

The solution of the 5-moment system is obtained on a grid of 1000 cells, with Rusanov fluxes and second order spatial accuracy (MUSCL linear reconstruction with symmetric van Albada limiter). The choice of Rusanov fluxes will be detailed later on, in Section 4.1.3. Fig. 4.4 shows the solution in the two limiting cases of free-molecular regime ($\text{Kn} = 100$) and continuum regime ($\text{Kn} = 0.0001$), and a comparison with the fully kinetic solution will be given in the next section. The right-column in Fig. 4.4 shows the values of σ as an indicator of non-equilibrium.

The continuum solution takes the expected hydrodynamic shape, showing (from left to right) a rarefaction fan (points i-iii), a contact discontinuity (iv-vi) and a shock wave (vii-x). The three regions are easily identified from both the density and the heat flux profiles. The fluid state between these three waves is at equilibrium (regions iii-iv and vi-vii), with a zero

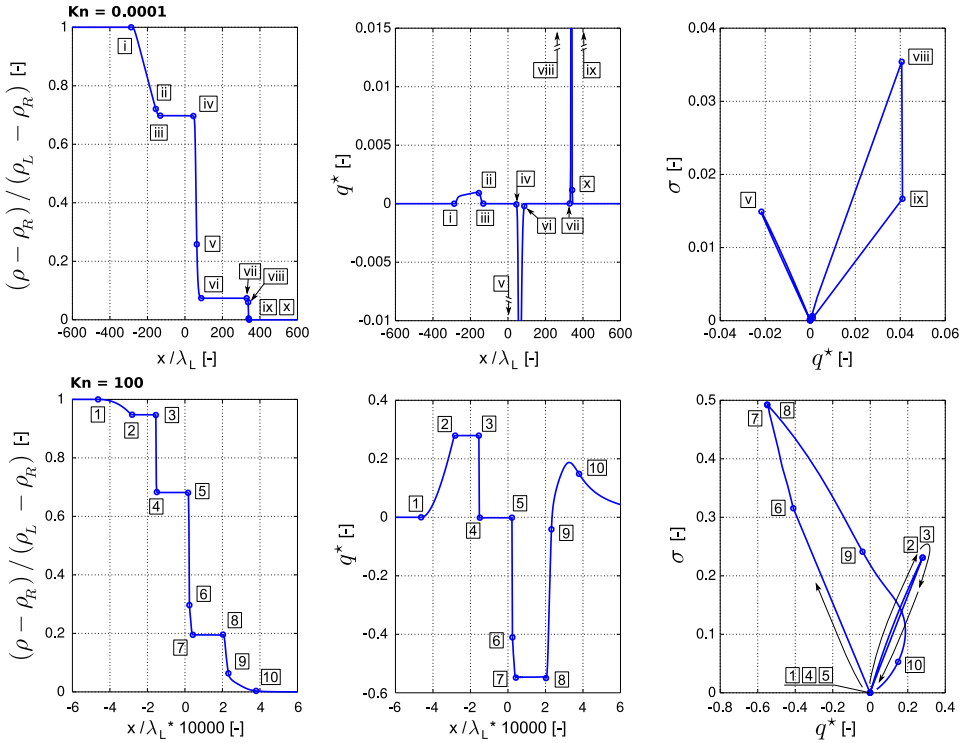


Figure 4.4: Dimensionless solution of the 5-moment system. Top: continuum regime; the simulated time is roughly 10 000 times the mean collision time τ_c . Bottom: free-molecular regime, simulated time is roughly 0.01 τ_c .

heat flux and $\sigma = 0$.

For the free-molecular solution, we use Arabic numbers, that do not necessarily match the Roman numbers of the continuum regime. The interpretation of the rarefied solution is less trivial as it is composed by multiple waves in the density profile. However, the dimensionless heat flux profile still allows for a direct comparison among the two regimes. Indeed, the rarefaction fan in the continuum regime (i-iii) has the same heat flux structure of points (1-4) for the free-molecular solution. Therefore, looking at the density profile, the 5-moment system appears to break the rarefaction fan into a smooth profile, followed by a density discontinuity. This region is then followed by an equilibrium region, both in the continuum (iii-iv) and in the free-molecular (4-5) regimes. The contact discontinuity is represented by the region (5-9) in the heat flux, that incorporates two jumps in density. From the sign of the heat flux, we see that the equilibrium region (vi-vii) separating the contact discontinuity from the shock wave disappears in the

free-molecular regime, as points (vi,vii) appear to merge into point (9). Finally, the region (9-10- ∞) will eventually give rise to the shock wave, as the Knudsen number is decreased. No discontinuous shock is seen in the density profile, that instead appears as a smooth transition to the right state.

Comparison of results

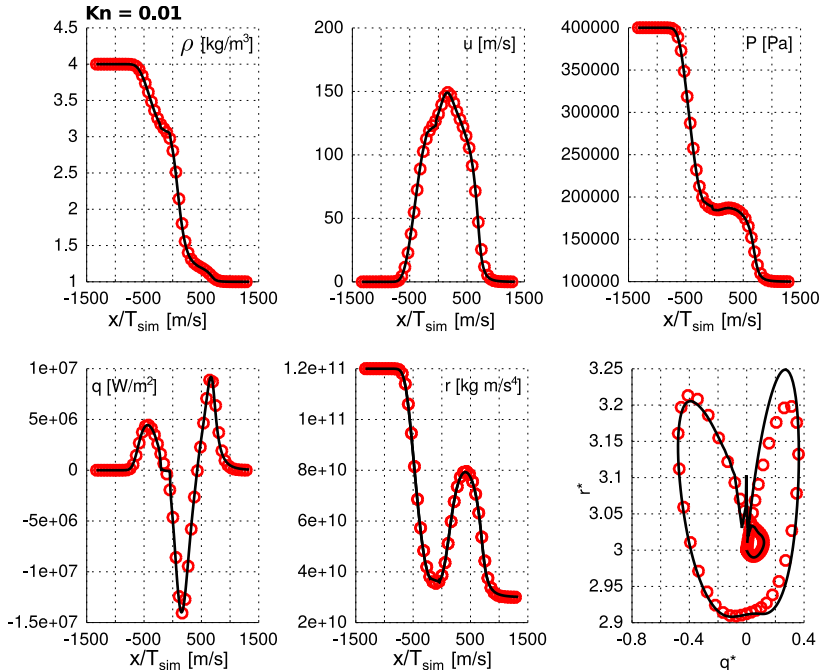


Figure 4.5: Solution of the 5-moment system (black line) and moments of the kinetic solution (symbols) for the case $\text{Kn} = 0.01$. Simulated time is $T_{\text{sim}} = 10^{-9}$ s.

Figures 4.5 and 4.6 compare the 5-moment system and the kinetic solutions for three transitional Knudsen numbers (defined based on the mean free path of the left state – and therefore somehow under-estimated – and the size of the simulated domain). For all cases, the maximum-entropy system reproduces accurately the magnitude of all moments, but includes some noticeable unphysical discontinuities already for $\text{Kn} = 0.1$. The trajectory in moment space shows that the solution needs to cross the Junk line. This appears to be of little importance in the $\text{Kn} = 0.01$ case, but is associated to some stronger deviation from the kinetic moment-space trajectory in the more rarefied cases.

It should be stressed that these results are obtained using the interpolative approximation of the entropy maximisation problem [67]. We expect

the global shape of the solution to be unchanged, however the details of the trajectory in moment space appear to be very sensitive to the employed grid, and are therefore likely to be affected by the details of the closure approximations.

4.1.3 Comparison of the HLL and Rusanov fluxes

As discussed in Section 3.2.2, few schemes are directly applicable to the maximum-entropy systems. In this section, we compare the often employed HLL scheme to the simpler Rusanov fluxes, for rarefied and continuum conditions. Lax-Friedrichs fluxes were also considered, but provided an overwhelmingly high numerical diffusion in the free-molecular regime, due to the high value of the wave speeds in non-equilibrium, such that no shock structure could be identified for the considered grids. A comparison of the HLL and Rusanov fluxes is shown in Fig. 4.7, using 500 grid cells and first order accuracy. A second order solution is also computed, using Rusanov fluxes on 5000 cells, as to show a reference shock profile.

The two methods appear roughly equivalent in continuum conditions, the Rusanov scheme showing only a very slight additional diffusion. On the other hand, in rarefied conditions, the HLL fluxes are significantly less diffusive than the Rusanov ones, but induce strong oscillations in the higher order moments. As previously mentioned, such oscillations may be connected by the prediction of non-realizable numerical fluxes, or states very close to the Junk line singularity, but this is to be investigated further. In any case, the oscillations are a major problem, as they prevent to obtain second order via piecewise limited reconstruction.

By employing Rusanov fluxes, we have no significant oscillations, and second order can be reached, thus offering a remedy to Rusanov's additional diffusion. Therefore, this will be the method of choice for most simulations in this work. The investigation and formulation of less diffusive fluxes is suggested as a future work activity (see the Conclusions chapter).

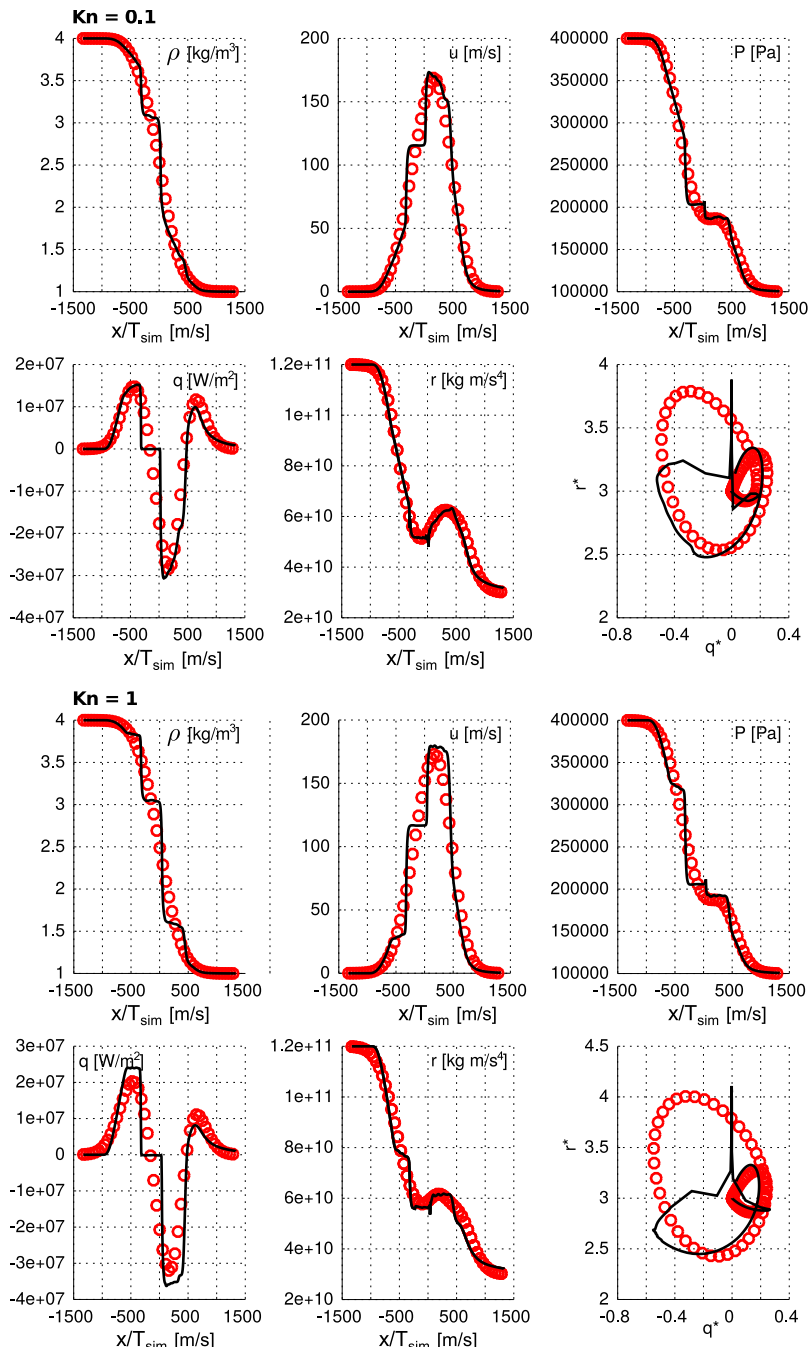


Figure 4.6: Solution of the 5-moment system (black line) and moments of the kinetic solution (symbols). Cases for $\text{Kn} = 1$ (simulated time $T_{\text{sim}} = 10^{-11} \text{ s}$) and $\text{Kn} = 0.1$ ($T_{\text{sim}} = 10^{-10} \text{ s}$).

4.1. The rarefied Sod shock tube problem

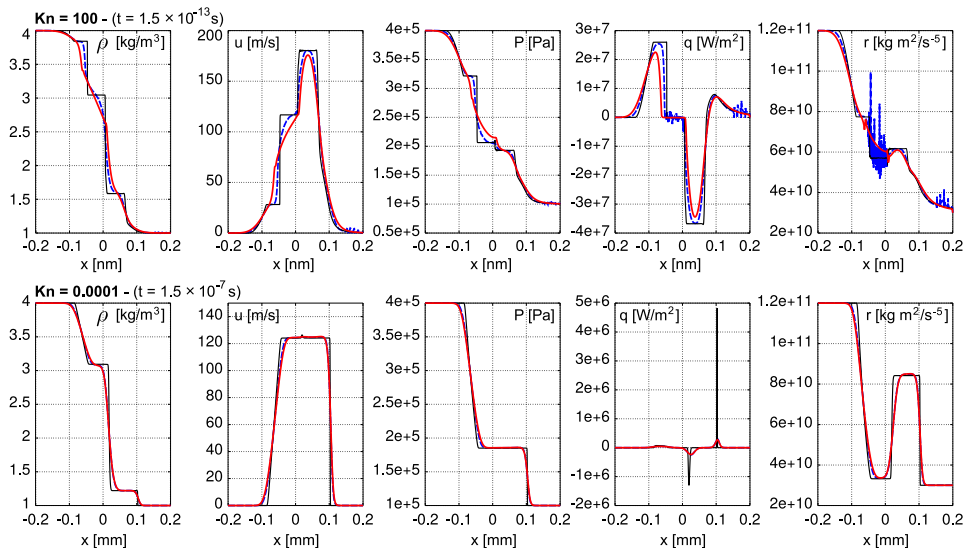


Figure 4.7: Solution of the 5-moment system for the Sod shock tube problem, in the free-molecular limit (Top) and in the continuum regime (Bottom). Black line: reference solution. Blue dashed and Red lines: HLL and Rusanov fluxes, 500 cells, first order in space.

4.2 Approximated wave speeds

The eigenvalues of a system (or at least the maximum and minimum wave speeds) play an important role in its numerical solution. As discussed in Chapter 3, explicit time integration schemes are stable for given values of the Courant number, that depends on the system wave speeds. A number of implicit formulations also require a knowledge of the Courant number (among others, we shall cite implicit dual-time stepping strategies [169–171] where a CFL evolution law is introduced). Also, many numerical fluxes formulations (such as the HLL, Rusanov or Kurganov-Tadmor to cite a few) also require the wave speeds, and their accuracy influences the numerical diffusion properties of such methods.

For the Euler system, the maximum and minimum wave speeds are easily obtained analytically and result in $u \pm a$, u being the bulk velocity and a the speed of sound. However, maximum-entropy systems have much more complex convective fluxes, that include singular closing terms. The analytical expression of such closing moments is either unknown (in the general maximum-entropy formulation) or at least rather complex (in the interpolative closure approximations). As a result, an analytical expression for the eigenvalues of the fluxes Jacobian is often not available. Numerically, this means that one has to (i) build a Jacobian⁵ and (ii) compute its numerical eigenvalues in each cell and at every time step. This dramatically reduces the efficiency of numerical computations, and may become unbearable if one considers multi-dimensional cases and non-equilibrium conditions, where the computational cost of maximum-entropy methods is already much higher than the Euler system (as will be discussed in Section 4.3). Therefore, some approximation of the wave speeds is required.

The simplest strategy, consists in assuming that the maximum and minimum wave speeds of a maximum-entropy system have the same form of the Euler wave speeds, but include a multiplying constant k :

$$w_{\min}^{\max} = u \pm ka . \quad (4.4)$$

An arbitrary value $k > 1$ is chosen, large enough to reproduce the wave speeds of the actual system, or anyway to introduce enough diffusion to allow for a solution. This strategy has been profitably employed in the transitional regime, see for example [154]. In that reference, it was however shown that the maximum-entropy wave speeds can be larger than the Euler equations by orders of magnitude, in non-equilibrium conditions.

⁵That is a 14 by 14 matrix for the 14-moment system.

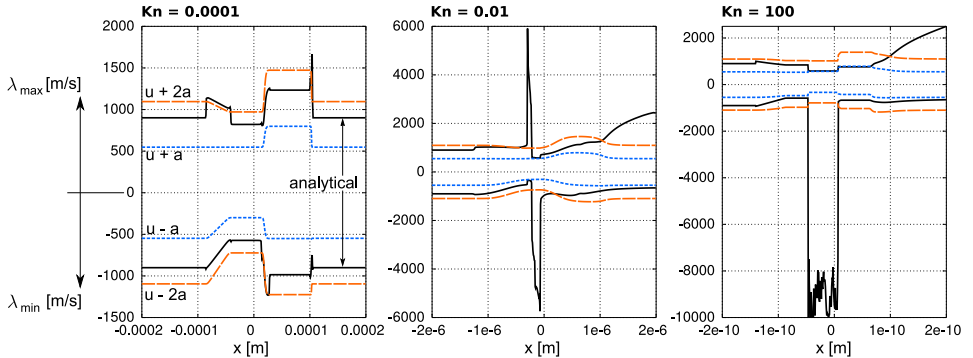


Figure 4.8: Sod shock tube problem at different rarefaction conditions. Black line: numerical value of the maximum and minimum wave speeds of the 5-moment system. Dotted and dashed lines: estimation of the wave speeds using Eq. (4.4) with $k = 1$ and $k = 2$.

Figure 4.8 shows this situation for the Sod shock tube test cases considered in the previous section, at different degrees of rarefaction. The approximation of Eq. (4.4) appears inaccurate for all test cases. For continuum conditions (case $\text{Kn} = 0.0001$) the approximated values are anyway reasonable, and may be employed profitably with limited addition of numerical diffusion. However, as rarefaction is increased, the wave speeds of the real system quickly depart from this approximation around the contact discontinuity region, where non-equilibrium is stronger. Therefore, in order to profitably employ Eq. (4.4), one would need a very large value of k , that ends up overpredicting the wave speeds in most of the domain, causing excessive numerical diffusion. Finally, if the largest wave speeds are not properly retrieved, the numerical discretization may be unstable.

The test case with $\text{Kn} = 100$ of Figure 4.8 shows a large amount of noise, while the previous moment profiles appeared to be reasonably clean. This is ultimately due to the strong dependence of the wave speeds on the heat flux, as will be discussed in the next sections, that amplifies the tiny numerical oscillations of the heat flux, visible from a close inspection of Fig. 4.6, probably originating from the second order discretization.

4.2.1 Approximated wave speeds for the 5-moment system

By numerical inspection, the magnitude of the dimensionless wave speeds of the 5-moment system⁶ can be seen to be proportional to σ^{-1} . Also, they appear to depend strongly on the dimensionless heat flux q^* . The maximum

⁶Being velocities, the wave speeds are non-dimensionalized by scaling with the characteristic velocity $\sqrt{P/\rho}$.

wave speed reaches infinity for $\sigma \rightarrow 0$ and positive values of q^* . The negative wave speed is symmetric in q^* , and thus approaches $-\infty$ for $\sigma \rightarrow 0$ and negative q^* .

Given the dependence on σ^{-1} , it is convenient to multiply the wave speeds by σ for the sake of the present analysis. As shown in Figure 4.9-Left, this makes all points roughly collapse on a single line, that is well approximated by an hyperbola,

$$\lambda_{max}\sigma \approx \frac{1}{2} \left(q^* + \sqrt{q^{*2} + 1} \right) . \quad (4.5)$$

A slightly different scaling could be obtained by dividing the heat flux by σ . This is shown in Fig. 4.9-Right, but will not be discussed further in this work.

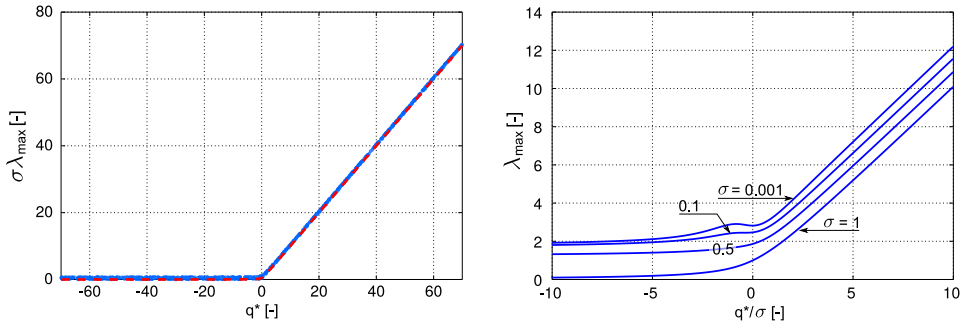


Figure 4.9: Maximum wave speed for the 5-moment system. *Left:* wave speed multiplied by σ , numerical values at random points on the $q^* - \sigma$ plane (blue points) and hyperbola of Eq. (4.5) (red dashed line). *Right:* scaling the heat flux axis by σ .

This simple expression of Eq. (4.5) appears to fit reasonably well the general behavior, but gives a rather high error near equilibrium, for $q^* = 0$. Solving this requires to introduce a function of σ inside the square root of the hyperbola. Also, one can introduce an offset proportional to $\sigma\sqrt{3 - 3\sigma}$ to increase further the accuracy. All these points have been considered more systematically by Baradaran [172], that has obtained approximated expressions for all five wave speeds of the 5-moment system by considering its limiting values in moment space.⁷ The maximum wave speed reads

$$\sigma\lambda_{max} \approx \frac{1}{2} \left[q_x^* + \sqrt{q_x^{*2} - \frac{4}{5}q^*\sigma C + 4\sigma^2 Y} \right] + \sigma E , \quad (4.6)$$

⁷Another reference discussing the wave speeds of the 5-moment system for a regularized closure is [159].

with

$$E = 8/10\sqrt{3 - 3\sigma} , \quad B = 5 - 4\sqrt{\sigma} + \sqrt{10 - 16\sqrt{\sigma} + 6\sigma} , \quad (4.7a)$$

$$C = \sqrt{3 - 3\sigma} , \quad Y = B + E^2 - 2E\sqrt{B} . \quad (4.7b)$$

These expressions will be empirically extended in the next sections.

Baradaran's approximations follow the aforementioned hyperbola structure, and are accurate in most of the domain, losing some accuracy only close to equilibrium, as shown in Fig. 4.10. Nonetheless, these small inaccuracies are most likely to play no role in most practical computations, where wave speeds are merely needed for computing the fluxes and for estimating the Courant number. Indeed, Fig. 4.11 shows that an accurate agreement is obtained between Baradaran's approximations and numerical wave speeds for the Sod shock problem.

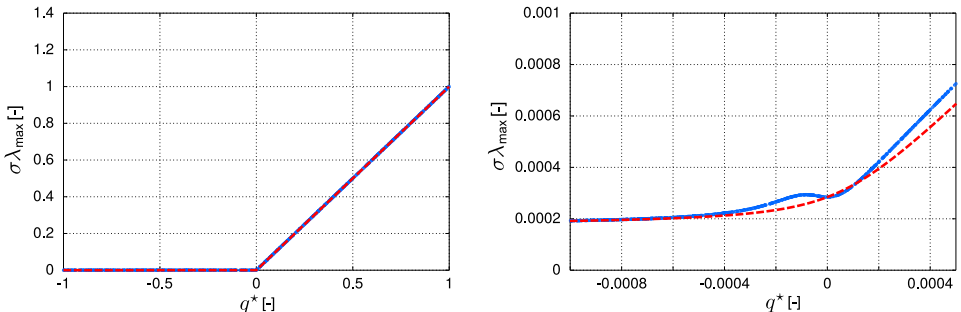


Figure 4.10: Maximum wave speed for the 5-moment system. Blue symbols: random values in the $q^* - \sigma$ plane. Red dashed line: Baradaran's approximation.

4.2.2 Extending the approximation to the 6-moment system

In this section, the wave speeds approximations are extended to the 14-moment system. The proposed formulation is empirical, and the final results are merely to be taken as approximations. Nonetheless, the results constitute a noteworthy improvement over the approximation of Eq. (4.4), still allowing us to avoid building a Jacobian and numerically computing its eigenvalues.

We shall start from a geometrically simplified version of the 14-moment system, obtained by considering a 1-dimensional geometry, with $P_{yy} = P_{zz} \equiv P_{rr}/2$, $P_{ij} = 0$ for $i \neq j$, $q_y = q_z = 0$ and $u_y = u_z = 0$. Note that in the further case where $P_{yy} = P_{zz} \rightarrow 0$, one retrieves the 1D1V case of the 5-moment system. For more details and an expression of the

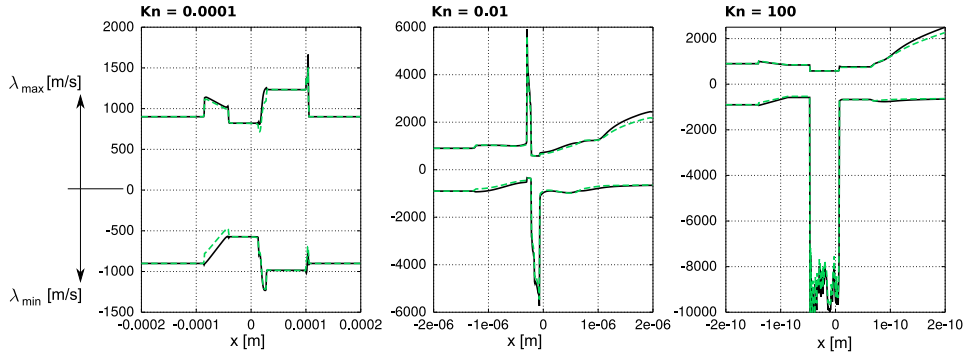


Figure 4.11: Sod shock tube problem at different rarefaction conditions. Black line: numerical value of the maximum and minimum wave speeds of the 5-moment system. Green dashed line: approximation by Baradaran.

fluxes, the reader is referred to McDonald & Torrilhon [67]. As for the 14-moment system, for the 6-moment system the dimensionless pressure reads $P_{xx}^* = (P_{xx})/P$, with $P = (P_{xx} + P_{yy} + P_{zz})/3$, and therefore $P_{xx}^* = 1$ at equilibrium.

The resulting system is composed by six independent moments: ρ , u_x , P_{xx} , P_{rr} , q_x and R_{ijjj} , and after non-dimensionalization, the independent variables in the fluid reference frame are only three: P_{xx}^* , q_x^* and σ (where σ is considered, in place of R_{ijjj}^*). Therefore, this case has only one additional variable with respect to the 5-moment system. Figure 4.12 shows a numerical inspection of the maximum wave speed for this system, in the $q_x^* - \sigma$ plane and for different values of P_{xx}^* .

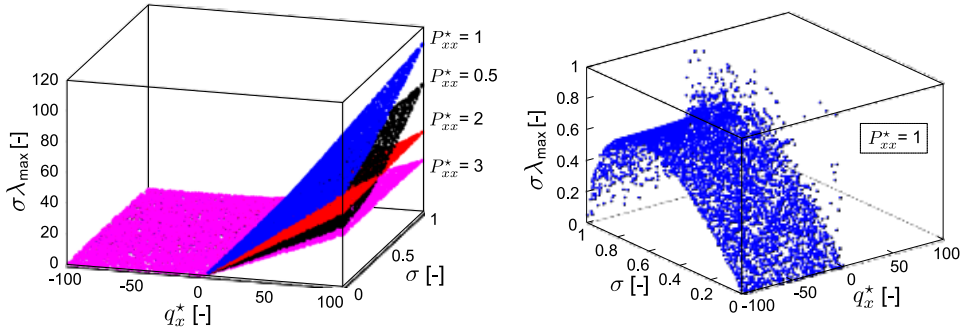


Figure 4.12: Maximum wave speed multiplied by σ for the 6-moment system. Left: random points in the $q_x^* - \sigma$ plane for assigned values of P_{xx}^* . Right: magnification for small values of q_x^* , with P_{xx}^* at equilibrium.

In order to embed a dependence on the pressure, with some foresight we

rewrite Baradaran's expression as

$$\sigma \lambda_{max} \approx W(P_{xx}^*) \frac{1}{2} \left[q_x^* + \sqrt{q_x^{*2} - \frac{4}{5} q^* \sigma C + 4 \sigma^2 Y} \right] + \chi(P_{xx}^*) \sigma E, \quad (4.8)$$

where a function $W(P_{xx}^*)$ was introduced, to multiply the hyperbola-like part, and a function $\chi(P_{xx}^*)$ multiplies the “offset”. We start by considering the limit $q_x^* \rightarrow -\infty$, where Eq. (4.8) becomes

$$\sigma \lambda_{max}|_{q_x^* \rightarrow -\infty} \approx \chi(P_{xx}^*) \sigma E. \quad (4.9)$$

This case is shown in Fig. 4.13-Left. The quantity $\chi(P_{xx}^*)$ can be determined by numerical inspection. Indeed, if we write $\chi E \sigma = A \sigma \sqrt{1 - \sigma}$, we find that the choice $A = \sqrt{3 P_{xx}^*}$ allows to match the pressure dependence, as shown in Fig. 4.13-Right. This fixes $\chi(P_{xx}^*) = \sqrt{P_{xx}^*}$.

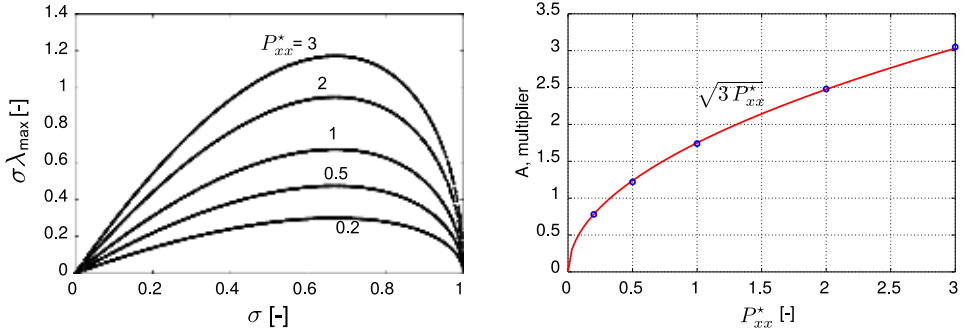


Figure 4.13: Left: wave speed multiplied by σ in the limit of $q_x^* \rightarrow -\infty$, for different values of P_{xx}^* . Right: required values of A for matching the Left figure (symbols) and function $A = \sqrt{3 P_{xx}^*}$.

We then move to the limit of large q_x^* . For the 5-moment case of the previous section, the quantity $\sigma \lambda_{max}$ would not depend on σ when evaluated for a fixed value of $q_x^* \gg 1$. However, Fig. 4.12-Left shows that this is not anymore the case for the 6-moment system, and both the slope and intercept of the function $(\sigma \lambda_{max})|_{q_x^*}(\sigma)$ depend on the pressure. For this reason, a quantity $W(P_{xx}^*)$ was introduced as to modify this part of the plot. We consider $W = a\sigma + b$, and determine the functions $a = a(P_{xx}^*)$ and $b = b(P_{xx}^*)$ by numerical inspection. The values for a and b that allow for Eq. (4.8) to match the 6-moment wave speed are shown in Fig. 4.14, together with a simple fit.

The approximated maximum wave speed for the 6-moment system is finally obtained as

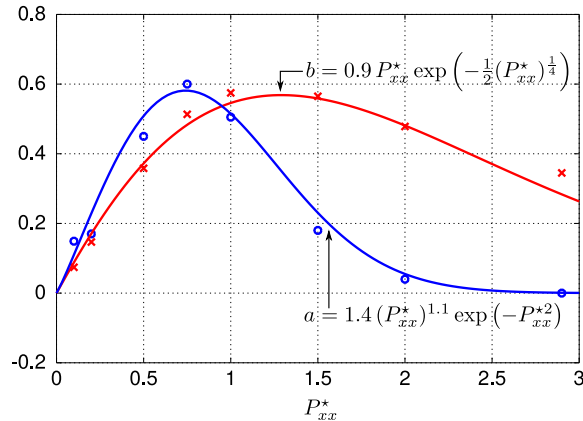


Figure 4.14: Fit of the slope a and intercept b as a function of the pressure.

$$\lambda_{\max}^{6mom} = \frac{a\sigma + b}{2\sigma} \left[q_x^* + \sqrt{q_x^{*2} - 4/5q_x^*\sigma C + 4\sigma^2 Y} \right] + E, \quad (4.10a)$$

$$a = 1.4 (P_{xx}^*)^{1.1} \exp [-P_{xx}^{*2}] , \quad b = 0.9 P_{xx}^* \exp [-1/2 (P_{xx}^*)^{1.4}] , \quad (4.10b)$$

$$E = \frac{8}{10} \sqrt{(3 - 3\sigma) P_{xx}^*} , \quad C = \sqrt{(3 - 3\sigma) P_{xx}^*} , \quad (4.10c)$$

$$B = 5 - 4\sqrt{\sigma} + \sqrt{10 - 16\sqrt{\sigma} + 6\sigma} , \quad Y = B + E^2 - 2E\sqrt{B} . \quad (4.10d)$$

The minimum wave speed is obtained from symmetry considerations: $\lambda_{\min}(q_x^*) = -\lambda_{\max}(-q_x^*)$. Figures 4.15 and 4.16 show that this approximation is able to retrieve the global features of the 6-moment wave speeds, within a maximum error of roughly 20% in most of the domain of interest. A larger error could be expected very close to the physical realizability boundary (Fig. 4.16-Bottom-Right).

4.2.3 Extending the approximation to the 14-moment system

In this section, the wave speeds approximation is extended to the 14-moment system. In principle, the complexity of such system is much greater than for the 6-moment case, as the number of dimensionless variables⁸ is nine: five independent pressure components P_{ij}^* (since the pressure $P = \text{tr}(P_{ij})/3$ is used to scale quantities), three heat fluxes q_x^* and σ (in place of R_{iijj}^*).

⁸After moving to a reference frame where the fluid is at rest.

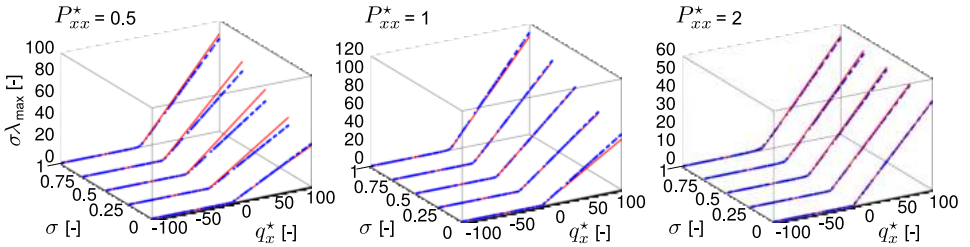


Figure 4.15: Maximum wave speed for the 6-moment system. Red lines: approximated values from Eq. (4.10). Blue dots: numerically computed values.

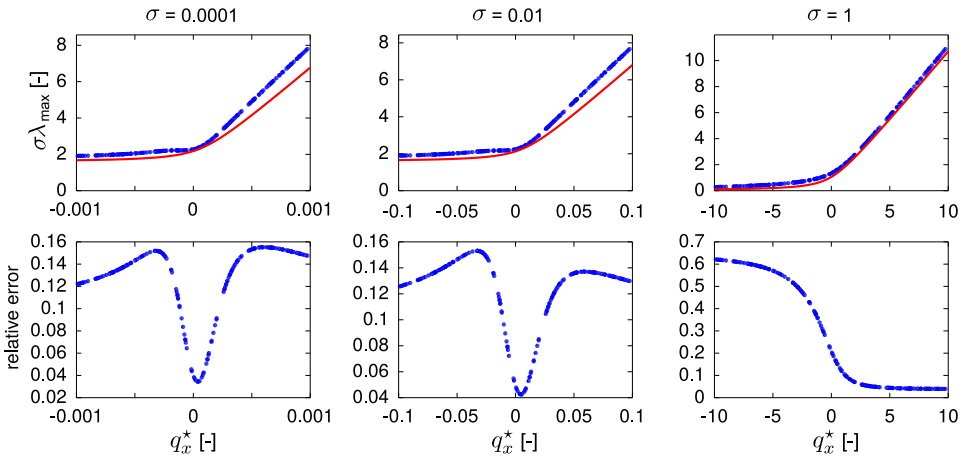


Figure 4.16: Maximum wave speed for the 6-moment system (Top) and relative error (Bottom) for $P_{xx}^* = 1$. Red lines: approximated values from Eq. (4.10). Blue dots: numerically computed values. Bottom: relative error.

Building an approximation for the quantity $\sigma\lambda_{max}$ should thus be done in a 9-dimensional space. Luckily, some simplifications are possible.

First, for the sake of computing the wave speeds along a given direction (say, x), the reference system can be arbitrarily rotated around such direction, as to make one of the two transverse heat flux components zero. In such reference system, the heat flux is $\mathbf{q} = (q_x, \tilde{q}_y, 0)$, with $\tilde{q}_y = \sqrt{q_y^2 + q_z^2}$. This brings the number of independent variables to eight.

This rotation would require the components of the pressure tensor to be rotated as well. However, one can observe⁹ that the maximum wave speed does not change dramatically after such rotation. Indeed, for the sake of obtaining approximated eigenvalues, one can preserve the pressure component P_{xx} , and assume that the rest of the pressure tensor is isotropic, with

⁹From numerical inspection of the wave speeds.

$\tilde{P}_{yy} = \tilde{P}_{zz} = (P_{yy} + P_{zz})/2$ and $P_{ij} = 0$ for $i \neq j$. This assumption removes additional unknowns and the dimensionless wave speeds are defined uniquely by the quantities P_{xx}^* , q_x^* , \tilde{q}_y^* , σ . This is just one additional quantity with respect to the 6-moment system.

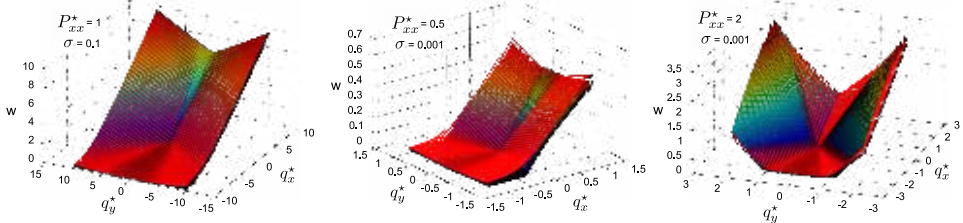


Figure 4.17: Maximum wave speed of the 14-moment system on the $q_x^* - q_y^*$ plane.

The transverse heat flux \tilde{q}_y has a strong effect on the wave speeds, as shown in Fig. 4.17. This effect is however quite predictable, and \tilde{q}_y^* appears to increase the wave speeds almost linearly. This can be reproduced by a redefinition of the heat flux as

$$\hat{q}_x = q_x + \alpha |\tilde{q}_y| = q_x + \alpha \sqrt{\tilde{q}_y^2}, \quad (4.11)$$

where α is to be defined. Substituting this definition in place of q_x , in the approximated 6-moment wave speeds of Eq. (4.10) has the effect of translating the hyperbola-like shape towards negative heat fluxes, whenever a non-zero \tilde{q}_y is present. By inspection of different conditions, this translation is seen to depend on the pressure, such that $\alpha = \alpha(P_{xx}^*)$. This function can be seen to be roughly a parabola, whose coefficients are easily found via fitting:

$$\alpha(x) = 0.6x^2 - 0.38x + 0.35. \quad (4.12)$$

This approximation results in a qualitative agreement with most values of P_{xx}^* . In general, this agreement is reasonably good, except that, for high values of σ and in presence of a non-zero \tilde{q}_y , the approximation strongly underpredicts the actual wave speed, posing some numerical stability issues. We correct this problem by introducing a factor $\tilde{q}_y^2/10$ inside the square root, in the hyperbola expression. This completely defines the proposed approximated expressions for the 14-moment system.

Figure 4.17 shows this approximation for different conditions. The proposed expressions appear to be over-predicting the true wave speeds (increasing the numerical diffusion) in certain regions, but only seldom under-predict them, and in such cases the difference is limited to roughly 20%.

Therefore, despite all assumptions, the proposed wave speeds constitute a useful improvement over the approximation “ $\lambda = u \pm ka$ ”.

Summary of the procedure

For clarity, we summarize here the procedure for obtaining the minimum and maximum wave speeds along the direction x .

1. First, the reference system is shifted as to have a zero bulk velocity. The state of the gas is then defined by $(\rho, P_{ij}, q_i, R_{iijj})$;
2. The reference system is rotated, and we define $\tilde{q}_y = \sqrt{q_y^2 + q_z^2}$;
3. The hydrostatic pressure is computed as $P = \text{tr}P_{ij}/3$, and the state is non-dimensionalized, dividing by the density and suitable powers of $\sqrt{P/\rho}$ (see Section 2.3.1). The system is now completely described by the dimensionless quantities $(P_{xx}^*, q_x^*, \tilde{q}_y^*, \sigma)$;
4. The dimensionless wave speeds are then obtained from:

$$\lambda_{\max}^{14mom} = \frac{a\sigma + b}{2\sigma} \left[\hat{q}_x + \sqrt{\hat{q}_x^2 - 4/5\hat{q}_x\sigma C + 4\sigma^2 Y + \tilde{q}_y^{*2}/10} \right] + E, \quad (4.13a)$$

$$\hat{q}_x = q_x^* + \sqrt{\tilde{q}_y^{*2} (0.6 P_{xx}^{*2} - 0.38 P_{xx}^* + 0.35)}, \quad (4.13b)$$

$$a = 1.4 (P_{xx}^*)^{1.1} \exp[-P_{xx}^{*2}], \quad b = 0.9 P_{xx}^* \exp[-1/2 (P_{xx}^*)^{1.4}], \quad (4.13c)$$

$$E = \frac{8}{10} \sqrt{(3 - 3\sigma) P_{xx}^*}, \quad C = \sqrt{(3 - 3\sigma) P_{xx}^*}, \quad (4.13d)$$

$$B = 5 - 4\sqrt{\sigma} + \sqrt{10 - 16\sqrt{\sigma} + 6\sigma}, \quad Y = B + E^2 - 2E\sqrt{B}, \quad (4.13e)$$

$$\lambda_{\min}^{14mom} = -\lambda_{\max}^{14mom}(-\hat{q}_x^*), \quad (4.13f)$$

where the minimum wave speed is obtained from symmetry considerations. For convenience, we provide an Octave/MATLAB implementation of the last step in Appendix D.

In order to test the approximated wave speeds, the Sod shock tube test case of the previous sections was re-computed using the 14-moment system. Figure 4.18 shows the actual wave speeds, compared to the approximation of Eq. (4.13) and to the simple approximation based on the speed of sound. While the accuracy is not excellent, the proposed approximation is

able to automatically retrieve reasonable values for all the considered rarefaction conditions. In Fig. 4.18, we also show the results of boosting the approximated wave speeds by a factor 1.2. This increases a bit numerical diffusion in some regions, but allows us to stay on the safe side. Notice that the wave speeds exceed the plot region in Fig. 4.18-Right, and magnification was reported for clarity. An analysis of the full scale suggests that in this condition, the proposed approximation appears to underpredict the actual wave speed by a factor of 2, in the region of the contact discontinuity. Therefore, in case an explicit method is to be used, it is suggested to keep the Courant number below 0.5 (although this may not be a strict requirement).

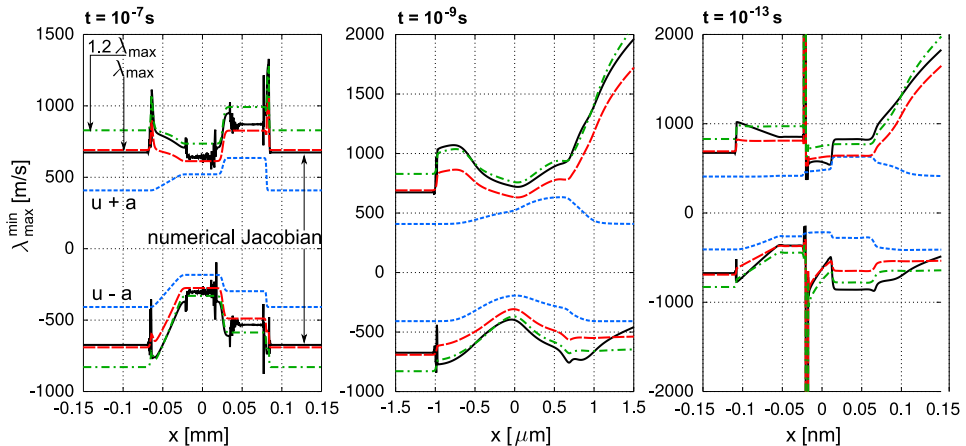


Figure 4.18: Maximum and minimum wave speeds of the 14-moment problem, for the Sod shock tube problem, at various degrees of rarefaction.

4.3 Computational efficiency and minimum allowed σ

This section discusses the computational cost required for solving the 14-moment maximum-entropy system, as compared to the Euler equations.

At a first glance, the most striking factor causing an increased computational cost may appear to be the larger number of equations composing the 14-moment system. This surely causes an increased number of operations. Besides that, the larger number of fields to be tracked is likely to reduce data locality, with a direct increase in the computational times. The numerosity of the closing moments is another important factor causing an increase in the computational cost, even in the case of the interpolative closure [67]. For comparison, all closing moments are simply zero in the Euler

equations, and no such computation is required.

Secondly, for certain density conditions, the collisional source terms may play the most important role. As it was discussed in Chapter 2, the mass, momentum and energy are collision invariants for a simple gas, and thus the Euler equations show no right-hand-side collision sources. Instead, for the 14-moments system, collisions have the effect of equilibrating the higher order moments, and thus impose an additional dynamics at the time scales of the collision frequency. To solve this problem, point-implicit schemes can be employed, although this was never necessary for the present work.

In the non-equilibrium conditions of this work, the most important contribution to the increase in computational cost was found to be played by the system eigenvalues, that determine the dynamics of the system. In particular, as discussed in Section 4.2, the wave speeds of the 14-moment system can be larger than the speed of sound by orders of magnitude in non-equilibrium situations. This forces one to employ smaller time steps in order to have a reasonable Courant number, and thus to follow the faster system dynamics. This is particularly important for time-explicit integration schemes.

Effect of the limiting value σ_{lim}

In Section 2.4, it was mentioned that a minimum threshold for σ is imposed in real simulations, denoted by σ_{lim} . In principle, smaller values of σ_{lim} imply a better accuracy. However, in the previous section, it was seen that the wave speeds are proportional to σ^{-1} . Therefore, the choice of σ_{lim} has a strong impact on the computational times, as smaller values of σ_{lim} increase the stiffness of the problem, allowing it to develop larger wave speeds. In the following, we consider again the Sod shock tube problem of Section 4.1: we compare the profiles obtained for increasing values of σ_{lim} and the resulting computational times. These results are clearly case-specific, but give a clear idea of the results that one may expect.

We consider first the free-molecular case ($\text{Kn} = 100$, simulated time $T_{sim} = 1.5 \times 10^{-13}$ s) and limiting values of $\sigma_{lim} \in (10^{-5}, \dots, 0.1)$. Typical values are in the range of $\sigma_{lim} \approx 10^{-4}$. The computational times are reported in Table 4.1. Grids of 1000 and 5000 cells were employed and showed the very same behavior.¹⁰ The continuum case ($\text{Kn} = 0.0001$, $T_{sim} = 1.5 \times 10^{-7}$ s) was then analyzed for a 5000 cells grid, and re-

¹⁰In principle, long simulation times should be employed for comparing the computational costs, as to exclude the problem setup overheads. However, the fact that a 1000 cells and a 5000 cells grid give the very same efficiencies indicates that the result is reliable.

sults are reported in Table 4.1. From these results, one can appreciate the strong dependence of the computational time with respect to the degree of non-equilibrium, whereas the cost of the Euler system is unchanged. In the non-equilibrium case, the computational cost of the maximum-entropy system is at least 10–30 times higher than for the Euler equations and may be 100–200 times higher if reasonable values of $\sigma_{lim} = 10^{-4} - 10^{-5}$ are used. On the other hand, in the continuum regime the problem is mitigated. The computational cost is always between 6 and 10 times larger than the Euler equation, even for small values of σ_{lim} . Indeed, in the continuum regime, the value of the dimensionless heat flux is limited, therefore reducing the wave speeds.

σ_{lim}	$T_{0.15\text{ ps}}^{1000}$	$T_{0.15\text{ ps}}^{5000}$	$T_{0.15\mu\text{s}}$
0.00001	80 s	1993 s	64 s
0.0001	24 s	631 s	64 s
0.001	8.8 s	215 s	61 s
0.01	5.4 s	137 s	57 s
0.1	3 s	79 s	49 s
Euler	0.34 s	7.1 s	7.2 s

Table 4.1: Computational time of the 14-moment system for different values of limiting σ , and compressible Euler equations. Time-explicit simulations, first order in time and space, CFL imposed to 0.5. The computations were run in serial on an Intel CORE i5 processor, with 12 GB of RAM.

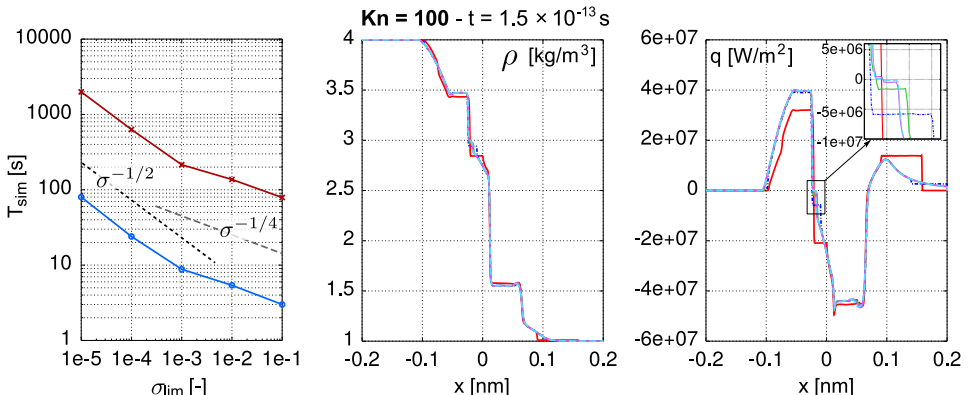


Figure 4.19: Solution of the 14-moment system for the Sod shock tube problem, for different values of σ_{lim} . Left: computational time (blue line with circles: 1000 cells, red line with crosses: 5000 cells). Center and right: density and heat flux. Cases $\sigma = 10^{-5}$ (light blue dashed), $\sigma = 10^{-4}$ (purple solid line) and $\sigma = 10^{-3}$ (green solid line) almost superimpose. Some deviation is visible for $\sigma = 10^{-2}$ (blue dash-dotted) and for $\sigma = 0.1$ the results deviate strongly.

The effects of the value of σ_{lim} are shown in Fig. 4.19 for the free-molecular case, together with the computational times. Obviously, while very large value of σ_{lim} are appealing in terms of computational efficiency, they introduce progressively larger errors in the closing fluxes. All choices of $\sigma_{lim} \leq 10^{-3}$ in Fig. 4.19 result roughly in the same profile, and only some details on the (unphysical) jumps differ. The final effect is however strongly case-sensitive, and ultimately depends on the importance of the closing moments. For the simulations performed in this work, values of $\sigma_{lim} = 10^{-3} - 10^{-5}$ are employed, and never larger.

Finally, it should be stressed that the present analysis considers a simple explicit time marching scheme. Different figures of merit are expected for implicit schemes, and one may employ preconditioning to improve the situation [172]. These points are however beyond the scope in this work.

4.4 2-dimensional test case: rarefied crossing jets

We conclude this first part of the chapter by considering a 2-dimensional test case. Two rarefied supersonic jets are simulated, injected from the sides of a square domain as to cross in the middle, forming an angle of 90° . The density of the jets is taken to be low enough to be in the free-molecular regime. On physical grounds, one would expect that the two jets do not interact, and eventually re-separate. The state in the crossing region is kinetically out of equilibrium, and is the superposition of the drifted VDFs of the two individual jets. A moment closure does not necessarily reproduce this non-equilibrium correctly, hence the motivation for this test case.

This test case is apparently not related to electric propulsion. However, one can consider a number of similarities, for example in the modeling of the thruster plume, where the ions created in the thruster channels cross at the axis and create a toroidal VDF [173]. In general, as we will be considering ions as collisionless, it is important to study the behavior of the 14-moment system for completely collisionless conditions, and a neutral fluid is a good starting point. A similar version of this problem was considered in [120].

A square domain of length $L_x = L_y = 1$ m is considered, and the two jets are centered on the left and on the bottom sides, with a size $\Delta x = \Delta y = L_x/7$ m. Argon neutral gas is simulated. The initial solution inside the domain is taken at a density $n_0 = 10^{10}$ m⁻³ and $T_0 = 300$ K. To simulate the jets, the ghost cells of the domain are set at a density $n_j = 10^{15}$ m⁻³, temperature $T_j = 300$ K and the velocity is set to give a Mach number $M = 5$. Both the initial state and the jets injection points are described by

a Maxwellian in velocity space.

4.4.1 Kinetic solution

In the fully collisionless regime, the kinetic solution is simply computed as a superposition of the particle streams that compose the two jet sources. For a single rarefied jet expanding into vacuum, the distribution function is known to present temperature anisotropy [174]. This is due to the geometry of the problem, combined with lack of collisions, as will be discussed in the following. A kinetic solution is here obtained by assuming that the domain is 2-dimensional and uniform along the third direction z . From this assumption, the *normalized* distribution function factorizes in

$$g(x, y, v_x, v_y, v_z) = g_z g_{xy} \quad \text{with} \quad g_z(v_z) = \left(\frac{m}{2k_B T_j} \right)^{1/2} \exp \left[-\frac{mv_z^2}{2k_B T_j} \right], \quad (4.14)$$

while $g_{xy} = g_{xy}(x, y, v_x, v_y)$ depends on the position to be probed. To evaluate it at a position (x_p, y_p) , we consider a small area centered around that point, as shown in Fig. 4.20, and divide the jet source in a number N_s of uniformly distributed point-source elements. The particles injected by the i -th source element will reach the probed area only if their velocities are directed within an angle $\theta \pm d\theta/2$. In terms of velocity distribution function, only a slice of the source VDF will reach the probed point, and will therefore contribute to the VDF at position (x_p, y_p) .

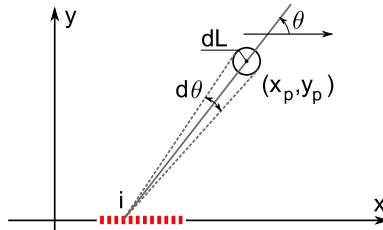


Figure 4.20: Scheme for the numerical evaluation of the collisionless kinetic solution.

The normalized VDF at the probed position (x_p, y_p) is thus obtained as a superposition of all source elements,

$$\tilde{g}_{xy}(x_p, y_p, v_x, v_y) \propto \sum_{i=1}^{N_s} g_i(x_i, y_i, v_x, v_y) \delta_\theta, \quad (4.15)$$

4.4. 2-dimensional test case: rarefied crossing jets

where the function δ_θ is defined as

$$\delta_\theta = \begin{cases} 1 & \text{if } (\theta - \frac{1}{2}d\theta) \leq \text{atan}(v_y/v_x) \leq (\theta + \frac{1}{2}d\theta), \\ 0 & \text{otherwise.} \end{cases} \quad (4.16)$$

Figure 4.21 shows the resulting VDFs at some selected locations, obtained on a velocity space grid composed by 2000×2000 elements, and where the two jet sources were discretized into 1000 point-sources each.

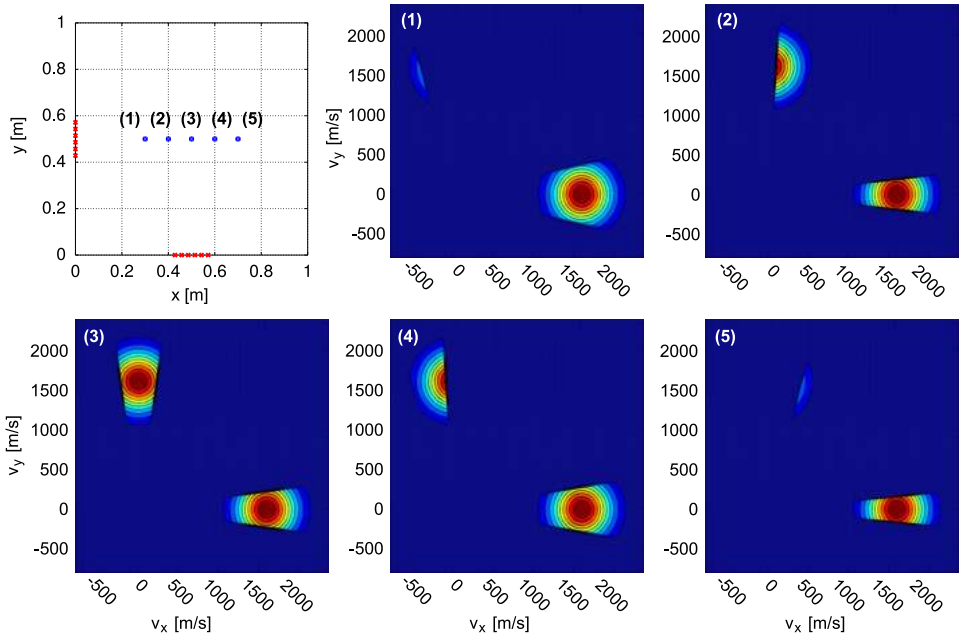


Figure 4.21: Crossing rarefied jets. Top-Left: spatial configuration of point-sources and probed points (1)–(5). The other boxes show the VDF (scaled arbitrarily) at such points, in the (v_x, v_y) plane.

Moments of the kinetic solution

In terms of moments of the VDF, convergence is already obtained for a grid of 1000×1000 elements in velocity space, and 200 point-sources for each jet. The VDFs of Fig. 4.21 are arbitrarily scaled, as no proportionality constant was expressed in Eq. (4.15). Such VDFs do not integrate to the real flow density, since the number of employed sources is not taken into account. However, for the sake of computing dimensionless moments, this

is not an issue. Instead, we first compute a “numerical density” n' as

$$n' = \int_{-\infty}^{+\infty} g_z(v_z) dv_z \iint_{-\infty}^{+\infty} g_{xy}(v_x, v_y) dv_x dv_y \quad (4.17)$$

where the “prime” superscript recalls that this does not necessarily match the physical density. The integral over v_z was separated since g factorizes. From the definition of g_z (Eq. (4.14)) this integral gives

$$\int_{-\infty}^{+\infty} g_z(v_z) dv_z = 1. \quad (4.18)$$

The average velocities u_x and u_y are obtained as averages of the numerically constructed g_{xy} ,

$$u_i = \frac{1}{n'} \int_{-\infty}^{+\infty} g_z(v_z) dv_z \iint_{-\infty}^{+\infty} v_i g_{xy}(v_x, v_y) dv_x dv_y. \quad (4.19)$$

Analogously, the temperatures in the x and y directions read

$$T_i = \frac{m}{n' k_B} \int_{-\infty}^{+\infty} g_z(v_z) dv_z \iint_{-\infty}^{+\infty} (v_i - u_i)^2 g_{xy}(v_x, v_y) dv_x dv_y. \quad (4.20)$$

The dimensionless heat fluxes are obtained by dividing the heat flux by the factor $\rho(P/\rho)^{3/2} = mn(k_B T/m)^{3/2}$, with $T = (T_x + T_y + T_z)/3$ and $T_z = 300$ K,

$$\begin{aligned} q_i^* &= \frac{1}{mn'(k_B T/m)^{3/2}} \iiint_{-\infty}^{+\infty} m c_i c^2 g_{xy}(v_x, v_y) g_z(v_z) dv_x dv_y dv_z \\ &= \frac{1}{n' (k_B T/m)^{3/2}} \left\{ 1 \times \iint_{-\infty}^{+\infty} c_i [(v_x - u_x)^2 + (v_y - u_y)^2] g_{xy} dv_x dv_y \right. \\ &\quad \left. + \int_{-\infty}^{+\infty} v_z^2 g_z(v_z) dv_z \iint_{-\infty}^{+\infty} c_i g_{xy}(v_x, v_y) dv_x dv_y \right\}, \end{aligned} \quad (4.21)$$

with $c_i = v_i - u_i$ and i either x or y . Notice that this time the velocity v_z appears in the integral (through the peculiar velocity term c^2). We have that

$$\int_{-\infty}^{+\infty} v_z^2 g_z(v_z) dv_z = \frac{k_B T}{m}, \quad (4.22)$$

finally giving

$$q_i^* = \frac{1}{n' (k_B T/m)^{3/2}} \iint_{-\infty}^{+\infty} c_i \left(c_x^2 + c_y^2 + \frac{k_B T}{m} \right) g_{xy}(v_x, v_y) dv_x dv_y. \quad (4.23)$$

These moments will be compared to the 14-moment solution in the next section.

4.4.2 14-moment and Euler solutions

In the free-molecular regime, the two rarefied jets should not interact. However, a general moment system does not necessarily reproduce correctly such behavior. To start off, we compute the solution of the 14-moment system for a single jet. This solution is then rotated by 90° and superimposed to itself, as to give artificially the expected result of two crossing jets that do not interact. This artificial solution is then compared to a full solution of two jets simulated simultaneously.

The problem is solved on a Cartesian grid of 1280×1280 cells. A time-marching approach is employed, with Courant number fixed to 0.5 and explicit Midpoint Euler time integrator. The steady state is reached after roughly 1.5 ms of simulation time. The same numerical settings are employed for both the single-jet and the two-jets simulations: in such way, both simulations show an analogous degree of numerical diffusion, and results can be compared.

The numerical solution of the full problem proceeds reasonably fast until the two jets cross. At such point, non-equilibrium increases (as the VDF deviates from the Maxwellian), and correspondingly the wave speeds also increase, and a smaller time step is needed in order to respect the CFL condition. In particular, the situation happens to be so strong that, when the second order MUSCL approach is enabled, the wave speeds become extremely large and the simulation becomes impractical. This problem could be solved by implicit time stepping, or by preconditioning the system. In this work, we simply give up with second order accuracy, but in order to reduce the high numerical diffusion of the Rusanov scheme, we adopt the partial MUSCL reconstruction of Eq 3.8, with $\beta = 0.75$.

Figure 4.22 shows the resulting density field from the 14-moment system, and compares the full solution of the two-jets to the artificially superimposed jets. From such solution, the values were extracted along the axis of one jet, on the line with $y = 0.5$ m, for $x \in (0, 1)$ m, and dimensionless moments were computed. These moments were also computed from the kinetic results, and are compared in Fig. 4.23. All these results confirm the quality of the 14-moment solution. It is useful to recall here reference [127], where various shapes of the attainable VDFs are shown for the 5-moment systems in moment space. The order-4 maximum-entropy system shows capable of representing a number of situations such as the bump-on-tail and bi-Maxwellians. Analogously, the 14-moment system is a reasonable choice for representing the VDFs of the present case, that are roughly the superposition of two drifted Maxwellians. We expect the

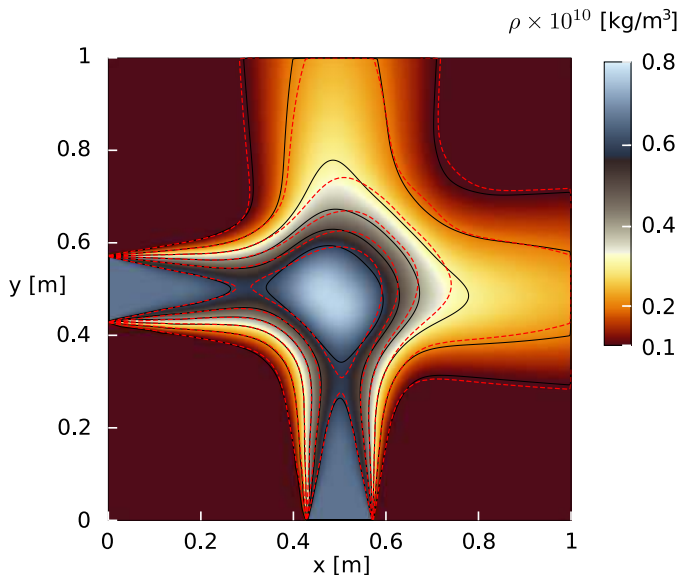


Figure 4.22: Crossing rarefied jets, solution of the 14-moment system. Colors and black lines: contours of the full two-jets solution. Red dashed lines: superimposed contours of the artificial superimposed-jets solution.

solution to quickly lose accuracy if more jets would be considered, as the VDF would show too many separate bumps to be properly reproduced. The limits of applicability are still to be properly investigated.

The current solution is obtained with a GPU-accelerated solver (see Appendix A) and requires roughly 20 hours of computational time. The inaccuracies of Figures 4.22 and 4.23 could probably be reduced by employing a finer grid.

Solution of the Euler equations

For comparison, the solution of the Euler equations is also computed. For this case, second order accuracy and HLL numerical fluxes are employed, as to reduce the numerical error. As discussed in Chapter 2, the Euler system is theoretically justified for Maxwellian VDFs. In absence of collisions, also the more general class of symmetric VDFs would respect the Euler closure. However, both situations are surely not representative of the present two-humped VDFs. Indeed, this system is not able to reproduce the jets separation, and once the jets cross, they interact forming an unphysical shock structure, as shown in Fig. 4.24. Moreover, for the considered conditions, this result appears to be unstable, and a symmetric oscillating solution quickly appears, eventually transitioning into asymmetric oscillations.

4.4. 2-dimensional test case: rarefied crossing jets

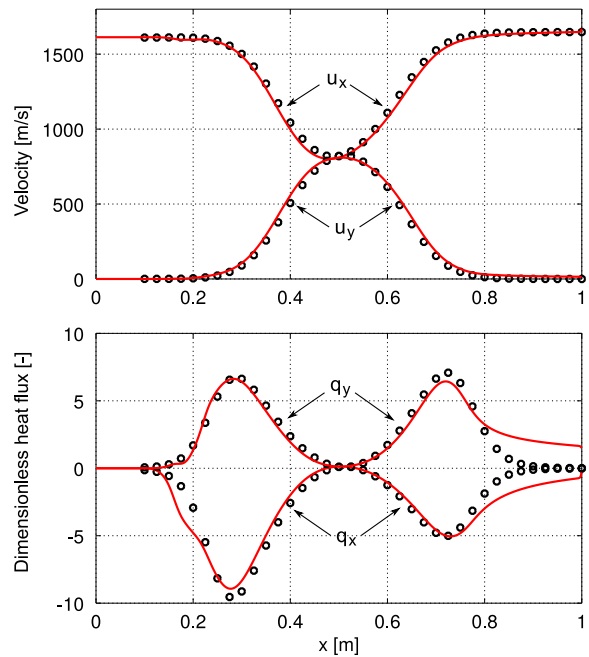


Figure 4.23: Crossing rarefied jets; moments extracted along a jet centerline, for $y = 0.5$ m. Symbols: kinetic solution. Solid line: 14-moment solution.

tions (Fig. 4.25).

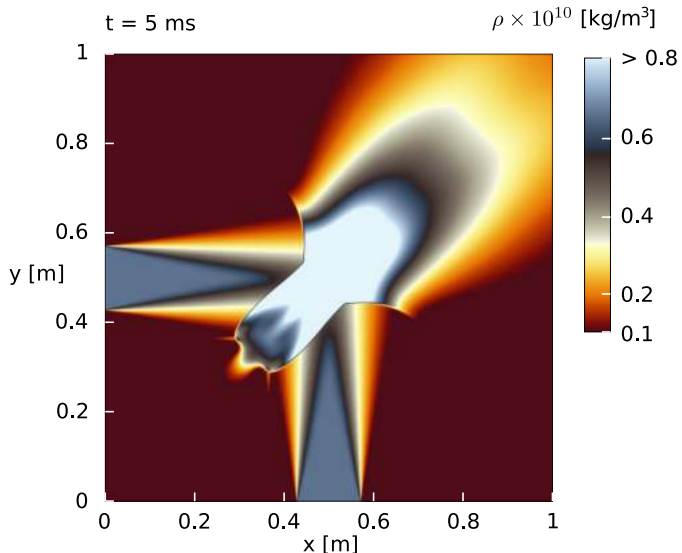


Figure 4.24: Solution of the Euler equations for two crossing jets at a timestep of 5 ms.

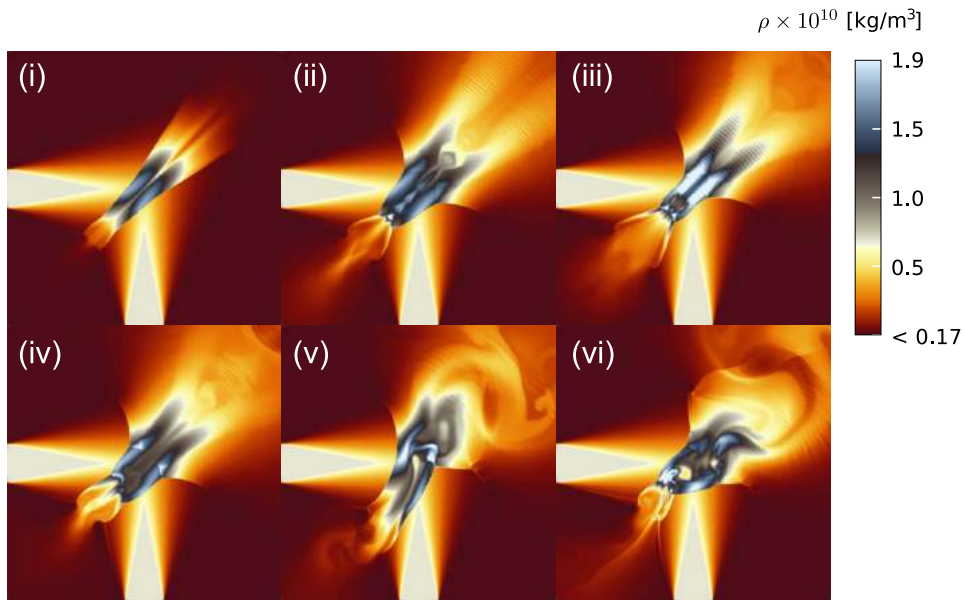


Figure 4.25: Solution of the Euler equations for two crossing jets at a different time steps. Density field. The solution is unstable, and shows first a symmetric instability (ii-iii), that develops into an asymmetric one (iv-v-vi).

Computational efficiency

An analysis of the computational times was performed, analogously to what was done in Section 4.3 for the Sod shock tube problem. Table 4.2 reports the computational times for the 14-moment and the Euler systems, for various values of the parameter σ_{lim} .

σ_{lim}	$T_{1.5 \text{ ms}}$	T^{14}/T^E
0.00001	16565 s	368.1
0.0001	8873 s	197.2
0.001	4948 s	109.9
0.01	2663 s	59.17
0.1	1973 s	43.84
Euler	45 s	-

Table 4.2: Computational time for the 14-moment system, for different values of limiting σ , and Euler equations. 2D crossing jets test case, simulated time: 1.5 ms. Time-explicit simulations, first order in time and space, CFL imposed to 0.5. Grid: 640×640 cells.

The efficiency analysis is done on a reduced grid of 640×640 cells, using a first order solution in time and space, and Rusanov fluxes for both the 14-moment and the Euler systems. For the analysis, the program was

run on an NVidia Tesla K20X GPU. Despite the differences with the Sod shock tube case of Section 4.3 (this simulation has higher dimensionality, and two different solvers are employed), the computational efficiencies are in line with the previous results of Table 4.1.

4.5 Electromagnetic source terms

The previous sections analyzed the maximum-entropy system in rarefied conditions. In order to apply the 14- and 5-moment systems to the simulation of plasmas, one also needs to develop the electromagnetic source terms G_{EB} . These terms have first appeared in the generalized moment equation, Eq 2.29, and for a given particle quantity ψ , they read

$$G_{\text{EB}}^{(\psi)} = \frac{q}{m} \left\langle (\mathbf{E} + \mathbf{v} \times \mathbf{B}) \cdot \frac{\partial \psi}{\partial \mathbf{v}} \right\rangle. \quad (4.24)$$

In the following, we shall detail their derivation for the 14- and 5-moment systems.

14-moment system

For the 14-moment system, the source terms become

$$\begin{aligned} G_{\text{EB}}^{(\psi)} = & \frac{q}{m} \left\langle E_x \frac{\partial \psi}{\partial v_x} + E_y \frac{\partial \psi}{\partial v_y} + E_z \frac{\partial \psi}{\partial v_z} \right\rangle + \frac{q}{m} \left\langle (v_y B_z - v_z B_y) \frac{\partial \psi}{\partial v_x} \right. \\ & \left. + (v_z B_x - v_x B_z) \frac{\partial \psi}{\partial v_y} + (v_x B_y - v_y B_x) \frac{\partial \psi}{\partial v_z} \right\rangle. \end{aligned} \quad (4.25)$$

The 14-moment closure is obtained by the choice $\psi = m(1, v_i, v_i v_j, v_i v^2, v^4)$, as discussed in Chapter 2. Since the order of indices is a possible source of error, the state vector is reported here in full form, for convenience:

$$\mathbf{U} = \begin{pmatrix} U_1 \\ U_2 \\ U_3 \\ U_4 \\ U_5 \\ U_6 \\ U_7 \\ U_8 \\ U_9 \\ U_{10} \\ U_{11} \\ U_{12} \\ U_{13} \\ U_{14} \end{pmatrix} = \begin{pmatrix} \langle m \rangle \\ \langle mv_x \rangle \\ \langle mv_y \rangle \\ \langle mv_z \rangle \\ \langle mv_x v_x \rangle \\ \langle mv_x v_y \rangle \\ \langle mv_x v_z \rangle \\ \langle mv_y v_y \rangle \\ \langle mv_y v_z \rangle \\ \langle mv_z v_z \rangle \\ \langle mv_x v^2 \rangle \\ \langle mv_y v^2 \rangle \\ \langle mv_z v^2 \rangle \\ \langle mv^4 \rangle \end{pmatrix} = \begin{pmatrix} \rho \\ \rho u_x \\ \rho u_y \\ \rho u_z \\ \rho u_x u_x + P_{xx} \\ \rho u_x u_y + P_{xy} \\ \rho u_x u_z + P_{xz} \\ \rho u_y u_y + P_{yy} \\ \rho u_y u_z + P_{yz} \\ \rho u_z u_z + P_{zz} \\ \rho u_x u^2 + \dots + q_x \\ \rho u_y u^2 + \dots + q_y \\ \rho u_z u^2 + \dots + q_z \\ \rho u^4 + \dots + R_{ijj} \end{pmatrix}. \quad (4.26)$$

Computing the source terms is only a matter of computing the derivatives of ψ with respect to the particle velocities, as reported in Table 4.3.

	ψ	$\partial\psi/\partial v_x$	$\partial\psi/\partial v_y$	$\partial\psi/\partial v_z$
1)	m	0	0	0
2)	mv_x	m	0	0
3)	mv_y	0	m	0
4)	mv_z	0	0	m
5)	$mv_x v_x$	$2mv_x$	0	0
6)	$mv_x v_y$	mv_y	mv_x	0
7)	$mv_x v_z$	mv_z	0	mv_x
8)	$mv_y v_y$	0	$2mv_y$	0
9)	$mv_y v_z$	0	mv_z	mv_y
10)	$mv_z v_z$	0	0	$2mv_z$
11)	$mv_x v^2$	$3mv_x^2 + m(v_y^2 + v_z^2)$	$2mv_x v_y$	$2mv_x v_z$
12)	$mv_y v^2$	$2mv_x v_y$	$3mv_y^2 + m(v_x^2 + v_z^2)$	$2mv_y v_z$
13)	$mv_z v^2$	$2mv_x v_z$	$2mv_y v_z$	$3mv_z^2 + m(v_x^2 + v_y^2)$
14)	mv^4	$4mv_x v^2$	$4mv_y v^2$	$4mv_z v^2$

Table 4.3: Velocity derivatives of particle quantities $\psi = m(1, v_i, v_i v_j, v_i v^2, v^4)$.

The resulting electric and magnetic sources are directly obtained. The electric sources \mathbf{G}_E involve first derivatives of ψ , hence the source for a

moment of order n involves only moments of order $n - 1$.

$$\begin{pmatrix} G_{\mathbf{E},1} \\ G_{\mathbf{E},2} \\ G_{\mathbf{E},3} \\ G_{\mathbf{E},4} \\ G_{\mathbf{E},5} \\ G_{\mathbf{E},6} \\ G_{\mathbf{E},7} \\ G_{\mathbf{E},8} \\ G_{\mathbf{E},9} \\ G_{\mathbf{E},10} \\ G_{\mathbf{E},11} \\ G_{\mathbf{E},12} \\ G_{\mathbf{E},13} \\ G_{\mathbf{E},14} \end{pmatrix} = \frac{q}{m} \begin{pmatrix} 0 \\ \mathbf{E}_x U_1 \\ \mathbf{E}_y U_1 \\ \mathbf{E}_z U_1 \\ 2\mathbf{E}_x U_2 \\ \mathbf{E}_x U_3 + \mathbf{E}_y U_2 \\ \mathbf{E}_x U_4 + \mathbf{E}_z U_2 \\ 2\mathbf{E}_y U_3 \\ \mathbf{E}_y U_4 + \mathbf{E}_z U_3 \\ 2\mathbf{E}_z U_4 \\ \mathbf{E}_x (3U_5 + U_8 + U_{10}) + 2\mathbf{E}_y U_6 + 2\mathbf{E}_z U_7 \\ 2\mathbf{E}_x U_6 + \mathbf{E}_y (U_5 + 3U_8 + U_{10}) + 2\mathbf{E}_z U_9 \\ 2\mathbf{E}_x U_7 + 2\mathbf{E}_y U_9 + \mathbf{E}_z (U_5 + U_8 + 3U_{10}) \\ 4\mathbf{E}_x U_{11} + 4\mathbf{E}_y U_{12} + 4\mathbf{E}_z U_{13} \end{pmatrix}. \quad (4.27)$$

The magnetic source terms \mathbf{G}_B on the other hand, other than the velocity derivative of ψ , also include a cross product with the particle velocity. Therefore, the final order of the velocity is the same, and the source for a moment of order n involves other moments of the same order in the veloc-

ity. The magnetic terms ultimately reads

$$\begin{pmatrix} G_{\mathbf{B},1} \\ G_{\mathbf{B},2} \\ G_{\mathbf{B},3} \\ G_{\mathbf{B},4} \\ G_{\mathbf{B},5} \\ G_{\mathbf{B},6} \\ G_{\mathbf{B},7} \\ G_{\mathbf{B},8} \\ G_{\mathbf{B},9} \\ G_{\mathbf{B},10} \\ G_{\mathbf{B},11} \\ G_{\mathbf{B},12} \\ G_{\mathbf{B},13} \\ G_{\mathbf{B},14} \end{pmatrix} = \frac{q}{m} \begin{pmatrix} 0 \\ \mathbf{B}_z U_3 - \mathbf{B}_y U_4 \\ \mathbf{B}_x U_4 - \mathbf{B}_z U_2 \\ \mathbf{B}_y U_2 - \mathbf{B}_x U_3 \\ 2(\mathbf{B}_z U_6 - \mathbf{B}_y U_7) \\ -\mathbf{B}_z U_5 + \mathbf{B}_x U_7 + \mathbf{B}_z U_8 - \mathbf{B}_y U_9 \\ \mathbf{B}_y U_5 - \mathbf{B}_x U_6 + \mathbf{B}_z U_9 - \mathbf{B}_y U_{10} \\ 2(\mathbf{B}_x U_9 - \mathbf{B}_z U_6) \\ \mathbf{B}_x U_{10} - \mathbf{B}_z U_7 + \mathbf{B}_y U_6 - \mathbf{B}_x U_8 \\ 2(\mathbf{B}_y U_7 - \mathbf{B}_x U_9) \\ \mathbf{B}_z U_{12} - \mathbf{B}_y U_{13} \\ \mathbf{B}_x U_{13} - \mathbf{B}_z U_{11} \\ \mathbf{B}_y U_{11} - \mathbf{B}_x U_{12} \\ 0 \end{pmatrix}. \quad (4.28)$$

As expected, the magnetic field has no effect on the mass (first equation) and the 14-th moment equation, that represents the average of the particle energies squared.

The electromagnetic source terms are closed, and do not require any moment other than these already appearing in the state vector \mathbf{U} . Also, the source terms are linear in the moments¹¹ and can be written as $\mathbf{G}_{\text{EB}} = \underline{\underline{A}} \mathbf{U}$. In the simple case of imposed electric and magnetic fields and no space gradients, the time variation of \mathbf{U} due to electric fields is thus

$$\frac{d\mathbf{U}}{dt} = \underline{\underline{A}} \mathbf{U} \implies \mathbf{U}(t) = \exp[\underline{\underline{A}}(t - t_0)] \mathbf{U}(t_0). \quad (4.29)$$

This could be employed for the formulation of time-integration methods, as to ensure that all moments are integrated consistently (see Appendix B).

5-moment system

For the 5-moment system, the situation is much simpler. Indeed, considering only one translational degree of freedom forces one to neglect the magnetic field, that would otherwise involve further directions. Strictly speaking, this system can still describe the dynamics *along* the magnetic

¹¹The electromagnetic fields do depend on the moments (density and current), but through the Maxwell equations. At a given time step of a time-explicit simulation, these fields are fixed.

field lines (and in absence of collisions), where \mathbf{B} has no effect and does not appear in the sources. The sources simplify to $G_{EB} = \langle E \partial\psi/\partial v \rangle$, which gives

$$G_{EB} = G_E = \begin{pmatrix} G_{E,1} \\ G_{E,2} \\ G_{E,3} \\ G_{E,4} \\ G_{E,5} \end{pmatrix} = \frac{q}{m} \begin{pmatrix} 0 \\ E U_1 \\ 2 E U_2 \\ 3 E U_3 \\ 4 E U_4 \end{pmatrix}. \quad (4.30)$$

4.6 Plasma dispersion relations

As a final analysis of the order-4 maximum entropy system, we consider the dispersion relation for electron and ion plasma waves. The reader is referred to classical references [5, 77] for more details. As the maximum-entropy systems are able to reproduce non-equilibrium conditions and embed a different thermodynamics than the Euler equations, we expect the dispersion relations to deviate from the classical values.¹² In this section, we only analyze electrostatic longitudinal waves. No collisions will be considered, and the only restoring force will be provided by the Poisson's equation,

$$-\varepsilon_0 \frac{\partial^2 \phi}{\partial x^2} = e(n_i - n_e). \quad (4.31)$$

In order to study dispersion relations, a small perturbation (subscript “1”) to an otherwise uniform state (subscript “0”) is considered. For the maximum-entropy system, all states in moment space can be selected as the linearization state “0”: both equilibrium and non-equilibrium points (where the state is described by a non-Maxwellian maximum-entropy distribution) are eligible. Indeed, since collision are disabled, all such initial states are also steady state conditions, as there is no mechanism that would drive the VDF towards a local Maxwellian. The only criteria for the choice of the linearization state will be space uniformity and to prevent no charge unbalance, or the Poisson’s equation would make such state unstable.

Wave-like solutions are then investigated, assuming a sinusoidal behavior of the perturbations

$$n_1 = \tilde{n}_1 \exp[i(kx - \omega t)], \quad (4.32)$$

¹²In the best case scenario, one wishes that a moment systems could reproduce the kinetic dispersion relations [77], although this point will not be analyzed in the present work.

and the same for all other variables. In the following, the symbol “ \sim ” will be dropped for simplicity. The stability in time of a perturbation of wave number k can be analyzed by checking the real and imaginary parts of the angular frequency $\omega(k)$ (see for example [62]). Writing $\omega = \omega_R + i\omega_I$ gives

$$n_1 = \tilde{n}_1 \exp(\omega_I t) \exp[i(kx - \omega_R t)], \quad (4.33)$$

hence, with this formulation, positive values of ω_I imply amplification of the perturbation, while negative values represent damping.

For wave-like solutions, the derivatives transform as $\partial_t \rightarrow -i\omega$, and $\partial_x \rightarrow ik$. Since the uniform state is taken as uniform, we obtain $\phi_0 = 0$, and the Poisson's equation transforms to

$$-\varepsilon_0 \frac{\partial^2 \phi_1}{\partial x^2} = e(n_i - n_e) \implies \phi_1 = \frac{e(n_{i1} - n_{e1})}{k^2 \varepsilon_0}. \quad (4.34)$$

At this point, the charges dynamics is described by introducing a fluid model. We consider here the Euler equations and the 5-moment system. The 14-moment system is not considered: indeed, in absence of a magnetic field, electrostatic waves are purely longitudinal and involve a single translational degree of freedom. Without collisions, this degree of freedom does not exchange energy with the other translational modes. For this same reason, in treating plasma waves, the authors typically set the adiabatic constant to $\gamma = 3$ (see [5, 53]). The Euler system is written in primitive variables and reads

$$\begin{cases} \partial_t \rho + u \partial_x \rho + \rho \partial_x u = 0, \\ \partial_t u + u \partial_x u + 1/\rho \partial_x P = -\frac{q}{m} \partial_x \phi, \\ \partial_t P + \gamma P \partial_x u + u \partial_x P = 0, \end{cases} \quad (4.35)$$

and after linearization, it is easily written in matrix form as

$$-i\omega \begin{pmatrix} \rho_1 \\ u_1 \\ P_1 \end{pmatrix} + ik \begin{bmatrix} u_0 & \rho_0 & 0 \\ 0 & u_0 & 1/\rho_0 \\ 0 & \gamma P_0 & u_0 \end{bmatrix} \begin{pmatrix} \rho_1 \\ u_1 \\ P_1 \end{pmatrix} = -ik \frac{q}{m} \begin{pmatrix} 0 \\ \phi_1 \\ 0 \end{pmatrix}. \quad (4.36)$$

The same can be done for the 5-moment system, that in primitive variables

reads

$$\left\{ \begin{array}{l} \partial_t \rho + u \partial_x \rho + \rho \partial_x u = 0, \\ \partial_t u + u \partial_x u + 1/\rho \partial_x P = -\frac{q}{m} \partial_x \phi, \\ \partial_t P + 3P \partial_x u + u \partial_x P + \partial_x Q = 0, \\ \partial_t Q + 4Q \partial_x u - 3P/\rho \partial_x P + u \partial_x Q + \partial_x R = 0, \\ \partial_t R + 5R \partial_x u - 4Q/\rho \partial_x P + u \partial_x R + \partial_x S = 0. \end{array} \right. \quad (4.37)$$

and the very same linearization can be done. Note that in both systems the electric field appears only in the velocity equation, since all other equations are those of the central moments, that are not affected by it. The further steps depend on the type of oscillations to be considered.

4.6.1 Electron waves

Let us start by analyzing longitudinal electron oscillations and waves. All moments n, ρ, u, P, Q, R are referred to the electron population. Given the large mass disparity, electron waves have a much higher frequency than ion waves, hence ions can be treated as a background of fixed neutralizing charges, with number density $n_i = n_{e0} = n_0$, and thus $n_{i1} = 0$. The linearized Poisson's equation gives $\phi_1 = -en_1/(k^2 \varepsilon_0)$, with n_1 the perturbed electrons number density. The Euler system thus becomes

$$\left\{ k \begin{bmatrix} u_0 & \rho_0 & 0 \\ 0 & u_0 & 1/\rho_0 \\ 0 & \gamma P_0 & u_0 \end{bmatrix} + \frac{1}{k} \frac{q^2}{m^2 \varepsilon_0} \begin{bmatrix} 0 & 0 & 0 \\ 1 & 0 & 0 \\ 0 & 0 & 0 \end{bmatrix} - \omega \begin{bmatrix} 1 & 0 & 0 \\ 0 & 1 & 0 \\ 0 & 0 & 1 \end{bmatrix} \right\} \begin{pmatrix} \rho_1 \\ u_1 \\ P_1 \end{pmatrix} = \begin{pmatrix} 0 \\ 0 \\ 0 \end{pmatrix}, \quad (4.38)$$

that is an eigenvalue problem. We write it as

$$\left\{ k [J_0] + \frac{1}{k} \frac{q^2}{m^2 \varepsilon_0} [M_\phi] - \omega [I] \right\} U_1 = 0 \quad (4.39)$$

with $[J_0]$ the Jacobian of the convective fluxes, evaluated at the linearization state, $[I]$ the identity matrix, and $[M_\phi]$ a matrix filled with zeros with a sole unitary entry in the first element (density) of the second row (momentum equation). The eigenvalues of such system can be easily obtained both analytically and numerically, and result in the classical (fluid) warm electrons dispersion relation

$$\omega^2 = \omega_p^2 + \frac{3}{2} k^2 (2k_B T/m) \quad (4.40)$$

where k_B is the Boltzmann constant, T and m are the electron temperature and mass and $\omega_p = \sqrt{n_0 e^2 / (m \varepsilon_0)}$ the electron plasma frequency.

The same calculations can be done on the 5-moment system and this also results in Eq. (4.39), with

$$[J_0] = \begin{bmatrix} u & \rho & 0 & 0 & 0 \\ 0 & u & 1/\rho & 0 & 0 \\ 0 & 3P & u & 1 & 0 \\ 0 & 4Q & -3P/\rho & u & 1 \\ \frac{\partial S}{\partial \rho} & 5R & -4Q/\rho + \frac{\partial S}{\partial P} & \frac{\partial S}{\partial Q} & u + \frac{\partial S}{\partial R} \end{bmatrix}_0, \quad (4.41)$$

and where the matrix $[M_\phi]$ reads

$$[M_\phi] = \begin{bmatrix} 0 & 0 & 0 & 0 & 0 \\ 1 & 0 & 0 & 0 & 0 \\ 0 & 0 & 0 & 0 & 0 \\ 0 & 0 & 0 & 0 & 0 \\ 0 & 0 & 0 & 0 & 0 \end{bmatrix}. \quad (4.42)$$

The dispersion relation is less trivial for this case, due to the higher dimensionality and the more complex structure of the fluxes Jacobian (attributed to the closing moment S). However, by numerical computation one can easily evaluate the dispersion relation at different points in moment space.

Dispersion relation at different points in moment space

The linearization condition for the numerical computation of the dispersion relation is taken as $n_0 = 10^{10} \text{ m}^{-3}$, $T_0 = 1000 \text{ K}$ and $u_0 = 0 \text{ m/s}$. The only ion property that matters for electron waves is the density, $n_{i0} = n_0$.

The 5-moment system without source terms is hyperbolic. Therefore, its eigenvalues are in the form $\omega(k) = k\lambda_i$, with λ_i the i -th (real) wave speed.¹³ The dispersion relation for the electrically neutral 5-moment system is thus composed by a straight line, with constant phase and group velocities for each fluid mode. When introducing the self-consistent electric field as a source term, we observe the very same feature in the limiting case of a very large wave number, $k\lambda_{\text{De}} \gg 1$ (with λ_{De} the Debye length for the considered n_0 and T_0). This is shown in Fig. 4.26 for equilibrium conditions ($Q^* = 0, R^* = 3$), where the numerical dispersion relation is seen to asymptote to the neutral-fluid dispersion relation. For lower wave numbers, the dispersion relation settles on the plasma frequency, as expected.

¹³This is evident if one considers the eigenvalue problem of Eq. (4.39), without electric fields, where the eigenvalues of the system are seen to be equal to ω/k .

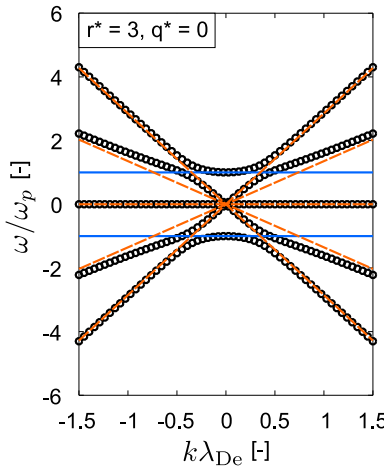


Figure 4.26: Dispersion relation around equilibrium. The full 5-moment system (symbols) retrieves the plasma frequency ω_p (blue horizontal line) for small wave numbers, and asymptotes to the convective-only dispersion relation (neutral fluid, orange dashed lines) for large wave numbers.

An analysis of the real and imaginary parts of ω shows that in some regions of the moment space, the problem may develop imaginary complex conjugate eigenvalues, associated to a growth or decay of the initial perturbation. Such region neighbors the physical realizability boundary, where the VDF is strongly non-Maxwellian and is composed by two Dirac deltas [127]. These results may reflect the presence of microinstabilities (see for example [35, 175]), and are to be further investigated in future works.

The maximum and minimum imaginary parts are shown in Fig. 4.27. For every point in this plot, the values q^*, R^* determine the thermodynamic state: such state was used to linearize the system and compute numerically the dispersion relation for various values of $k \in (0.001, 10)\lambda_{De}$. The maximum and minimum imaginary parts refer to the maximum and minimum among all eigenvalues and for whatever considered value of k .

The dispersion relation is then analyzed more in detail at the locations marked by labels “R” (for “real”) or “C” (complex) in Fig. 4.27. These are shown in Fig. 4.28 for the real points, where the fluid dispersion relation of Eq. (4.40) is also reported. The 5-moment results match closely the warm fluid approximation for small values of k , but quickly departs from it, having higher convective wave speeds.

The dispersion relation for the points (C1),(C2) and (C3) is shown in Fig. 4.29. The presence of two complex conjugate eigenvalues is clearly

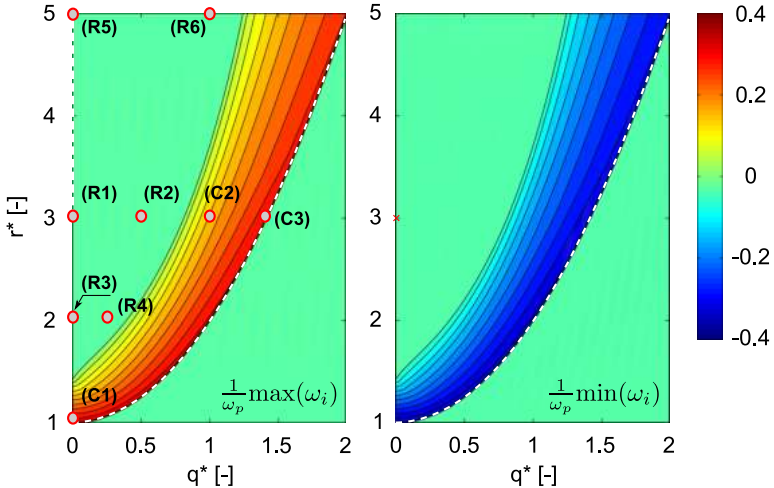


Figure 4.27: Maximum and minimum imaginary part of ω in the moment space, scaled by the plasma frequency. Only positive values of k are considered, for $k \in (0.001, 10)\lambda_{\text{De}}$. The plot is symmetric with respect to q^* . The white dashed line indicates the physical realizability boundary. The symbols in the plot identify points that are inspected in Figures 4.28 and 4.29.

seen in the dispersion relation, as one line suddenly branches for a given value of k , and can also be seen in the complex plane plot of Fig. 4.29-Bottom. In order to provide a more clear interpretation, the trajectory of the eigenvalues in the complex plane is shown in Fig. 4.30 for one selected case, where different eigenvalues are identified with different colors.

4.6.2 Ion acoustic waves

If the low-frequency response of ions is considered, one can assume that the motion of electrons is fast enough as to shield the ion displacement. Following [5], the electron density is approximated by the Boltzmann relation, that we linearize assuming small perturbations, giving

$$n_e = n_0 \exp \left[\frac{e\phi}{k_B T_e} \right] \approx n_0 + n_0 \frac{e\phi}{k_B T_e} = n_0 + n_{e1}, \quad (4.43)$$

where $\phi = \phi_1$ as before. This results in an expression for the electrons perturbation $n_{e1} = n_0 e \phi_1 / (k_B T_e)$, that can be inserted into the linearized Poisson's equation, giving

$$\varepsilon_0 k^2 \phi_1 = e n_{i1} - \frac{e^2 n_0}{k_B T_e} \phi_1 \implies \varepsilon_0 \phi_1 (k^2 \lambda_{\text{De}}^2 + 1) = e n_{i1} \lambda_{\text{De}}^2, \quad (4.44)$$

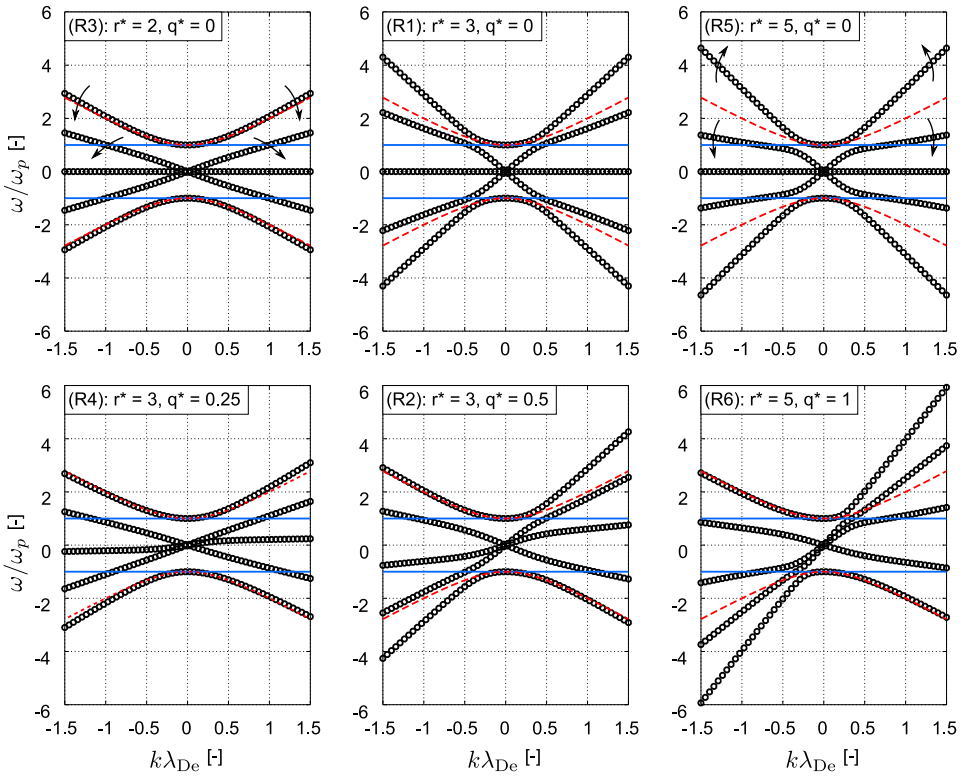


Figure 4.28: Eigenvalues of the 5-moment system (symbols) at locations (R1)–(R6) in moment space. The plasma frequency (blue solid line) and the fluid warm electrons dispersion relations are retrieved for $k = 0$ and $k\lambda_{De} \ll 1$ respectively. Arrows indicate how the eigenvalues have changed, with respect to equilibrium.

where the Debye length $\lambda_{De}^2 = \varepsilon_0 k_B T_e / (e^2 n_0)$ appears. Then, the potential ϕ_1 can be substituted into the momentum equation, resulting in an eigenvalue problem in the form

$$\left\{ k [J_0] + \frac{k\lambda_{De}^2}{k^2\lambda_{De}^2 + 1} \frac{q^2}{m^2\varepsilon_0} [M_\phi] - \omega [I] \right\} U_1 = 0. \quad (4.45)$$

The fluxes Jacobian and the matrix $[M_\phi]$ are the same as before, but this time are referred to the ion population. Before inspecting the dispersion relation numerically, it should be noted that

$$\lim_{k\lambda_{De} \rightarrow \infty} \frac{k\lambda_{De}^2}{k^2\lambda_{De}^2 + 1} \frac{q^2}{m^2\varepsilon_0} = \frac{1}{k} \frac{q^2}{m^2\varepsilon_0}, \quad (4.46)$$

that is the same factor appearing in the previously studied electron eigenvalue problem. This results in a vanishing importance of the self-consistent

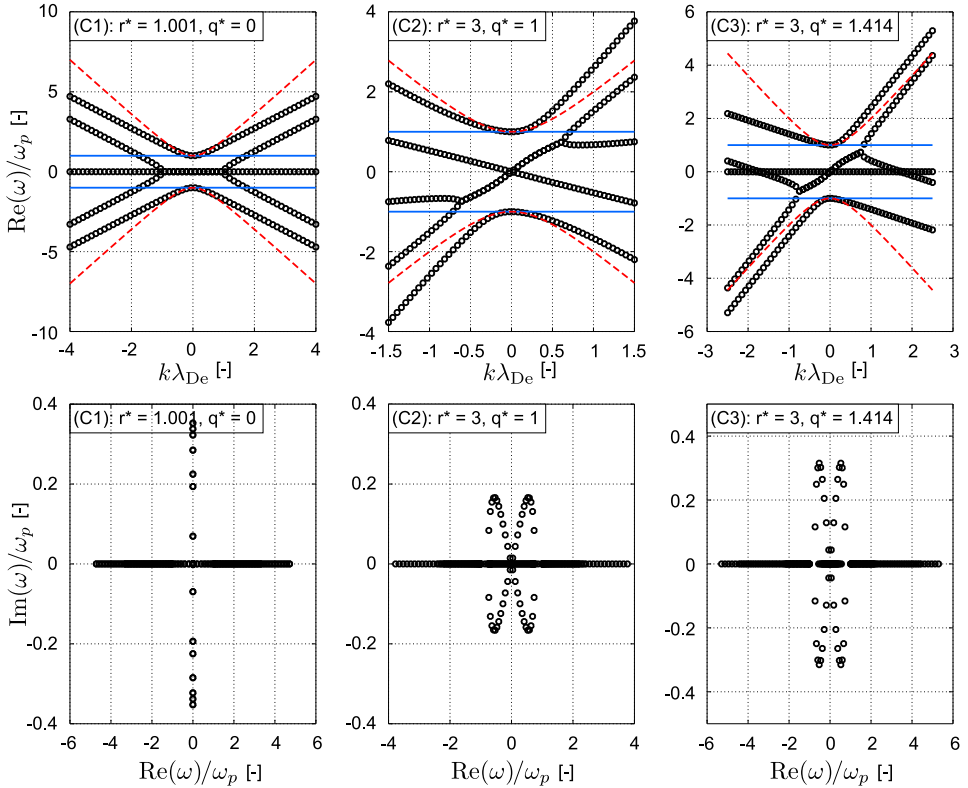


Figure 4.29: Real (Top row) and imaginary (Bottom) parts of the eigenvalues at moment space locations (C1), (C2) and (C3). The eigenvalues of the 5-moment system (symbols) appear to retrieve the plasma frequency (blue solid line) and the fluid warm electrons dispersion relations for $k = 0$ and $k\lambda_{\text{De}} \ll 1$ respectively.

field, and the system will eventually asymptote to the convective wave speeds. Therefore, except for the presence of the ion mass in place of the electron mass, we expect this problem to retrieve the same eigenstructure for large values of k . The effect of electrons in the ion acoustic modes is thus predominant for small wave numbers, or long wave lengths if compared to the Debye length. This is very reasonable, since the shielding happens indeed at such scales.

These observations hold for both equilibrium and non-equilibrium states. Moreover, in non-equilibrium, the eigenvalues that assume a non-zero imaginary part are the same as for the previous case, and the imaginary parts also show the same amplitudes. For these reasons, results are shown only for two selected cases at $r^* = 3$, with $Q^* = 0$ and $Q^* = 1.414$, in Fig. 4.31. The eigenvalues in such figure are computed for argon ions, the electron

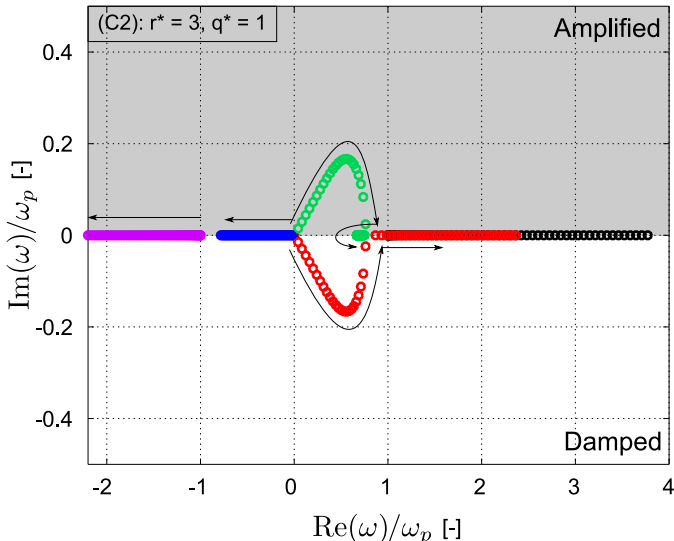


Figure 4.30: Evolution of the eigenvalues (identified with different colors) in the complex plane. Arrows indicate increasing values of $k \in (0, 1.5\lambda_{De})$.

temperature¹⁴ is fixed to $T_e = 10$ eV, the ion temperature is $T_i = 500$ K and the equilibrium density is $n_0 = 10^{15} \text{ m}^{-3}$. Again, for small wave numbers k , the 5-moment system retrieves closely the classical fluid results.

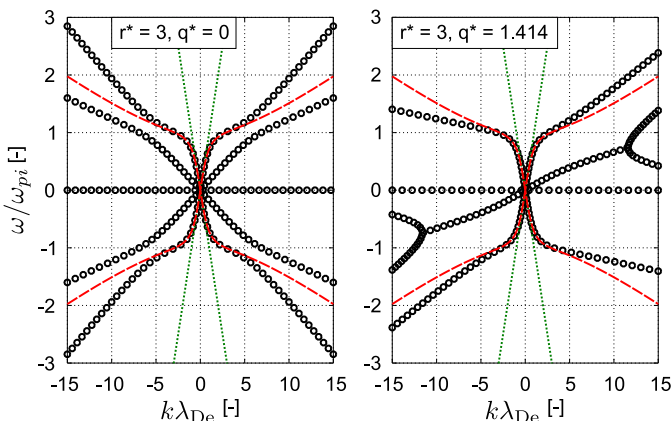


Figure 4.31: Ion-acoustic dispersion relation at two selected locations in moment space. Symbols: eigenvalues of the 5-moment system. Red dashed lines: classical ion-acoustic dispersion relation. Green dotted lines: electron fluid acoustic velocity.

¹⁴Appearing through the Debye length.

4.7 Conclusions

This chapter has introduced some developments and analysis preliminary to the practical application of the order-4 maximum-entropy systems to rarefied gases and plasmas.

First part of the chapter: rarefied gases

First, a rarefied test case was defined as a reference: the Sod shock tube problem was studied numerically from the free-molecular to the continuum regime. This allowed us to compare the accuracy of the maximum-entropy solution to the kinetic solution. The structure of the 5-moment solution, composed by five waves in the rarefied regime, was also analyzed. The Rusanov scheme was identified as the scheme of choice for this work, as it does not need a detailed knowledge of the system eigenstructure (but only the maximum wave speed) and appears to be more robust than the HLL scheme.

This test case was then employed as a benchmark to analyze the wave speeds of the maximum-entropy system. It was observed that these can exceed the speed of sound by orders of magnitude, and some approximations were developed for the 6-moment and 14-moment systems. These approximations allow for more stable and much less diffusive numerical solutions.

A further test case was then defined, in two dimensions, to study the behavior of the 14-moment system, test the formulated wave speeds approximation and to test second order accuracy in space. With these developments, the methods is ready and tested for tackling collisionless situations.

Second part of the chapter: plasmas

Then, attention was put to develop and characterize the plasma capabilities of the method. In particular, the electromagnetic source terms were developed for the 5 and 14-moment equations, and then plasma dispersion relations were analyzed, for electrostatic waves.

Based on these developments and analysis, the next chapters will deal with an application of the method to Hall thruster conditions.

CHAPTER 5

Collisionless ions in Hall thrusters: an analytical axial model and a simple fluid closure

The content of this chapter was published in [176]: Boccelli, S., Charoi, T., Alvarez Laguna, A., Chabert, P., Bourdon, A., Magin, T.E., *Collisionless ion modeling in Hall thrusters: analytical axial velocity distribution function and heat flux closures*, Physics of Plasmas 27 (7), 073506.

In the previous chapters, the theoretical basis for the description of rarified gases and plasmas were introduced, and the order-4 maximum-entropy systems were adapted to tackling plasma simulations. In this chapter, we start the analysis of Hall thruster-like problems. However, before applying the maximum-entropy system, some preliminary study of the problem is in order. In particular, in this chapter we start by considering the axial evolution of ions in a Hall thruster channel, with the aims of:

- Obtaining an understanding of the problem, from both the kinetic and fluid perspectives;

- Developing reference solutions to be further analyzed, in the later chapters, by the maximum-entropy system.

The preliminary analysis of Section 2.2 indicated that ions are, to a first approximation, collisionless, unmagnetized and strongly affected by the electric field. This causes the axial VDF to deviate from a Maxwellian, as shown by both experiments and kinetic simulations [177–179].

Outside of the thruster channel, as the plume develops and the electric field weakens, the effect of charge exchange (CEX) and momentum exchange (MEX) collisions eventually becomes dominant [180, 181]. The present analysis focuses on the interior or near-plume of the thruster, neglecting all collisions. Only ions will be considered in this chapter: electrons and neutrals will not be accounted for, and their interaction with ions is introduced by assigning a given electric field and ionization profile. In such way, it is possible to compare different ion models without introducing any error or assumptions related to the electrons model.

In Section 5.1, we consider the axial ion VDF, and describe its features based on the structure of the ionization and electric field profiles. An analytical solution of the kinetic equation is then obtained in Section 5.2 and is compared to PIC simulations (Section 5.2.2) and to experimental measurements (Section 5.2.3). Then, a 3-equations fluid model is developed in Section 5.3. The mass, momentum and energy equations are derived, and an ad hoc non-Fourier closure for the heat flux is formulated in Section 5.3.2. This formulation is then compared to the PIC simulations in Section 5.3.3.

5.1 Genesis of the axial VDF

We start by a qualitative description of the ion axial VDF.

The shape of the ion VDF is conveniently explained by assuming steady state conditions. Steady state is not necessarily realized in real situations: this assumption could however be interpreted as a *quasi*-steady state in case of low-frequency oscillations (such that the characteristic time is longer than the transit time of ions into the channel) or as a time average for faster modes.

In this section, we import the spatial profiles of the electric field (assumed purely axial) and ionization source from [182]. The fields were slightly adapted as to remove the negative electric field region, and are shown in Fig. 5.1-Left. The maximum electric field for such case is $E_{max} \approx 20 \text{ kV/m}$ and the ionization source $S_{max} \approx 2.5 \times 10^{23} \text{ ions}/(\text{m}^3\text{s})$. In Hall thruster channels, the ionization source peak often precedes the peak in the

electric field, creating a distinction between the ionization and the acceleration regions. However, the two regions partially overlap, and this allows us to understand the particular shape for the ion VDF. A point of ion velocity inversion is predicted in a number of thruster models (see for example [90]): this is neglected for simplicity in the present section, but will be recovered later on along the chapter.

During an ionizing collision between a fast moving electron with a background neutral, the energy exchange is highly inefficient due to the large mass ratio ($m_e/m_{Xe} \approx 4 \times 10^{-6}$). Therefore, at a first approximation, an ionizing collision can be described as an electron removing a bounded electron from the background neutral, without changing its velocity appreciably. The velocity distribution describing the newly born ions is therefore equal to the neutral VDF, that we assume to be a Maxwellian with average velocity u_n and a temperature T_n . For the sake of this section, we assume $T_n \rightarrow 0$, such that ion creation is monoenergetic at velocity $v = u_n$.

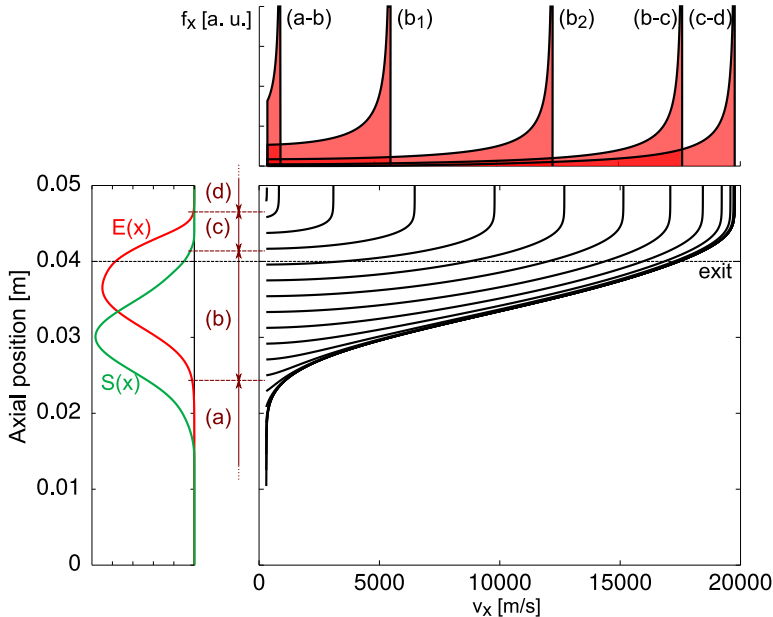


Figure 5.1: Genesis of the ion axial VDF. Left: imposed Electric field and ionization profile, and identified regions (a)–(d). Center: particle trajectories in phase space. Top: axial VDFs at the interface of the identified regions.

Ions are generated in phase space along a line at $v = u_n$ and are accelerated due to the imposed electric field. Phase space trajectories are easily computed numerically and are shown in Fig. 5.1. To obtain a qualitative understanding of the problem, it is convenient to divide the domain in a

series of regions. At the beginning of the ionization region (Region (a) in Fig. 5.1), the electric field is low, such that all the created ions cumulate, with negligible acceleration. This will create a sharp peak in the axial VDF. Such ions travel towards the channel exit at low velocity, until they reach the ionization region and start to accelerate. At first (Region (b)), the ionization source is still dominant, and despite ions being accelerated towards a higher average velocity, low-velocity ions are still being produced at each location. This will generate a plateau in the ion VDF. Then (Region (c)), the ionization term vanishes, while the electric field is in most cases still non-negligible. Only few new ions are created in such region, and this region is thus responsible for a translation of the VDF towards higher velocities. At this point ions have typically entered the plume. Further on in the trail (Region (d)) both electric field and the ionization term are small, and collisions play a major role in the evolution of the VDF.

The steady state axial VDF at the interface between the said regions is shown in Fig. 5.1-Top, obtained as discussed in the following section.

5.2 Analytical axial VDF

For collisionless unmagnetized ions, the kinetic equation reads

$$\frac{\partial f}{\partial t} + \mathbf{v} \cdot \frac{\partial f}{\partial \mathbf{x}} + \frac{q\mathbf{E}}{m} \cdot \frac{\partial f}{\partial \mathbf{v}} = \mathcal{S}(\mathbf{x}, \mathbf{v}), \quad (5.1)$$

where q and m are the ion charge and mass respectively, and $f = f(\mathbf{x}, \mathbf{v}, t)$ is the velocity distribution function. Under the assumptions of (i) monoenergetic ion creation, (ii) 1-dimensional electric field and (iii) steady state conditions, it is possible to obtain an analytical expression for the ion axial VDF. Steady state conditions imply $\partial_t f \equiv 0$. The monoenergetic ion creation assumption simplifies the ionization source term as

$$\mathcal{S}(\mathbf{x}, \mathbf{v}) = S(x)\delta(v_x - v_n)\delta(v_y)\delta(v_z), \quad (5.2)$$

with v_n the (monoenergetic) velocity of neutral particles, corresponding to their average velocity, $v_n = u_n$ for $T_n \rightarrow 0$. Note that $S(x)$ represents the number of ions created per unit time per unit physical volume: $[S] = s^{-1}m^{-3}$ and its profile is imposed. Finally, the problem is simplified by restricting the analysis to the centerline of the thruster channel. By assuming a purely axial electric field $\mathbf{E} = E\hat{x}$, neglecting all azimuthal and radial variations, then $\partial_y = \partial_z = 0$. Moreover, the VDF loses its dependence on the y and z coordinates: $f(\mathbf{x}, \mathbf{v}) = f(x, \mathbf{v})$. All such assumptions are questionable in real Hall thruster geometries, due to the presence of walls.

Nonetheless, the present model allows to gain a noteworthy insight in the problem, and may still be reasonable close to the channel centerline.

In the said simplifying assumptions, the three components of particle velocities are decoupled. The (steady state) kinetic equation for f can be recast into an equation for the marginal distribution function f_x by integrating over the v_y and v_z velocity components,

$$v_x \frac{\partial f_x}{\partial x} + \frac{qE}{m} \frac{\partial f_x}{\partial v_x} = S(x) \delta(v_x - v_n), \quad (5.3)$$

with the marginal distribution function $f_x = f_x(x, v_x)$ defined as

$$f_x(x, v_x) \equiv \iint_{-\infty}^{+\infty} f(x, v_x, v_y, v_z) dv_y dv_z. \quad (5.4)$$

A solution to Eq. (5.3) is easily found by following the characteristic lines, that correspond to ion trajectories in the 1D1V phase space. The solution discussed in the following is an adaptation of a classical solution to the Tonks-Langmuir sheath [183–185]. To our knowledge, it is the first time that such solution is applied to a Hall thruster channel.

In the collisionless regime, ions fall freely along the electrostatic potential ϕ . Therefore, an ion injected at position x_0 with velocity $v_0 = v_n$ will reach at position x a velocity

$$v_x(x_0; x) = \left[\frac{2q}{m} (\phi(x_0) - \phi(x)) + v_0^2 \right]^{1/2}. \quad (5.5)$$

With reference to Fig. 5.1, one can see that particles being injected between the positions x_0 and $x_0 + dx$ will have, at position x , a velocity between $v_x(x_0, x)$ and $v_x(x_0, x) + dv$. One can thus write the balance

$$v_x f_x(v_x) dv_x = -S(x_0) dx_0, \quad (5.6)$$

with the minus sign accounting for the inverse relation between an increase in x_0 and the final corresponding velocity. From Eq. (5.5), one computes

$$\frac{dv_x}{dx_0} = \frac{d}{dx_0} \left[\frac{2q}{m} (\phi(x_0) - \phi(x)) + v_n^2 \right]^{1/2} = -\frac{q}{m} \frac{E(x_0)}{v_x(x_0; x)}, \quad (5.7)$$

that can be inserted into Eq. (5.6), giving $f(x, v_x) = -\frac{S(x_0)}{v_x} \frac{dx_0}{dv_x}$, and thus

$$f_x(x, v_x) = \frac{m}{q} \frac{S(x_0)}{E(x_0)}. \quad (5.8)$$

Eq. (5.8) gives the marginal VDF at position x and velocity v_x as a function of the ratio S/E evaluated at the injection position x_0 . Note that x_0 is linked to v_x , and is obtained by inverting Eq. (5.5). Practically, one does not invert the relation, but instead the following procedure is adopted (in the following, the \bullet symbol denotes a numerical array):

1. The desired location x is chosen, where the VDF is to be obtained;
2. An array of values \underline{x}_0 is created (with $x^* \leq \underline{x}_0 \leq x$, with x^* to be discussed in the following), and the fields S and E are sampled at such locations;
3. An array of values \underline{v}_x is obtained from Eq. (5.5) from the target location x and the array of locations \underline{x}_0 ;
4. Finally, by plugging the array \underline{x}_0 into Eq. (5.8), an array of values \underline{f}_x is obtained and can be plotted against \underline{v}_x .

This process can be explained intuitively: the VDF at a location x is obtained as the contribution of all ions that reach such position. In case the electric field is positive all along the domain, one needs to consider ions created from the very beginning of the domain, until the desired location. Therefore, $x^* = 0$ (or whatever the initial coordinate is). For a negative electric field, the opposite considerations stand. If the electric field changes sign along the domain, additional care should be taken.

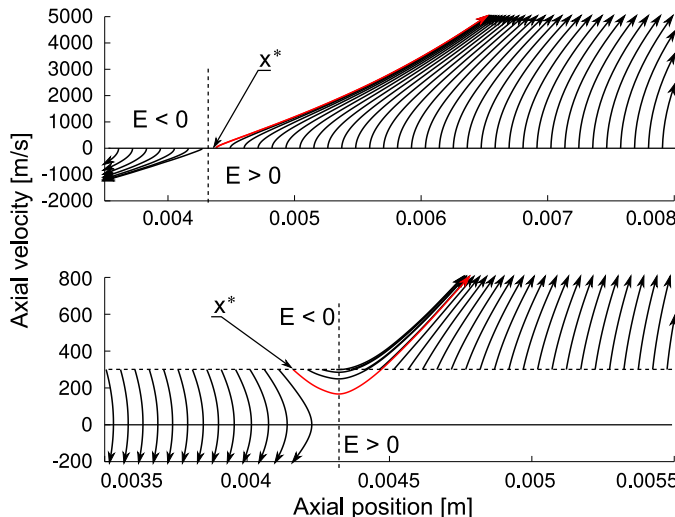


Figure 5.2: Phase space trajectories for electric fields with changing sign; choice of x^* .
Top: injection with $v_n = 0$. Bottom: $v_n > 0$.

Let us consider first the case of zero injection velocity, $v_n = 0$. The situation is depicted in Fig. 5.2-Top. In such case, for a given probed position x located downstream of the point where the electric field reverses, all ions created in the region of $E > 0$ will eventually reach x . On the other hand, all ions produced in the region of $E < 0$ will never reach x . In this case, the choice of x^* simply coincides with the point where $E = 0$.

In case ions have a non-zero birth velocity $v_n \neq 0$, some energy is available to overcome the adverse field, as depicted in Fig. 5.2-Bottom. For a given position x located in the positive- E region, an additional contribution is to be considered, and x^* is to be taken upstream of the nodal point for E . One can easily find x^* by equating the birth kinetic energy to the electrostatic potential energy. Another possibility consists in locating x^* graphically, after a numerical computation of some particle trajectories.

Finally, note that this analysis does not account for closed islands of electric field lines, that would trap particles indefinitely.

5.2.1 Moments of the analytical VDF

The moments of the analytical VDF (superscript “ a ” in the following) are easily obtained from the kinetic definition (see Section 2.3.1). As we are here interested in axial quantities only, the integral over the velocity space can be performed selectively on the v_y and v_z components, leaving the dependence of v_x . The moments definition is recast into an integral over the marginal VDF, $f_x dv_x$. This integral is transformed into an integral over the axial coordinate through Eq. (5.6), and involves the ionization profile. The analytical moments read:

$$n^a(x) = \int_{-\infty}^{+\infty} f_x(v_x) dv_x = \int_{x^*}^x \frac{S(x_0)}{v(x_0; x)} dx_0, \quad (5.9a)$$

$$u^a(x) = \frac{1}{n_a(x)} \int_{-\infty}^{+\infty} v_x f_x(v_x) dv_x = \int_{x^*}^x S(x_0) dx_0, \quad (5.9b)$$

$$P_x^a(x) = \int_{x^*}^x m \frac{S(x_0)}{v(x_0; x)} [v(x_0; x) - v_x^a(x)]^2 dx_0, \quad (5.9c)$$

$$Q_x^a(x) = \int_{x^*}^x \frac{m}{2} \frac{S(x_0)}{v(x_0; x)} [v(x_0; x) - v_x^a(x)]^3 dx_0, \quad (5.9d)$$

$$N_x^a(x) = \int_{x^*}^x m \frac{S(x_0)}{v(x_0; x)} [v(x_0; x) - v_x^a(x)]^n dx_0, \quad (5.9e)$$

where $N_x^a(x)$ denotes all further central moments of order $n > 3$. Notice that, differently from the previous definitions, **in this section a factor 1/2**

was embedded in the definition of the heat flux Q_x^a . It is important to stress that such moments rely on the same assumptions as the analytical VDF: monoenergetic ion birth, collisionless ions, quasi-steady state.

5.2.2 Comparison with 2D PIC simulations

The analytical results are here compared to 2D PIC simulations that represent the axial-azimuthal plane of a Hall thruster geometry. The PIC simulations model both electrons and ions and the electric field is computed self-consistently through the Poisson's equation. In order to compare with the analytical VDF and its moments, the ionization profile and the azimuthally averaged axial electric field are extracted from the simulations and imposed in Eqs. (5.8) and (5.9).

Description of the PIC cases

The PIC simulations described here are only used as a reference for comparison, and were not developed in this work, but instead performed by Charoy et al., at Laboratoire de Physique des Plasmas (École Polytechnique, Paris) [50, 186], based on the previous test case by Boeuf & Garrigues [49]. The reader is referred to these references for a full description of the problem, and the setup is only sketched here.

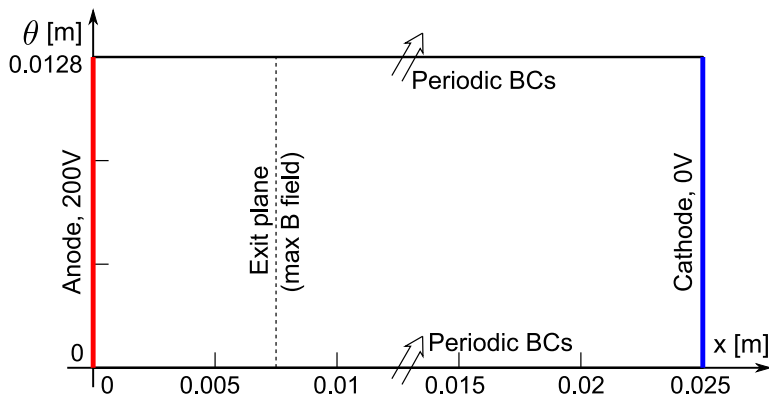


Figure 5.3: Computational domain for the PIC simulations.

The selected 2D test cases aim at studying the development of electron-drift instabilities, commonly arising in Hall thrusters. The computational domain is shown in Fig. 5.3. To simplify the setup and speed-up the computation the simulations are completely collisionless and a fixed ionization

profile is imposed with a cosine spatial shape:

$$S(x) = \begin{cases} S_0 \cos\left(\pi \frac{x-x_M}{x_2-x_1}\right) & \text{if } x_1 \leq x \leq x_2 \\ 0 & \text{otherwise} \end{cases} \quad (5.10)$$

with $x_M = (x_1 + x_2)/2$ and where the quantity S_0 ultimately defines the total current. Ions are injected from a Maxwellian distribution at a temperature $T_{i0} = 0.5$ eV and negligible average velocity.

In the simulations, the radius of curvature is assumed to be infinite, such that the azimuthal direction “ θ ” is effectively Cartesian. As mentioned, the PIC simulations show travelling azimuthal instabilities, that affect the ion moments quantities and the electric field. In order to apply the analysis developed in the previous section, the PIC results are averaged in time on 40 different time steps, spaced by 5000 time steps each. Subsequently, the results are averaged azimuthally.

PIC and analytical axial VDFs

Three different PIC simulations are considered for the comparison, with a different position and maximum value of the ionization profile, as shown in Fig. 5.4 together with the averaged axial electric field. Figure 5.5 shows the averaged axial (marginal) VDFs extracted at different channel locations from the simulation (A). Cases (B) and (C) show qualitatively analogous VDFs.

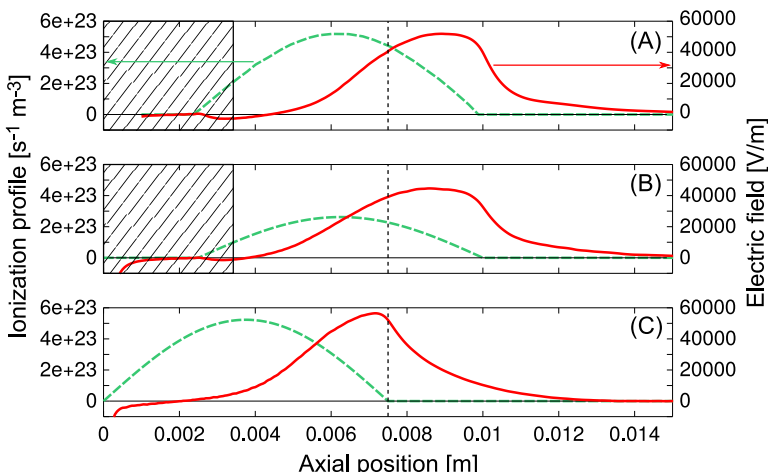


Figure 5.4: Ionization profile and azimuthally averaged electric field for the three considered test cases (A), (B) and (C). The shaded areas represent regions excluded from the fluid simulations of Section 5.3.

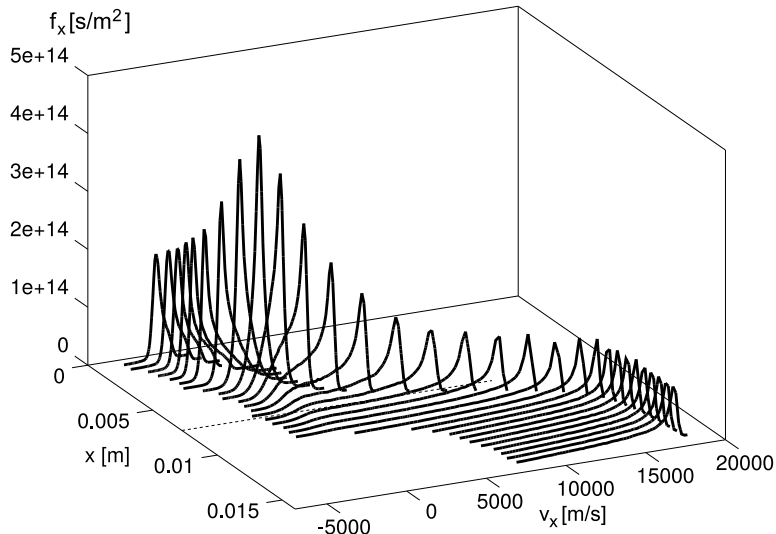


Figure 5.5: Axial VDFs extracted from a PIC simulation. The anode is located at $x = 0$ m and the cathode is out of the shown domain, at $x = 0.025$ m. Position $x = 0.0075$ m marks the assumed exit plane.

Such VDFs show the characteristic shape discussed in Section 5.1. In the ionization region, the acceleration is small, the injection temperature dominates, and the VDFs appear approximately Maxwellian. As the ions accelerate, a peak is formed at the high-velocity side. This peak shifts to higher velocities inside the acceleration region, and is followed by a plateau (or a long tail). Eventually, after the acceleration region, the VDF stops evolving.

The analytical VDFs are compared to the PIC ones in Fig. 5.6 for test case (A). Some error is visible in the ionization region ($x \approx 5$ mm), and is due to the assumption of monoenergetic ion birth. However, as soon as acceleration starts, this error becomes negligible since the dynamics is dominated by the electric field. The remarkable accuracy of the simple analytical model in the acceleration region confirms the validity of the assumptions for the considered collisionless test case, despite the unsteady nature of the PIC simulations.

A comparison of the moments of the analytical VDF against the moments from PIC is shown in Fig. 5.7. The moments of the analytical VDF are computed only for the region of positive electric field. An analogous computation could be performed around the point of electric field inversion, but would require additional care in matching the two results. The accuracy in the considered moments is also confirmed. The only mismatch

5.2. Analytical axial VDF

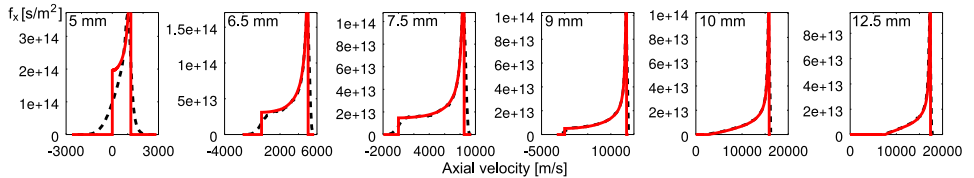


Figure 5.6: VDFs at different locations along the channel for test case (A). Red line: analytical axial VDFs from the averaged electric field and ionization profile. Black line: azimuthally and time-averaged VDFs from PIC

appears in the heat flux plot for the test case (C), in the plume region. This is likely to be attributable to the unsteady behavior of the PIC simulations, and may be due to a poor time average or to the presence of some stronger transiting wave.

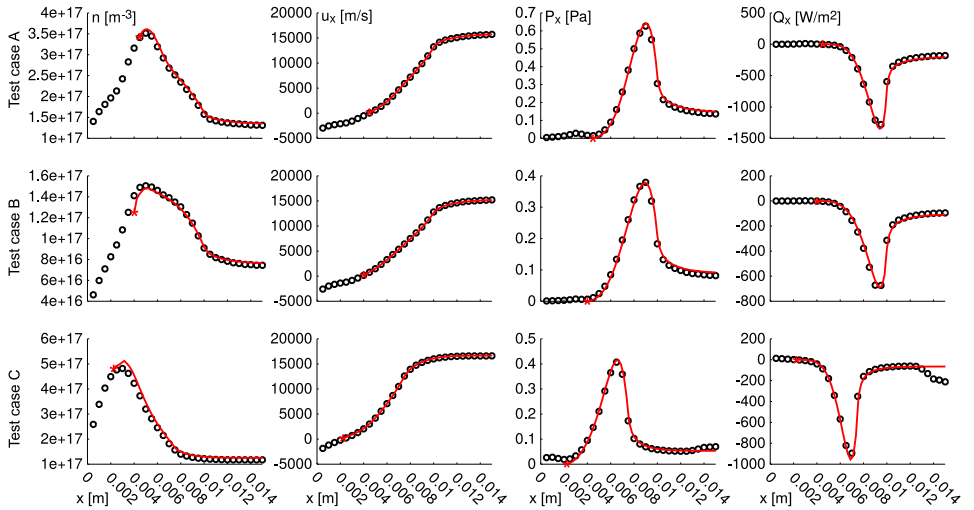


Figure 5.7: Moments of the analytical VDF against PIC results.

5.2.3 Comparison with experimental results

Experimental measurements of the ion VDF is available from a number of works. However, complete information over the VDF, the ionization profile and the electric field is much less frequent. In this section, a comparison attempt is made for the experimental conditions by Mazouffre & Bourgeois [178]. The ionization profile for the same conditions is reported in Garrigues et al. [187]. We assume an average velocity for ion birth equal to $v_n = 600 \text{ m/s}$, inferred from the experimental VDFs. This determines the

lower tail of the ion VDF.¹ The “current break mode” in the experimental results is considered.

Unfortunately, the choice of the starting point x^* is not trivial due to the uncertainties in the ion birth velocity and the electric field measurements, together with the added uncertainty coming from the electric field reconstruction technique [99]. Such uncertainties affect the assumed phase-space trajectories and ultimately the accuracy of the analytical solution. A starting position $x^* = 0.015$ m is chosen, that is reasonably close to the position of electric field inversion.

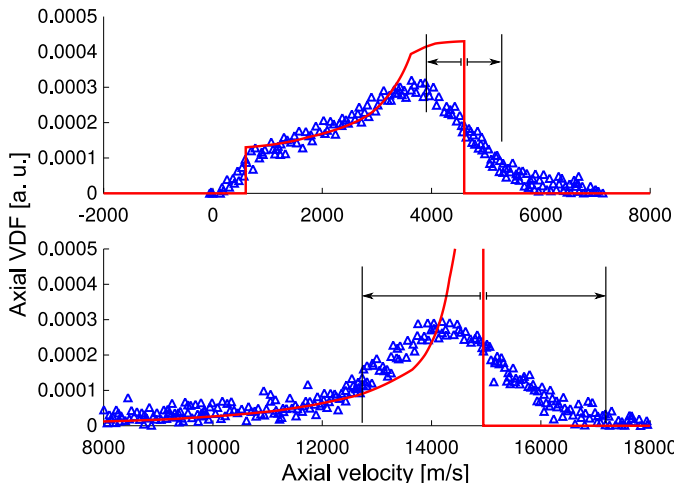


Figure 5.8: Analytical VDF (red line) compared to LIF measurements (symbols) of the axial VDF (points imported manually from [178]). Arrows represent an oscillation of the 15% of the velocity peak. Top: 2 mm from the exit plane, inside the thruster. Bottom: 8 mm out of the exit plane, in the plume.

A comparison of the analytical VDF from the experimental data is shown in Fig. 5.8. The VDFs are scaled to have a unit integral, as to allow for a direct comparison. Besides the mentioned accuracies, one should consider some additional factors. First, the injection temperature of ions is assumed to be zero in the analytical expression, while it is obviously finite in the experiments. Considering a thermal velocity of the background neutrals in the range of 310 m/s (as suggested by the authors [178]), this can explain the diffused low-velocity tail of the VDF, in Fig. 5.8-Top. This effect also contributes to partially smoothing the high-velocity discontinuity. Collisions would also smear the VDF. However, these two effects alone are not sufficient to explain the discrepancy at the high velocity tails.

¹Another option could be inferring this quantity from the propellant mass flow rate, neutral temperature and the channel width.

Instead, one should consider that experiments report the presence of breathing mode oscillations, that cause an oscillation of the average velocity of roughly 15%. This oscillation will likely affect not only the average velocity, but all points of the axial VDF. By superimposing this effect on the plot, it is clear that oscillations alone could explain the mismatch at the high velocity side of the VDF and would smear the VDF discontinuity. In principle, it would be possible to repeat the analytical computations for different values of an oscillating electric field, at the breathing mode frequency, and computing its average over a period. However, a knowledge of the moving ionization profile would also be needed, but is not available. Therefore, such analysis will not be performed here.

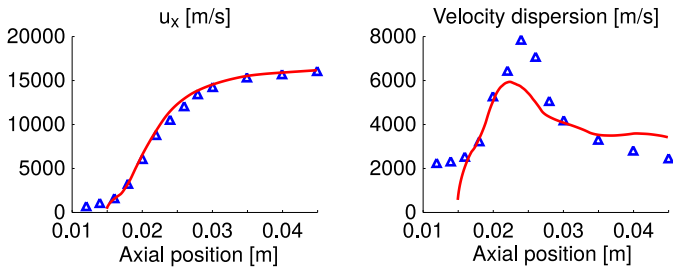


Figure 5.9: Comparison of the average velocity and velocity dispersion. Red line: analytical moments along the channel. Symbols: experiments.

A comparison is also performed in terms of average velocity and velocity dispersion (as defined in Gawron et al. [188]) and is shown in Fig. 5.9. It should be noted that the strong ion acceleration in Hall thrusters is such that convective terms are often much larger than the thermal contribution, and the average velocity is comparable and often much larger than the thermal velocity. For such supersonic flows, the shape of the VDF (and therefore, of non-equilibrium) has a limited effect on the average velocity. On the other hand, the detailed shape of the VDF always plays a large role in central moments such as the velocity dispersion. The VDF smearing due to electric field oscillations can thus be expected to play a large role in Fig. 5.9-Right.

Finally, the heat flux can also be computed from the two experimental VDFs of Fig. 5.8, and is compared to the analytical one in Fig. 5.10. It should be stressed that, since only two experimental points are available, this comparison is merely indicative.

5.2.4 Notes: beyond monoenergetic ion birth

Monoenergetic ion birth was described to create a sharp discontinuity in both the low and high-velocity sides of the axial VDF. As seen, this effect

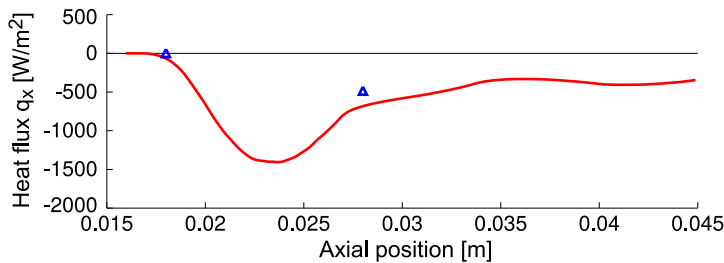


Figure 5.10: Heat flux from the analytical VDF (red line) and two experimental points (symbols).

has little importance in the acceleration region, but may be important in the first part of the ionization region, for low values of the electric field. Considering the VDF in the ionization region (marked by (i) in Fig. 5.11, whose position is x_i), and assuming for simplicity a strictly positive electric field, the VDF at such location will be determined by three contributions:

1. Ions created for $x < x_i$ contribute to the red (positive-velocity) side of the VDF at x_i ;
2. Ions created for $x > x_i$ but having a sufficient negative velocity to overcome the electric field may backstream up to position x_i and will contribute to the blue part (negative velocity) of the VDF;
3. The same ions will eventually be stopped by the electric field and be re-accelerated towards the exit, reaching again position x_i at later times and contributing to the positive velocity side.

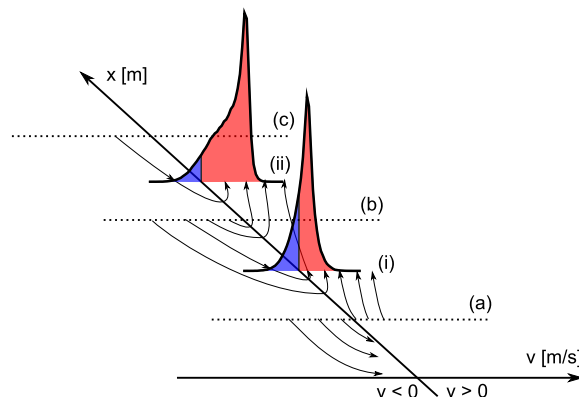


Figure 5.11: Ion trajectories in the phase space for a positive electric field.

A generalization of the monoenergetic model could be formulated by assuming injection from a local Maxwellian distribution. However, such a model should carefully take into account the aforementioned contributions.

5.3 A fluid model with ad hoc heat flux closure

As shown in the previous sections, the ion axial VDF is strongly non-Maxwellian. This section aims at formulating a simple fluid model that can profitably reproduce such non-equilibrium. Given the collisionless nature of the ion flow and the electrostatic acceleration, the continuum assumption is questionable. Therefore, in place of the Fourier's formula for the heat flux, an ad hoc expression is derived by assuming a shape for the VDF.

5.3.1 Derivation of the fluid equations

As discussed in Chapter 2, a generalized moment equation, Eq. (2.29) can be obtained by computing averages of the kinetic equation. For collisionless and unmagnetized ions, and considering the mentioned symmetry assumptions, Eq. (2.29) becomes

$$\frac{\partial n \langle \psi \rangle}{\partial t} + \frac{\partial}{\partial x} [n \langle v_x \psi \rangle] = \frac{nqE}{m} \frac{\partial \langle \psi \rangle}{\partial v_x} + \left\langle \frac{\delta \psi}{\delta t} \right\rangle_r, \quad (5.11)$$

where the last term at the right hand side represents the variation of the moment associated to ψ due to production of ions ("r" for reactions). The operator $\langle \bullet \rangle$ represents an average of quantity \bullet over the distribution function $f(v_x, v_y, v_z)$. As the aim is obtaining a simple set of governing equations for the axial quantities, we choose $\psi = m(1, v_x, v_x^2/2)$, and this leads to

- The continuity equation;
- One equation for the momentum in direction x ;
- One equation for the energy associated to the x-component of the particle velocity, $\rho e_x = \rho u_x^2/2 + P_{xx}/2$;

Note that writing equations for the x-component of the particle velocity alone is conceptually equivalent to considering a gas with one single translational degree of freedom, whose adiabatic constant would be $\gamma = 3$, whose total energy is $\rho e_x = \rho u_x^2 + P_{xx}/(\gamma - 1)$. In this formulation, only the axial component of the pressure tensor P_{xx} appears. As ions are assumed to be a perfect gas, the axial temperature and pressure will follow the relation $P_{xx} = nk_B T_x$. The resulting governing equations can be written in

conservative form, defining a vector of conserved variables \mathbf{U} , the fluxes \mathbf{F} and the source term \mathbf{G} ,

$$\frac{\partial \mathbf{U}}{\partial t} + \frac{\partial \mathbf{F}}{\partial x} = \mathbf{G}, \quad (5.12)$$

with

$$\mathbf{U} = \begin{pmatrix} \rho \\ \rho u_x \\ \frac{1}{2}\rho u_x^2 + \frac{1}{2}P_{xx} \end{pmatrix}, \quad \mathbf{F} = \begin{pmatrix} \rho u_x \\ \rho u_x^2 + P_{xx} \\ \frac{1}{2}\rho u_x^3 + \frac{3}{2}P_{xx}u_x + Q_x \end{pmatrix}. \quad (5.13)$$

The only closing moment in such problem is the scalar quantity Q_x , defined as

$$Q_x(x) = \iiint_{-\infty}^{+\infty} \frac{m}{2} v_x^3 f(x, v_x, v_y, v_z) d^3v = \int_{-\infty}^{+\infty} \frac{m}{2} v_x^3 f_x(x, v_x) dv_x. \quad (5.14)$$

It should be noted that a factor $1/2$ was embedded in the definition of Q_x , differently from the definition employed in Chapter 2. Also note that, differently from the usual definition of the heat flux vector, the quantity Q_x considered here only includes contributions from the axial velocity v_x . The source terms \mathbf{G} are also obtained as simple averages from Eq. (5.11), and are composed by a contribution from the electric field and a contribution due to the chemical source. Ions are created from the neutrals population, with an average momentum $m u_n$ and an average energy $m_n u_n^2 / 2 + k_B T_n / 2$.

$$\mathbf{G} = \begin{pmatrix} 0 \\ nq\mathbf{E} \\ nqu_x\mathbf{E} \end{pmatrix} + \begin{pmatrix} mS \\ mSu_n \\ S \left(\frac{1}{2}m_n u_n^2 + \frac{1}{2}k_B T_n \right) \end{pmatrix}, \quad (5.15)$$

with $S = S(x)$ the assigned ionization profile measured in $[m^{-3}s^{-1}]$ and n the ion number density.

5.3.2 Heat flux closure

The system of equations needs a closure for the heat flux Q_x , as a function of the lower moments. As the heat flux measures the skewness of the distribution function, it is unlikely that the Euler adiabatic closure $Q_x = 0$ could describe the strongly asymmetric ion VDFs. Instead, this section proposes an ad hoc closure that accounts for this skewness.

The simplest geometrical shapes that approximate the asymmetry of the ions VDFs are polynomials of order p of the velocity, limited between two

velocities V_A and V_B . For the sake of formulating a closure, the axial VDF is approximated as

$$f_x(v_x) \approx f^{(p)}(v_x) = \begin{cases} a(v_x - V_A)^p & \text{for } v_x \in [V_A, V_B] \\ 0 & \text{otherwise,} \end{cases} \quad (5.16)$$

where a, V_A, V_B depend on the position x and p is a fixed constant of the model. The values $p = 1, 2, 3$ correspond to approximating the axial VDF with a triangle, a parabola and a cubic function, with support $[V_A, V_B]$. For example, the triangular distribution is shown in Fig. 5.12, with the additional definition of the distribution width $L = |V_B - V_A|$. It should be stressed that the present approximation is limited to the axial VDF, and no assumption is being made on the v_y and v_z axes, whose marginal VDF could assume whatever shape.

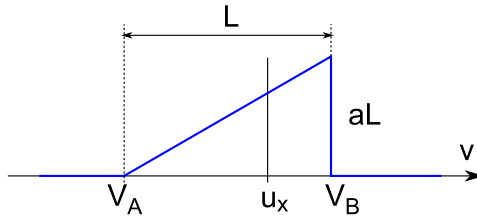


Figure 5.12: Triangular approximation ($p = 1$) for the axial VDF.

The definition in Eq. (5.16) is built on three parameters, a , V_A and V_B (for a chosen order p defined a priori). These parameters are directly connected to the density, average velocity and temperature of such distributions, and this allows us to ultimately write the heat flux Q_x^p as a function of such moments. The calculations will be shown here for the case of a cubic function, where $p = 3$, since this case showed the best accuracy. The other cases are analogous. First, the number density is obtained as

$$n = \int_{-\infty}^{+\infty} f_x(v_x) dv_x = \int_{V_A}^{V_B} a(v_x - V_A)^3 dv_x = \frac{aL^4}{4}. \quad (5.17)$$

The average axial velocity reads

$$u_x = \frac{1}{n} \int_{-\infty}^{+\infty} v_x f_x(v_x) dv_x = \int_{V_A}^{V_B} v_x a(v_x - V_A)^3 dv_x, \quad (5.18)$$

which is easily integrated by introducing the change of variables $\xi = v_x -$

Chapter 5. Collisionless ions in Hall thrusters: an analytical axial model and a simple fluid closure

V_A , with $\xi \in [0, L]$. After substituting the number density, this gives

$$\begin{cases} V_A = u_x - \frac{4}{5}L, \\ V_B = u_x + \frac{1}{5}L. \end{cases} \quad (5.19)$$

Finally, the temperature allows us to obtain an expression for the width L ,

$$\rho e_x = \frac{P_{xx}}{2} = \frac{n k_B T_x}{2} \equiv \int_{V_A}^{V_B} \frac{ma}{2} (v_x - u_x)^2 (v_x - V_A)^3 dv_x, \quad (5.20)$$

where the same change of variable done before gives

$$L = \sqrt{\frac{75}{2} k_B T_x / m}. \quad (5.21)$$

These results completely define the approximated VDF, given the lower moments n, u_x and T . The same calculations can be done for a generic order p . In the following, we use the following notation: the subscript “ (p) ”, refers to the order of the method, while when “ p ” appears alone, it refers to the numerical value. This results in

$$a_{(p)} = (p+1) n L_{(p)}^{-p-1}, \quad (5.22a)$$

$$\begin{cases} V_{A,(p)} = u_x - \frac{p+1}{p+2} L_{(p)} \\ V_{B,(p)} = u_x + \frac{1}{p+2} L_{(p)} \end{cases}. \quad (5.22b)$$

$$L_{(p)} = \sqrt{\frac{k_B T_x}{m} \left[\frac{p+1}{p+3} - \left(\frac{p+1}{p+2} \right)^2 \right]^{-1}}. \quad (5.22c)$$

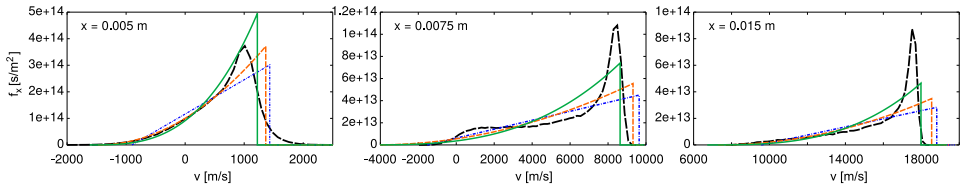


Figure 5.13: Triangular ($p = 1$, blue dot-dashed lines), parabolic ($p = 2$, orange dashed lines) and cubic ($p = 3$, green solid lines) approximations compared to the PIC VDF (black thick dashed lines).

Fig. 5.13 compares the triangular, parabolic and cubic approximations and the PIC VDFs at selected locations. The approximations appear rather rough, however, it should be noted that (i) the position of the VDFs’ peak

is reasonably well captured by the position V_B , especially for the cubic closure; (ii) what really matters in terms of the closure is the heat flux Q_x , not the VDF *per se*.

As done for the lower moments, the heat flux for a polynomial VDF is obtained from the kinetic definition,

$$Q_{x,(3)} = \int_{V_A}^{V_B} \frac{ma}{2} (v_x - u_x)^3 (v_x - V_A)^3 dv_x = -\frac{2\rho}{875} \left(\frac{75 k_B T_x}{2m} \right)^{3/2}. \quad (5.23)$$

This gives the required closure $Q_{x,(3)}(\rho, T_x)$. As expected, since the heat flux is a central moment, it does not depend on the average velocity u_x . For a generic p ,

$$Q_{x,(p)} = \frac{\rho L_{(p)}^3}{2} \left[\frac{p+1}{p+4} - 3 \frac{(p+1)^2}{(p+2)(p+3)} + 2 \left(\frac{p+1}{p+2} \right)^3 \right]. \quad (5.24)$$

Note that, whatever the value of p , the heat flux is proportional to the VDF width L to the power of 3. Since $L \propto \sqrt{T}$, one has that $Q_x \propto T^{3/2}$, as physically expected.

A preliminary verification of such closures can be obtained even without running a full fluid simulation. Indeed, it is possible to extract the moments ρ, T_x from the PIC simulation and plug them into the closures for Q_x , comparing the approximated heat flux to the PIC heat flux. This is shown in Fig. 5.14 for the conditions of test case (A) (see Section 5.2.2). The triangular closure ($p = 1$) reproduces a qualitatively correct heat flux, but misses the peak by roughly a factor 2. The parabolic ($p = 2$) and cubic ($p = 3$) closures improve the accuracy further. We now focus on the case of $p = 3$. Higher orders will not be investigated.²

The developed approximations appear to work well in the acceleration region, but their validity is questionable inside the ionization region or near the anode. The next section will address these issues.

Correction for negative and low velocities

The formulated closures implicitly assume that the ion velocity u_x is positive. In order to describe regions of negative ion velocity (as may be the case in certain regions of Hall thruster channels [90]) one would need to mirror the polynomial distributions, such as to make them face the negative axis. This is done by simply including a $\text{sign}(u_x)$ function in the heat

²Indeed, it is likely that the accuracy is strongly dependent on the considered test case, and it makes little sense to be excessively specific at this stage.

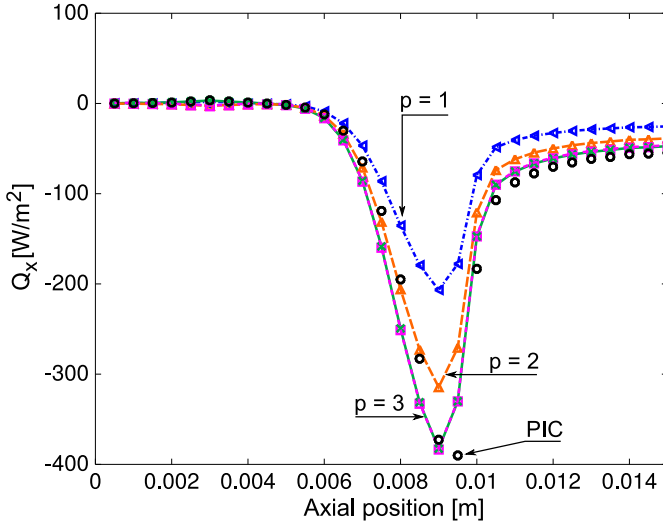


Figure 5.14: Approximated polynomial heat fluxes (lines with symbols) and PIC heat flux (black circles) for the conditions of test case (A) of Section 5.2.2.

flux. However, this introduces an issue, namely, Q_x would jump from a positive to a negative value around a point of velocity inversion. Instead, what we would intuitively expect from the previously developed model is that, when the velocity reverses, the VDF will be sort of symmetric, with a zero heat flux. Moreover, whenever the average velocity is small (or anyway lower than the thermal speed) the assumption of a polynomial VDF becomes questionable, as the distribution function may be strongly influenced by the (often Maxwellian) ion birth distribution.

To embed such effects into the model, we introduce an arbitrary limiting on the heat flux. First, we define the parameter $\Delta = |V_B - u_x|$ (with $\Delta = L/3, L/4$ and $L/5$ for $p = 1, 2, 3$ respectively). This parameter is ultimately a measure of the thermal speed. Then, we arbitrarily decide to limit the heat flux whenever $u_x < 2\Delta$, meaning that the limiting will be in place for somehow subsonic ions and will vanish in the limit of hypersonic ions. The simplest choice consists in a linear function, where the limited heat flux would read

$$Q_{x,(p)}^{\text{lin. lim}} = \begin{cases} \text{sign}(u_x) \frac{|u_x|}{2\Delta} Q_{x,(p)} & \text{if } |u_x| < 2\Delta, \\ \text{sign}(u_x) Q_{x,(p)} & \text{otherwise.} \end{cases} \quad (5.25)$$

However, a smooth limiting may be preferable (both for numerical reasons and to prevent unexpected unphysical results). One possibility is thus employing a sigmoid function such as the error function $\text{erf}(\chi)$. In such

case, we define $\chi = u_x/\Delta$ (that will result in a limiting whenever $u_x \lesssim 2\Delta$) and the limited heat flux reads

$$Q_{x,(p)}^{\text{erf lim}} = \text{sign}(u_x) \operatorname{erf}(|u_x|/\Delta) Q_{x,(p)}. \quad (5.26)$$

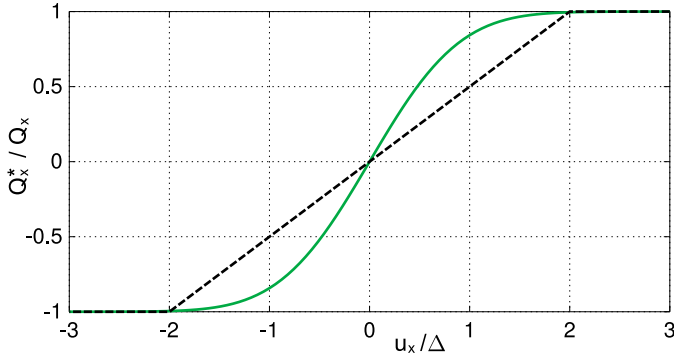


Figure 5.15: Linear (dashed line) and erf (solid line) limiting strategies.

A graphical comparison of the two limiting strategies is given in Fig. 5.15. The latter expression, together with the choice $p = 3$, gives the best results among the considered test cases. The suggested heat flux closure is therefore:

$$Q_x = -\text{sign}(u_x) \operatorname{erf} \left(\frac{|u_x|}{\Delta} \right) \frac{2\rho}{875} \left(\frac{75 k_B T_x}{2m} \right)^{3/2}. \quad (5.27)$$

As anticipated, the effect of the limiting is particularly important for low velocities. This is shown in Fig. 5.16, that magnifies the previous Fig. 5.14 in the region of velocity inversion.

5.3.3 Comparison with PIC simulations

The fluid equations of Eq. (5.12) with the heat flux closure of Eq. (5.27) are here compared to the azimuthally averaged moments of the PIC test cases (A), (B), (C) of Section 5.2.2.

The electric field and ionization profile are taken from Fig. 5.4. The shaded region in Fig. 5.4 is excluded from the domain, and only the region of positive velocity is simulated. This choice is necessary due to the test case assumptions. Indeed, by conservation of mass, a fluid model would always predict (at steady state) a singularity in the density whenever the velocity goes to zero, creating issues at the point of velocity inversion. Such

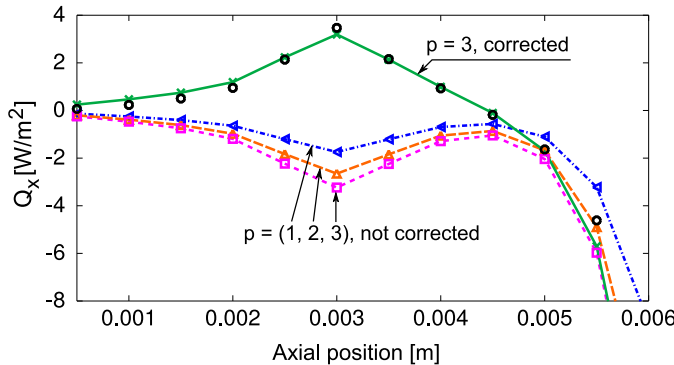


Figure 5.16: Proposed heat flux closures and PIC heat flux. Magnification of Fig. 5.14. The $p = 3$ corrected case is the closure of Eq. (5.27).

singularity does not affect particle-based simulations.³ In any case, cropping the domain as shown does not have any impact on the validity of the solution. The present method can be easily employed in a fully coupled multi-fluid plasma simulation without taking such precautions.

The fluid equations are solved with the finite volume method, with second order spatial accuracy obtained by van Leer's MUSCL method, HLL numerical fluxes and van Albada slope limiter. The solution is marched in time until convergence with a first order point-implicit Euler scheme. Note that the heat flux closure would alter the eigenvalues of the fluxes Jacobian, and would thus influence the maximum and minimum wave speeds to be employed in the HLL scheme. A possibility consists in computing numerically the Jacobian's eigenvalues. A less rigorous option would be treating the heat flux derivative as a source term, and discretizing it with centered finite differences. Both approaches have been tested and did not bring noticeable differences.

A comparison with the PIC test cases is given in Fig. 5.17. The adiabatic closure ($Q_x = 0$) leading to the Euler equations shows able to retrieve accurately the density and average velocity, due to the low ion pressure for the considered case. However, a significant error appears in the pressure field. The heat flux closure of Eq. (5.27) improves the situation and produces a pressure field much closer to the target PIC results.

³Particle-based simulations are always unsteady at the particle level, and anyway the probability of creating particles with exactly a zero velocity is small.

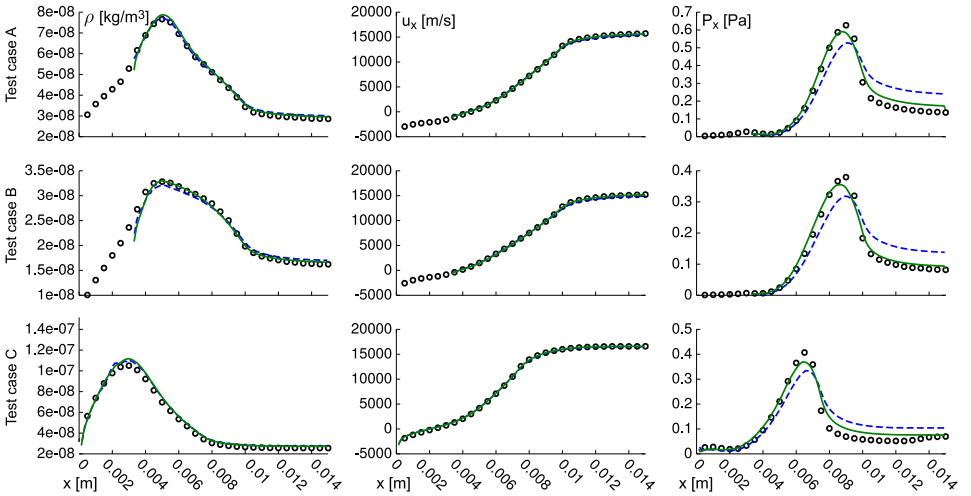


Figure 5.17: Azimuthally averaged moments from the PIC simulations (symbols) and solution of the fluid equations: Euler equations with zero heat flux (blue dashed line) and heat flux closure of Eq. (5.27) (green line).

5.4 Conclusions

This chapter was devoted to the study of the axial VDF for collisionless ions in Hall thrusters, and serves as a preliminary analysis for the next chapters, where ion modeling will be approached using the maximum-entropy closure.

An analytical solution of the kinetic equation for the axial VDF was derived, based on a classical result by Tonks & Langmuir [183]. Such solution showed remarkable accuracy if compared to PIC simulations of Charoy et al. [50], in terms of both the VDF itself and its moments. A comparison with the experimental results of Mazouffre & Bourgeois [178] was also attempted. However, this task is made more complicated by the uncertainties in the electric field measurements, and particularly by the presence of breathing mode oscillations. Nonetheless, by considering the magnitude of the latter effect, the inaccuracies in the analytical model could be explained to a satisfactory degree.

A fluid model was then formulated, and a non-Fourier closure was proposed, based on approximating the axial VDF by a polynomial function. This led to the formulation of an algebraic closure, that allows us to compute the heat flux from the lower order moments, ρ , u_x and T_x . A numerical solution of the fluid equations with such closure showed a good matching with the PIC results, and a superior accuracy with respect to the simpler

Euler adiabatic closure. As a final note, we shall stress that while a “cold ions” formulation is often sufficient for retrieving the ion velocity profile in simple 1D cases, an accurate reproduction of the pressure profile may play an important role in a number of circumstances, such as in determining the saturation of instabilities, due to ion trapping (see for example [48, 58]).

CHAPTER 6

Maximum-entropy modeling of ions

As discussed in the previous chapter, the low collisionality of ions inside Hall thrusters, together with a strong accelerating field, causes the VDFs to deviate from the equilibrium Maxwellian. A phenomenological fluid formulation was derived in Chapter 5 to describe the evolution of axial quantities, even out of equilibrium. However, such formulation is very specific and a generalization to different kinetic phenomena characterizing Hall thrusters (such as wave-trapping, happening in the azimuthal direction in presence of instabilities [58, 59]) would require further ad hoc modeling.

The advantage of employing a general formulation, such as a moment method, is to provide a unified framework, that automatically adapts to different types of non-equilibrium. The aim of this chapter is to investigate how well the order-4 maximum-entropy method (in its one-dimensional 5-moment version or in the full 14-moment form) can reproduce different non-equilibrium situations, commonly arising in low-temperature plasmas.

As did in Chapter 5, all cases discussed in this chapter consider ions only. Electrons are not explicitly simulated, but instead an electric field and an ionization profile are imposed in space. Besides simplifying the analysis, this allows for a direct comparison between kinetic and fluid methods, where additional sources of error may be introduced due to different elec-

trons modeling.

Due to the low-pressure conditions, the numerical simulations presented in this chapter are performed using scaled units, where picograms are used in place of kilograms, and the remaining units are chosen accordingly, as discussed in Section 3.3.

First, in Section 6.1, the maximum-entropy equations describing collisionless ions are recapped. The equations are then applied, in Section 6.2, to the very same case of Chapter 5, describing the axial ion evolution in a Hall thruster channel. Section 6.3 then investigates the classical problem of a Tonks-Langmuir sheath, describing a wall-bounded plasma. Sections 6.4 and 6.5 consider charged particles inside a stationary or moving electric field wave, showing ion wave trapping. This case is then extended to two-dimensions in Section 6.6, that aims at investigating traveling azimuthal waves in a 2D Hall thruster-like geometry, in presence of an assigned axial field.

6.1 Order-4 maximum-entropy systems for collisionless and unmagnetized ions

The general theory regarding maximum-entropy moment methods was discussed in Section 2.4. This section describes the application of such system to collisionless and unmagnetized ions.

6.1.1 Governing equations for ions: 5-moment system

For collisionless and unmagnetized particles in 1D geometries, the three velocity components are often decoupled, and one may write governing equations for a single degree of freedom. In such case, the order-4 maximum-entropy system is composed by 5 equations. In conservative form, we write

$$\frac{\partial \mathbf{U}_5}{\partial t} + \frac{\partial \mathbf{F}_5}{\partial x} = \mathbf{G}_5, \quad (6.1)$$

where the vector of conserved variables \mathbf{U}_5 and the fluxes \mathbf{F}_5 were defined in Section 2.4.2. For collisionless and unmagnetized ions, the source term \mathbf{G}_5 only includes the (x-component of the) electric field and chemical production terms due to ionization: $\mathbf{G}_5 = \mathbf{G}_5^E + \mathbf{G}_5^{iz}$. The electric field \mathbf{G}_5^E term was developed in Section 4.5.

The ionization term \mathbf{G}_5^{iz} depends on the considered reactions and is discussed in the following. We consider that ions are created from a background of neutral particles only due to electron-neutral collisions. Ionization due to neutral-neutral collisions are neglected due to the low tempera-

ture of the background gas. Neutrals are assumed to be Maxwellian, characterized by an average velocity u_n , temperature T_n and density n_n . Such quantities may depend on the position x , but will be assumed uniform in the present chapter.

We define by $g_n^{\mathcal{M}} = g_n^{\mathcal{M}}(v; u_n, T_n)$ the normalized Maxwellian distribution of neutrals, that integrates to unity. When an ionizing electron-neutral collision happens, we assume that the neutral loses one electron without changing its velocity, due to the small electron-to-neutral mass ratio.¹ Therefore, the distribution of ion birth is characterized by the very same normalized distribution $g_n^{\mathcal{M}}$. The 1D1V kinetic equation for ions thus reads

$$\frac{\partial f_i}{\partial t} + v \frac{\partial f_i}{\partial x} + \frac{q_i E}{m_i} \frac{\partial f_i}{\partial v} = S_{iz} g_n^{\mathcal{M}} \quad (6.2)$$

with $S_{iz} = S_{iz}(x)$ the ionization profile expressed in [ions/s/m³]. The ionization source term for the moment $\langle \psi_i \rangle$ of the microscopic ion quantity ψ_i (as defined in Chapter 2) reads:

$$\left. \frac{\partial \langle \psi_i \rangle}{\partial t} \right|_{iz} = S_{iz} \int_{-\infty}^{+\infty} \psi_i g_n^{\mathcal{M}} dv = \frac{S_{iz}}{n_n} \int_{-\infty}^{+\infty} \psi_i f_n dv, \quad (6.3)$$

where the neutral distribution function $f_n = n_n g_n^{\mathcal{M}}$ was introduced. The 5-moment system is obtained by the choice $\psi_i = m_i(1, v, v^2, v^3, v^4)$. Since we assume that a neutral turns into an ion by a simple loss of an electron, without changing its velocity, we have $\psi_i = \psi_n m_i / m_n$ (with $m_i / m_n \approx 1$), and the source terms thus become

$$\left. \frac{\partial \langle \psi_i \rangle}{\partial t} \right|_{iz} = \dots = \frac{S_{iz}}{n_n} \frac{m_i}{m_n} \int_{-\infty}^{+\infty} \psi_n f_n dv = S_{iz} \frac{m_i}{m_n} \frac{\langle \psi_n \rangle}{n_n}. \quad (6.4)$$

In other words, the source for the moment $\langle \psi_i \rangle$ of the ion population is the value of the same moment for the neutral population, $\langle \psi_n \rangle$, normalized with respect to the neutral number density and corrected by the ratio m_i / m_n . The ionization source terms for ions finally read

$$G_5^{iz} = \left. \frac{\partial U_5}{\partial t} \right|_{iz} = S_{iz}(x) \frac{m_i}{m_n n_n} \begin{pmatrix} \rho_n \\ \rho_n u_n \\ \rho_n u_n^2 + P_n \\ \rho_n u_n^3 + 3u_n P_n + g_n \\ \rho_n u_n^4 + 6u_n^2 P_n + 4u_n g_n + r_n \end{pmatrix}, \quad (6.5)$$

¹For a kinetic analysis of the problem, the reader can refer to [189], where an analysis of the scaling is also performed.

with $q_n = 0$ and $r_n = 3P_n^2/\rho_n$ (since neutrals are Maxwellian) and with $P_n = n_n k_B T_n$. More concisely,

$$\mathbf{G}_5^{\text{iz}} = \frac{\partial \mathbf{U}_5}{\partial t} \Big|_{\text{iz}} = S_{\text{iz}}(x) \frac{m_i}{\rho_n} \mathbf{U}_{5,n}. \quad (6.6)$$

6.1.2 Governing equations for ions: 14-moment system

Beyond the 1D1V approximation, one may go for the full 14-moment system. We write the system (in two dimensions) in conservative form as

$$\frac{\partial \mathbf{U}_{14}}{\partial t} + \frac{\partial \mathbf{F}_{14,x}}{\partial x} + \frac{\partial \mathbf{F}_{14,y}}{\partial y} = \mathbf{G}_{14}, \quad (6.7)$$

where the vectors of conserved variables \mathbf{U}_{14} and fluxes $\mathbf{F}_{14,x,y}$ were defined in Section 2.4.2. The source terms $\mathbf{G}_{14} = \mathbf{G}_{14}^E + \mathbf{G}_{14}^{\text{iz}}$ are composed by the electric field contribution (derived in Section 4.5) and the ionization source. The latter is obtained in the very same way as discussed in the previous section for the 5-moment case, and ultimately reads

$$\mathbf{G}_{14}^{\text{iz}} = \frac{\partial \mathbf{U}_{14}}{\partial t} \Big|_{\text{iz}} = S_{\text{iz}}(x) \frac{m_i}{\rho_n} \mathbf{U}_{14,n} \quad (6.8)$$

with $\mathbf{U}_{14,n}$ the very same 14 moments as in the ion description, but evaluated for the neutral population, at the temperature T_n , average velocity \mathbf{u}_n , number density n_n , and where (since neutrals are assumed Maxwellian), $q_n = 0$ and $R_{ijj,n} = 15P_n^2/\rho_n$.

6.2 Axial ion acceleration in a Hall thruster channel

As a first application of the maximum-entropy closure, we consider the very same problem of Chapter 5, describing the axial acceleration of ions in a Hall thruster channel. Since the problem is 1D1V, we solve the 5-moment system of Eq. 6.1, thus considering only the axial ion velocity component. Xenon ions are considered ($m_{Xe} = 2.18 \times 10^{-25}$ kg), and the electric field and ionization profile are these of test case (B) (see Section 5.2.2):

$$S_{\text{iz}}(x) = S_0 \cos [\pi(x - x_M)/(x_2 - x_1)], \quad (6.9)$$

with $x_1 = 0.0025$ m and $x_2 = 0.01$ m, $x_M = (x_1 + x_2)/2$ and $S_0 = 2.62 \times 10^{23} \text{ m}^{-3}\text{s}^{-1}$. The electric field $E(x)$ is imported from the PIC simulation. The chemical production term due to ionization reactions was developed in

6.2. Axial ion acceleration in a Hall thruster channel

Section 6.1.1 and is defined by a temperature of the background neutrals $T_n = 5802.3 \text{ K} \approx 0.5 \text{ eV}$ and average velocity $u_n = 0$.

The numerical solution to the 5-moment system is obtained with a finite-volume scheme, second order in space (Rusanov fluxes with wave speeds estimation from [172], with MUSCL reconstruction and symmetric van Albeda limiter), marching in time until convergence. The boundary ghost cells are set with a low value of the ion density and temperature, and a velocity of 50 000 m/s leaving the domain (negative for the left ghost cell and positive for the right one). Note that, due to the hyperbolic nature of the equations (and the finite-volume framework), this choice does not impose any Dirichlet boundary conditions, but merely allows for ions to freely leave the domain.²

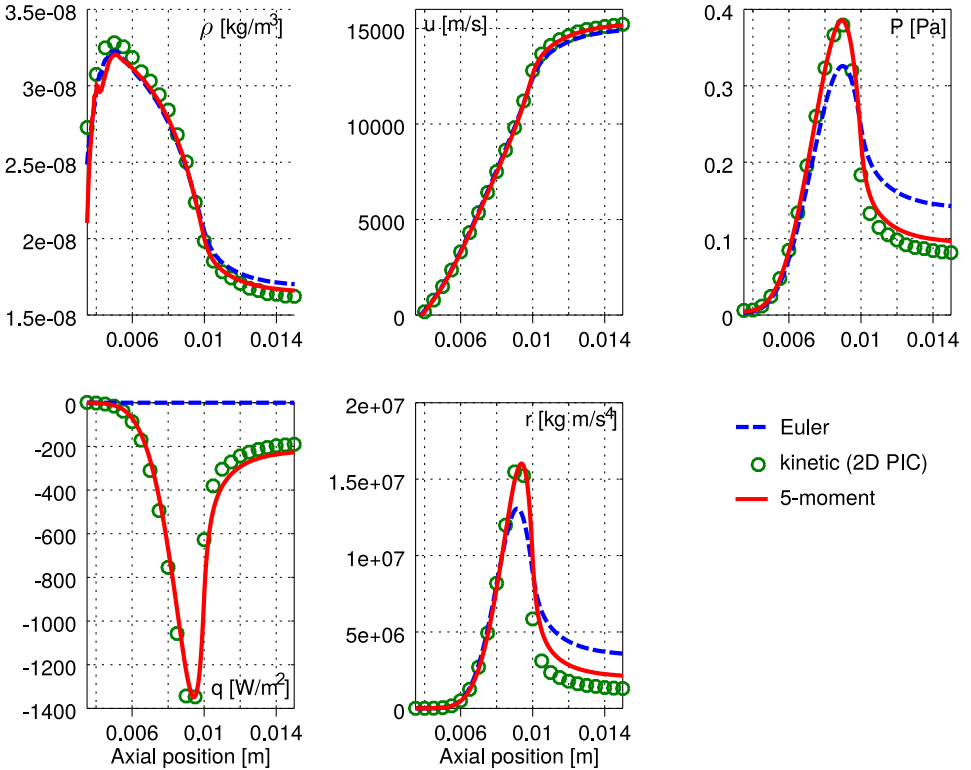


Figure 6.1: Evolution of axial quantities in a 1D Hall thruster channel, for the conditions of test case (B) of Chapter 5.

A comparison of the 5-moment system to the Euler equations and to the azimuthal average of the 2D PIC simulations is shown in Fig. 6.1. The 5-

²An alternative option could consist in setting the ghost cells dynamically in time, fixing the derivative of the solution at the boundaries.

moment system appears to improve strongly both the Euler equations and the ad hoc approximation previously built in Chapter 5.

6.3 Tonks-Langmuir sheath

In this section, the maximum-entropy closure is then applied to the study of ion evolution inside a plasma sheath. A sheath appears whenever a plasma interacts with a solid wall [5, 190] and is due to the cumulation of negative charges at an insulating surface. Indeed, the thermal velocity of electrons is often much larger than that of ions, due to the much lower mass and higher temperature (the latter being particularly true in low-temperature plasmas), and this results in a higher electron flux at the walls. Such charge causes a charge unbalance in the plasma (with an excess of positive charges near the wall) and neutrality is restored at a distance of several Debye lengths λ_D . Under the assumption of collisionless ions, the problem takes the name after Tonks and Langmuir, who have first obtained an analytical model [183].

6.3.1 Description of the case

Since this case is not strictly related to electric propulsion but rather to general plasma physics, we consider argon ions in this section, with $m_{Ar^+} = 6.6337 \times 10^{-26}$ kg. While the sheath forms due to the electrons thermal velocity, we are here interested only in the description of ions. Therefore, the Debye length and the resulting electric field profile will be imposed. We consider a one-dimensional domain $x \in [0, L]$ with $L = 0.1$ m, and assume that the right and left walls are at the same potential for symmetry. At a physical level, this configuration could represent a radio-frequency excited plasma between insulating walls (see for example [190]). In order to study a sheath-like configuration, we shall employ a realistic potential distribution. Therefore, the electric potential profile is assumed to follow the Child-Langmuir formula [190]:

$$\phi(x) = -\phi_0 \left[e^{-x/\lambda_D} + e^{-(L-x)/\lambda_D} \right]. \quad (6.10)$$

Since we are only interested in a *reasonable* potential profile for the sake of computing the ions evolution, we impose $\lambda_D = L/10$, and take $\phi_0 = 5$ V. The latter value is reasonable for low-temperature plasmas and could be estimated from the electron temperature as

$$\phi_0 \approx -\frac{k_B T_e}{2 q_e} \log \left[\frac{m_i}{2\pi m_e} \right] \approx 5 \text{ V}, \quad (6.11)$$

where the electron temperature was taken as $T_e = 11604$ K (thus corresponding to 1 eV). In the present formulation, ϕ_0 is assumed to represent the potential difference between the walls and the plasma bulk, the latter being taken as zero in Eq. (6.10). In any case, any shift in the potential does not change the electric field, that is obtained by differentiation and only the difference ϕ_0 matters. The electric field thus reads

$$E(x) = -\frac{\phi_0}{\lambda_D} [e^{-x/\lambda_D} - e^{(x-L)/\lambda_D}] . \quad (6.12)$$

The electric field and the potential are shown in Fig. 6.2.

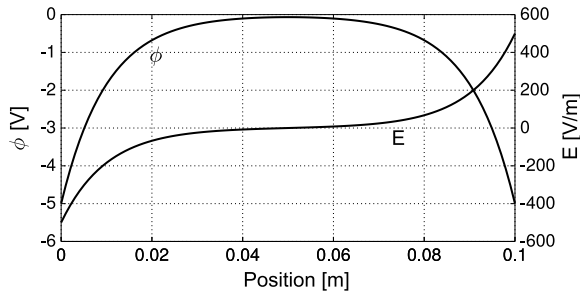


Figure 6.2: Imposed potential and electric field for the Tonks-Langmuir plasma test case.
Note that the electric field is zero at the symmetry plane.

A production term for ions is imposed, uniform along the domain. Its values is arbitrarily fixed to $S_{iz} = 5 \times 10^{20}$ [particles/m³s]. This value is reasonable, as can be seen from the following check. First, the resulting plasma density will be in the order of $n \approx 10^{16}$ m⁻³. Therefore, assuming an electrons temperature, one can estimate the density of background neutrals that would guarantee such ionization term. Considering then the ion-neutral cross section and such neutral density, one can confirm that ions are indeed rather rarefied in this condition.

Ions are assumed to be created from a cold and slow neutral background, such that the kinetic equation reads

$$\frac{\partial f_i}{\partial t} + v \frac{\partial f_i}{\partial x} + \frac{q_i E}{m_i} \frac{\partial f_i}{\partial v} = S_{iz} \delta(v) , \quad (6.13)$$

with $\delta(v)$ the Dirac delta function.

6.3.2 Kinetic solution

As mentioned, an analytical solution is available for Eq. (6.13), as also discussed in Chapter 5. Nonetheless, a numerical solution is here employed,

solving the kinetic equation with the deterministic solver discussed in Section 3.2.5. on a phase space grid composed by 1000×1000 cells, with a second order accuracy in space and velocity, and marching in time until convergence. The time integrator is a first order forward Euler scheme (the time integration error vanishes at convergence, anyway). The VDF is initialized to zero in the domain, and is set to zero in the boundary ghost cells, allowing for ions to flow freely out of the domain.

The numerical solution is shown in Fig. 6.3. Clearly, the solution is symmetric. If one considers only half of the domain, the problem is qualitatively similar to the previously analyzed creation and acceleration of ions into the acceleration region of a thruster channel. Indeed, also in this case, the VDF arises from the interplay between electrostatic acceleration and ion chemical production sources. The VDF shows a peak at the high-velocity side, that is followed by a plateau (or a thick low-velocity tail), arising from the production of ions all throughout the domain. A logarithmic scale is employed in the figure, as to avoid the colors saturation due to the leading peak. Moments are computed numerically from the kinetic solution and are shown in Fig. 6.4.

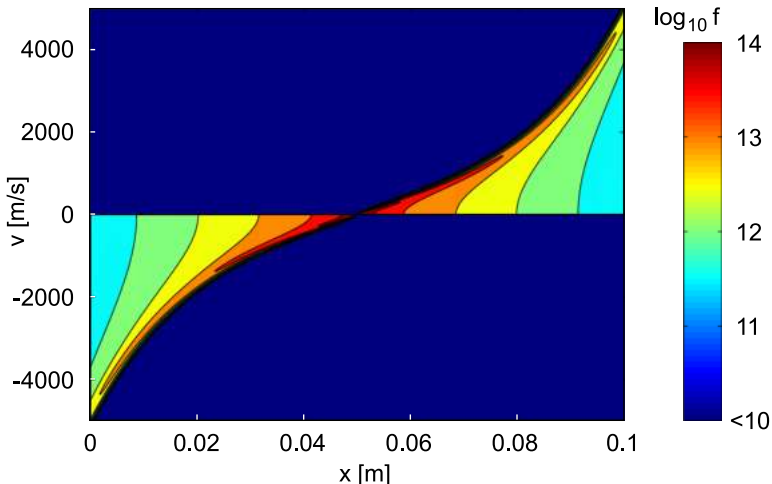


Figure 6.3: Kinetic solution in the phase-space, logarithm of the distribution function.

6.3.3 5-moment maximum-entropy solution

The problem is then approached using the 5-moment system of Eqs. (6.1). The chemical production source terms are these of Eq. (6.5), where neutrals have a zero average velocity $u_n = 0$ and are assumed to be cold, implying that $P_n \rightarrow 0$ and $r_n \rightarrow 0$.

The solution is obtained on a grid of 2048 cells, first order in space (fine enough to provide space convergence). A second order solution based on van Leer's MUSCL scheme was not employed due to the density singularity that appears at the point of zero velocity. This can be seen in Fig. 6.4 as a peak in the density profile. Such issue arises due to the 1D formulation of the problem, and is worsened by assuming a zero birth temperature for ions (reducing diffusion) and by using a fixed electric field. Employing a first order scheme provides some numerical dissipation in that region, and contributes to reduce such unphysical behavior.

An initial density of $n_{i0} = 10^{10}$ [ions/m³] is chosen, together with a temperature of 300 K, zero heat flux and equilibrium for the order-4 moment, $r_0 = 3P_0^2/\rho_0$. The left and right ghost cell values are assigned a density equal to the initial density, and a velocity of 10 000 m/s leaving the domain. A time step $\Delta t = 0.4$ ns allows us to respect the CFL condition and to properly follow the ionization rate. The solution is integrated in time with an explicit forward Euler scheme, and the simulation is completely converged after roughly 0.2 ms.

The solution is shown in Fig. 6.4 and shows a very accurate match with the kinetic solution for all moments. Fig. 6.4-Bottom-Right shows the solution in moment space, as a function of the dimensionless moments q^* and r^* . Due to the strong acceleration, the VDF is deformed and assumes a strongly asymmetric and peaked shape. Correspondingly, the 5-moment solution approaches the physical realizability boundary near the right and left domain boundaries. In the middle of the domain, where the electric field is low, the solution appears to cross the Junk subspace. This may be an artifact of the grid size though, that appears to be fine enough to provide space accuracy, but results rather coarse in such region of moment space. This was not investigated further, as the presence of the unphysical density peak at the symmetry line would not allow us anyway to obtain a definite answer.

6.3.4 Euler system solution

Finally, the system is solved using the Euler system of equations, with adiabatic constant $\gamma = 3$ as to represent one single translational degree of freedom. The boundary conditions are the same as for the 5-moment system, and the source terms (in the cold and slow neutrals limit) reduce to:

$$\frac{\partial}{\partial t} \begin{pmatrix} \rho_i \\ \rho_i u_i \\ \rho_i E_i \end{pmatrix} \Bigg|_{iz} = m_i S_{iz} \begin{pmatrix} 1 \\ 0 \\ 0 \end{pmatrix}. \quad (6.14)$$

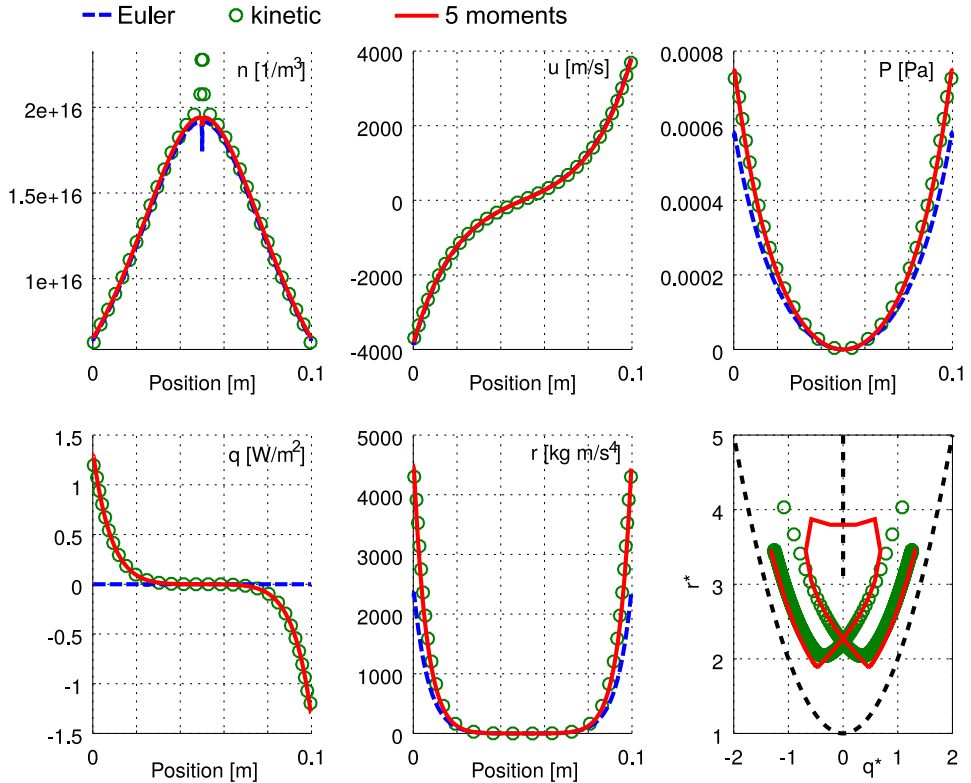


Figure 6.4: Tonks-Langmuir test case, comparison of maximum-entropy, Euler system and kinetic solution.

We note that for the considered case, the Euler equations allow for a reasonably accurate match with the kinetic solution, especially in the lower order moments, as also discussed in the results of Chapter 5. Note that, in Fig. 6.4, a value for the heat flux q and the order-4 moment r are shown also for the Euler system, although it does not solve explicitly for them. These values are taken from the Maxwellian VDF, that is implicitly assumed by the Euler system formulation.

6.4 Ions in a stationary wave

In this section, we consider a periodic system with an imposed sinusoidal longitudinal electric field. The kinetic solution for such problem is strongly non-equilibrium and consists in a progressive rolling up (in phase space) of the initial VDF, that eventually develops filamentation. This problem has been studied extensively, and analytical kinetic solutions are available (see

for example [191, 192]). Not only this test case is interesting *per se*, but is also propaedeutic to the study of travelling waves that mimic azimuthal instabilities in Hall thrusters.

6.4.1 Description of the case

Xenon ions are simulated, in a periodic one-dimensional domain with $x \in [0, 0.01]$ m. Ions are initialized uniformly in the domain, following a 1D1V Maxwellian VDF with zero average velocity and a temperature of 10 eV. Since the domain is periodic, no ionization source term is used. An electric potential is imposed, and reads

$$V = V_0 \cos(kx). \quad (6.15)$$

The wave number k is chosen as to have four peaks in the simulated domain, $k = 2N\pi/L$, with $N = 4$. The electric field is simply obtained by differentiating the potential,

$$\mathbf{E} = kV_0 \sin(kx). \quad (6.16)$$

Since the ion temperature was assigned, the electric potential amplitude V_0 determines the dynamics of the problem. Indeed, on a particle perspective, all ions with an initial energy $\varepsilon_i < V_0$ (with ε_i expressed in [eV]) will be trapped inside the electric field profile and will oscillate back and forth. On the other hand, ions with energy $\varepsilon_i > V_0$ will manage to overcome the electric field barrier, but will be perturbed by it. Finally, the ions for which $\varepsilon_i \gg V_0$ will travel almost unperturbed by the electric field. Different regimes are thus obtained for different values of the ratio of the initial ion thermal energy over the electrostatic energy. We consider the two cases:

- Case 1) $V_0 = T_i$ [eV];
- Case 2) $V_0 = 5 T_i$ [eV].

6.4.2 Kinetic solution

As mentioned, no chemical production source term is considered. Therefore, the kinetic equation corresponds to the 1D1V Vlasov equation with imposed electric field. The kinetic solution is obtained with the deterministic solver, with 2048×2048 grid cells in physical space and velocity, second order in phase space and first order in time. The computations were performed with different time steps and phase space grids as to ensure convergence. The phase space grid needs to be rather refined, especially due to the appearance of filamentation and therefore strong gradients.

Fig. 6.5 shows the kinetic solution for the case of $V_0 = T_i$ [eV], at two different time steps. A logarithmic scaling is used in the figure, as to highlight the tails. From the figure, it is clear that the particles constituting the bulk of the initial VDF are strongly accelerated and such portion of the VDF curls on itself, while the high-velocity tails (both positive and negative) are perturbed but not trapped by the electric field.

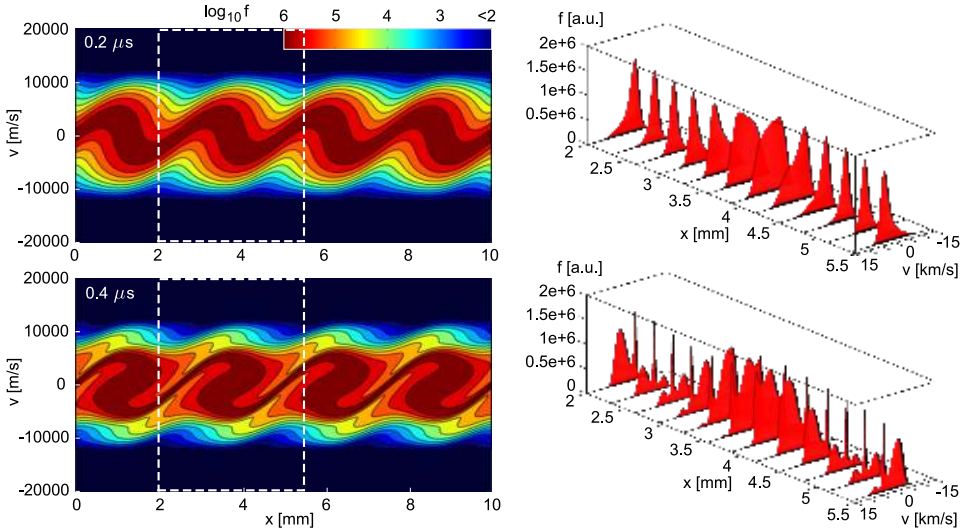


Figure 6.5: Kinetic solution for $V_0 = T_i$ [eV] in phase space. Logarithm of the 1DIV distribution function. The moments of this VDF will be shown in Figs. 6.8 and 6.9, in the region highlighted in white.

Filamentation is seen to start after the VDF has done a 180° turn on itself (time $t \approx 0.4 \mu\text{s}$) and causes sudden spikes in the VDF, as clearly visible from Fig. 6.5-Right. The situation becomes even worse as time goes by, and the VDF keeps rolling and creating more spikes, as shown in Fig. 6.6. A detailed reproduction of such kinetic behavior using moment methods would likely require a quite large number of simulated moments. Eventually, for longer times, the number of spikes increases up to a point where the solution appears to recover a Maxwellian-like appearance. Simulating such long times requires some additional care on the time integration (clearly, higher order is better) and especially an even more refined grid as to resolve all peaks and also minimize numerical dissipation.

The kinetic solution for the case of $V_0 = 5 T_i$ [eV] is shown in Fig. 6.7. The result is qualitatively analogous to the previous case, except that virtually all particles are trapped by the electric field, and this results in an even more extreme filamentation.

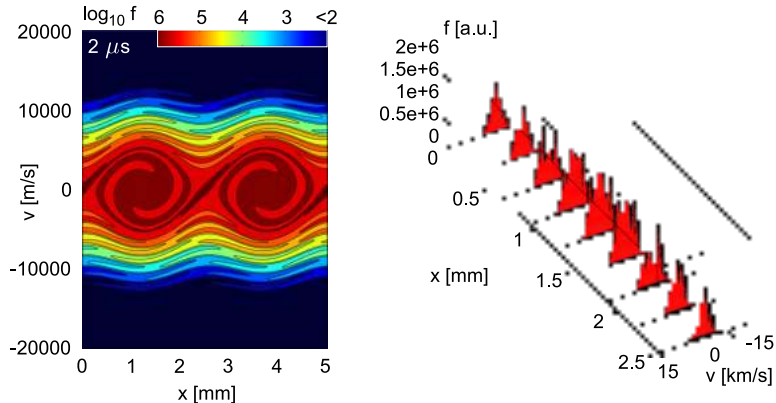


Figure 6.6: Kinetic solution for $V_0 = T_i$ [eV] in phase space, at $t = 2\mu s$. This simulation was performed on a smaller domain, as to allow for a finer grid and to capture more accurately the filaments.

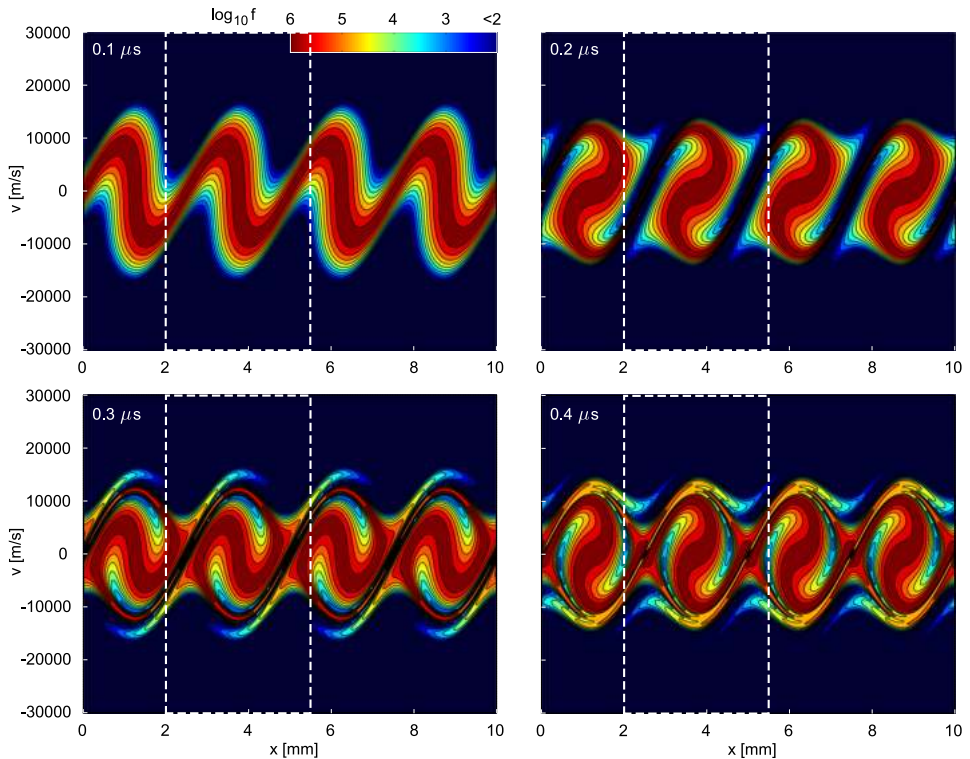


Figure 6.7: Kinetic solution for $V_0 = 5 T_i$ [eV] in phase space. Logarithm of the 1D1V distribution function. The moments of this VDF will be shown in Figs. 6.10 and 6.11, in the region highlighted in white.

6.4.3 5-moment and Euler solutions

The solution to the 5-moment and Euler systems are obtained on a space grid of 2048 cells, second order both in space and time. The ionization source terms are put to zero for this test case. The results are compared to the kinetic solution in Figs. 6.8 and 6.9 for the $V_0 = T_i$ [eV] case and in Figs. 6.10 and 6.11 for the case of $V_0 = 5 T_i$ [eV]. Since the solution is periodic, only a portion of the domain is shown in such figures, as to make the results more clear.

The lower moments appear well reproduced by both the Euler and 5-moment systems at early times ($t \approx 0.1 \mu\text{s}$), while the Euler system already shows some inaccuracy in the higher moments. As time passes, for $t = 0.2 \mu\text{s}$, the accuracy of the 5-moment system is still high, while the Euler solution starts to show some artifacts and shock waves. Eventually, as non-equilibrium keeps increasing, even the 5-moment solution starts to deviate from the kinetic solution, especially in terms of the lower moments. Remarkably, though, the higher moments maintain a higher accuracy even for relatively long times. This behavior can be observed for both test cases.

As may be expected, the plot in moment space $q^* - r^*$ shows that the second case ($V_0 = 5 T_i$ [eV]) is much farther from equilibrium than the previous one. Indeed, in the second case, the moment space trajectory reaches both higher values for q^* and r^* , and also gets much closer to the physical realizability boundary. The Junk subspace appears to be crossed already at early times. In terms of the interpolative maximum-entropy closure, we can expect the parameter σ to assume very small values even far from equilibrium, and correspondingly we expect wave speeds to deviate strongly from the equilibrium values. This makes a time-explicit numerical solution of the 5-moment system much more stiff than its Euler counterpart.

In terms of long-time solution, the kinetic equation would predict an increasing number of filaments, with an increasingly small thickness, up to the point where the VDF could appear macroscopically analogous to a Maxwellian. Therefore, as a future work activity, we suggest the study of the asymptotic behavior of the 5-moment system for this problem.

6.4. Ions in a stationary wave

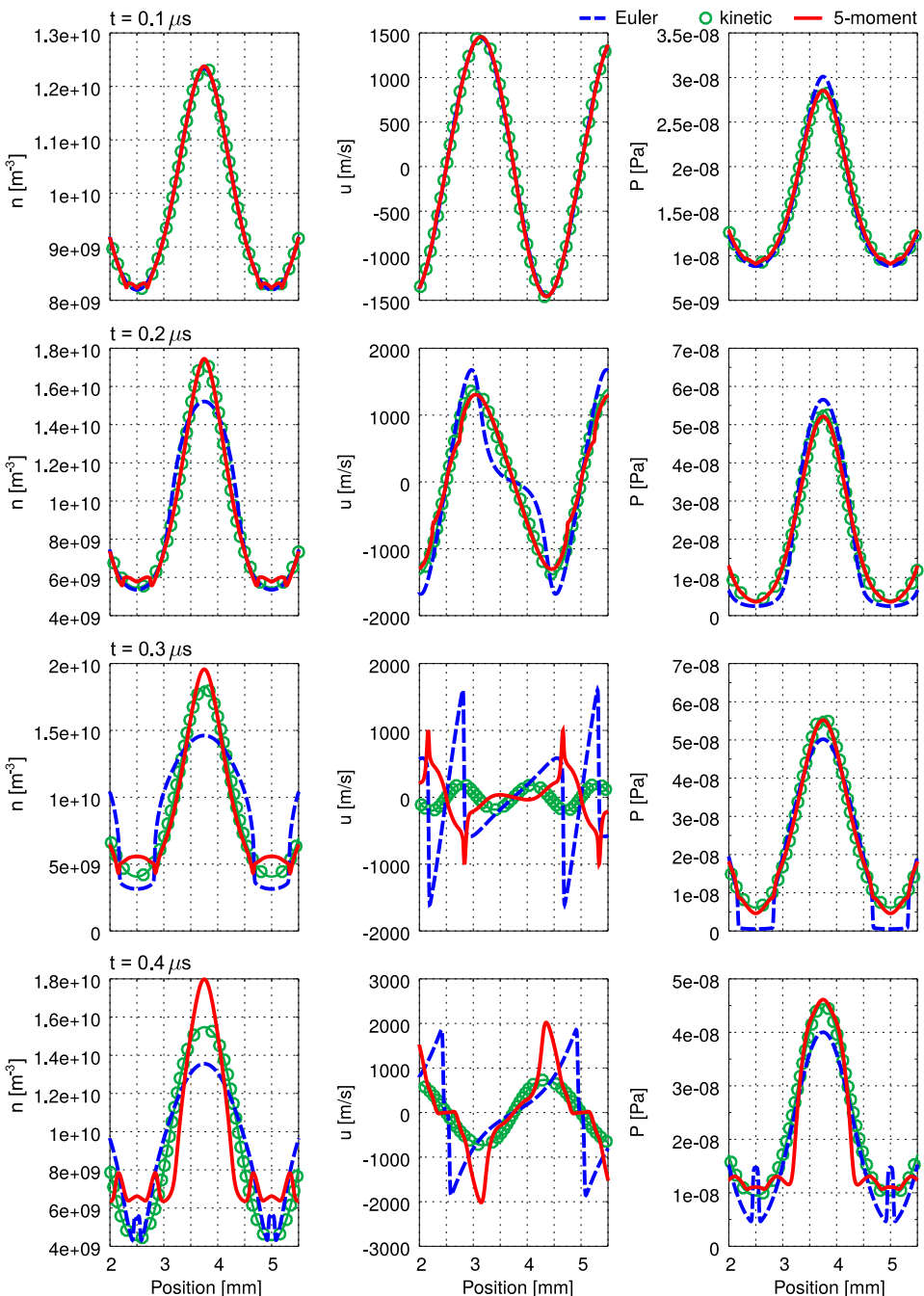


Figure 6.8: Case $V_0 = T_i$ [eV]; first three moments at different times. Green symbols+line: kinetic solution. Blue dashed line: Euler. Red line: 5 moments.

Chapter 6. Maximum-entropy modeling of ions

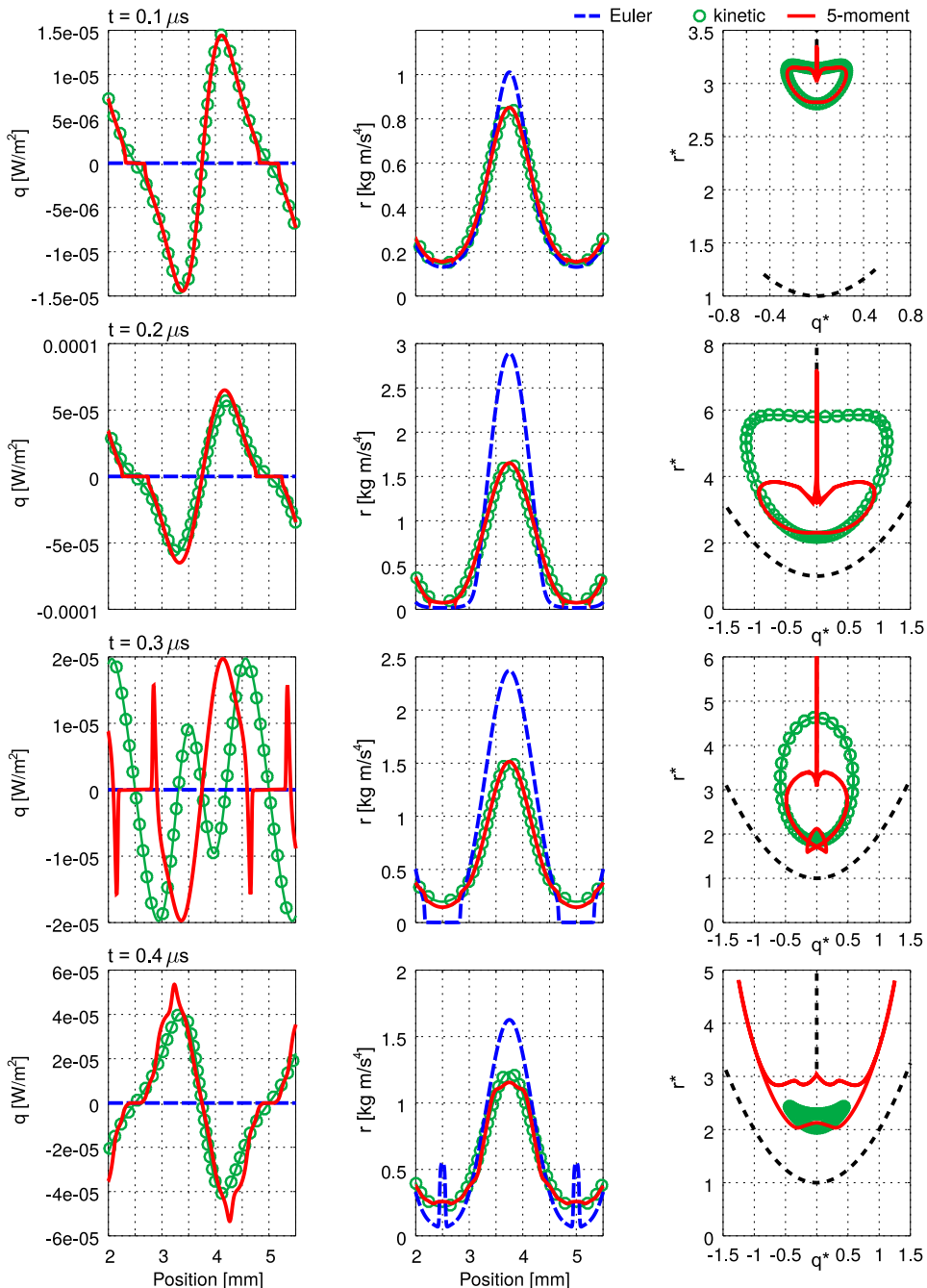


Figure 6.9: Case $V_0 = T_i$ [eV]; heat flux, order-4 moment and trajectory in moment space at different times. Green symbols+line: kinetic solution. Blue dashed line: Euler. Red line: 5 moments.

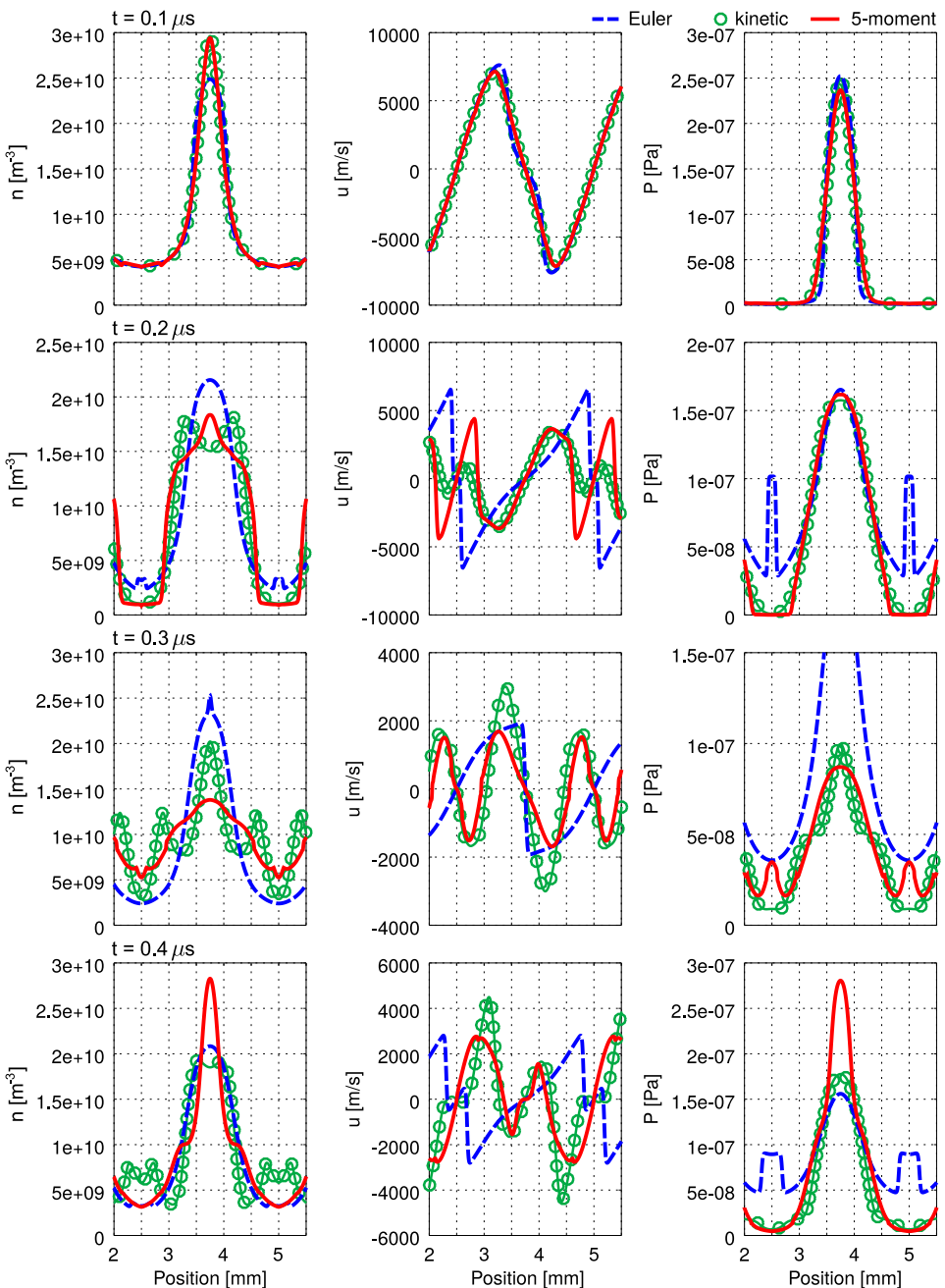


Figure 6.10: Case $V_0 = 5 T_i$ [eV]; first three moments at different times. Green symbols+line: kinetic solution. Blue dashed line: Euler. Red line: 5 moments.

Chapter 6. Maximum-entropy modeling of ions

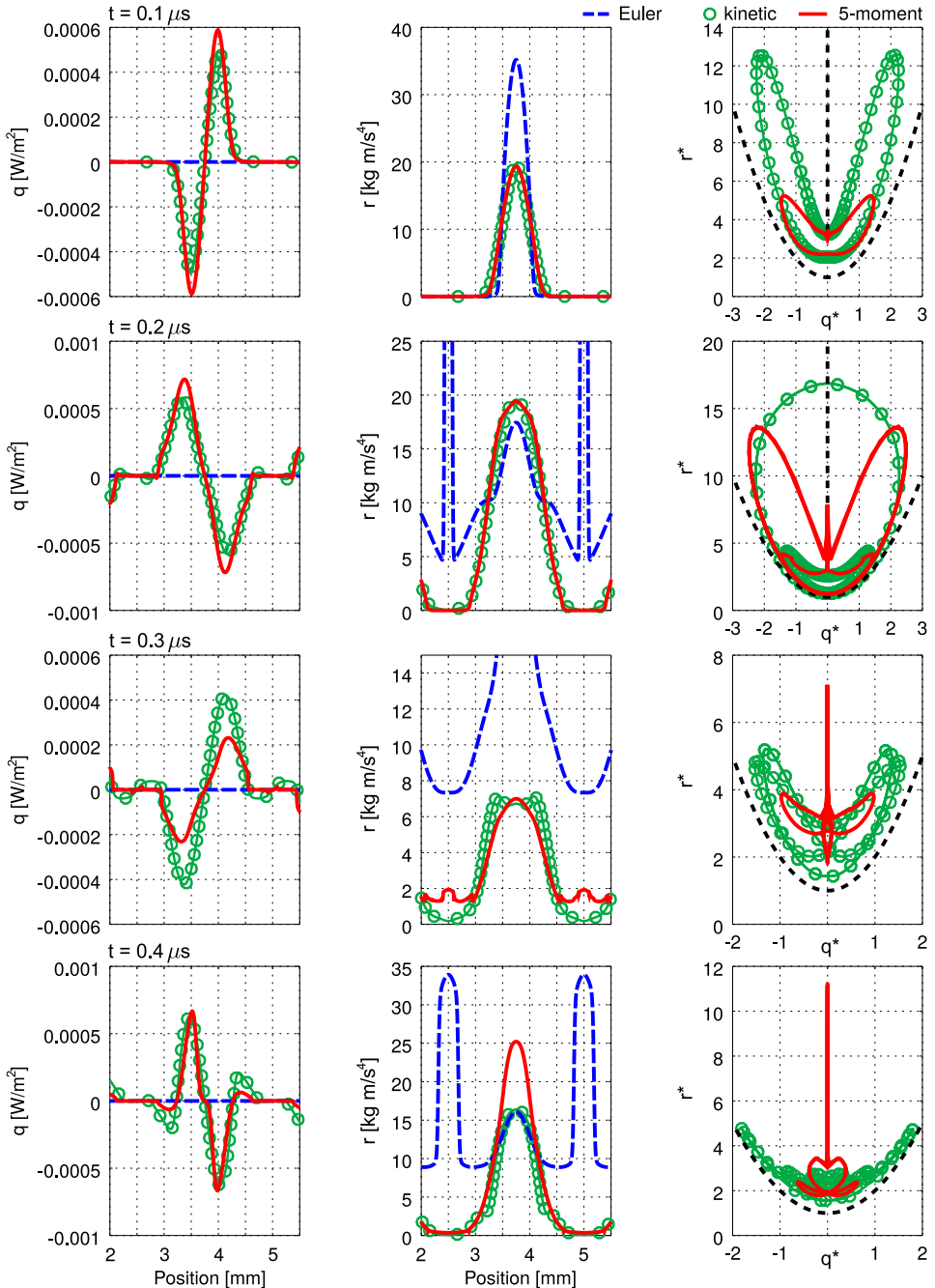


Figure 6.11: Case $V_0 = 5 T_i$ [eV]; heat flux, order-4 moment and trajectory in moment space at different times. Green symbols+line: kinetic solution. Blue dashed line: Euler. Red line: 5 moments.

6.5 Ions in a travelling wave

In this section, we investigate the behavior of ions inside a travelling electric field wave. The test case setup is identical to the one described in the previous section, except that a non-zero phase velocity is added into the sinusoidal electric field profile. The same phenomenology as for the previous test case will be observed, but this time acting on a tail of the VDF rather than on its bulk, and thus showing ion-trapping. The latter has been identified as one possible mechanism for the saturation of azimuthal electron drift instabilities in Hall thruster discharges [58], making the present test case particularly interesting in view of further more complete applications.

As for the previous test case, the potential profile is in the form

$$V(x, t) = V_0 \cos(\omega t + kx) , \quad (6.17)$$

where x could represent the azimuthal direction in a Hall thruster geometry. By differentiation, the electric field reads

$$\mathbf{E}(x, t) = V_0 k \sin(\omega t + kx) , \quad (6.18)$$

A domain $x \in [0, L]$ is employed, with $L = 0.01$ m. To simulate four electric field peaks in the domain, we consider $N = 4$ and

$$k = N2\pi/L \approx 2513.27 \text{ m}^{-1} \quad (6.19)$$

These choices allow us to select a regime that somehow resembles the oscillations observed in the numerical simulations of Boeuf & Garrigues [49], at least for their lower current test cases. An analogous test case is performed by Charoy et al. [50]: by estimating the value of V_0 from this reference, we see that $V_0 \approx T_i$ [eV]. Therefore, after having arbitrarily chosen $T_i^{\text{eV}} = 10$ eV, we select V_0 consistently as $V_0 = 10$ V.

From the numerical dispersion relation reported in [50], the wave appears to be traveling at roughly twice of the ion thermal speed. The phase velocity is thus set to

$$v_p = \frac{\omega}{k} = 2\sqrt{\frac{8k_B T_i}{\pi m}} , \quad (6.20)$$

resulting in $\omega \approx 21.745$ MHz. The choice of these values is highly approximated, but gives anyway a reasonable starting point.

Kinetic, 5-moment and Euler simulations

The setup for the kinetic, 5-moment and Euler system simulations are the same as described in the previous section.

The kinetic solution is obtained on 2048×2048 cells, with a time step of $dt = 5 \times 10^{-11}$ s, and is shown in Fig. 6.12. The kinetic solution shows the characteristic ion wave-trapping behavior, also observed in the self-consistent PIC simulations.

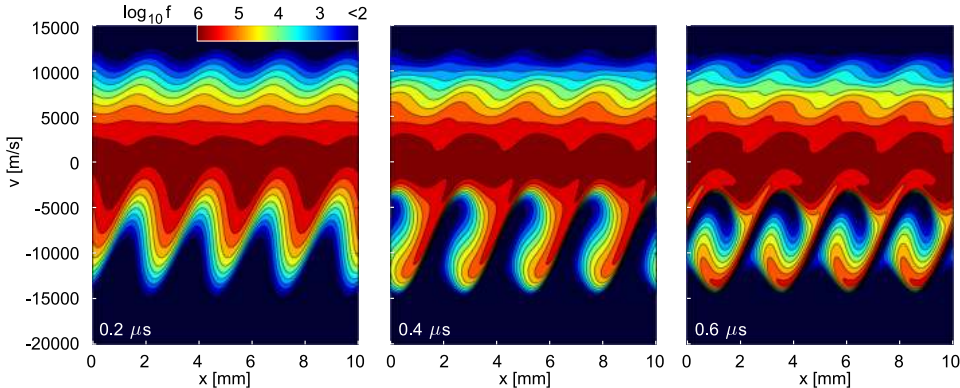


Figure 6.12: Travelling electric field test case. Kinetic solution at three time steps.

Figures 6.13 and 6.14 compare the moments of the kinetic solution to the 5-moment and Euler systems. The 5-moment system reproduces accurately the kinetic solution from the beginning of the simulation up to $2 \mu\text{s}$, while Euler already appears to deviate considerably. At later times, when the phase-space distribution is gradually degenerating into spirals, the 5-moment system still reproduces the general behavior, but progressively decreases its accuracy.

The high accuracy in the initial stages of the phase-space vortices formation is highly encouraging. Considering for example the Hall thruster case, ions produced in the channel will be accelerated towards the exit and only briefly pass through the region where the wave appear. The instability could thus saturate at a point that is somehow intermediate between the formation and the full 1D phase-space spirals development. This problem will be studied in the next section.

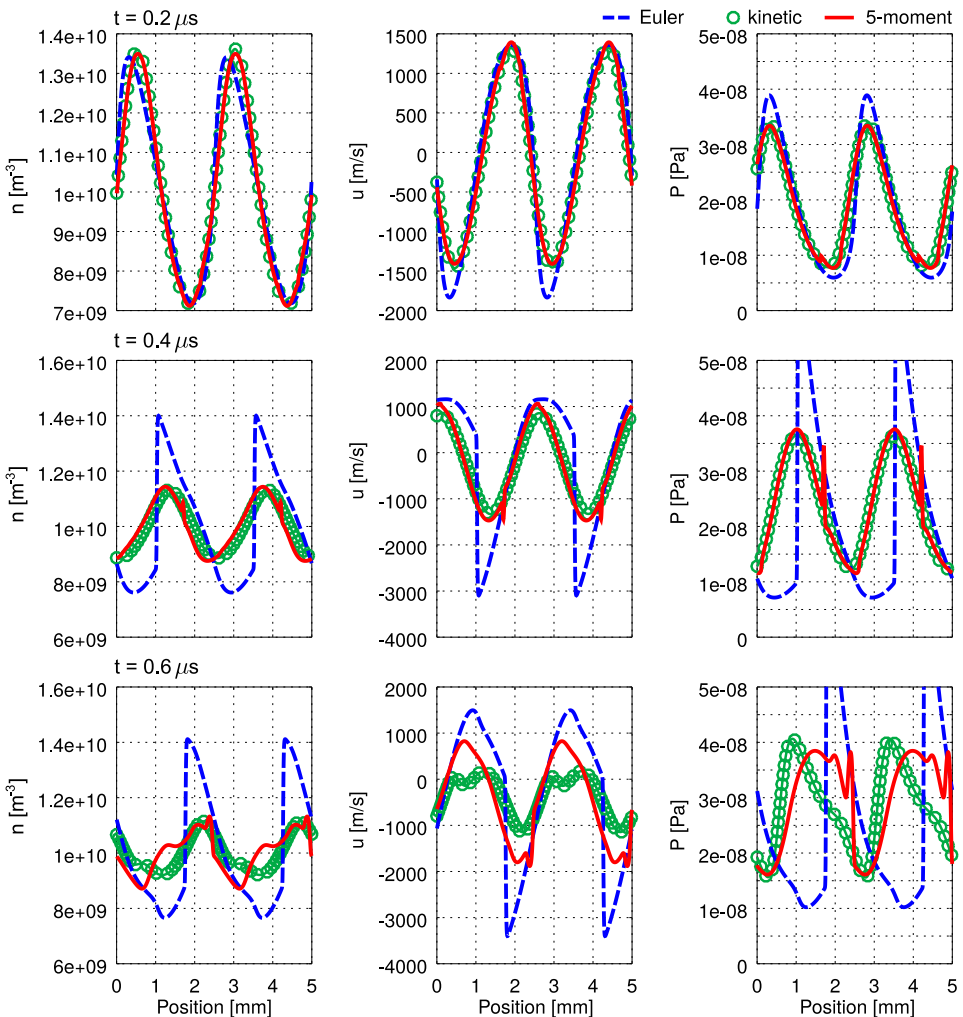


Figure 6.13: Travelling electric field test case. Density, velocity and pressure at three time steps. Symbols: kinetic solution. Red line: 5-moment system. Blue dashed line: Euler system.

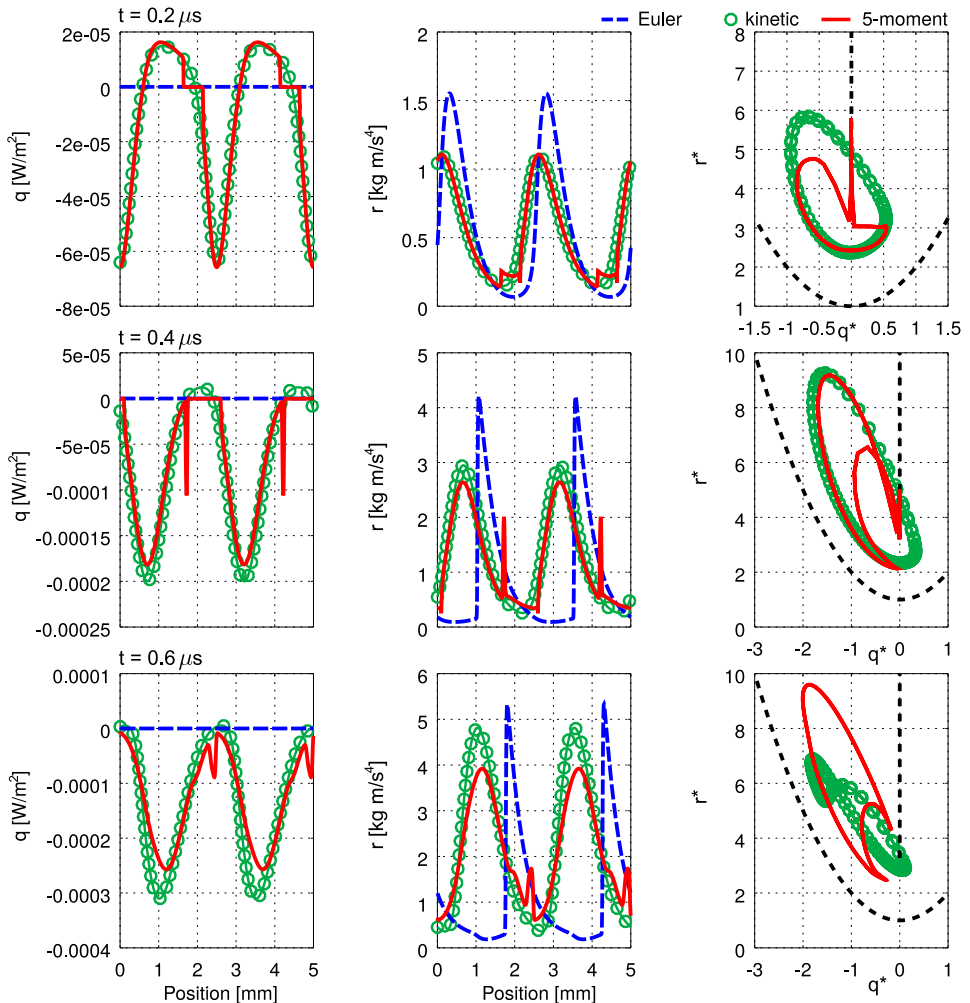


Figure 6.14: Travelling electric field test case. Heat flux and order-4 moment at three time steps. Symbols: kinetic solution. Red line: 5-moment system. Blue dashed line: Euler system.

6.6 Ions in axial-azimuthal 2D plane

The test case considered in this section combines the axial acceleration case of Section 6.2 and the azimuthal waves considered in Sections 6.4 and 6.5. A two-dimensional domain is here considered, open in the x -direction and periodic along y . Xenon ions are simulated inside imposed electric fields, and four different methods are compared:

- i) A cold-ions (pressureless gas) approximation;
- ii) The Euler equations;
- iii) The 14-moment maximum-entropy system of equations;
- iv) A particle solution of the kinetic equation.

The cold-ions approximation [193] consists in neglecting the pressure contribution to the ion momentum equation, and was introduced in Section 2.3.3. This eliminates the need to solve the ion energy equation. Such approximation is often employed due to its simplicity (see for example [90, 194–197]) and will be here compared to the more complete models.

6.6.1 Description of the case

As for the previous test cases, the domain size is taken to resemble the test cases described in [49, 50], also discussed in Section 5.2.2: $x \in [0, 0.025]$ m represents the axial direction of a Hall thruster channel and $y \in [0, 0.0128]$ m the azimuthal direction, assumed to be Cartesian for simplicity (infinite radius). The ionization source term has a cosine profile (limited between positions $x_1 = 0.0025$ m and $x_2 = 0.01$ m),

$$S(x) = \begin{cases} S_0 \cos\left(\pi \frac{x-x_M}{x_2-x_1}\right) & \text{if } x_1 \leq x \leq x_2 \\ 0 & \text{otherwise,} \end{cases} \quad (6.21)$$

with $x_M = (x_1 + x_2)/2$. The value of S_0 fixes the maximum ion current density J_{max} ,

$$J_{max} = \int_{x_1}^{x_2} S(x) dx = \frac{2eS_0}{\pi}(x_2 - x_1). \quad (6.22)$$

A value of $S_0 = 6.62 \times 10^{23}$ [ions/m³s] results in a maximum current of $J_{max} = 200$ A/m². As mentioned in the original work [49], such value is rather low. However, this choice does not impact the validity of the present

analysis, as the electric field is not self-consistent but rather externally imposed. The ion creation happens from a background neutrals Maxwellian distribution with a temperature of 0.5 eV, and a zero average velocity.

The imposed electric field is composed by a fixed longitudinal accelerating field E_x with a Gaussian shape in x , and an azimuthal travelling wave E_y , whose amplitude is lower than E_x by a factor α

$$\begin{cases} \mathbf{E}(x, y, t) &= E_x(x) \hat{x} + E_y(x, y, t) \hat{y}, \\ E_x(x) &= E_0 \exp [-(x - x_0)^2 / L_0^2], \\ E_y(x, y, t) &= \alpha E_x(x) \sin(\omega_y t + k_y y), \end{cases} \quad (6.23)$$

with $E_0 = 50\,000$ V/m and $\alpha = 0.1$. The Gaussian profile is centered around $x_0 = 0.008$ m and has a width $L_0 = 0.0025$ m. The value of k_y is chosen as to show three peaks, $k_y = 3 \times 2\pi/L_y$, with $L_y = 0.0128$ m. Finally, the frequency is arbitrarily chosen as $\omega_y = 2$ MHz. Note that for a given value of k_y , the choice of ω_y sets the phase velocity of the azimuthal wave. As discussed in the Sections 6.4 and 6.5, different wave speeds result in different portions of the ion VDF being trapped in the electric field. We can therefore expect different values of ω_y to have different effects on the degree of non-equilibrium. The electric field components at time $t = 0$ s are shown in Fig. 6.15.

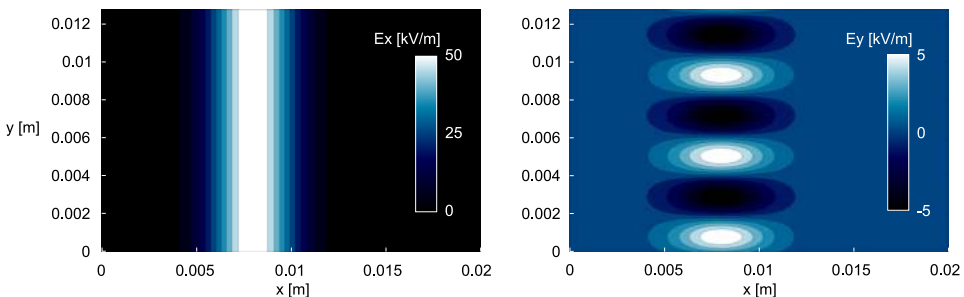


Figure 6.15: Imposed electric field at time $t = 0$ s. The E_y wave moves towards negative values of y .

In the previous 1D periodic cases, the solution was seen to be unsteady, and composed of VDFs progressively curling on themselves. In the present 2D case, ions are not strictly confined in the region of the azimuthal field, but accelerate axially and eventually leave the domain under the effect of the axial field. Therefore, the ultimate non-equilibrium reached at steady state will result as a balance between wave-trapping (in the azimuthal field) and axial acceleration. A periodic steady state is eventually reached, as

shown in the next sections.

6.6.2 Kinetic solution

A solution to the kinetic equation is obtained using a 2D PIC approach with imposed fields. At each time step, a number of particles is injected in the domain and is advected according to the imposed fields. For a given ionization profile $S(\mathbf{x})$, and a simulated volume V , the number of ions produced in the simulated volume is

$$\dot{N} = \int_V S(\mathbf{x}) \, dx \, dy \, dz \quad \left[\frac{\text{ions}}{\text{s}} \right]. \quad (6.24)$$

In terms of a 2D particle simulation, we consider a fictitious z -dimension of size $L_z = 1$ m. Considering that $S(\mathbf{x})$ is uniform along y for the whole length L_y , and only depends on x , the number of particles to be injected during the time step dt is

$$N_{dt} = dt L_y L_z \int_0^{L_x} S(x) \, dx = dt L_y L_z S_0 \frac{2(x_2 - x_1)}{\pi}. \quad (6.25)$$

The particles must be injected following the $S(x)$ cosine profile. This is done as follows. A cosine distribution is first defined as

$$g(x) = \begin{cases} I^{-1} \cos(ax + b) & \text{if } x_1 \leq x \leq x_2, \\ 0 & \text{otherwise,} \end{cases} \quad (6.26)$$

with $a \equiv \pi/(x_2 - x_1)$, $b \equiv -\pi x_M/(x_2 - x_1)$ (notice the negative sign), and where the division by its integral $I = 2(x_2 - x_1)/\pi$ makes the distribution unitary. The cumulative distribution $G(x)$ of Eq. 6.26 is easily computed,

$$G(x) = \int_{x_1}^x I^{-1} \cos(ax + b) \, dx = I^{-1} \left[\frac{1}{a} \sin(ax + b) - \frac{1}{a} \sin(ax_1 + b) \right] \quad (6.27)$$

where $G(x) = 0$ for $x < x_1$. This relation is easily inverted, since $G(x)$ is monotonic. By defining a uniformly distributed random number $\mathcal{R}_1 \in (0, 1)$, we invert the previous relation and define

$$X = \frac{1}{a} \sin^{-1} [aI\mathcal{R}_1 + \sin(ax_1 + b)] - \frac{b}{a}. \quad (6.28)$$

The quantity X is thus distributed as a cosine between x_1 and x_2 and represents the position at which a particle is to be created. Also, one should

consider that the particle injection happens continuously in time. Once the particle is created, a fraction of the time step is selected as $\mathcal{R}_2 dt$, with $\mathcal{R}_2 \in (0, 1)$, sampled from a uniform distribution, and the particle is advected accordingly.

The time integration scheme is a simple first order forward Euler integrator. A time step $dt = 5 \times 10^{-9}$ s proved to be small enough to make the time integration error negligible. All particles reaching the x -boundaries are removed from the simulation, while particles crossing the y -boundaries are re-introduced periodically. Since no electric field is computed (but instead, it is artificially imposed) and since all collisions are neglected, there is no need to employ a grid in the computation. A grid is created only a posteriori, during the post-processing, for the sake of grouping particles and computing their moments.

6.6.3 Fluid simulations

The simulation is then repeated using fluid models, solving the pressureless gas (cold ions), the Euler equations and the 14-moment system. For all cases, a grid of 640×320 cells is employed. The cold ions and Euler systems are solved using HLL fluxes, achieving second order space accuracy by use of a MSUCL linear reconstruction and symmetric van Albada limiter. However, the HLL scheme was shown to introduce some oscillations in the maximum-entropy simulations (see Section 4.1.3), therefore a more diffusive Rusanov scheme is employed. The higher diffusivity is reduced by following the “partial-MUSCL” approach of Eq. (3.8), using $\beta = 0.7$ and the symmetric van Albada limiter. Some attempts of employing a vanilla MUSCL approach to the 14-moment system were done. However, this resulted in some extreme non-equilibrium states (probably, much of which is due to numerical error or oscillations), that would eventually limit the time step to extremely low values, practically stalling the simulation. With the simple modification of $\beta = 0.7$, the results are slightly more diffuse, but the simulation ran faultlessly.

Along y , symmetric boundary conditions are imposed by use of two layers of ghost cells at each side. At the left and right boundaries, the density in the ghost cells is set to the low value of $n_0 = 10^{10} \text{ m}^{-3}$ and with a supersonic velocity of 20 000 m/s leaving the domain. No other boundary condition is necessary for the pressureless gas system. For the Euler and 14-moment systems, a temperature of 10 000 K is imposed in the ghost cells, and other moments of the 14-moment system are at equilibrium. The same conditions are imposed throughout the domain for the initial time $t = 0$,

except that the velocity is assumed to be zero.

A second-order Midpoint Euler time integration is employed. The time step was obtained by fixing the Courant number to 0.5. An upper limit to $dt = 10^{-9}$ s is anyway imposed due to the presence of the electrical and chemical source terms, and this proved particularly important in the starting phases of the simulation. As to speed-up the computations, GPU acceleration is employed (see Appendix A). Double precision is employed (strictly required for using the 14-moment closure), with 16×8 threads per block along x and y respectively.

6.6.4 Comparison of the results

All simulated systems quickly settle to a periodic solution that follows the azimuthally travelling wave. After ions have been created in the ionization region, they travel towards the positive- x direction by effect of the electric field. In the meanwhile, the azimuthal field is responsible of compressing them into streaks, as shown in Fig. 6.16.

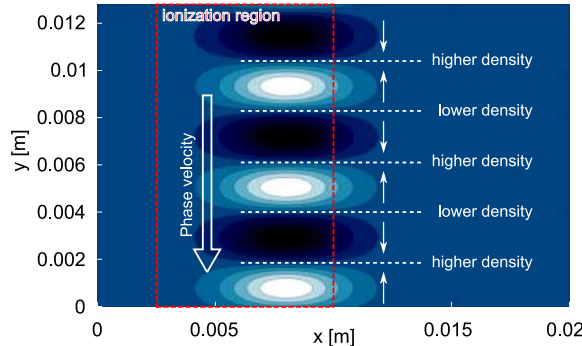


Figure 6.16: Scheme of the expected solution. Ion streaks form due to the azimuthal electric field E_y . The streaks move downwards, in phase with the wave. Colours: contours of E_y .

The results obtained from the different methods are shown in Fig. 6.17 for the density and in Fig. 6.18 for the azimuthal velocity u_y . The pressureless gas system shows some δ -shocks, appearing as singularities in the density. This is a known characteristic of weakly-hyperbolic systems [193, 198, 199]. The Euler system on the other hand appears prone to reproduce shock waves, even where they should not be present in the (fully collisionless) PIC simulation. Indeed (as was discussed in Section 4.4 by analyzing crossing rarefied jets), the Euler system cannot reproduce collisionless crossing streams of particles, and always has them interacting. The

“crossing” effect here is due to the sinusoidal azimuthal acceleration. On the other hand, the 14-moment system appears to reproduce closely the PIC results. A good accuracy is shown for other moments as well, as shown in Fig. 6.19.

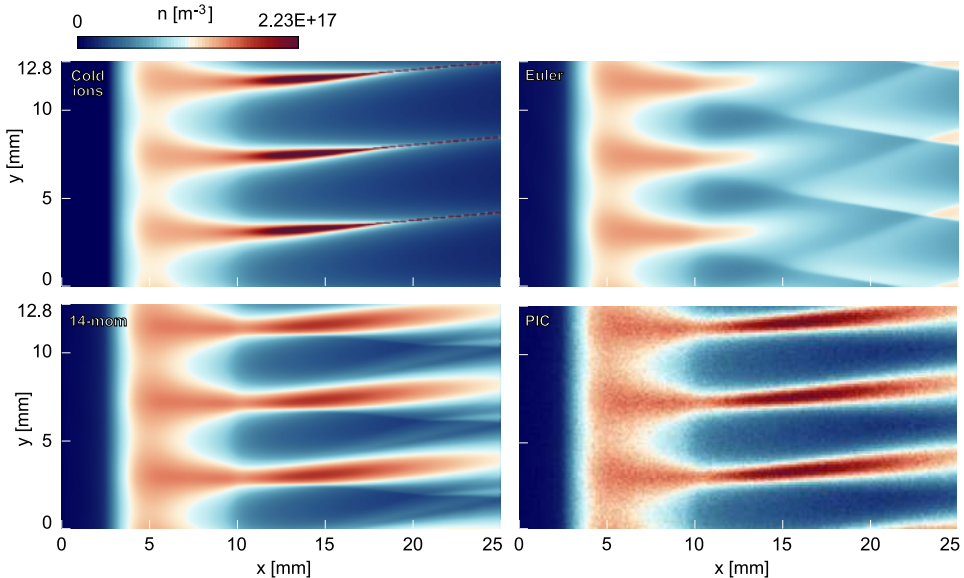


Figure 6.17: 2D ion evolution inside an axial and a travelling azimuthal electric fields. Number density at time $t = 50 \mu\text{s}$ as predicted by different models.

6.7 Conclusions

In this chapter, we have investigated the accuracy of the 5 and 14-moment maximum-entropy systems for problems related to plasma physics and Hall thrusters. The method was seen to bring drastic improvements over the Euler equations for all tested situations, often reproducing the kinetic results very accurately. In all cases, a profitable solution was obtained, despite the strong non-equilibrium arising from the electric field and the collisionless assumptions. In particular, the 2D test case suggests that the 14-moment maximum-entropy method could be an appealing approach to substitute the kinetic treatment for the study of Hall thruster plasmas.

It should be recalled that the 14-moment system has a much higher computational cost than the Euler equations (confirming the previous results of Section 4.3). However, this cost was seen to be lower by at least one order of magnitude with respect to the kinetic simulations. A possible application of this approach could regard hybrid methods (kinetic ions + fluid elec-

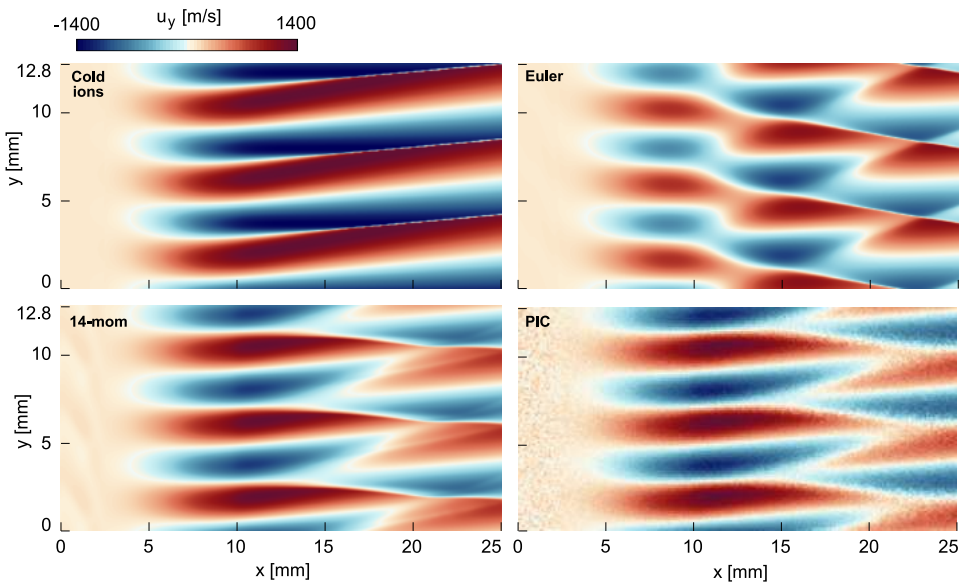


Figure 6.18: 2D ion evolution inside an axial and a travelling azimuthal electric fields. Azimuthal velocity u_y at time $t = 50 \mu\text{s}$ as predicted by different models.

trons). In place of a kinetic description, one could employ a 14-moment modeling of ions. Among other advantages, such approach would remove the costly particle-deposition procedure, characteristic of kinetic methods, and the ion quantities would be known at the same grid points as the electrons fluid. This further computational advantage is still to be investigated, and is suggested as a future work.

This chapter concludes the study of ions. In the next chapter, the maximum-entropy method will be applied to electrons, that further include the modeling complexity associated to the magnetic field.

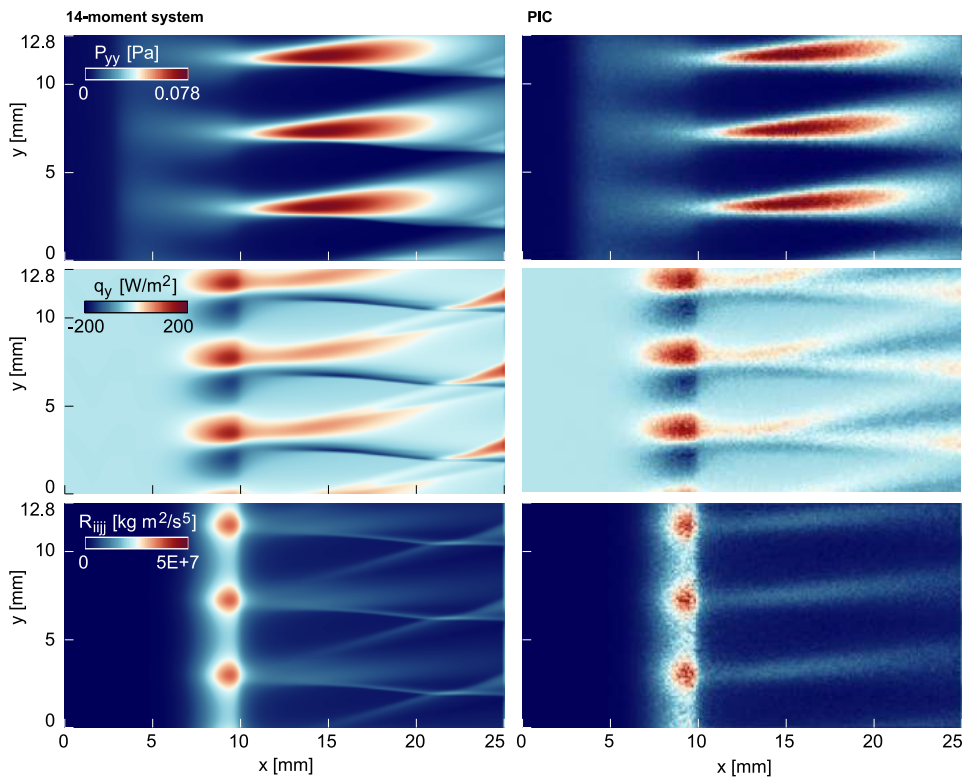


Figure 6.19: 2D ion evolution inside an axial and a travelling azimuthal electric fields. Comparison of the 14-moment system and PIC solutions for selected moments. Time $t = 50 \mu\text{s}$.

7

CHAPTER

Maximum-entropy modeling of electrons

The content of this chapter was partly published in [200]: Boccelli, S., Giroux, F., Magin, T.E., Groth, C.P.T., McDonald, J.G., *A 14-moment maximum-entropy description of electrons in crossed electric and magnetic fields*, Physics of Plasmas 27 (12), 123506; and partly presented at the 73rd Gaseous Electronics Conference [201].

While ions in Hall thrusters are fundamentally unmagnetized, a computation of the Larmor radius reveals that electrons are strongly affected by the magnetic field, due to their small mass. Together with the axial electric field, electrons are subject to a drift in the $\mathbf{E} \times \mathbf{B}$ direction. Also, while ions were assumed to be collisionless, electrons collisions are much more frequently, mostly with background neutrals, and such collisions are important in terms of cross-field electron transport, but not strong enough to keep electrons close at thermodynamic equilibrium. Indeed, we will see that electrons can be expected to develop strongly non-Maxwellian VDFs. This chapter is aimed at investigating the maximum-entropy closure in such conditions.

Due to the low plasma density, Coulomb collisions will be neglected and only collisions with background neutrals will be accounted for. Only

electrons will be simulated, and the electric and magnetic fields will be prescribed.

This chapter is structured as follows. First, Section 7.1 gives an overview of the main non-equilibrium effects that affect electrons in Hall thrusters. Most of these will not be considered, and attention will be focused on cross-field transport. Then, in Section 7.2, a simplified steady state problem is considered, and the 14-moment maximum-entropy VDF is obtained and compared to analytical results, together with both its tracked and its closing moments. Section 7.3 is devoted to the development of BGK-like collision terms for the 14-moment equations. Such terms are then employed in Section 7.4 to study a space-homogeneous time-relaxation problem, where electrons are initialized from a drifted Gaussian distribution, and evolve following the $E \times B$ fields and in presence of background neutrals. Finally, 1D test cases are considered in Section 7.5, where we study the expansion of electrons along a longitudinal electric field but in presence of a localized magnetic field barrier.

Note that besides Hall thrusters, the results of this chapter could be applied in other $E \times B$ devices such as in magnetrons [45, 202], where analogous conditions are often encountered (except for a generally higher background pressure, and consequently an increased collisionality).

7.1 Overview of non-equilibrium effects for electrons in Hall thrusters

Non-equilibrium in the electron velocity (VDF) and energy (EDF) distribution functions has been studied extensively in the past [203–205]. This section offers a summary of the main points.

First, the presence of crossed electric and magnetic fields causes the electron VDF to deviate from a Maxwellian. From the point of view of single-particle trajectories, crossed E and B fields cause electrons to move along a trochoid, and this gives rise to a ring-shaped VDF, centered around the drift velocity $u_d = E/B$ (see [206, 207]). Collisions on the other hand tend to thermalize the VDF, but in presence of low-collisionality, the combined effects of collisions and $E \times B$ make the VDF asymmetrical [44, 208, 209], and thus introduce a non-zero heat flux (and further odd-order moments).

In actual Hall thrusters, a number of other conditions are responsible for non-equilibrium. For example, interaction with the walls plays an important role. At the walls, electrons having a sufficient energy (“loss cone” in the electron VDF) can overcome the potential barrier created across the

sheath and are effectively lost, while low-velocity electrons are reflected back into the plasma bulk [210]. Secondary electron emission (SEE) at the walls is responsible for creating low-temperature electrons [57, 211] and is known to cause near-wall conductivity (NWC) in presence of $\mathbf{E} \times \mathbf{B}$ fields [31]. Inelastic collisions also cause the VDF to deviate from a Maxwellian, since the cross-section is non-linear and only higher-energy electrons have sufficient energy to excite/ionize the background neutrals. This depletes the tails of the Maxwellian (see for example [133]). Finally, instabilities and kinetic effects such as Landau damping are an important contributions to non-equilibrium (see for example [41]).

7.2 14-moment formulation against analytical VDFs

As a first step towards assessing the quality of the maximum-entropy closure for modeling electrons, we assess how well the 14-coefficient distribution function f_{14} can reproduce analytical VDFs for a simplified problem. A simple space-homogeneous steady state case is considered, with imposed $\mathbf{E} \times \mathbf{B}$ fields, and only elastic collisions of electron with the background neutrals. By assuming a BGK collision operator, the kinetic equation is written as

$$\frac{q_e}{m_e} (\mathbf{E} + \mathbf{v} \times \mathbf{B}) \cdot \frac{\partial f}{\partial \mathbf{v}} = -\nu(f - \mathcal{M}_b), \quad (7.1)$$

where ν is the electron-neutral collision frequency and where electrons that experience a collision are assumed to be described by a Maxwellian VDF \mathcal{M}_b , subscript “ b ” standing for “birth”. Under such assumptions, Shagayda has obtained an analytical solution for the electrons VDF [44]. In such reference, the post-collision Maxwellian is written as

$$\mathcal{M}_b = n_e (h_b/\pi)^{3/2} \exp(-h_b v^2), \quad (7.2)$$

with $h_b = m_e/(2k_B T_b)$ and T_b the birth temperature. This assumes that after a collision, the electron velocity is completely reset and assumes an un-drifted Maxwellian distribution at T_b . The analytical solution of [44] depends on the inverse Hall parameter $\beta \equiv \nu/\omega_c$, with $\omega_c = |q_e \mathbf{B}/m_e|$ the electron cyclotron frequency, and on the value of the drift velocity $u_d = \mathbf{E}/\mathbf{B}$.

7.2.1 Preliminary considerations

Fig. 7.1 shows an example of a possible electron VDF, obtained from this model. It is clear that a moment method aiming to reproduce this kind of non-equilibrium needs to:

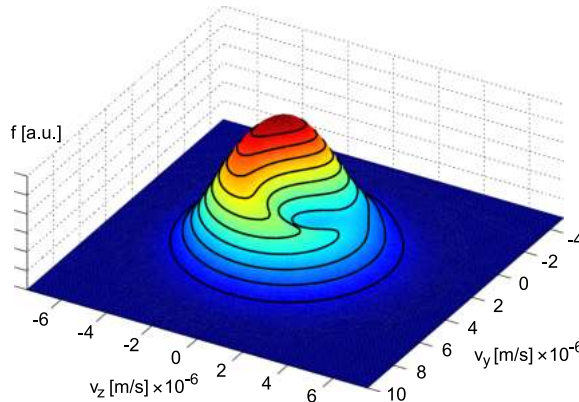


Figure 7.1: Example of a stationary electron VDF in the plane perpendicular to the magnetic field, with simplified BGK collision operator, obtained from the model in [44] with parameters $T_b = 10^5$ K, $\beta = 0.3$, $E/B = 2.5 \times 10^6$ m/s.

- 1) Include pressure (temperature) anisotropy, not only between the parallel and perpendicular directions, but also within the parallel plane;
- 2) Include a treatment for the heat flux due to the strong asymmetry;
- 3) Allow for ring-like distributions, resulting in super-Maxwellian order-4 moment: $R_{ijjj} > 15P^2/\rho$.

The 14-moment system is the first member of the maximum-entropy family that allows us to reproduce such features. The previous member (the 10-moment method) is instead based on a Gaussian closure, and therefore misses requirements 2) and 3). In any case, a perfect match of the VDF is not strictly required for the sake of reproducing moments, and the 10-moment method could thus prove effective anyway, in certain situations.

7.2.2 Analytical and maximum-entropy VDFs

To assess the accuracy of the 14-moment VDF, we consider a range of values for $\beta \in [0, 0.5]$. Two different drift velocities are considered, obtained by setting $B = 0.01$ T and either $E = 25\,000$ V/m or $50\,000$ V/m. This results in a collisionless drift velocity $u_d^{c-less} = 2.5 \times 10^6$ m/s and 5×10^6 m/s respectively. We select the birth temperature as $T_b = 100\,000$ K, and this results in a final temperature $T \approx 500\,000$ K.

The procedure for comparing the 14-moment distribution to the analytical VDF is the following:

1. The analytical VDF is constructed, for a given value of β and $u_d = E/B$;

2. Its first 14 conserved moments are computed numerically (together with the closing moments Q_{ijk} , R_{ijkk} , S_{ijjkk} , for a further comparison);
3. Such 14 moments are used as a target to obtain the maximum-entropy distribution, by solving the entropy maximisation of Section 2.4.1;
4. The analytical and the maximum-entropy distributions are compared, in terms of VDF and EDF.

The results are shown in Fig. 7.2 for the velocity components in the perpendicular plane. The VDF in the parallel plane is simply Maxwellian. Considering the ratio between the drift and thermal velocity of electrons, the case of Fig. 7.2-Top-Left is the most representative of Hall thrusters, where commonly $\beta \rightarrow 0$. The VDF in such case appears to have a flat top if compared to a Maxwellian, and appears to approach the Druyvenstein distribution, with $f \propto \exp(-v^4)$. This is well reproduced by the f_{14} VDF. A small hole in the center is also observed in the analytical VDF, but this does not appear in the f_{14} .

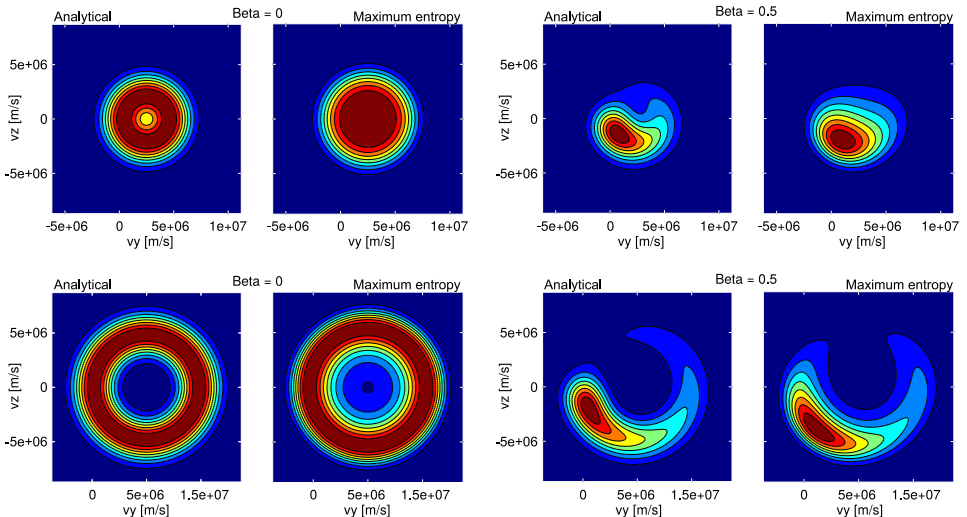


Figure 7.2: Comparison of analytical and 14-moment maximum-entropy VDFs in the perpendicular plane for different values of the collisionality and electric field. Top: $E = 25 \text{ kV/m}$. Bottom: $E = 50 \text{ kV/m}$. $B = 0.01 \text{ T}$, $T_b = 100\,000 \text{ K}$.

By increasing the electric field, the drift velocity is also increased. In the velocity space, electrons are created from the un-drifted Maxwellian of Eq. (7.2), and drift in circles with a radius equal to the drift velocity. Therefore, when the ratio between drift and thermal velocity is larger than

one, the perpendicular VDF assumes a ring-like shape. The f_{14} distribution appears to recover this accurately. Some accuracy is lost as collisionality is increased, and asymmetry is introduced correspondingly. This most likely results in some accuracy loss in the heat fluxes. These cases are shown in Fig. 7.2-Bottom.

An analysis of the EDF (computed numerically from the VDF) shows an even better agreement, as shown in Fig. 7.3 for the collisionless cases $\beta = 0$. This is expected, since the EDF is obtained from an integration of the VDF over constant velocity shells. The two bumps described in [206, 207] are retrieved. For the lower values of the drift velocity, the two bumps are only slightly visible, and the distribution is reasonably well reproduced by a drifted Maxwellian. For higher drift velocities instead, the drifted Maxwellian deviates strongly from the actual EDFs, and we may expect a strong effect of non-equilibrium on the collisionality (and thus ionization rates) in such conditions, due to the non-linearity of the cross-sections.

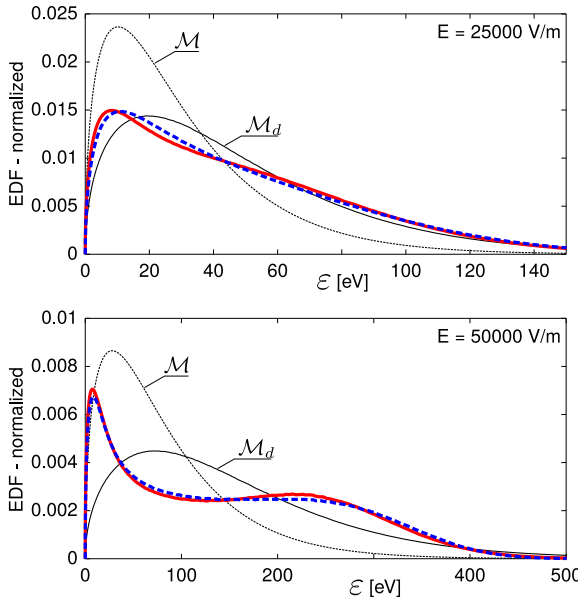


Figure 7.3: Normalized EEDFs obtained from the $\beta = 0$ cases of Fig. 7.2. Red solid line: Shagayda's analytical results. Blue dashed lines: f_{14} . Thin black lines: un-drifted (\mathcal{M}) and drifted (\mathcal{M}_d) Maxwellians.

The moments of the analytical VDF are then compared to those of f_{14} in Fig. 7.4. Note that only closing moments are shown, since there is no point in comparing the first 14 moments. Indeed, these are used as target moments for computing f_{14} , and coincide to the analytical ones to numerical

accuracy.

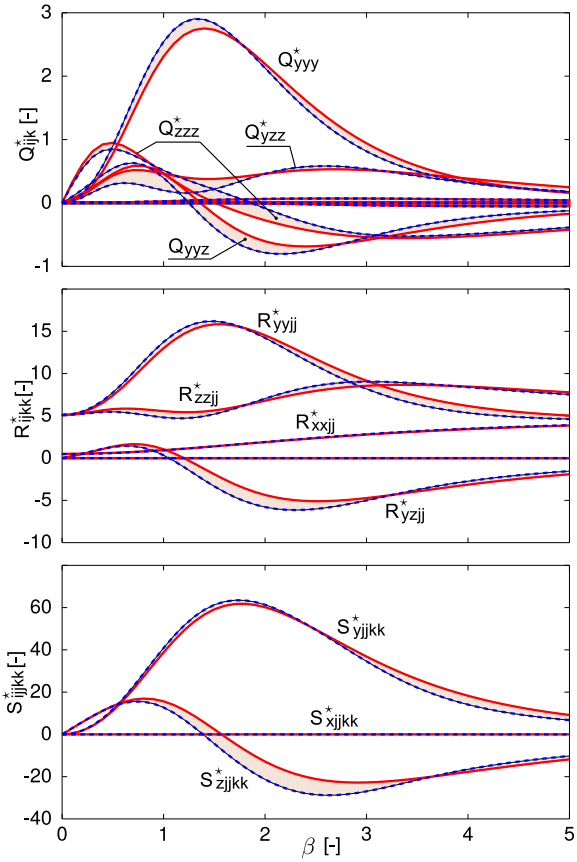


Figure 7.4: Dimensionless closing moments vs β for the case $E = 50 \text{ kV/m}$. Analogous accuracy is shown for $E = 25 \text{ kV/m}$.

For all considered collisionalities, the closing moments appear reasonably accurate. In particular, the accuracy appears to be very good for Hall thruster conditions ($\beta \approx 0$). For $\beta \rightarrow \infty$, collisions eventually turn the VDF into a Maxwellian, and all moments correspondingly reach their equilibrium value: odd-order moments vanish, the pressure tensor becomes isotropic and diagonal, and the components of the order-4 moment tensor become $R_{ijkk} \rightarrow 5P^2\delta_{ij}/\rho$, such that their contraction results in $R_{iiji} = 15P^2/\rho$. This comparison is of particular interest, since the final goal is simulating the actual 14-moment system of equations, where closing moments play a crucial role through the convective fluxes. Nonetheless, an exact match is probably not strictly required, as the importance of the closing moments is anyway mitigated, to some degree, by the presence

of many other lower order (convective) moments. The moments in Fig. 7.4 are shown in dimension-less form (see Section 2.4.1). The computation was repeated using the interpolative closure [67], and this resulted in the same degree of accuracy.

Finally, despite not being necessary in terms of the closure, it is interesting to consider the limiting values of the average velocities. These are shown in Fig. 7.5. For $\beta = 0$, the value of u_y coincides with the collisionless drift velocity $u_d = E/B$ and is progressively reduced as the collisions are increased. The velocity u_z on the other hand can be seen to follow exactly the classical mobility across a magnetic field,

$$u_z = \frac{e/(m\nu)}{\omega_c^2/\nu^2 + 1} E = \mu E, \quad (7.3)$$

with μ the classical mobility. At first, it may seem surprising that such an accurate match is obtained despite the strong non-equilibrium. However, this is to be expected, since the collision frequency ν is being imposed in the present test case. In a real scenario, ν would be obtained from the state of the gas, and would depend on the actual VDF.

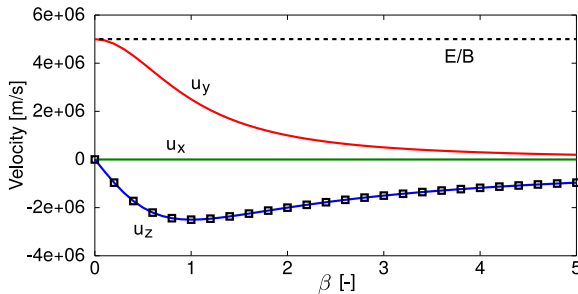


Figure 7.5: Solid lines: average velocities for the case $E = 50$ kV/m. Symbols: classical cross-field transport from Eq. (7.3).

7.3 BGK-like source terms for electron-neutral collisions

After having verified the capability of the 14-moment closure of reproducing the electron non-equilibrium, the next step consists in testing a direct application of the 14-moment governing equations, discussed in Section 2.4.1,

$$\frac{\partial \mathbf{U}}{\partial t} + \frac{\partial \mathbf{F}_x}{\partial x} = \mathbf{G}_E + \mathbf{G}_B + \mathbf{G}_c, \quad (7.4)$$

where the electric and magnetic sources $\mathbf{G}_{E,B}$ were obtained in Section 4.5. The source term \mathbf{G}_c for electron-neutral collisions is still to be derived, and

this is the aim of the present section. In this work, we are mostly interested in the study of the streaming part of the system, therefore a simplified treatment of collisions will be sufficient. The BGK collision operator [80] is a convenient choice, as it allows for a simple derivation of the source terms for the moment equations. Moreover, the BGK operator automatically recovers the Boltzmann's H-theorem, as relaxation happens towards a Maxwellian. Such operator has been employed in a number of scenarios, including multi-temperature monatomic/polyatomic gases and reacting mixtures [83–85].

In the following, we develop a BGK-like collision operator for electron collisions with background neutrals, in the conditions of low-temperature non-thermal plasmas, where the electron temperature is much higher than the neutral temperature. First, we write

$$\mathcal{C} = \left(\frac{\delta f}{\delta t} \right)_c = -\nu (f - f_p) , \quad (7.5)$$

where f_p is the distribution that characterizes the post-collision state of electrons and where the collision frequency ν only depends on the macroscopic parameters. The latter choice implies that all moments relax at the same rate, which is unphysical, or at least inaccurate. An improvement could be obtained by taking ν as a function of the particle velocity (and thus not only depending on the macroscopic quantities), at the price of increasing the model complexity [62, 86].

In the work of Shagayda [44], the post-collision distribution f_p is assumed Maxwellian. However, from a physical standpoint, this is not necessarily the case. As mentioned, such choice allows us to retrieve the H-theorem, which is surely desired for ordinary gases in absence of external fields, but is not necessarily representative of low-temperature plasmas. Indeed, while in an ordinary gas all species relax towards a common temperature (consider for example the relaxation behind a strong shock wave), low-temperature plasmas typically settle to a multi-temperature steady state: electrons are typically in the [eV] range (being excited by external fields), neutrals have a temperature often comparable to the walls temperature and ions are somewhere in the middle. Therefore, the collision operator must be formulated as to represent such steady state non-thermal conditions.

A second important aspect to be considered is mass disparity: as electrons have a much lower mass than neutrals, the energy exchange becomes extremely ineffective. In particular, considering the binary collision between a lightweight particle of mass m and a heavy particle of mass M , the

exchange of energy $\Delta\varepsilon/\varepsilon$ results, in the limiting case of $m \ll M$ [212],

$$\frac{\Delta\varepsilon}{\varepsilon} = 2 \frac{m}{M} (1 - \cos \chi) , \quad (7.6)$$

where χ is the deflection angle. Considering collisions of electrons with xenon atoms, $m_e/M_{Xe} \approx 4 \times 10^{-6}$, such that the initial energy of a hot electron will be transferred to the neutrals, in average, after some 10^5 – 10^6 elastic collisions.

In the following, we will consider isotropic scattering, that is a reasonable approximation for low collision energies [133, 213].

7.3.1 A simple Maxwellian-relaxation collision model

The simplest choice for the post-collision distribution consists in assuming that $f_p = \mathcal{M}$, with \mathcal{M} the local Maxwellian, as also done in [44]. This resembles a classical single-species BGK formulation, but differs in that:

- Neutrals are cold and slow with respect to the colliding electrons;
- The energy exchange $\Delta\varepsilon/\varepsilon$ is here neglected, and the energy of the electrons population is conserved;
- Scattering is assumed isotropic in the center of mass frame, that approximately coincides with the center of mass of the heavy neutral particle.

From these assumptions, the post-collision Maxwellian is characterized by a zero average velocity, and collisions have the effect of transforming the whole initial energy (kinetic + thermal) into thermal energy. Therefore, the post-collision electron temperature is obtained from

$$\frac{3}{2}k_B T_p = \frac{3}{2}k_B T + \frac{1}{2}m_e u^2 , \quad (7.7)$$

with T and u the temperature and average velocity of electrons. The post-collision pressure simply reads $P_p = nk_B T_p$, where the local density n is unchanged by the collision process, since only elastic collisions are being considered.

The source terms for the 14-moment equations are then obtained as averages over this collision term (see Chapter 2). After having defined the vector of generating functions $\Psi = m(1, v_i, v_i v_j, v_i v^2, v^4)$, composed by 14 entries, the collisional sources are obtained as

$$G_c^{\mathcal{M}} = -\langle \Psi \nu (f - \mathcal{M}) \rangle = -\nu [\langle \Psi f \rangle - \langle \Psi \mathcal{M} \rangle] . \quad (7.8)$$

In other words, the source terms for the 14-moment equations are the difference between the moments themselves (the term $\langle \Psi f \rangle$) and their value for a non-drifted Maxwellian at temperature T_p , weighted by the collision frequency ν . From symmetry considerations, all odd-order central moments of the Maxwellian are zero, and the source terms are easily evaluated by considering that

- All odd-order moments $(u_i, q_i, Q_{ijk}, S_{ijjk})$ relax to zero;
- Even-order moments relax to their Maxwellian value ($P_{ij} \rightarrow P\delta_{ij}$, $R_{iijj} \rightarrow 15P^2/\rho$).

This is easily verified by a direct calculation from Eq. (7.8), and ultimately gives

$$\mathbf{G}_c^{\mathcal{M}} = \left(\frac{\delta \mathbf{U}}{\delta t} \right)_c = -\nu \begin{pmatrix} 0 \\ U_2 \\ U_3 \\ U_4 \\ (U_5 - P_p) \\ U_6 \\ U_7 \\ (U_8 - P_p) \\ U_9 \\ (U_{10} - P_p) \\ U_{11} \\ U_{12} \\ U_{13} \\ (U_{14} - 15P_p^2/\rho) \end{pmatrix}. \quad (7.9)$$

7.3.2 Collision model for large mass disparity

In the previous section, the post-collision distribution was assumed to be Maxwellian. Such assumption is not physically justified for electron-neutral collisions, and was only based on simplicity. Indeed, during a single electron-neutral collision, not only energy is (to a first approximation) conserved at the population level, but also the energy of the single electron is conserved. Therefore, the distribution that characterizes the post-collision state is not a Maxwellian, but rather a distribution that has the very same energy content as the initial distribution f . Therefore, when plotted in the energy variable,

we have

$$f_p(\varepsilon) = f(\varepsilon) \implies f_p(v^2) = f(v^2). \quad (7.10)$$

For simplicity, we further assume that collisions are isotropic, and therefore f_p is symmetric, and we denote it by f_p^{iso} for clarity. As before, the source terms are obtained from

$$\mathbf{G}_c^{\text{iso}} = -\langle \Psi \nu (f - f_p^{\text{iso}}) \rangle = -\nu [\langle \Psi f \rangle - \langle \Psi f_p^{\text{iso}} \rangle]. \quad (7.11)$$

For the sake of obtaining the source terms, an explicit knowledge of the shape of f_p^{iso} is not necessary, and the following considerations are sufficient:

- Since f_p^{iso} is isotropic, its odd-order central moments are zero;
- The average velocity of f_p^{iso} is also zero, as we consider isotropic scattering around a fixed target heavy particle;
- The temperature of f_p^{iso} is also obtained from Eq. (7.7).

Some more considerations are required regarding the order-4 moment, $U_{14} = \langle mv^4 \rangle$. Intuitively, one can realize that, since the electron energy is conserved in each collision, its square will also be conserved. Therefore, the moment $\langle mv^4 \rangle$ will be a conserved quantity, being the average of individually conserved quantities. This is easily shown at a formal level by writing the definition of the order-4 moment in spherical coordinates, for the post-collision isotropic distribution:

$$\langle mv^4 \rangle_p^{\text{iso}} = \int mv^4 f_p^{\text{iso}}(v^2) v^2 \sin \theta \, dv \, d\psi \, d\theta, \quad (7.12)$$

where the dependence on the velocity modulus is highlighted in the distribution function by writing v^2 . From Eq. (7.10), since $f_p^{\text{iso}}(v^2) = f(v^2)$, we simply obtain that

$$U_{14,p} = \langle mv^4 \rangle_p^{\text{iso}} = \langle mv^4 \rangle = U_{14}. \quad (7.13)$$

Therefore, energy preserving collisions do make the distribution isotropic, but have no effect on the contracted order-4 moment, and the energy spectrum of the VDF is preserved. Ultimately, the collisional sources from this model are equal to the previous Maxwellian-relaxation sources, differing only in the 14-th element:

$$\mathbf{G}_c^{\text{iso}}(1, \dots, 13) = \mathbf{G}_c^{\mathcal{M}}(1, \dots, 13) \quad \text{and} \quad \mathbf{G}_c^{\text{iso}}(14) = 0. \quad (7.14)$$

7.3.3 Elastic collisions with energy loss

In the previous sections, the energy exchanged by electrons via collisions with neutrals was neglected in view of the large mass disparity. We discuss here how to include such effect.

Eq. (7.6) gives the energy transferred from a given electron to a target neutral, $\Delta\varepsilon/\varepsilon = 2m/M(1 - \cos \chi)$, as a function of the deflection angle χ and the mass ratio. In general, the deflection angle is a function of the impact parameter b and of the collision energy, through the differential cross section. We assume isotropic scattering for simplicity, hence, the deflection angle only depends on the impact parameter b . In the assumption that the position of the electron and the location of the target neutral are uncorrelated, the impact parameter b is linearly distributed (fewer electrons have a head-on collision, and more electrons experience a grazing collision). From this observation, we can obtain the distribution of angles χ , that is sinusoidal. The average deflection angle is $\pi/2$, and by definition $\chi \in [0, \pi]$. The quantity $(1 - \cos \chi)$, appearing in the expression for the energy loss, can be seen to be uniformly distributed (see [212]) over the interval $[0, 2]$, and averages to 1. Therefore, given all possible impact parameters, and consequent deflection angles χ , the electron in average loses an amount of energy $\langle \Delta\varepsilon/\varepsilon \rangle_\chi = 2m/M$.

Let us now consider the whole population of electrons. In the previous case, in the limit of an infinitely large mass disparity, the total energy of the electron population was conserved. In the present case, the post-collision energy should be investigated by averaging the energy loss over the electron energy distribution function. An accurate analysis would also consider that more energetic electrons collide more frequently than slow-moving ones. However, such effects are neglected in a BGK-like approach, and we thus limit ourselves to the following observation: if the energy lost by an electron, whatever the deflection angle, is $2m/M$ times the initial energy, then the post-collision energy of the whole population shall be reduced by the same factor. Therefore, we modify Eq. (7.7) into

$$\frac{3}{2}k_B T_p = \left(\frac{3}{2}k_B T + \frac{1}{2}m_e u^2 \right) \left(1 - \frac{2m}{M} \right). \quad (7.15)$$

Notice that the post-collision distribution is still symmetric, due to isotropic scattering, and its odd-order central moments and the average velocity are still zero. The pressure tensor relaxes to $P_{ij} = nk_B T_p \delta_{ij}$, as for the previous cases, with T_p from Eq. (7.15). This completely extends the Maxwellian model of Section 7.3.1 to include energy losses.

Regarding the general isotropic-collision model of Section 7.3.2, the fourth-order moment still needs to be investigated. We recall that the order-4 moment is defined as $\langle mv^4 \rangle$, that is proportional to the average of the squared particle energies.¹ By squaring Eq. (7.6), one can obtain the post-collision quantity $(mv'^2)^2$ of an electron i deflected by the angle χ ,

$$\begin{aligned} m^2 v_i'^4 &= m^2 v_i^4 \left(1 - \frac{2m}{M} (1 - \cos \chi) \right)^2 \\ &= m^2 v_i^4 \left(1 + \frac{4m^2}{M^2} (1 - \cos \chi)^2 - \frac{4m}{M} (1 - \cos \chi) \right). \end{aligned} \quad (7.16)$$

This eventually allows us to estimate the post-collision value for the order-4 moment. At first, we shall average this term over all possible deflection angles. Following the previous discussion, by considering that the impact parameter is linearly distributed, the quantity $(1 - \cos \chi)$ is found to be uniformly distributed for isotropic collisions. The probability distribution of $(1 - \cos \chi)^2$ is thus also known, and can be seen to have an average value of $4/3$ (see [214]). Therefore, averaging Eq. (7.16) over χ , one ultimately finds the (average over the possible deflection angles) post-collision velocity as

$$v_i'^4 = v_i^4 \left(1 + \frac{16}{3} \frac{m^2}{M^2} - \frac{4m}{M} \right). \quad (7.17)$$

Notice that the quantity inside the parenthesis is smaller than 1, such that $v_i'^4 < v_i^4$. As done for the post-collision temperature, we write the post-collision order-4 moment as the pre-collision moment reduced by the quantity appearing in the parenthesis:

$$\langle mv^4 \rangle_p^{\text{iso}} = \left(1 + \frac{16}{3} \frac{m^2}{M^2} - \frac{4m}{M} \right) \langle mv^4 \rangle. \quad (7.18)$$

With this definition, the isotropic-collision model is also completely defined. In particular, the isotropic-collision source terms are thus equal to their Maxwellian counterpart for moments 1 to 13, and differ only for the last moment:

$$\mathbf{G}_c^{\text{iso}}(14) = \nu U_{14} \left(\frac{16}{3} \frac{m^2}{M^2} - \frac{4m}{M} \right). \quad (7.19)$$

This term is in general small (being proportional to m/M) and negative, slowly reducing the R_{ijjj} moment in time. For $t \rightarrow \infty$, if no energy is externally supplied to the system, this collision operator would result in a pro-

¹Except for a multiplying coefficient proportional to the mass.

gressive cooling down of electrons. For this reason, this model is not suitable for reproducing standard gas dynamic situations, but is instead targeted towards conditions of sustained temperature non-equilibrium. More comprehensive models that retrieve a common equilibrium temperature, equal among all species, could be developed [83, 215].

7.3.4 Excitation and ionization reactions

The developed models could be extended towards inelastic collisions such as excitation and ionization processes. First, obviously, the collision frequency ν is to be taken relative to the considered process. For electron-neutral excitation collisions, the source terms will be in the very same form as for the elastic case, the only difference being that the post-collision temperature must be reduced by the excitation energy (as also discussed in [44]),

$$\frac{3}{2}k_B T_p^{\text{exc}} = \frac{3}{2}k_B T + \frac{1}{2}m_e u^2 - \varepsilon_{\text{exc}}. \quad (7.20)$$

A separate term should be introduced for each considered excitation process, or multiple processes could be lumped in a single term, properly averaging the excitation energies, and summing up the collision frequencies.

In case of ionizing collisions, one should first include a factor *two* in the number density of the post-collision distribution, since each electron produces an additional electron. Then, besides subtracting the ionization energy from the initial energy, one must also divide the residual energy between the two electrons,

$$\frac{3}{2}k_B T_p^{\text{iz}} = \frac{1}{2} \left(\frac{3}{2}k_B T + \frac{1}{2}m_e u^2 - \varepsilon_{\text{iz}} \right). \quad (7.21)$$

Note that the division by a factor of two (rather than the subtraction of the ionization energy) is the main cause of cooling, and is the reason why ionization (rather than excitation) often plays the major role in the energy balance of a low-temperature plasma.

7.3.5 Collision frequency and non-equilibrium

As to complete the BGK model, we shall discuss the choice of a collision frequency. From its definition, the frequency at which one electron (indexed as “*i*”) of velocity \mathbf{v} collides with a population of neutrals is obtained as an integral over the distribution of relative velocities, $g_r(v_r)$,

$$\nu(v) = n_n \iiint_{-\infty}^{+\infty} \sigma(v_r) v_r g_r(\mathbf{v}_r) d\mathbf{v}_r. \quad (7.22)$$

In the present case, electrons are much faster than neutrals, and the relative velocity thus coincides with the electron velocity. Therefore, $\mathbf{v}_n \approx 0 \implies \mathbf{v}_r \equiv \mathbf{v}$, and $g_r(\mathbf{v}_r) \equiv \delta(|\mathbf{v}_r - \mathbf{v}|)$. The collision frequency of a given individual electron thus simplifies to the well-known expression

$$\nu(v) = n_n \sigma(v) v , \quad (7.23)$$

that is a velocity-dependent collision frequency. Given a population of electrons, a single “averaged” collision frequency can be obtained by averaging over the whole electron population:

$$\nu = \frac{1}{n_e} \iiint \nu(v) f_e(\mathbf{v}) d\mathbf{v} = \frac{n_n}{n_e} \iiint \sigma(v) v f_e(\mathbf{v}) d\mathbf{v} . \quad (7.24)$$

The detailed shape of the electron VDF (or better, the electron EDF) is therefore expected to play an important role, especially for non-uniform cross-sections. A precise calculation of this term under whatever non-equilibrium conditions would require the knowledge of f_e , but this knowledge is not available for the 14-moment system, and would require to solve the entropy-maximisation problem at each time step. Some approximation is thus required.

We consider here only the simplistic case of a uniform cross section, $\sigma(v) \equiv \bar{\sigma}$. In such case, the population-averaged collision frequency becomes

$$\nu = n_n \bar{\sigma} \left[\frac{1}{n_e} \iiint |v| f_e(\mathbf{v}) d\mathbf{v} \right] = n_n \langle |v| \rangle \bar{\sigma} , \quad (7.25)$$

where the average velocity magnitude $\langle |v| \rangle$ appears. For a Maxwellian distribution with zero drift velocity, this term will be proportional to the thermal velocity v^{th} . In the general case, this term will be influenced by the non-equilibrium shape of f_e and by the drift velocity. Considering only the thermal velocity would miss the latter effects. By neglecting non-equilibrium for the time being, the effect of the drift velocity can be embedded by approximating $\langle |v| \rangle$ by using the total energy (in place of the thermal energy):

$$\langle |v| \rangle \approx \sqrt{\frac{8k_B T^{\text{tot}}}{\pi m}} \quad \text{with} \quad T^{\text{tot}} = \frac{2n\varepsilon^{\text{tot}}}{3k_B} \quad \text{and} \quad \varepsilon^{\text{tot}} = \frac{u_e^2}{2} + \frac{3}{2} \frac{k_B T}{m_e} , \quad (7.26)$$

with n the electron number density, and the collision frequency is approximated as

$$\nu = n_n \bar{\sigma} \sqrt{\frac{16\varepsilon^{\text{tot}}}{3\pi}} . \quad (7.27)$$

7.4. Application: homogeneous relaxation towards non-equilibrium

Fig. 7.6 shows this approximation to the collision frequency against a direct integration of the fully non-equilibrium VDF, for some conditions of Section 7.2. Different values of the electric field are considered, which directly maps to different drift velocities. For comparison, the simple un-drifted Maxwellian approximation $\nu \approx n_n \bar{\sigma} v^{\text{th}}$ is also shown, with $v^{\text{th}} = \sqrt{8k_B T_e / (\pi m_e)}$. It can be seen that including the drift velocity using Eq. (7.27) allows us to retrieve the full non-equilibrium case almost exactly, while the thermal-only collision frequency includes a substantial error. This is expected, as for the considered conditions, the drift and the thermal velocities are indeed comparable, and one cannot simply neglect one of the two.

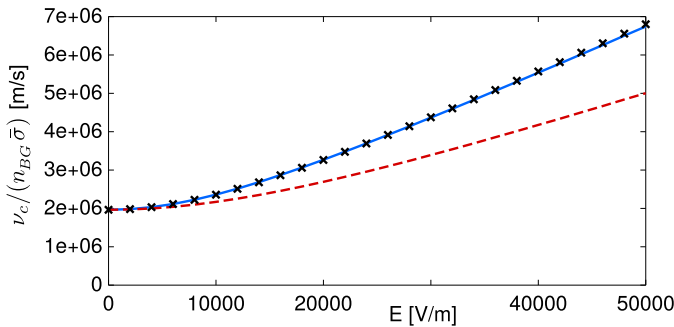


Figure 7.6: Collision frequency for a constant cross-section, for the cases of Section 7.2, at different values of the electric field. $B = 0.01$ T, $T_b = 100\,000$ K and $\beta = 0$. Blue solid line: numerical computation from non-equilibrium VDF. Dashed line: un-drifted Maxwellian approximation ($\nu = n_n \bar{\sigma} v^{\text{th}}$). Black symbols: approximation from Eq. (7.27).

It should be stressed that the analysis of this section has been obtained in the assumptions of a constant cross-section. This assumption is hardly realistic even for elastic collisions, if Ramsauer gases are considered. Therefore, further analysis on this topic is suggested as a future activity. Nonetheless, the simple example considered here clearly remarks the crucial importance of considering the drift velocity inside the collision frequency (and therefore inside chemical rates as well).

7.4 Application: homogeneous relaxation towards non-equilibrium

In this section, the 14-moment system together with the developed collision terms is applied to the study of a space-homogeneous (zero-dimensional) relaxation of electrons in a bath of cold and slow neutrals. This case extends the steady state analysis of Section 7.3 and embeds the collision terms de-

veloped in the previous section. The results of this section are propaedeutic to 1-dimensional applications, that will be considered in the next section.

Electrons are initialized from a drifted Gaussian distribution (anisotropic Maxwellian),

$$\begin{cases} f_{e,0} = A \exp \left[-\frac{m}{2k_B} \left(\frac{v_x^2}{T_{0x}} + \frac{(v_y - u_{0y})^2}{T_{0y}} + \frac{v_z^2}{T_{0z}} \right) \right], \\ A = n_0 \left(\frac{m}{2\pi k_B} \right)^{3/2} \left(\frac{1}{T_{0x} T_{0y} T_{0z}} \right)^{1/2}, \end{cases} \quad (7.28)$$

with initial density $n_0 = 10^{17}$ m⁻³, initial velocity $u_{0y} = 30\,000$ m/s and temperatures $T_{0x} = 10\,000$, $T_{0y} = 20\,000$ and $T_{0z} = 5\,000$ K. Electric and magnetic field are enabled at time $t = 0$ s and have a constant value of $\mathbf{E} = 20\,000 \hat{z}$ V/m and $\mathbf{B} = 0.02 \hat{x}$ T. Electric quantities are chosen to be somehow representative of Hall thrusters, and thermodynamic quantities are initialized as to present some degree of anisotropy, in order to stress the model. On a physical standpoint, this problem is characterized by at least three time scales:

1. At the time scales of the cyclotron frequency, electrons spiral along magnetic field lines. This will be associated to oscillations in the moments, as the initial anisotropy is transferred between the directions perpendicular to the magnetic field;
2. At the collision frequency, the VDF tends to relax toward a somehow isotropic distribution and the electron average velocity adapts to the velocity of the neutral background (zero in this case);
3. At a time scale that depends on both the collision frequency and the mass ratio, the temperature of electrons tends to equilibrate with the background temperature.

Notice that a number of other scales are typically present in low-temperature plasmas. The plasma oscillations for example have not been accounted for (since the electric field is being imposed), as well as all time scales associated to inelastic collision processes. Given the large mass disparity, the energy relaxation time scale (the third one in the list) happens to be almost decoupled from the first two. Moreover, if the ultimate equilibrium temperature is required, including ionization and excitation reactions become necessary. Neglecting them would result in an unphysically large heating due to the lack of energy absorption mechanisms.

In this section, we consider a simpler toy model: the collision operator is approximated by the BGK-like model of Section 7.3, and the post-collision

7.4. Application: homogeneous relaxation towards non-equilibrium

temperature is not taken from the electron energy during the simulation, but is instead imposed to the value $T_p = 10\,000$ K. The collision frequency is also imposed, equal to a fraction of the cyclotron frequency, such that $\beta = \nu/\omega_c = 0.3$. These two assumptions are a strong simplification, but allow us to get rid of the longer time scale associated to energy relaxation. Using the simple Maxwellian relaxation model, the kinetic equation reads

$$\frac{\partial f}{\partial t} + \frac{qE}{m} \frac{\partial f}{\partial v_z} + \frac{qB}{m} \left[v_z \frac{\partial f}{\partial v_y} - v_y \frac{\partial f}{\partial v_z} \right] = -\beta \omega_c [f - \mathcal{M}(T_p)]. \quad (7.29)$$

This problem is solved using a PIC method, to obtain a reference kinetic solution. The time step for such simulation was taken as $\Delta t = 1/(100\nu)$ and 10^7 particles were simulated. BGK collisions are implemented in a simple stochastic way: for every simulated particle, the collision probability is computed as $P_c = 1 - \exp(-\nu \Delta t)$; a random number \mathcal{R} is computed at every time step for each particle, and if $\mathcal{R} < P_c$, a collision is performed by resetting the particle velocities to random values sampled from a Maxwellian at T_p . Note that the same procedure could be followed for implementing the isotropic BGK-like collision operator of Section 7.3.2, the only difference being that in place of sampling the new velocity from a Maxwellian, one should rotate randomly the velocity vector without changing its magnitude. With the considered time step and number of particles, the kinetic solution requires a few hours on a 32 cores machine. As expected, an analysis of the VDF shows a complete overlap to the analytical VDFs of Shagayda [44], once steady state is reached.

The solution of the 14-moment system is then computed by solving the set of Eqs. (7.4) with source terms from Eq. (7.9), using the same initial conditions. Being zero-dimensional, the 14-moment system reduces to a system of ODEs, and is conveniently integrated using an adaptive Runge-Kutta algorithm for instance. The computation takes only a few seconds of wall time.

A comparison of the two methods is shown in Fig. 7.7. The left column shows some of the moments that are present in the state vector of the 14-moment closure. After an initial oscillation at the time scale of the cyclotron frequency, the solution appears to settle to an equilibrium after a comparable (actually, slightly longer) time has passed. This was expected, given the choice of $\beta = 0.3$. Also, the average velocity component u_z (parallel to the electric field) is seen to settle on the value given by the classical mobility of Eq. (7.3), $u_z \approx 2.7 \times 10^5$ m/s. The u_y velocity (in the $\mathbf{E} \times \mathbf{B}$ direction) is essentially equal to the value $E/B = 10^6$ m/s.

It is important to notice that, since the problem is zero-dimensional,

no space fluxes are present, and the solution is totally independent from closing fluxes. Therefore, for zero-dimensional problems, the 14-moment solution is exact. This is indeed seen in Fig. 7.7-Left, where all moments match the kinetic solution to numerical precision.

Anyway, the closing moments have also been calculated alongside the relaxation, for the sake of a comparison with the kinetic scheme. Closing moments are obtained using the iterative solution to the entropy-maximisation problem. The interpolative closure of McDonald & Torrilhon [67] resulted in analogous closing moments. These moments are shown in Fig. 7.7-Right. Closing moments from the maximum-entropy approximation appear to reproduce very closely the kinetic moments, and some discrepancies are observed mainly for the heat flux tensor Q_{ijk} terms. This could result from the fact that both R_{ijkk} and S_{ijjk} contain some contractions over the velocity components, that could mitigate some error. However, it is important to remark that an analysis of the closing moments in dimensionless form (superscript $*$) shows that R_{ijkk}^* and S_{ijjk}^* roughly have the same importance, while the Q_{ijk}^* terms are about 10 times smaller (and thus less important). The test case thus confirms the quality of the 14-moment description, for the conditions considered here.

7.5 Application: a one-dimensional test case

As a final application for the 14-moment system, we consider a 1D simulation of electrons flowing along a longitudinal electric field and through a perpendicular magnetic field. An electron-emitting cathode at a potential $\phi_c = 0$ V is located at the right extreme of the domain, and the left boundary is assumed to be an anode at $\phi_a = 300$ V. The distance between anode and cathode is $L = 0.1$ m and such axis is denoted by x . Axes y and z are not simulated, and we thus assume symmetry in such directions. Still, the of having a non-zero velocity in such directions (driven by the magnetic field) is retained, as the equations for the respective quantities are solved anyway.

The electron density is assumed small enough as to give negligible space-charge effects. The potential distribution is therefore linear, and the electric field is constant. In particular, in the simulations we do not solve the Poisson equation, but instead impose an electric field $E = (\phi_a - \phi_c)/L = 3000$ V/m along x . This quantity is lower than the typical values found in Hall thrusters by roughly a factor 10. This comes from having neglected space-charge, that cumulate due to the magnetic confinement. As to restore a partial similarity with Hall thrusters, the amplitude of the imposed

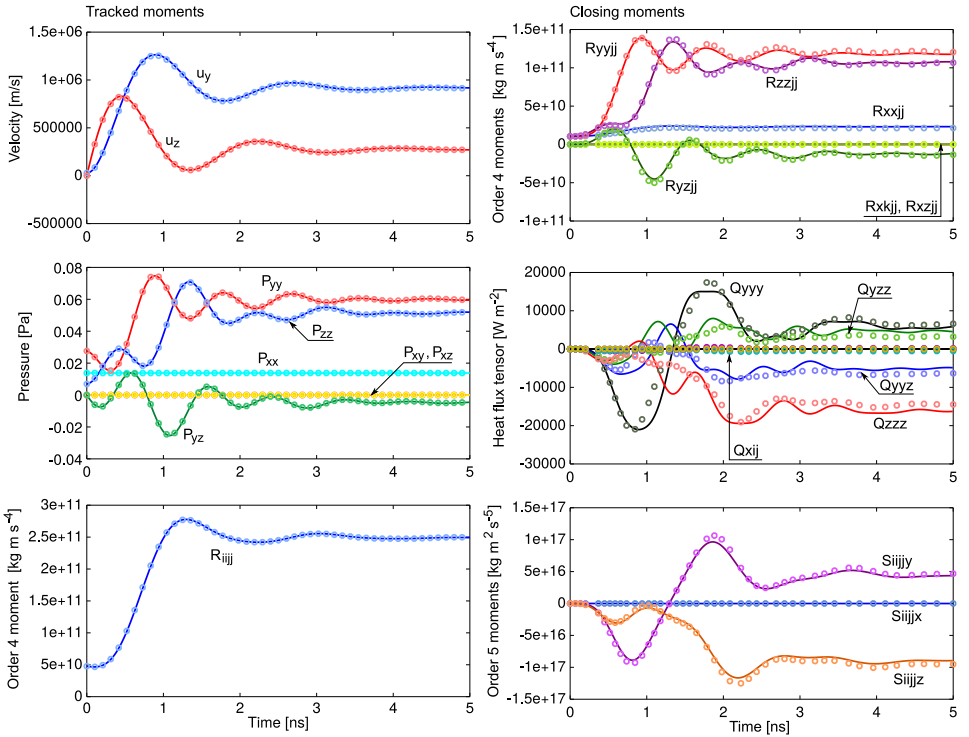


Figure 7.7: Homogeneous relaxation to a fixed temperature. Symbols: kinetic particle-based solution. Lines: 14-moment maximum-entropy system with iterative closure. Left column: some of the tracked moments, reproduced exactly. Right column: closing moments. The label Q_{xij} refers to all entries in the heat flux tensor that include the x -velocity component.

magnetic field is therefore also down-scaled by a factor 10, to a value of $0.001 \text{ T} = 10 \text{ Gs}$. This allows to retrieve a reasonable drift velocity of $u_d = E/B = 3 \times 10^6 \text{ m/s}$. The magnetic field profile follows a Gaussian, centered in the middle of the domain ($x = 0.05 \text{ m}$), with a width of 0.01 m ,

$$\mathbf{B} = 0.001 \exp \left[-(x - 0.05)^2 / 0.01^2 \right] \hat{z}. \quad (7.30)$$

The case is completely collisionless, and no chemical production terms are considered. Electrons are injected from the right boundary, from a Maxwellian distribution with a number density $n_0 = 10^{10} \text{ m}^{-3}$, temperature $T_0 = 5500 \text{ K} \approx 0.5 \text{ eV}$ and with an average velocity $u_{0x} = -5 \times 10^6 \text{ m/s}$, entering the domain. Considering that the resulting thermal velocity is $v^{\text{th}} \approx 4 \times 10^5 \text{ m/s}$, the electron injection is supersonic, and the corresponding electron current is $J_e \approx 8 \text{ mA/m}^2$. Notice that reproducing the current of an actual thruster is not required, since the electric and

magnetic fields are here imposed.

Numerical solution

This problem is solved by (i) a kinetic PIC scheme, (ii) the 14-moment maximum-entropy and (iii) the Euler systems. In the kinetic simulation, all particles crossing both the left and right boundaries are removed from the domain, and particles are injected from the right boundary by sampling a drifted Maxwellian. To reproduce the same conditions in the fluid simulation, the state in the left ghost cell consists in a low density of $n^L = 10^5 \text{ m}^{-3}$, and negative velocity of $u_x^L = -5 \times 10^7 \text{ m/s}$, as to induce a supersonic flux towards the left. The remaining conditions are $u_y^L = u_z^L = 0 \text{ m/s}$ and equilibrium conditions at a temperature $T^L = 5500 \text{ K}$, $P_{ij}^L = P\delta_{ij}$, $q_i^L = 0$, and $R_{iijj}^L = 15P^2/\rho$. The conditions in the right ghost cells are at equilibrium, with the aforementioned values for the cathode injection. For the initial condition, an empty domain is used for the kinetic simulation. In the fluid simulations, a small density $n_0 = 10^5 \text{ m}^{-3}$ is employed, with a zero average velocity $u_{x0} = u_{y0} = 0 \text{ m/s}$ and $T_0 = 5500 \text{ K}$.

A Boris time integration scheme is used in the particle simulations. The fluid systems are solved using a second order Midpoint Euler explicit time integration scheme, marching until convergence. A space discretization of 1000 cells is employed, with Rusanov fluxes and second order space accuracy is achieved with van Leer's MUSCL scheme, with symmetric van Albada limiter.

The computational cost of the Euler simulation was approximately 2 minutes on a single-core machine, while the 14-moment approximation required roughly 10 minutes. The kinetic solution on the other hand required around 1 hour on a 16-cores machine, as to converge the simulation and reduce the statistical error to an acceptable value.

Results

The results of the numerical simulations are shown in Fig.7.8.

Once injected from the cathode with initial velocity $u_{x0} = 5 \times 10^6 \text{ m/s}$, electrons are accelerated by the electric field towards the anode, at $x = 0 \text{ m}$. The magnetic field acts as a barrier and converts part of the momentum into the y direction, generating a drift velocity $u_y \approx 3 \times 10^6 \text{ m/s}$, as mentioned previously. After the electrons have passed the magnetic field region, there is no mechanism to restore the value of u_y , that therefore remains constant. The density profile is affected by the magnetic field, that concentrate some

electrons at the middle of the domain. A stronger magnetic field would result in a stronger confinement and would cause a bump around $x = 0.05$ m.

If compared to the kinetic solution, the Euler system appears to reproduce to an excellent accuracy the density and average velocity, and, as expected, the 14-moment system further reproduces accurately the temperature anisotropy and the order-4 moment.

Finally, we note that the heat flux is reproduced only qualitatively by the 14-moment method. This may be puzzling, also in view of the previous results for ions, where the heat flux was well reproduced for apparently similar configurations (Sections 6.2 and 6.3). Further electrons simulations without any magnetic field give an analogous error in the heat flux. Therefore, the magnetic field is not the cause of such inaccuracy. Instead, one should consider the following points.

First, a comparison with the ions case is not entirely correct. Indeed, in the ion test cases, a chemical source was introduced with the form $S_{iz} = S_0 \delta(v)$. This term causes a creation of particles along the line $v = 0$, in phase space, and resulted in a VDF with a heavy low-velocity tail, thus showing strong asymmetry. In the present case on the other hand, no chemical source is being considered. Electrons are only injected at the cathode, from a Maxwellian distribution, and keep roughly the same distribution, as the axial electric field mostly has the effect of shifting the average velocity, and a limited distortion is introduced [216]. Also, the absence of electron-neutral collisions is such that the asymmetric VDFs of Section 7.2 do not arise in this case. From these considerations, one could expect the heat flux to be small for the considered problem. A computation of the dimensionless moments confirms that this is indeed the case, as can be seen by analyzing the magnitudes of q_i^* in Fig. 7.9. Therefore, in the considered case, the 14-moment method appears inaccurate for the heat flux, but such moment is anyway rather small and does not matter for the present solution.

7.6 Conclusions

This chapter was devoted to the application of the maximum-entropy method to the modeling of non-equilibrium electrons in $\mathbf{E} \times \mathbf{B}$ configurations. First, the method was shown to reproduce some analytical EDFs very accurately, while the VDFs were reproduced slightly less precisely, but still showing all the major features of anisotropy, asymmetry and excess of kurtosis.

While electromagnetic source terms had been previously developed in Chapter 4, in this Chapter we specified the source terms for electron collisions with a background of cold and slow-moving neutrals. Two models

Chapter 7. Maximum-entropy modeling of electrons

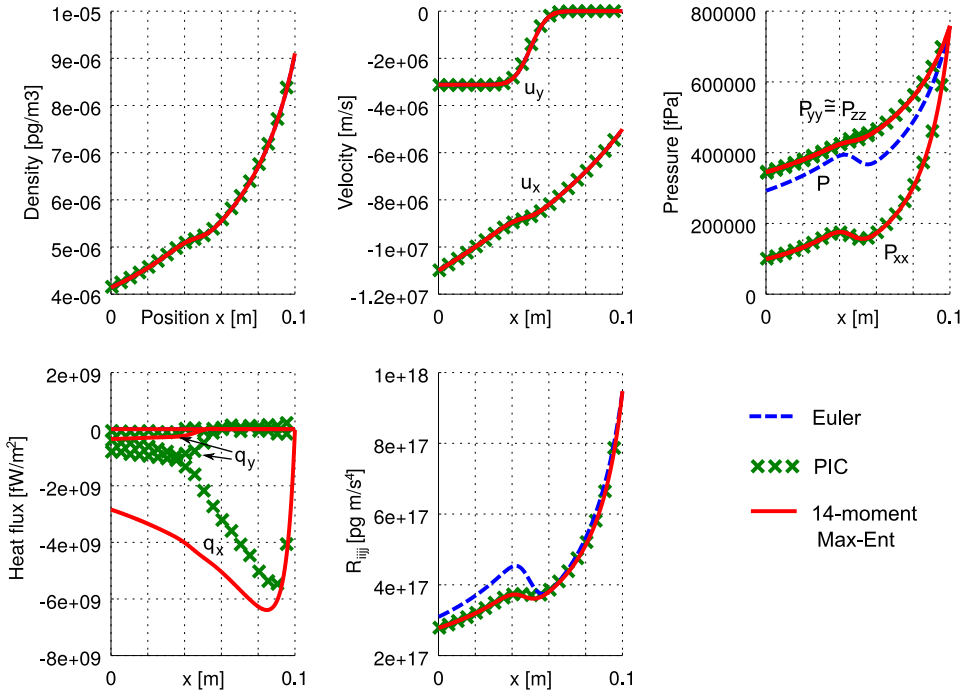


Figure 7.8: One-dimensional acceleration of electrons through a magnetic field barrier.

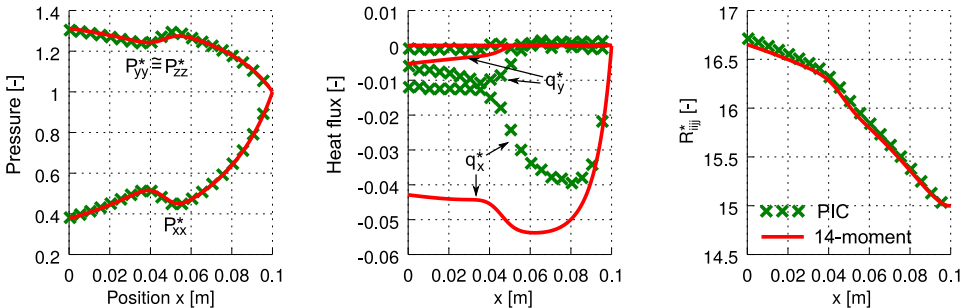


Figure 7.9: One-dimensional acceleration of electrons through a magnetic field barrier; dimensionless moments.

were proposed, one based on a simple Maxwellian relaxation, and a second model where the only assumption on the post-collision VDF is isotropy.

These developments allowed us to tackle first a space homogeneous time relaxation test case, and then a 1-dimensional simulation. This latter case mimics the electron dynamics in a Hall thruster channel, in strongly simplified conditions, where the electrons are injected at the cathode and are accelerated by an axial electric field, but whose mobility is reduced by a

perpendicular magnetic field.

With this chapter, we conclude the part of this work related to maximum-entropy modeling. Among the future developments, together with attempting a coupling with ions (and thus solving the full self-consistent problem), it will be necessary to develop chemical source terms for electron-neutral collisions, that take into account non-equilibrium conditions without requiring to solve the entropy-maximisation problem at each time step.

CHAPTER 8

DSMC and TPMC analysis of the neutral gas injection: an alternative gas feed configuration

The content of this chapter is also discussed in [217]: Boccelli, S., Magin, T.E., Frezzotti, A., *Numerical investigation of reversed gas feed configurations for Hall thrusters*, under review.

In the previous chapters, we have investigated the non-equilibrium regime that characterizes ions and electrons. So far, neutrals were always treated as a fixed background of cold and slow-moving particles.

In this chapter, we shift the attention on the neutral population, and investigate their dynamics from the injection to their expansion into the vacuum. The rarefaction degree will be seen to be high enough to require a kinetic modeling, as the Knudsen numbers approach unity. No fluid modeling will be attempted in this chapter, but we will focus instead on the discussion of the effect of different injection configurations. The typical injection strategy consists in placing the gas feed at the anode, located at the closed end of the thruster channel. This setup will be here analyzed numerically, and an alternative feed configuration will then be proposed, where

the propellant is injected backwards from a slit located near the exit plane. As will be discussed, different injection configurations are likely to result in quite different thruster efficiencies. In particular, the ionization efficiency can be estimated from the distribution of (and the average) residence times of neutral particles, inside the ionization region. The proposed reversed injection strategy causes an increased residence time, and this ultimately affects the thruster mass utilization efficiency.

This chapter is structured as follows. After some preliminary considerations about the degree of rarefaction and the mass utilization efficiency, drawn in Section 8.1, a simplified analysis is proposed in Section 8.2, where the ionization probabilities and an estimate of the thruster efficiency are considered for a simplistic case that neglects all gas-phase collisions, and employs a specular wall scattering kernel. All simplifying assumptions are then relaxed in Section 8.3, where DSMC simulations are performed for the SPT-100 thruster geometry, including gas-phase collisions and assuming diffusive wall interactions. A test-particle Monte Carlo algorithm is then introduced in Section 8.4, and is employed in Section 8.5 to obtain the distribution of residence times of neutral particles inside the thruster channel and inside a region that we arbitrarily identify as the ionization region. From such results, the efficiency of the reversed injection is analyzed and compared to the direct injection strategy in Section 8.5.3, and maps of the improved efficiency are given.

Only neutrals are considered in this chapter, and the interaction with electrons and ions is completely disregarded, apart from an increased temperature of the anode: two cases are considered, a cold anode at 300 K and a warm anode at 1000 K.

8.1 Preliminary considerations

The neutral flow is characterized by rather large Knudsen numbers, $\text{Kn} = \lambda/L_{tc}$, where λ is the mean free path and L_{tc} is a characteristic dimension of the thruster channel, such as its width or length. The propellant flow may be initially transitional at the injection point, but soon increases to $\text{Kn} \approx 1$ during the expansion into the channel, and eventually reaches the free molecular regime $\text{Kn} \gg 1$ in the plume. In this work, we will consider the SPT-100 geometry [89], where “100” stands for the diameter of the outer wall in millimeters, and the inner diameter is 70 mm. As will be seen in the next sections, Kn roughly ranges between $\text{Kn} \approx 0.1 - 1$ for such configuration. The neutrals analysis should therefore be tackled with kinetic methods, such as the Direct Simulation Monte Carlo (DSMC) and

8.2. Direct and reversed injection: a simplified analysis

the test-particle Monte Carlo methods. Other methods such as radiosity methods could be employed for the higher rarefaction conditions [218], whenever low mass flow rates¹ or smaller thrusters such as the SPT-50 or SPT-20 are employed [219].

The neutral density and velocity profiles have strong influence on the performance of the thruster, in particular the mass utilization efficiency (also known as “propellant efficiency”) is defined as [220]

$$\eta_m = \dot{m}_i / \dot{m}_p, \quad (8.1)$$

with \dot{m}_i the mass flux of ions created inside the thruster and accelerated outwards, and \dot{m}_p the propellant mass flow rate. For maximising η_m , the residence time of neutrals inside the ionization region shall be maximised, as to ensure the highest ionization probability. In operating Hall thrusters, the quantity \dot{m}_p is composed by two contributions: most of the propellant is injected at the anode and is actually ionised inside the chamber; a small fraction of the propellant is used by the hollow cathode, and is effectively lost. In the present chapter, we neglect for simplicity this second contribution. This will be equivalent to considering a filament cathode in place of a hollow cathode, as frequently done in laboratory experiments [219].

The mass utilization efficiency varies widely with the operating conditions and the thruster size [221, 222], and ranges from below 0.5 for micro-thrusters, up to above 0.9 for the SPT-100. The gas feed configuration plays an important effect on η_m , and a number of designs have been investigated in the past, including the presence of injection ports along the channel [223, 224].

8.2 Direct and reversed injection: a simplified analysis

As a starting point, we consider the simplified problem depicted in Fig. 8.1 and assume

1. Monoenergetic injection of particles (no thermal velocity, $T \rightarrow 0$ K);
2. Free-molecular flow (no gas-phase collisions);
3. Specular reflection as a particle-wall interaction.

From the first assumption, all particles have the same axial velocity, that we denote by v_z . In free-molecular conditions and with specular reflection

¹In highly rarefied conditions, the Knudsen number is inversely proportional to the mass flow rate, since the latter directly influences the density in the chamber. As continuum Knudsen numbers are approached, this dependence mitigates and additional fluid dynamic effects emerge.

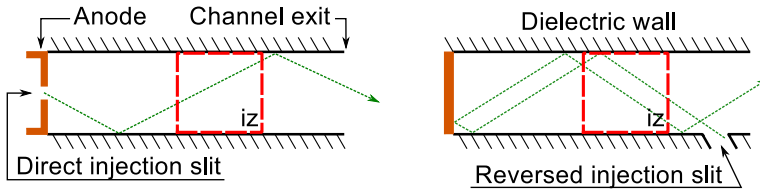


Figure 8.1: Trajectory of a particle with specular wall scattering in absence of gas-phase collisions. Left: direct injection from the anode. Right: Reversed injection. Label “iz” denotes the ionization region.

at the walls (no momentum/energy accommodation), a particle injected at the anode will spend inside the ionization region a time $\tau^{\text{dir}} = L_{\text{iz}}/v_z$, with L_{iz} the length of the ionization region. On the other hand, if the neutral was to be injected at the exit of the channel, backwards, the ionization region would be traversed twice, doubling the residence time: $\tau^{\text{rev}} = 2\tau^{\text{dir}}$. The probability that during the time τ a given neutral particle inside the ionization region will be ionized by collision with an energetic electron is

$$P_{\text{iz}} = 1 - \exp[-\nu_{\text{iz}}\tau], \quad (8.2)$$

where ν_{iz} is the ionization frequency, function of the local electron distribution function (mostly, function of their density, temperature and drift velocity, as discussed in Section 7.3.5). The value of ν_{iz} does not need to be specified further for the sake of this section, and it will be considered as an effective value over the ionization region. From this definition, we obtain a relation between the ionization probabilities in the direct and reversed injection cases,

$$P_{\text{iz}}^{\text{rev}} = 1 - (1 - P_{\text{iz}}^{\text{dir}})^{\tau^{\text{rev}}/\tau^{\text{dir}}}, \quad (8.3)$$

where in the simple case of Fig. 8.1, $\tau^{\text{rev}} = 2\tau^{\text{dir}}$ and thus $P_{\text{iz}}^{\text{rev}} \geq P_{\text{iz}}^{\text{dir}}$, with the largest improvement for small values of $P_{\text{iz}}^{\text{dir}}$. In other words, if a thruster has a small ionization efficiency, it will benefit the most from a reversed injection strategy. The next sections will be devoted to removing the aforementioned simplifying assumptions and to obtain estimates of the ionization probability for selected configurations, and ultimately to estimating the mass utilization efficiency.

8.3 DSMC simulations

A comprehensive estimation of the neutral dynamics in the chamber can be obtained by solving the Boltzmann equation with the Direct Simulation Monte Carlo (DSMC) method. The simplifying assumptions of the

previous section are removed: monoenergetic injection is substituted by injection from a Maxwellian distribution with a finite temperature, gas-phase collisions are enabled, and the simple specular reflection scattering kernel is replaced by more reasonable diffuse reflections (with accommodation coefficient of 1) with the effect of reducing the mobility along the channel.

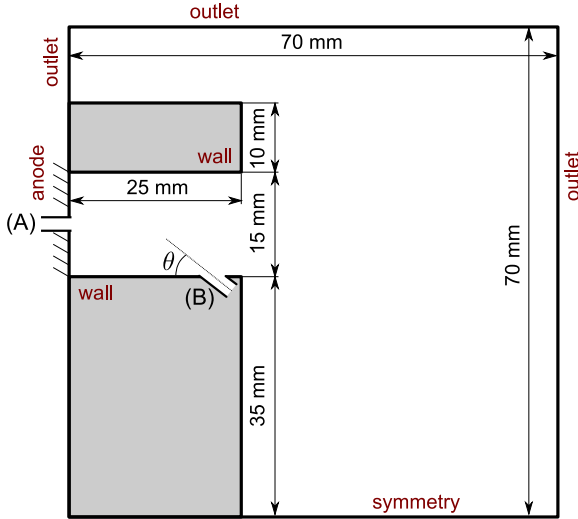


Figure 8.2: Domain and boundary conditions for the DSMC simulations of the neutrals injection.

The simulations shown in this section are obtained using the SPARTA DSMC software [225]. The simulated geometry is axisymmetric and consists in a slice of an SPT-100 thruster in the radial-axial plane ($R - z$), and is shown in Fig. 8.2. Xenon atoms are simulated, and the mass flow rate is fixed to 5 mg/s (see for example [88, 89]), equivalent to $\approx 50 \text{ sccm}^{\text{Xe}}$. Different injection configurations are simulated. A direct injection is tested by feeding the propellant either uniformly from the anode surface (case A1), or from a slit of 1 mm located on the anode at the channel centerline (case A2). Reversed injection is considered in the test cases labeled by “B”: the propellant is introduced in the chamber an angle θ with respect to the axial direction ($\theta = 90^\circ$ is a radial injection) from a slit located on the internal wall at position z_s . Cases B30_1, B60_1 and B90_1 consider angles of $\theta = 30^\circ, 60^\circ$ and 90° respectively, and the slit is located near the exit plane. Cases B30_2, B30_3 and B30_4 retain the angle $\theta = 30^\circ$ and investigate the effect of moving the slit inwards, towards the anode.

	$z_s = 22.5 \text{ mm}$	18.5	15.5	12.5
$\theta = 30^\circ$	B30_1	B30_2	B30_3	B30_4
$\theta = 60^\circ$	B60_1	-	-	-
$\theta = 90^\circ$	B90_1	-	-	-

Table 8.1: Test cases for the reversed injection configuration.

As previously mentioned, no electrons and ions will be accounted for, but only neutrals are simulated. However, it is crucial to consider a reasonable anode temperature, whose value affects the thruster efficiency [226, 227]. The anode temperature strongly depends on the operating conditions and may require some hours to reach a steady state [228, 229]. For these reasons, all simulations are repeated using two different anode temperatures of $T_a = 300 \text{ K}$ and $T_a = 1000 \text{ K}$. The walls temperature is kept at $T_w = 300 \text{ K}$ for simplicity.

The injection velocity, temperature and density are selected as follows. For the case A1 (uniform injection), the anode temperature is used, and injection happens uniformly from $R = 35 \text{ mm}$ to 50 mm , with a zero average velocity. The inlet flux is thus completely thermal, and the number density of the injection Maxwellian is selected as to result in the required mass flux of 5 mg/s . For the slit-injection cases, the choice is less trivial. Indeed, the boundary conditions to reproduce an orifice expansion should be carefully selected (see for example [230]) and ultimately depend on the structure of the gas feed. We consider here a slit size of 1 mm (both for case A2 and all B cases), and assume sonic injection for simplicity, at the anode temperature for case A2 and at the walls temperature for the B cases. The average velocity is thus 177.91 m/s for the 300 K temperature and 323.81 m/s for the 1000 K injection. The number density is chosen accordingly, as to give the required mass flux. The average velocity vector has an angle θ for the B cases.

A grid composed by 280×280 cells proved adequate to resolve the local mean free path, and the time step was set to $1 \mu\text{s}$ as to resolve the mean free time. At steady state, the simulation reaches roughly $150\,000$ simulated particles, ensuring sufficient resolution inside the channel and the first part of the plume. A VSS collision model is chosen, with parameters taken from [129]: a reference diameter $d_{\text{ref}} = 5.65 \times 10^{-10} \text{ m}$ at the reference temperature of $T_{\text{ref}} = 273.15 \text{ K}$, a viscosity index of $\omega = 0.85$ and scattering parameter $\alpha = 1.44$. Each simulation takes approximately 15 minutes on a laptop (Intel i5 processor, single core computation).

The resulting density and velocity fields are shown in Fig. 8.3, where the profiles at the channel centerline are shown in the Left and Center columns,

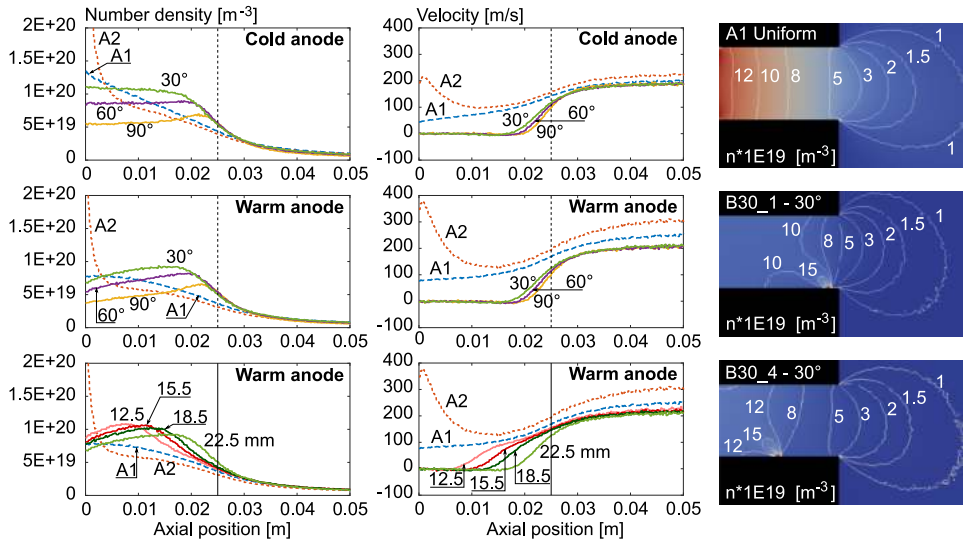


Figure 8.3: DSMC simulations. Left and Center: density and velocity at the channel centerline. A1, A2: direct injection. B: reversed injection. Right column: number density contours for cases A1, B30_1 and B30_4, cold anode.

and some 2D density fields are shown in the Right column. As one may expect, the anode temperature can be seen to decrease the density and increase the average velocity. The reversed injection also appears to have a strong impact on these moments, leveling the average velocity inside the chamber and lowering the average velocity to zero. In particular, the highest density is obtained with an injection angle of $\theta = 30^\circ$. The results showing a low (zero) average velocity suggest that the reversed injection could increase the residence time of neutrals in the ionization region, as desired. However, it should be considered that the average fields offer only a marginal picture of the problem, due to the strong rarefaction. A more in-depth analysis will be performed in Section 8.5.

From Fig. 8.3-Right, one can see that the $\theta = 30^\circ$ density contour shows an injection jet directed at an angle closer to 45° . This apparent inconsistency can be explained by considering that, at such rarefaction conditions, the velocity field is an average of (1) the population of injected particles (at an actual average angle of 30°) and (2) the particles that after having collided with the wall are now directed towards the exit. At collisions with an angle $\theta \rightarrow 0^\circ$, we may expect the latter effect to become particularly important, as roughly 50% of the particles would collide with the internal wall immediately after injection.

The effect of the slit position is shown in Fig. 8.3-Bottom. By shifting

the slit towards the anode, the density and velocity profiles approach the uniform injection case A1, as one may expect. Only the warm anode case is shown, as the results for the cold anode case are qualitatively analogous.

From the DSMC simulations, it is possible to gain an even deeper insight by analyzing directly the particle data, in place of only considering the averages. This gives the possibility to reconstruct the VDF at different locations and times, and beyond that, this would also allow us to reconstruct the history of *individual* simulated particles. From such data, it is possible to calculate how much time the particles spend inside the ionization region, and thus estimate the ionization probabilities. The simplest way to obtain this information is to embed a “timer” variable to the particle object, and update such timer whenever the particle resides in a requested region. However, these features are often not included in standard software and would require some ad-hoc modification. Instead, in the following section we shall employ a test-particle Monte Carlo algorithm for this purpose.

8.4 Test-particle Monte Carlo simulations: the method

As mentioned, the average fields shown in the previous section only provide a marginal view of the problem. Rather than the average velocity, we aim at obtaining the *distribution of residence times* of neutral particles inside the ionization region. From such information, one can compute the ionization probability and ultimately the thruster efficiency.

A possible alternative to DSMC consists in test-particle Monte Carlo (TPMC) algorithms, see for example [231]. In this section, we discuss a TPMC algorithm that tracks single particles inside a pre-computed background. The procedure goes as follows. First, a baseline DSMC simulation is run, resulting in the average density, velocity and temperature fields; then, the TPMC algorithm is started:

1. A test particle is injected from the gas feed, with velocity sampled from a Maxwellian distribution at the injection conditions;
2. The particle is advected ballistically for a time step, and wall collisions are performed, if any;
3. After the translation step, gas-phase collisions are performed with a probability that depends on the local density and temperature of the background;
4. When the particle eventually leaves the domain, the particle is destroyed and a new particle is simulated.

8.4. Test-particle Monte Carlo simulations: the method

A “timer” variable is attached to each particle, and is updated at each time step whenever the particle is inside the ionization region. When the particle leaves the domain and is destroyed, such variable is saved into an array. At the end of the simulation, this array allows us to compute the distribution of residence times. The domain simulated by the TPMC algorithm is shown in Fig. 8.4 for the direct and backward injection cases.

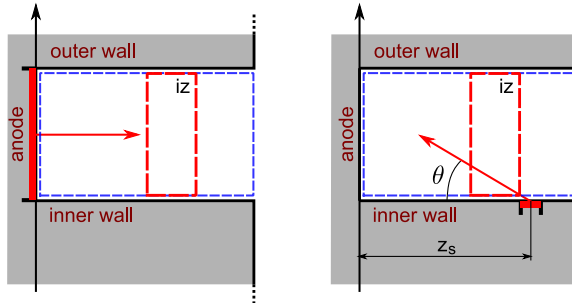


Figure 8.4: Computational domain for the test-particle Monte Carlo algorithm, for the direct injection (left) and the reversed injection configurations (right). Blue box: external domain. Red box: ionization region. Red thick line: injection points.

This scheme can be seen as a simplified version of the DSMC method, where particles collide with a prescribed background. This results in an embarrassingly parallelizable algorithm, that requires no communication or particle re-ordering. The procedure is particularly well suited to free-molecular flows, where one simply removes the gas-phase collision phase, and no baseline DSMC computation would be required. Such case is of interest whenever lower mass flow rates are considered, or for smaller thrusters that show an increased surface-to-volume ratio. Also, for the free-molecular flow cases, results scale linearly with the dimension of the thruster and can thus be extrapolated to scaled geometries. Residence times can be expected to scale with the square root of the surface temperature, with higher temperatures causing higher thermal velocities and thus lower residence times. This scaling is now trivial though, as one should consider that the anode and wall temperatures may be different.

Since collisions are performed with a background (and not among simulated particles), this method conserves energy only at a statistical level (as happens for instance to the Nanbu’s algorithm [232]). This is not a problem for the present case though, since the domain is open and new fresh particles are constantly re-injected.

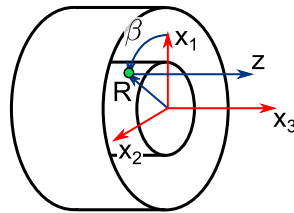


Figure 8.5: Cartesian and cylindrical reference systems for the test-particle Monte Carlo simulations.

Advection step

Fig. 8.5 shows the reference system employed by the TPMC simulations, mapped on the Hall thruster channel. The simulation is 2D axysymmetric. Advection is however performed in the three directions (x_1, x_2, x_3), but after every time step the particle position is rotated back on the (x_1, x_3) plane, thus imposing axial symmetry. This is done as follows: the cylindrical coordinates are found as

$$\begin{cases} R = [x_1^2 + x_3^2]^{1/2}, \\ \beta \equiv \text{atan}(x_2/x_1), \\ z \equiv x_3, \end{cases} \quad (8.4)$$

and the new particle position is

$$\begin{pmatrix} x'_1 \\ x'_2 \\ x'_3 \end{pmatrix} = \begin{pmatrix} R \\ 0 \\ x_3 \end{pmatrix}. \quad (8.5)$$

The velocity is rotated by the same angle β ,

$$\begin{pmatrix} v'_1 \\ v'_2 \\ v'_3 \end{pmatrix} = \begin{bmatrix} \cos \beta & \sin \beta & 0 \\ \sin \beta & \cos \beta & 0 \\ 0 & 0 & 1 \end{bmatrix} \begin{pmatrix} v_1 \\ v_2 \\ v_3 \end{pmatrix}. \quad (8.6)$$

When a particle crosses the wall, a wall-collision is detected. Then, (1) the position at which the surface was crossed is recorded, (2) the particle velocity is discarded and sampled from a Maxwellian normalized distribution with zero average velocity and the surface temperature, and (3) the particle is advected for the remaining of the time step.

Collision step

In case gas-phase collisions are also to be accounted for, a collision routine is called after the advection phase. The density, velocity and temperature fields are imported as a 2D matrix from the baseline simulation, in the $R - z$ plane (example fields are shown in Fig. 8.6).

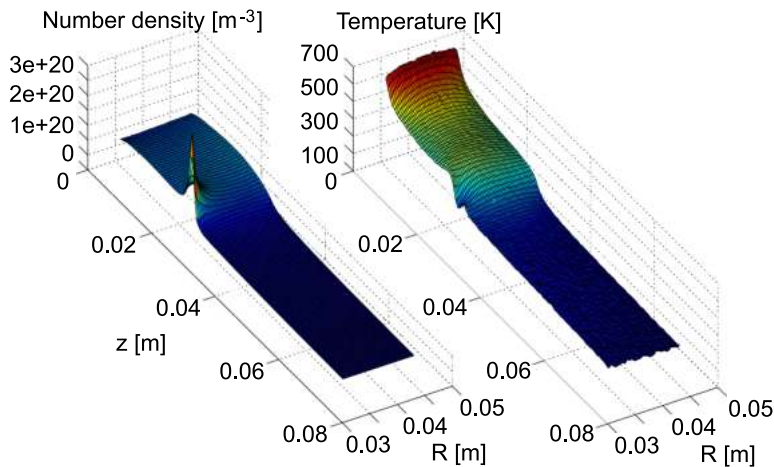


Figure 8.6: Baseline density and temperature profiles for case B30_1, with warm anode, extracted for a strip of the DSMC simulations.

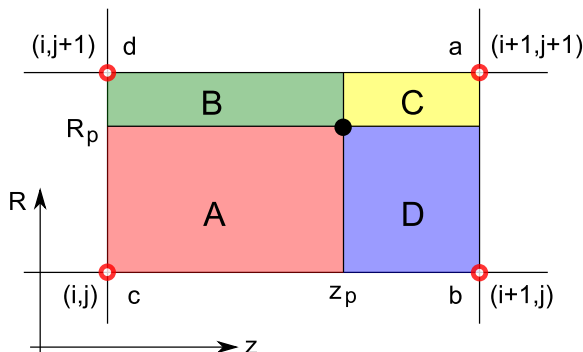


Figure 8.7: Schematic of the bilinear interpolation procedure.

These quantities are computed at the particle location using a bilinear interpolation, as shown in Fig. 8.7. Given the particle position (z_p, R_p) , the four neighboring points are located, with subscripts i and j for the axial and

radial locations respectively. The areas A, B, C and D are then defined as

$$A = [z_p - z_i][R_p - R_j] \quad (8.7a)$$

$$B = [z_p - z_i][R_{j+1} - R_p] \quad (8.7b)$$

$$C = [z_{i+1} - z_p][R_{j+1} - R_p] \quad (8.7c)$$

$$D = [z_{i+1} - z_p][R_p - R_j], \quad (8.7d)$$

and the interpolated value of the field $f_p = f(z_p, R_p)$ reads

$$f_p \approx \frac{A f_{i+1,j+1} + B f_{i+1,j} + C f_{i,j} + D f_{i,j+1}}{A + B + C + D}. \quad (8.8)$$

For example, referring to Fig. 8.7, it can be seen that in the limiting case of $(z_p, R_p) \rightarrow (z_{i+1}, R_{j+1})$, the area A becomes the leading term, and Eq. (8.8) rightfully returns $f_{i+1,j+1}$. In such way, one samples the background density n_{BG} , velocity \underline{v}_{BG} and temperature T_{BG} at the particle location. The relative velocity between the particle and the *average* background velocity is $g \equiv |\underline{v} - \underline{v}_{BG}|$.

Collisions are evaluated using a hard-sphere (HS) model, for simplicity. For a Maxwellian background, the velocity-dependent collision frequency ν for the HS potential reads [81]

$$\nu(g) = \frac{\sigma n_{BG}}{\pi} \sqrt{\frac{2\pi k_B T_{BG}}{m}} \psi \left(g \sqrt{\frac{m}{2k_B T_{BG}}} \right), \quad (8.9)$$

with $\sigma = 1.0351 \times 10^{-18} \text{ m}^2$ is the xenon HS cross-section from [129], m the mass of xenon particles and the function ψ reads

$$\psi(x) \equiv e^{-x^2} + \left(2x + \frac{1}{x} \right) \frac{\sqrt{\pi}}{2} \text{erf}(x). \quad (8.10)$$

In place of the HS model, one should in principle employ the VHS or the VSS collision models, for consistency with the previous DSMC simulations. However, the expression for the velocity-dependent collision frequency is not trivial in such case, and one should employ a numerical estimate instead. Nonetheless, by running such computations, we have verified that the results do not change considerably for the considered conditions. We therefore only consider HS collisions. Once the collision frequency is known, the probability that the test particle collides with another background neutral during the time step Δt is

$$P_c = 1 - \exp(-\nu(g)\Delta t). \quad (8.11)$$

Notice that the time step must ensure that $P_c \ll 1$. Not respecting such conditions would result in a practical under-estimation of the collision frequency. Since $\nu = \nu(g)$ depends on the velocity of the test particle and also on the local collisions, one should ensure this condition all along the simulation. In order to perform a collision, a random number $\mathcal{R} \in (0, 1)$ is sampled, and the collision is performed if $\mathcal{R} < P_c$. If this is the case, a colliding pair is created by sampling from a Maxwellian distribution at the local conditions, and the collision is performed by random rotation of the relative velocity vector [233]. After the collision, the colliding pair particle is discarded.

Numerical implementation

As to exploit the embarrassingly parallelizable nature of the algorithm, a GPGPU version of the TPMC algorithm was implemented in CUDA Fortran and is available at [234] (also see Appendix A). Since all particles are independent, the parallel implementation allows for an optimal speed-up. Speed-ups of 1600 times were obtained while simulating 10^6 particles on an NVidia GTX 760 GPU (compute capability 3.0), with respect to a serial implementation running on an Intel CORE i5 processor with 12 GB of RAM. The parallel simulations for 10^6 particles require just a few seconds.

8.5 Test-particle Monte Carlo simulations: results

The algorithm introduced in the previous section is here applied to the analysis of residence times inside the ionization region. In this section, we assume the ionization region is a square block located at $x \in [13, 18]$ mm (see [90]), as depicted in Fig. 8.4.

8.5.1 Preliminary analysis in the free-molecular limit

To start, we consider in this section a simplified case that allows us to gain an insight on the dynamics of neutral particles. We assume free-molecular conditions and neglect all gas-phase collisions. The cases A1, A2 and all B cases of Table 8.1 are simulated, for both the cold and warm anode case. In such simulations, the residence time of each neutral particle *in the whole channel* is tracked.

The results are shown in Fig. 8.8, where the distribution of *logarithms* of residence times is shown, for clarity. The distribution appears rather simple for the uniform injection case A1. On the other hand, the direct injection from a slit (case A2) shows a bimodal distribution: the low-times

Chapter 8. DSMC and TPMC analysis of the neutral gas injection: an alternative gas feed configuration

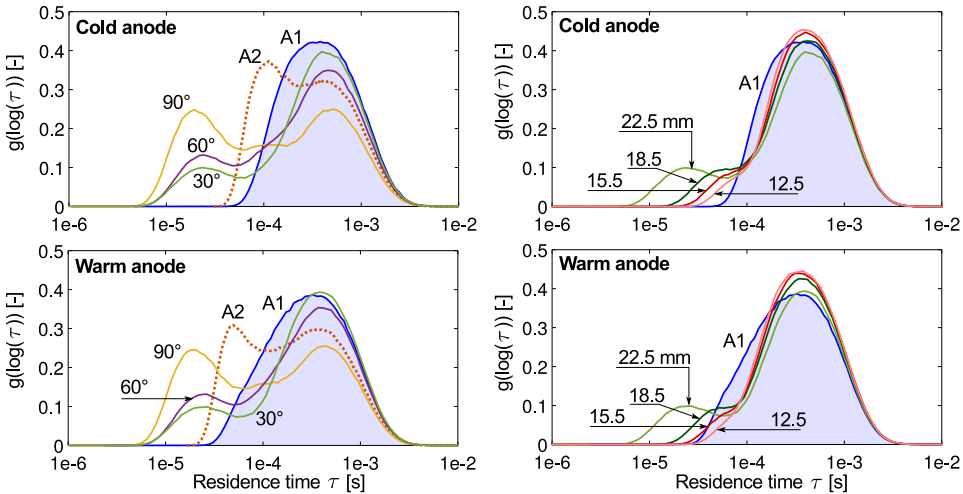


Figure 8.8: Normalized distribution for the logarithm of residence times of neutral particles in the whole channel, in the free-molecular limit. Left: effect of the injection angle. Right: effect of the slit position.

peak is constituted by particles that, being injected from the slit at a higher velocity, leave the channel without colliding with walls. This confirms the intuitive criterion that velocity should be kept as low as possible, in order to increase the residence time. The high-times peak on the other hand is due to particles that suffered a wall collision and are thus slowed-down. The anode temperature is seen to increase this effect, due to the even higher thermal velocity at the injection point. Indeed, for a sonic injection at 300 K, the average velocity is $u_z = 177.91$ m/s and particles take roughly 1.4×10^{-4} s to reach the channel exit, while for the warm anode case $T_a = 1000$ K, $u_z = 324.8$ m/s and the time is reduced to 7.7×10^{-5} s. This qualitatively matches the low-residence-times peaks in Fig. 8.8. Rightfully, the high-times peak is unchanged by the anode temperature, as the walls are kept at $T_w = 300$ K in all simulations.

In the reversed injection simulations, a bimodal distribution is also observed. In this case, the low-residence-time peak is caused by the finite injection temperature: despite the inward injection angle, some particles may have a positive initial velocity and thus reach the exit prematurely, being effectively wasted. This effect is clearly the largest for the 90° injection case. For this reason, the injection strategy proposed by Garrigues et al. [224] may be sub-optimal unless the injection position is carefully selected, as discussed in the following. We also note that, as expected, the low-residence-times peak does not depend on the anode temperature.

An analysis of Fig. 8.8-Left shows that all cases perform worse than the direct injection case A1, but the B30_1 case, with $\theta = 30^\circ$ appears to be the least worst option. The performance can be improved by shifting the slit position inwards, thus reducing the number of wasted particles. This is shown in Fig. 8.8-Right, for a fixed value of the injection angle $\theta = 30^\circ$ and a slit position z_s progressively approaching the anode. As mentioned in Section 8.3, in the limiting case of $z_s \rightarrow 0$ one expects to retrieve a result similar to the direct injection case A1, as the injected particles would collide on the anode and be scattered towards the exit.

Note that the mass flow rate has no effect on the collisionless results of this section, and that the residence times scale linearly with the thruster size.

8.5.2 Collisional case and residence time in the ionization region

In order to identify the best configuration, we repeat the simulations of the previous section by including gas-phase collisions. From the previous section, the 30° case showed to be the most promising candidate, as it allowed us to minimize the fraction of lost particles. Therefore, in this section, only the B30 cases are considered. This time, the residence time will be computed *in the ionization region*, allowing for a computation of the ionization probabilities. A distribution of residence times is not shown in this section. Indeed, since only the ionization region is considered, all particles leaving the channel prematurely would not be accounted for, making a comparison of the results less intuitive.

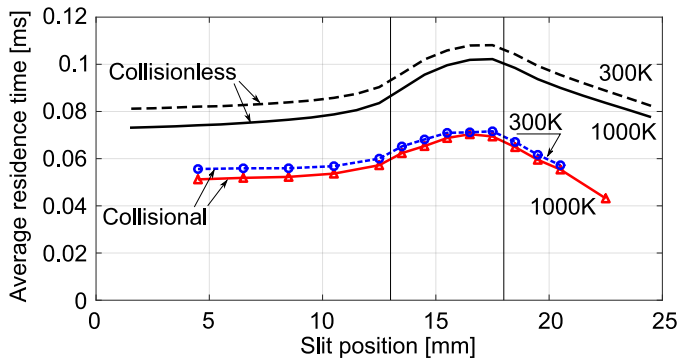


Figure 8.9: Average residence time of neutral particles in the ionization region for different slit positions and anode temperatures. The vertical lines identify the ionization region.

We start by performing a parametric analysis, computing the average

residence time at different slit positions. This is done both assuming collisionless conditions and including gas-phase collisions. In the latter case, a number of additional baseline DSMC simulations were needed. The results are shown in Fig. 8.9. One can clearly see that moving the slit very close to the anode results in a plateau, and the average residence time retrieves the uniform injection case, as mentioned in the previous sections. All particles injected too early would bounce on the anode and cross the ionization region only once. On the other hand, placing the slit too close to the exit results in a large number of particles to be lost. The best results are obtained by centering the 1 mm slit at $z_s \approx 16.5$ mm, in the second half of the ionization region. In such case, the maximum gain is $(\Delta\tau/\tau^{\text{dir}})\% \approx 28\%$ for the collisional case, and about 40% for the collisionless case.

Fig. 8.10 shows two sample trajectories in the (z, R) plane, extracted from the collisional TPMC simulations. Some trajectories appear curved, due to the azimuthal motion out of the plane. The rarefaction conditions appear evident, as the mean free path is comparable to the channel width.

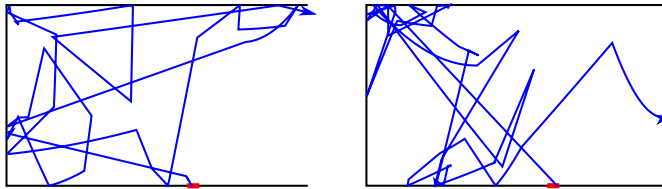


Figure 8.10: Trajectories of two test particles for the axisymmetric simulations of case B30_3. The red line marks the injection slit.

8.5.3 Estimation of the mass utilization efficiency

Finally, from the simulations of the previous section, we are in the position of estimating the ionization probability and thus the mass utilization efficiency of a thruster. We assume that, while inside the ionization region, a neutral particle i may be ionized by effect of an electron collision with probability $P_{iz,i}$. As seen in Eq. (8.2), $P_{iz,i}$ depends on the residence time τ_i and is thus different for each considered particle. Slow-moving particles will spend more time in the ionization region and are thus more likely to be hit by a fast electron, and the opposite stands for fast-moving neutrals. The mass utilization efficiency η_m describes the fraction of ionized particles over the total injected ones, and can therefore be estimated from:

$$\eta_m = \frac{1}{N_s} \sum_{i=1}^{N_s} P_{iz,i} = \sum_{i=1}^{N_s} \frac{1 - \exp(-\nu_{iz} \tau_i)}{N_s} \quad (8.12)$$

where N_s is the total number of simulated particles and $\sum_{i=1, N_s} P_{iz,i} = N_{iz}$, the number of ionized particles. In the present chapter, electrons are not being simulated, and a value of ν_{iz} is a priori unknown. However, our aim is not to determine the efficiency of the reversed injection *per se*, but instead to determine the efficiency increase with respect to a direct injection case. We therefore employ the following strategy:

1. First, a standard-injection configuration is considered for a given thruster, with direct efficiency η_m^{dir} . This may be for example $\eta_m^{\text{dir}} = 0.95$ for the SPT-100, or lower for smaller thrusters;
2. After running the TPMC algorithm on such configuration, we obtain an array of simulated values τ_i ;
3. We then plug τ_i and η_m^{dir} into Eq. (8.12) and invert it numerically, resulting into an estimate for ν_{iz} . This value represents an average, or anyway an effective value over the ionization region;
4. Finally, a reversed injection configuration is considered: a TPMC simulation is run, and a value of η_m^{rev} is computed, using the previously found value of ν_{iz} .

This strategy allows us to find the efficiency of the reversed configuration as a function of the initial direct-injection efficiency. Note that in the most general scenario, $\nu_{iz}^{\text{dir}} \neq \nu_{iz}^{\text{rev}}$, since different neutral profiles have a different influence on the electron mobility and thus on their space profile. Also, if the reversed injection would increase the ionization efficiency, more ions would be produced, resulting in some additional ion-neutral collisionality. Our simplified analysis completely neglects all these phenomena. Nonetheless, this assumption allows for a simple analysis of the problem and permits to easily compute maps of the effectiveness of the reversed injection, without the need of a full (and much more expensive) PIC model of the problem. Given the tightly coupled nature of the plasma problem and the large number of uncertainties involved in the determination of the electrons mobility in Hall thruster channels (such as the wall conductivity and various types of instabilities), we believe that the present analysis is a valuable preliminary investigation tool.

Fig. 8.11 shows the maps of the mass utilization efficiency, computed as $100(\eta_m^{\text{rev}} - \eta_m^{\text{dir}})/\eta_m^{\text{dir}}$, for an injection at 30° and different slit positions, in the cold and warm anode cases (left and right columns). The collisional cases (bottom) are obtained for a mass flow rate of $\dot{m} = 5 \text{ mg/s}$. The collisionless cases on the other hand are completely independent on the mass

Chapter 8. DSMC and TPMC analysis of the neutral gas injection: an alternative gas feed configuration

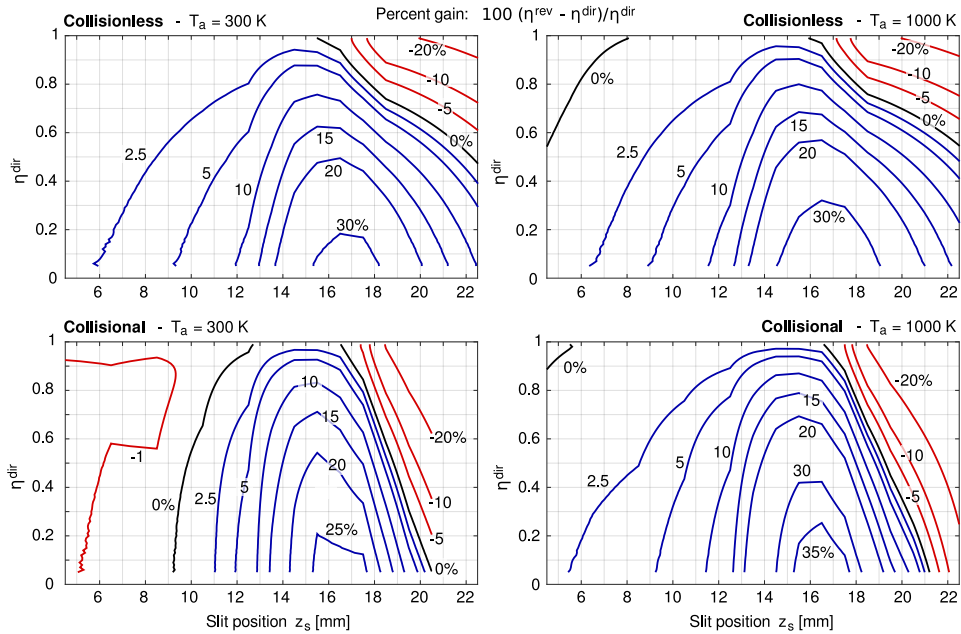


Figure 8.11: Percent gain for different locations of the slit center z_s at different values of η^{dir} . Injection angle $\theta = 30^\circ$. Left columns: cold anode. Right: warm anode.

flow rate (as discussed in Section 8.5.1), and can thus be directly applied to scaled-down or scaled-up thruster geometries. Considering thrusters with a high initial efficiency $\eta^{\text{dir}} > 0.8$, the computations suggest that a maximum gain of 15% can be achieved, while for lower-efficiency thrusters (say, $\eta^{\text{dir}} \approx 0.5$), the improve can reach 20–30%. Finally, it should be noted that the gain is referred to the uniform injection case, that is an idealized configuration. Real gas feeds do not provide a uniform injection along the anode but most likely expand the propellant, causing some acceleration and thus a (at least slight) degradation of the performance. Considering such cases in place of an ideal uniform injection would result in a higher gain of the reversed injection strategy.

8.6 Conclusions

In this chapter, the dynamics of the propellant injection and evolution inside the channel of an SPT-100 thruster was studied numerically, for different gas feed configurations, and neglecting plasma species. The density and velocity fields were seen to depend markedly on the details of the gas injector, ultimately influencing the mass utilization efficiency. An alternative injec-

tion strategy was then proposed, where the propellant is injected backwards, from a slit located near the exit plane, and is directed towards the anode. A comparison of the distribution of residence times of neutrals in the ionization region, obtained from DSMC and TPMC simulations, showed that the proposed reversed-injection configuration could improve the mass utilization efficiency from 5–10% up to 20–30%, according to the efficiency of the baseline thruster.

A number of simplifying assumptions were introduced in this section. Most notably, the analyses are run for a switched-off thruster, neglecting all interaction between neutrals and electrons or ions. The only considered plasma effect was an increased temperature of the anode. A suggested future work activity would consist in repeating the simulations including at least neutral-ion momentum exchange and charge exchange interactions. After verifying the influence of such effects on the final efficiency maps, a next step would be performing a fully coupled simulation, as to retrieve self-consistently the ionization region and electron transport.

Conclusions and future work

This work aimed at investigating the modeling of low-temperature plasmas using moment methods. In particular, Hall thruster plasmas were considered. In such device, ions are collisionless, to a first approximation. The acceleration is achieved by creating a region of higher electron density, trapping them via a radial magnetic field. The axial electric field, combined with the radial magnetic field, makes electrons drift in the $\mathbf{E} \times \mathbf{B}$ direction. Together with the low pressure, all such effects are strong sources of non-equilibrium.

This work investigated kinetic and fluid strategies for modeling these situations, through a selection of simple test cases. In particular, the order-4 maximum-entropy moment methods showed an excellent potential for describing the mentioned non-equilibrium, often offering a solution as accurate as the kinetic method, but at a lower computational cost, as discussed in the following. The maximum-entropy methods employed in this work are the 14-moment system, together with the 5-moment system, describing a particle with a single translational degree of freedom.

Developing the maximum-entropy method

Applying the maximum-entropy methods required first of all to develop such systems for profitably dealing with the conditions of ions and electrons. In particular, the following results were needed:

- Achieving an affordable computational cost;
- Ensuring a profitable treatment of collisionless conditions;

- Developing electromagnetic source terms;
- Developing sources for the collisions of warm electrons with cold and slow neutrals.

An affordable computational cost is particularly important in plasmas, where the tiny time scales associated to plasma waves, and the refined grids arising from the need to resolve the Debye length, often make the system particularly stiff. In the current state-of-the-art, the 14-moment system is already much more affordable than traditional maximum-entropy formulations, thanks to the development of approximated solutions of the entropy-maximisation problem. However, a significant part of the remaining computational cost was seen to be the approximation of the system eigenvalues. From the analysis that we performed, traditional approximations for the maximum and minimum wave speeds of the 14-moment system appeared to bring an excessive degree of diffusion when strong non-equilibrium situations are considered. For this reason, part of this work was devoted to the development of approximated formulas, that allow us to retrieve an accurate estimate of the system wave speeds, without the need of numerically computing the fluxes Jacobian² and its eigenvalues at each iteration.

Among the drawbacks of the method, we should certainly cite the computational cost. Through the rarefied test cases, it was seen that the method can be somewhere between 7 and 100 times more expensive than the Euler equations (less for continuum conditions, more when strong non-equilibrium appears). However, these figures of merit were obtained with simple explicit time integration strategies, that make the solution completely dependent on the system eigenvalues, through the CFL conditions. Among the strategies to mitigate this problem, we shall cite for example preconditioning [235].

The crossing of the Junk line, in some test cases, requires a careful selection of the numerical schemes. For continuum conditions, the frequently employed HLL fluxes work faultlessly, but in rarefied simulations, they showed to cause strong oscillations, especially in the higher order moments. The Rusanov fluxes appear to introduce sufficient diffusion to solve the issue, and thus allow us to apply reconstructions (such as in van Leer's MUSCL scheme) that allow us to reach higher orders in space.

Electric and magnetic source terms were developed for the 5-moment and the 14-moment systems, starting from the generalized moment equation, and were employed for the study of plasma waves. The dispersion relations showed to retrieve the expected fluid behavior for small values

²It should be recalled that, for the 14-moment system, the Jacobian is a 14×14 matrix.

of the wave number k , and asymptote to the convective eigenvalues when $k\lambda_{De} \gg 1$. Also, it was noted that some regions of the moment space are associated to unstable eigenvalues, which may be associated to the presence of micro-instabilities, and will be suggested as a future work activity.

Regarding collisional source terms, only simplified formulations were attempted, and merely for electron-neutral interactions, being the most important collisional phenomena in Hall thrusters. The formulations were based on the BGK collision operator, where the effect of a large electron-neutral mass disparity was embedded.

Applying the maximum-entropy method to plasma systems

The aforementioned developments allowed us to apply the 14 and 5-moment systems to the modeling of ions and electrons. A set of test cases was identified, describing individual non-equilibrium effects arising in Hall thruster plasmas. The aim of such test cases was to compare the accuracy at which the fluid and moment methods can reproduce the kinetic features. For this reason, in all test cases, an individual species was studied. The effect of the other species was embedded by prescribing the electric field. The investigated problems are therefore not self-consistent from the plasma point of view. However, this allows to perform a detailed comparison of the results from each method, overruling all inaccuracies associated to the modeling of the other species. A coupling of the models for the different species will be suggested as a future work activity.

Ions

Regarding ions, the first problem considered consists in the 1-dimensional collisionless acceleration in a Hall thruster-like channel. For this problem, we have investigated an analytical solution of the kinetic equation, and then developed an ad-hoc fluid model that includes only the lower three moments of the distribution function, but retrieves non-equilibrium through a non-Fourier closure for the heat flux. These models appeared very accurate if compared to fully kinetic simulations, and at least reasonable when compared to experimental results. Further test cases were then developed for investigating the accuracy of the maximum-entropy closure in such condition. In most test cases, the maximum-entropy method allowed us to reproduce the kinetic results to a very good accuracy.

The most notable exception consists in the study of charged particles in a closed system, and in presence of an imposed sinusoidal electric field. Such test case results in a progressively increasing non-equilibrium, show-

ing filamentation in phase space. The maximum-entropy method appeared to reproduce very closely the first instants of the simulation (much better than the simpler Euler system) but eventually breaks apart for long times. Such test case was chosen as to reproduce the ion wave trapping, appearing in Hall thrusters due to the presence of azimuthal instabilities.

In terms of application to Hall thrusters however, the situation is less dramatic: once this case was extended in two dimension, the axial acceleration showed to be a crucial factor, limiting the permanence of ions in the region of azimuthal travelling waves. The resulting non-equilibrium conditions appear to be reproduced with high accuracy by the 14-moment system, confirming the quality of such approximation.

Electrons

Finally, regarding electrons, the presence of a magnetic field introduces further non-equilibrium features, where ring-like, asymmetric and anisotropic distribution functions appear. For this problem, the 14-moment approximation appeared to be an ideal approach, as the 14-parameter maximum-entropy distribution function is able to naturally reproduce such features. A comparison of the analytical and maximum-entropy velocity distribution functions showed very promising results (yet not exact), while the *energy* distribution function appeared to reproduce the analytical results extremely closely. Analogously, space-homogeneous time relaxation problems, as well as the study of a 1-dimensional test case confirmed the quality of the maximum-entropy formulation for this problem.

For what concerns electron modeling, the main disadvantage of the maximum-entropy formulation consists in source terms. Indeed, unless one solves the full costly entropy-maximisation problem, the shape of the distribution function is not known from its moments. Such knowledge would be needed if one is to formulate accurate non-equilibrium (both elastic and inelastic) collision terms that embed non-linear cross-sections. At the moment, this is an open problem that will be suggested as a future research activity.

Other results

To conclude, we should mention a couple of further activities performed in the framework of this thesis.

First, a study of the dynamics of neutral particles was conducted with Direct Simulation Monte Carlo and test-particle Monte Carlo methods. In this study, we have proposed an alternative gas feed strategy, that could

allow one to increase significantly the residence time of neutral particles in the ionization region. The expected gains in mass utilization efficiency range from 5–10% to 20–30% for the less efficient thrusters. Such analysis is however approximated, as it neglects all interactions between neutrals and the charged species. This is equivalent to considering the efficiency of a switched-off thruster, except that different anode temperatures have been considered.

Finally, we should cite a further activity, uncorrelated to neutrals, but aimed instead at approximating the maximum and minimum wave speeds of the maximum-entropy systems by use of artificial neural networks. This work is preliminary, and is thus confined to an appendix. Nonetheless, this strategy is quite interesting, as it could be easily generalized to whatever system.

Future work

Based on this work, a number of future research activities are suggested.

Numerical solution of the 14-moment method

A number of developments will be in order for increasing the accessibility and effectiveness of the 14-moment solution. In particular,

- Developing higher-accuracy numerical fluxes, extending existing formulations based on the Euler/Navier-Stokes equations (such as the AUSM family of schemes), or investigating kinetic fluxes;
- Improving the empirical wave speeds approximation formulated in this work, embedding more physical considerations and removing the questionable assumptions;
- Investigating pre-conditioners and implicit methods, in order to lower the spread in computational cost if compared to fluid simulations.

Maximum-entropy system for plasma modeling

The most compelling developments for what concerns running plasma simulations are

- Developing non-equilibrium collisional source terms for the 14-moment equations, especially regarding electron-neutral collisions, but also charge and momentum exchange ion-neutral collisions. In particular, we suggest a comparison of such collision models against PIC-MCC

algorithms and other moment methods, starting from 0-dimensional reactor configurations;

- Investigating fully coupled problems, employing a multi-fluid formulation and the Poisson's equation for the description of the electric field.

Moreover, a number of further analyses are possible. We shall cite for example:

- Extending the study of the dispersion relation for plasma waves, and investigating how the maximum-entropy systems can develop micro-instabilities;
- Extending the affordable interpolative closure to higher order maximum-entropy systems, that could reproduce even stronger non-equilibrium situations;
- Comparing hybrid methods (kinetic ions and fluid electrons) to a moment – fluid approach, where ions are modeled with the 14-moment system and electrons are fluid. For Hall thruster problems, this could give analogous accuracies to the hybrid method, but at a lower computational cost, and with a simpler data structure, since electron and ion quantities will be known at the same grid points.

The methods developed in this thesis may find a direct application to a number of other plasma configurations, such as the study of the Hall thruster plume. Besides the important problem of the plume-spacecraft interaction, an electric propulsion device can be used as a particle flow generator for the ground simulation of satellites in low Earth orbit conditions, and for investigating air-breathing electric propulsion configurations [236–238]. Currently, a new rarefied facility is being built at the von Karman Institute for Fluid Dynamics, targeted to such problems, and numerical tools are being developed for the characterization of the facility. Together with such tools, the developments of this thesis may prove useful, for example, for the simulation of the chamber operating conditions and of the plume non-equilibrium, allowing us to ensure that the required testing specifications are met.

APPENDIX A

Notes on the GPU implementation

In this work, graphics cards were used to accelerate the 2-dimensional finite volume computations of crossing rarefied jets (Section 4.4), ions in travelling electric fields (Section 6.6), as well as the test-particle Monte Carlo computations of the neutral injection, in Chapter 8. This appendix briefly reviews the caveats of such GPU implementation, and is based on the NVidia GTX760 (compute capability 3.0) and the Tesla K20X (compute capability 3.5). The implementations are based on CUDA Fortran (see for example [239]).

At a simplistic level, the GPU is composed by a large number of processors that can be run in parallel. All processes have direct access to the GPU memory, that is composed by a global memory (typically the largest), and various levels of smaller (but faster) memories, as shown in Fig. A.1. For storing the physical constants, one can employ the constant memory, that has a fast access but cannot be modified during the execution. The texture memory has some peculiar interpolation features, but was not employed in this work. Since the memory is dedicated, the access via CPU is a rather slow operation, showing an important latency. For this reason, provided that the GPU memory is sufficient to hold all necessary data for the simulation, one typically tries to follow the strategy:

Appendix A. Notes on the GPU implementation

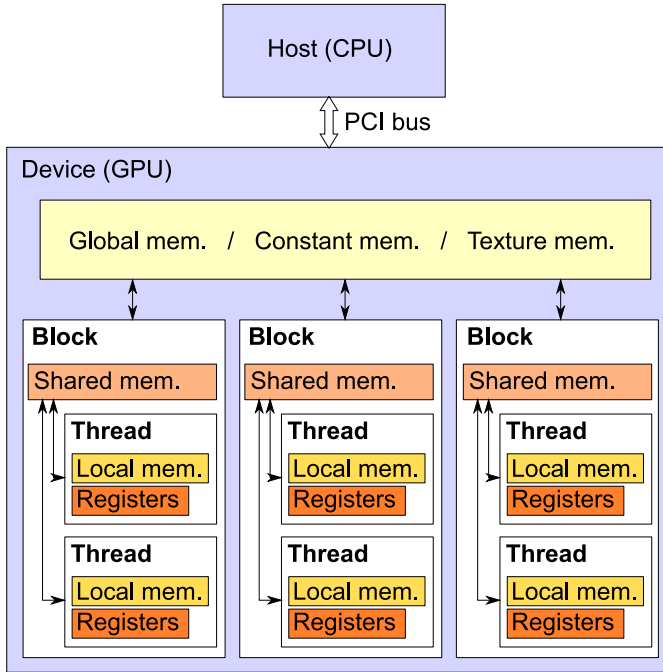


Figure A.1: Schematic of the memory organization of a typical GPU.

1. Initialize the data on the host (for simplicity);
2. Copy the data to the GPU;
3. Perform all computations on the GPU;
4. Only in the end, download the data.

Parallel implementation for the test-particle Monte Carlo simulations

The test-particle Monte Carlo algorithm of Chapter 8 is easily parallelized, since every particle is run independently from the others. Our implementation is freely available at [234]. At the beginning of the simulation, the background density, velocity and temperature fields are loaded in the global memory as 2D matrices. The number of particles to be simulated is then decided, and each particle is mapped to a different thread. When a particle leaves the domain, the process for such thread is concluded.

Unfortunately, each particle follows a different path, due to the random injection and collisions. Therefore, all threads need to execute different code operations. This is known to be a non-optimal situation, since some

groups of threads (warps) potentially have the possibility to run exactly concurrently in a branchless program. However, the fact that all particles are independent and that no communication with the host is necessary during the computation, makes our simple GPU parallelization extremely efficient, reaching a speed-up of above 1600 times, on the GTX760.

2D finite volume solver

The implementation of the 2D finite volume scheme requires some additional care, and one needs to ensure that the quantities have been updated in each cell before the solver moves to the next step.

Every cell in the 2D grid is mapped to one thread, and a number of $N_x \times N_y$ threads forms a block, for a maximum of 1024 threads. The GPU contains a number of multiprocessors (MP, 14 for case the Tesla K20X), each one being mapped to a grid block. When a GPU function or “kernel” is launched, it is executed in parallel on each multiprocessor, and therefore the code is executed for MP grid blocks in parallel. Once the execution is done, the device moves to the successive MP blocks, and so on until the kernel is over.

This behavior is to be carefully considered when designing the solver. For example, considering the forward Euler time integrator (discussed in Chapter 3),

$$\mathbf{U}^{n+1} = \mathbf{U}^n + \sum_i \frac{\Delta t}{L_i} \mathbf{F}_i^n \cdot \hat{\mathbf{n}}_i + \Delta t \mathbf{G}^n, \quad (\text{A.1})$$

one needs to ensure that all fluxes are properly computed before the solution is updated. This can be ensured by breaking the solver into separate kernel calls, ensuring that a given operation is run on all blocks before the program moves on. As a practical example, Fig. A.2 shows the outcome of a wrong implementation, where the program is solving 14 MPs (and thus blocks) at a time, each composed by 32×32 threads (one for each cell) and is not waiting for the kernel to be launched on other blocks before updating the solution.

Historically, GPUs are single precision devices, whereas most current GPUs also support double precision, many of them even natively. The solution of the maximum-entropy 14-moment system showed some issues with single precision, with every test case performed. The issues seemed to be mostly attributable to the computation of the closing moments, especially in the inversion of the matrix B_{ij} . Employing double precision removed all such issues.

Another issue appears when trying to solve the 14-moment system on

Appendix A. Notes on the GPU implementation

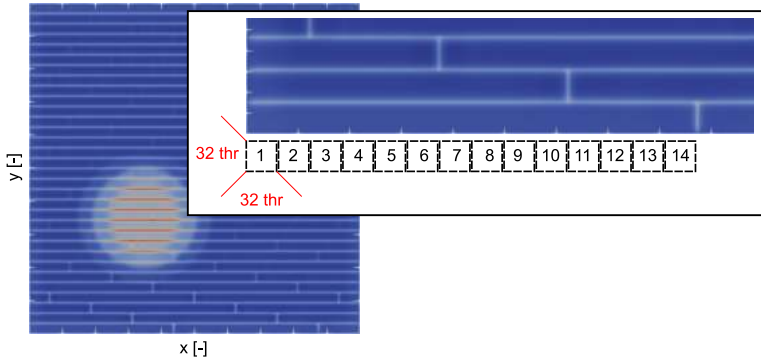


Figure A.2: Density field from a test simulation. Example of a numerical artefact due to improper implementation of the time integrator.

the GPU. With respect to the Euler equations, the closing moments of the 14-moment system are numerous, and their computation from the interpolative approximation requires to define a number of local working variables. As a result, one may run out of registers, and this forces one to run on less threads per block. In the present implementation, the Euler computations were easily run on 32×32 threads per block, while for the 14-moment system this needed to be reduced to 16×16 or even 16×8 (for rectangular grids).

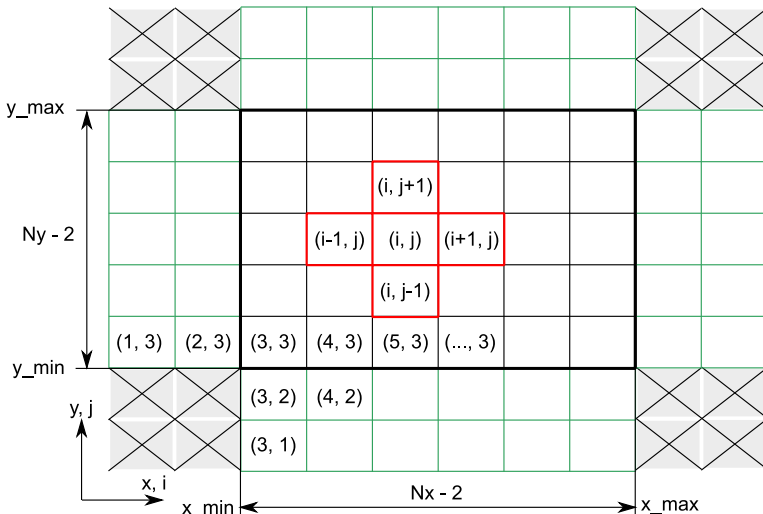


Figure A.3: Schematic of the finite volume 2D Cartesian grid. The black thick line delimits the actual computational domain. Green boxes are ghost cells.

To remove the need to store a grid in the GPU memory, a (structured)

Cartesian grid is employed, as shown in Fig A.3, where cells numbering starts from 1 as custom in Fortran implementations. Two layers of ghost cells are employed at each side of the domain, simplifying the numerical implementation of second order accuracy at the boundaries. Four “dead cells” are present in each corner: these are kept in the arrays for simplicity, but are not taken into account during the actual computations.

The present implementation is based on a single GPU and is rather simplistic. More advanced strategies could be employed, exploiting various features of the GPU (for example, leveraging on shared memory) and multiple-GPU configurations (see for example [240, 241]).

APPENDIX

Time integration error for accelerated gases

The discretization error intrinsic to time integration methods may play an important role in numerical simulations, when closed systems are to be described or the long-time behavior is of interest. This appendix is based on the conservative form of the governing equations. When the equations are written in primitive variables, this analysis does not hold anymore as some errors disappear.

Considering a uniform slab of gas subject to a uniform and constant force F , the mass, momentum and energy equations give

$$\frac{d\rho}{dt} = 0 , \quad \frac{d}{dt}(\rho u) = F , \quad \frac{d}{dt}(\rho E) = Fu . \quad (\text{B.1})$$

The density is therefore constant, while the velocity grows linearly in time:

$$u(t) = u(0) + F t / \rho , \quad (\text{B.2})$$

and the energy changes quadratically:

$$\begin{aligned} (\rho E)(t) &= (\rho E)(0) + \int_0^t Fu(t) dt = (\rho E)(0) + \int_0^t F(u(0) + F t / \rho) dt , \\ &= (\rho E)(0) + Fu(0)t + F^2 t^2 / \rho . \end{aligned} \quad (\text{B.3})$$

Appendix B. Time integration error for accelerated gases

For a time integrator to behave properly, we expect this basic feature to be retrieved, but this is not the case for most schemes. The simple forward Euler integrator for example evaluates the source terms at time n and thus gives a linear estimate in time of both velocity and energy:

$$\begin{cases} u^{n+1} = u^n + \Delta t F/\rho, \\ (\rho E)^{n+1} = (\rho E)^n + \Delta t F u^n / \rho. \end{cases} \quad (\text{B.4})$$

This situation is depicted in Fig. B.1-Left and -Center and leads to under-predicting the total energy. When the temperature is reconstructed by removing the velocity squared (that is integrated exactly) from the total energy ρE (that contains the integration error), one obtains a progressive cooling down (or heating up) of the gas, which may eventually lead to negative temperatures. Increasing the order of the method does increase the accuracy, but does not necessarily solve the problem.

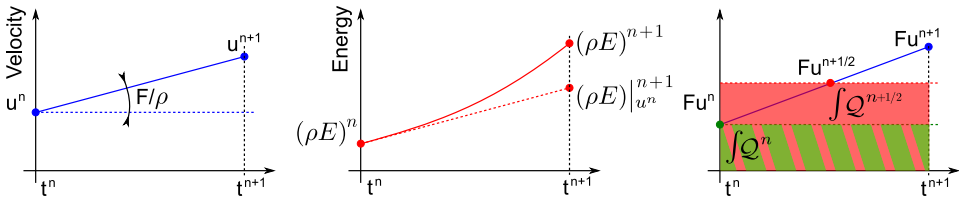


Figure B.1: Analytical and discrete velocity (Left) and total energy (Center). Right: source term for the energy equation, evaluated at the initial time n or at the midpoint $(n + 1/2)$.

Remedy: the Midpoint Euler scheme

Given the structure of the sources, if one would account for the linear evolution of the velocity, the source term for the energy equation would be correctly reproduced. The simple Midpoint Euler scheme (see Chapter 3) solves the problem by employing such strategy. By performing a half time step, the velocity is integrated exactly to the midpoint value, and this is enough for integrating correctly the source term for the energy equation, $Q = Fu$, as shown in Fig. B.1-Right.

A numerical example

As a numerical example, we solve Eqs. (B.1) for $F = nqE$, with $n_0 = 10^{15} \text{ m}^{-3}$ the initial number density, $q = 1.602 \times 10^{-19} \text{ C}$ the particles charge, with the imposed field $E = 10 \text{ kV/m}$, particle mass $m = 2.18 \times 10^{-25} \text{ kg}$ and initial temperature $T_0 = 100 \text{ K}$. Figure B.2 compares the

temperature, using the forward Euler, the Heun, Runge-Kutta 4 and the midpoint Euler methods. As expected, the higher order methods behaves better than the forward Euler scheme, but still fail to predict the expected constant temperature at larger time steps. The midpoint Euler, despite being only second order, solves this problem exactly, to numerical accuracy.

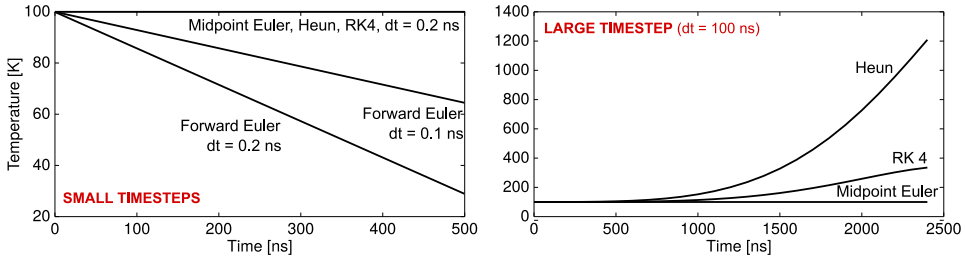


Figure B.2: Temperature of a gas under uniform and constant accelerating field, as predicted by different integration schemes. The forward Euler method is not shown in the Right figure, as it is not stable for the large time step.

APPENDIX C

Wave speeds approximation via Artificial Neural Networks

In Section 4.2, approximated expressions for the wave speeds of the 6 and 14-moment maximum-entropy systems were formulated. Before finding these approximations, an alternative approach based on Artificial Neural Networks was initially attempted. Such approach will be discussed in this appendix. Many important observations of Section 4.2, such as the dependence of the wave speeds on σ^{-1} , were not initially accounted for. Doing so would surely improve the quality of the present appendix. Nonetheless, the approach outlined here is useful as it outlines the procedure and the accuracy that can be expected.

In this work, we are interested in obtaining the wave speeds w by feeding the gas state \mathbf{U} to the artificial neural network (ANN). Roughly speaking:

$$(w_{\min}, w_{\max}) = \text{ANN}(\mathbf{U}). \quad (\text{C.1})$$

To do that, the actual procedure is as follows:

- 1) From the gas state \mathbf{U} , move in the reference frame with zero velocity and compute dimensionless variables;

- 2) Scale dimensionless variables with proper functions, as to highlight the equilibrium region;
- 3) Scale the data to unit range;
- 4) Apply the artificial neural network and obtain the wave speeds;
- 5) Scale back the wave speeds to dimensional units.

Points 1 and 4 were detailed in Chapter 2.

Feedforward Artificial Neural Networks (ANN)

We consider feedforward artificial neural networks (ANN), and employ the TensorFlow [242] and Theano [243] implementations, with the Keras API [244]. For a complete introduction, the reader is referred to [245].

ANNs are composed by one input layer, a number of hidden layers, and an output layer. The k -th layer takes as input the values of the layer $k - 1$ and predicts an output as a linear combination, further processed by a non-linear activation function $a()$,

$$u_k = a \left(\underline{W}_k \underline{u}_{k-1} + \underline{b}_k \right), \quad (\text{C.2})$$

where \underline{u} is the vector of node values, \underline{W} are the weight coefficients and \underline{b} is the “bias” vector. The weights and biases are determined by the training process, and are chosen as to represent best the desired output. In this work, we consider a tanh activation function for internal layers, while a linear activation function is chosen for the output layer [246].

Creating the data for training the ANNs

The ANN approximation is investigated for the parameters $\sigma \in [10^{-5}, 1]$, and for the non-dimensional heat flux $q^* \in [-70, 70]$. The latter allows us to represent shock waves up to Mach number $M = 100$, as shown in Fig. C.1.

For the 5-moment system, q^*, σ completely define the dimensionless wave speeds. A plot of the maximum wave speed in such plane is shown in Fig. C.2-a), where a logarithmic scaling of the wave speed is introduced as to make the plot intelligible. As studied in Section 4.2, the wave speeds span many orders of magnitude for $\sigma \rightarrow 0$. Moreover, one may be interested in reproducing well the equilibrium region. However, representing such a complicated and widely varying function is a difficult task for an ANN. We decide therefore to transform the data, as to make the job simpler to the ANN. First, as mentioned, a logarithmic scaling (subscript “ s ”)

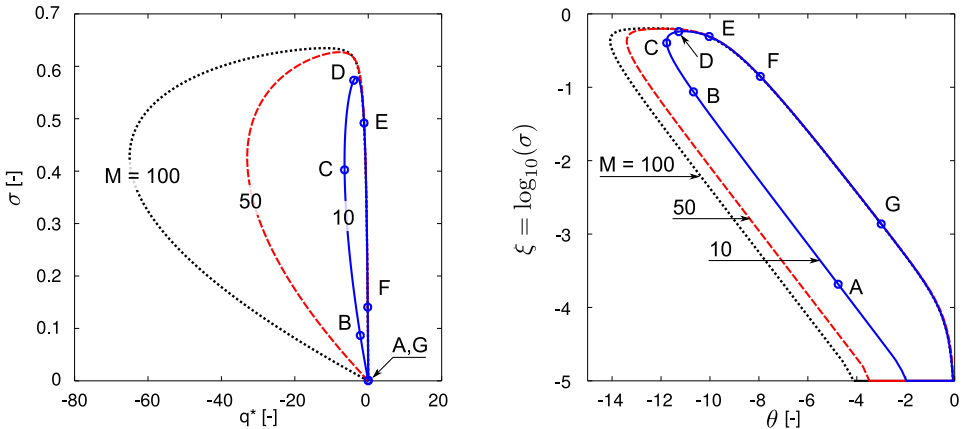


Figure C.1: Shock wave structure in the $q^* - \sigma$ plane, as predicted from the 5-moment system, for Mach numbers $M = 10, 50$ and 100 . Left: linear space. Right: scaled variables $\xi = \log_{10}(\sigma)$ and $\theta = \operatorname{asinh}(Aq^*)$, with $A = 10\,000$.

is introduced on the wave speeds, observing that in the reference frame of the bulk velocity, w_{\max} and w_{\min} are always positive and negative respectively:

$$\begin{cases} w_{\max}^s = \log_{10}(w_{\max} + 1), \\ w_{\min}^s = -\log_{10}(-w_{\min} + 1). \end{cases} \quad (\text{C.3})$$

Then, in order to attribute more importance to the equilibrium region, σ is scaled by introducing the quantity $\xi = \log_{10}(\sigma)$, such that for $\sigma \in [10^{-5}, 1]$, $\xi \in [-5, 0]$. The heat flux is scaled using a sigmoid function, that is steep in the origin as to emphasize such region,

$$\begin{cases} \theta = \operatorname{asinh}(A q^*), \\ A = 10\,000. \end{cases} \quad (\text{C.4})$$

The data after all the scalings is shown in Fig. C.2-c). As mentioned, by embedding the considerations of Section 4.2 one can probably obtain a more rigorous scaling.

The training data is generated by sampling points randomly in the ξ, θ plane. At first, a uniform sampling was attempted, but this provided a good fit in the smooth regions and a poor-quality near equilibrium. Therefore, we decided to divide the plane in patches and sampling a various amounts of points, as detailed in Table C.1. A total of roughly 4×10^6 points was employed. Increasing this number further did not appear to improve the results.

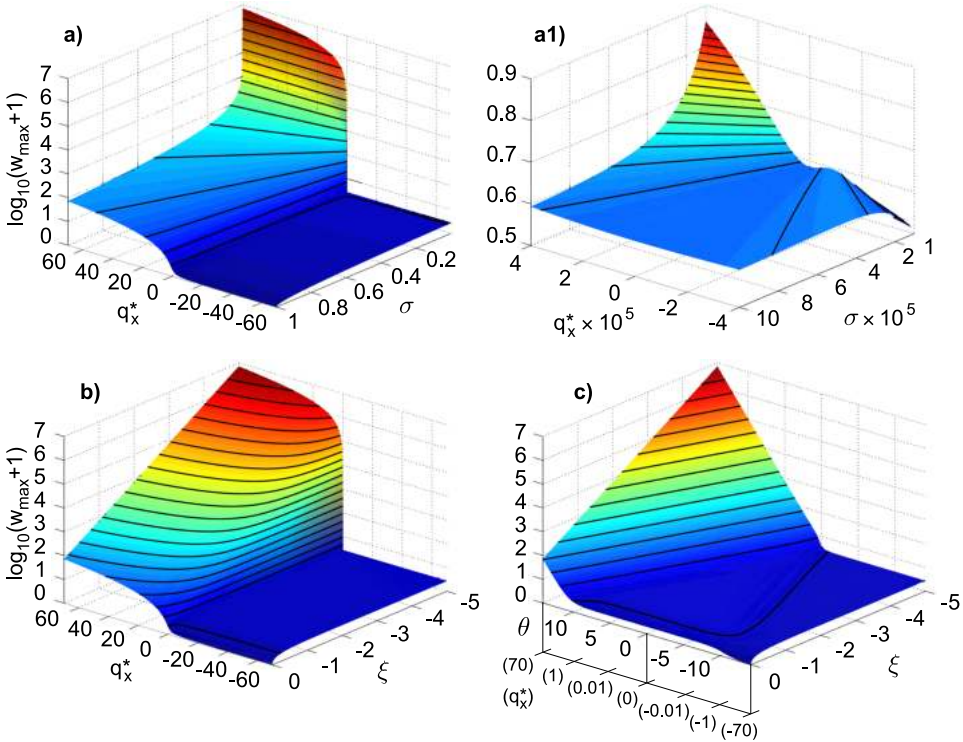


Figure C.2: Maximum Wave speed of the 5-moment system, scaled for a more accurate representation with ANNs. a) logarithmic scaling of the wave speed; a1) magnification near the origin (equilibrium point); b) logarithmic scaling of σ ; c) sigmoid scaling of q^* .

ANN architecture and training

The most suitable architectures for ANNs are typically defined empirically, by training different layouts and analyzing the accuracy. In terms of CFD applications, small ANNs are better, as they can be evaluated with fewer computational resources. We discuss here a selection of the analysis performed. Some possible three-hidden-layer architectures are shown in Fig. C.3.

Before feeding the data to the ANN, a unit scaling is employed to both the input quantities (ξ and θ), and the resulting scaled wave speeds,

$$h_{(1,-1)} = 2 \frac{h - \min(h)}{\max(h) - \min(h)} - 1. \quad (\text{C.5})$$

with h the quantity to be scaled. Scaling the data to $[0, 1]$ provided analogous final accuracies. Note that the values $\min(h)$ and $\max(h)$ of the

Number of points	σ range	q^* range
640 000	$[10^{-5}, 1]$	$[-70, 70]$
160 000	$[10^{-5}, 10^{-4}]$	$[-10^{-3}, 10^{-3}]$
160 000	$[10^{-5}, 5 \times 10^{-5}]$	$[-5 \times 10^{-5}, 5 \times 10^{-5}]$
900 000	$[0.7, 1]$	$[-70, 70]$
600 000	$[0.95, 1]$	$[-70, -10]$
600 000	$[0.95, 1]$	$[10, 70]$
900 000	$[10^{-4}, 10^{-5}]$	$[-70, 70]$

Table C.1: Patches in the (ξ, θ) plane for creating training data. The equivalent values of σ and q^* are shown for clarity.

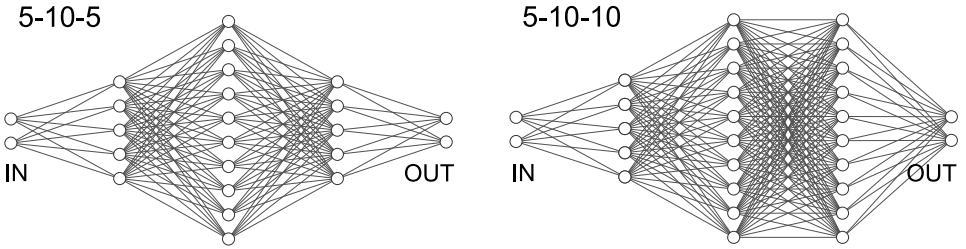


Figure C.3: Examples of ANNs with three hidden layers. The inputs are two for the 5-moment system, and should be three for the 6-moment system. The outputs are two: the maximum and minimum wave speeds.

training data are to be stored, as they are needed for evaluating the ANN, during CFD computations.

Given the training data and the ANN architecture, training is performed by selecting a number of 800 epochs and a batch size of 1000. The convergence history suggests that this is enough for reaching a satisfactory convergence. Training points are fed in random order by the algorithm. The wave speed predictions obtained from the training process are shown in Fig. C.4.

The quality of a trained ANN is then analyzed, by considering the error. Figure C.4 appears to give an accurate match, with negligible error. However, what really matters in terms of CFD computations is the error in the full non-scaled wave speeds: indeed, a small error for $w^s = \log_{10}(w)$ is amplified once we compute the exponential to retrieve w . The error is defined as

$$E = \frac{w_{\max} - w_{\max}^{\text{NN}}}{w_{\max}}, \quad (\text{C.6})$$

and is evaluated on a uniform grid in the $\sigma - q^*$ plane, and is shown in Fig. C.5. Additionally, the error is evaluated on a set of 50 000 random points, and the average error and 95th percentile are given in Ta-

Appendix C. Wave speeds approximation via Artificial Neural Networks

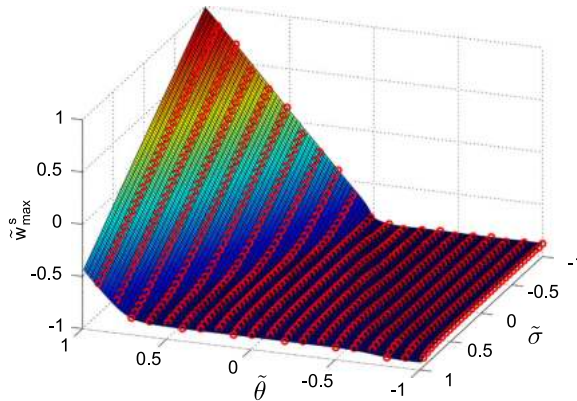


Figure C.4: Predicted maximum wave speed from a 5-10-5 hidden layers architecture (surface plot) and exact values (red symbols), in the scaled variables domain, with additional unit-scaling.

ble C.2. Slightly different results may be obtained in different runs due to the stochastic nature of the training.

Architecture	$\mu(E)$	$P_{95\%}(E)$
5-10-5	2.312 %	6.127 %
5-10-10	2.761 %	6.527 %
10-10-5	2.189 %	4.303 %
5-10-10-5	2.202 %	3.889 %
8-20-15-8	2.076 %	3.144 %
15-20-15-10	2.110 %	2.939 %

Table C.2: Error for different tested ANN architectures, computed on 50 000 random points. $\mu(|E|)$ and $P_{95\%}(|E|)$ indicate the average of the absolute error and the 95th percentile.

From an analysis of the reported results, we propose the following:

- If a rough reproduction of the wave speeds is sufficient, with an error below $\pm 10\%$ in the whole domain, we propose to employ the three-layer 5-10-5 architecture. The 5-10-10 and 10-10-5 architectures increase the complexity without increasing significantly the accuracy;
- If a lower error is required, a 15-20-15-10 architecture allows for a prediction within $\pm 3\%$ in most of the domain and in any case below $\pm 5\%$, but at the cost of operating with larger matrix.

Further analysis could allow one to identify simpler network layouts with analogous or higher accuracies, but this is beyond the scope of the present work.

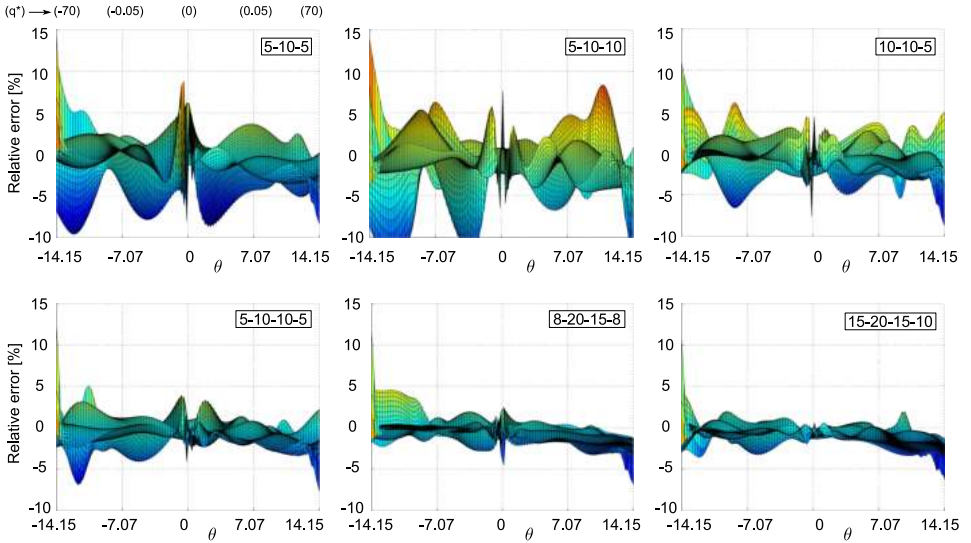


Figure C.5: Relative error in the full-scale wave speeds from Eq. (C.6). The error is plotted against the θ axis, and the error for different values of σ is superimposed.

6-moment system

We then consider the 6-moment system [67], where the fitting is to be done on three dimensionless variables instead of two, including the dimensionless pressure P_{xx}^* . In this section, we arbitrarily decide to nondimensionalize variables using the quantity $\text{tr}P_{ij}$. With this choice, at equilibrium we have $P_{xx}^* = 1/3$, and in the limit of $P_{yy} = P_{zz} \rightarrow 0$, the 5-moment system is retrieved, with $P_{xx}^* = 1$.

The closing moments (and thus ultimately the fluxes Jacobian and its eigenvalues) are obtained from the interpolative closure [67]. This closure, when applied to the 6-moment and 14-moment system, is known to embed some small regions of slight non-hyperbolicity, where eigenvalues take a small imaginary part. This is shown in Fig. C.6. On practical grounds, this fact does not constitute a difficulty, and in the present work we circumvent this by considering only the magnitude of the wave speeds, properly multiplied by the sign of the real part,

$$\tilde{w} = \text{sign}(\text{Re}(w))\sqrt{\text{Re}(w)^2 + \text{Im}(w)^2}, \quad (\text{C.7})$$

Regarding the magnitude of the maximum wave speed in the $q_x^\sigma - \sigma$, one can see a qualitatively similarity with respect to the 5-moment system, but also a strong influence of the pressure.

For the 6-moment system, the wave speeds show much steeper gradients

Appendix C. Wave speeds approximation via Artificial Neural Networks

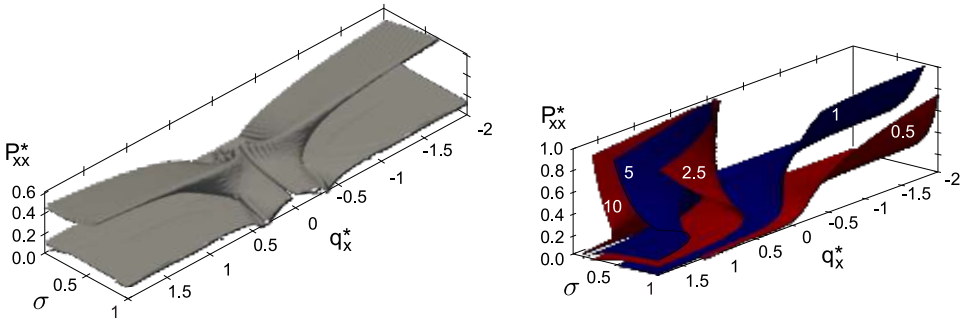


Figure C.6: Left: Hyperbolicity region for 6-moment system. The region enclosed in the contour has an imaginary part larger than 0.001. Right: Maximum dimensionless eigenvalue for the 6-moment system.

near equilibrium. Therefore, the scaling for the heat flux is modified to

$$\theta = \operatorname{asinh}(50\,000 q_x^*) . \quad (\text{C.8})$$

We then define $\xi = \log_{10}(\sigma)$ as before, and the wave speeds are also scaled as for the 5-moment system. By inspection of different $P_{xx}^* - \sigma$ planes for different values of q_x^* , the wave speeds appear to be smooth with respect to P_{xx}^* , except in the limit of $P_{xx}^* \rightarrow 0$, where the wave speeds quickly drop to zero. To alleviate this, a scaling $\zeta = \sqrt{P_{xx}^*}$ is introduced for the pressure. At equilibrium we have $\zeta = \sqrt{1/3}$. The maximum wave speeds after this scaling are shown in Fig. C.7 for some slices in the $(P_{xx}^*, q_x^*, \sigma)$ space.

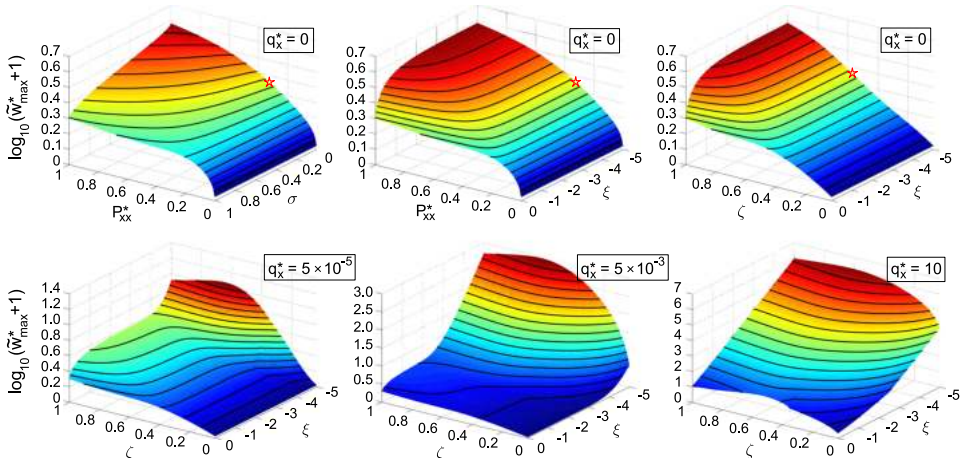


Figure C.7: Maximum wave speed of the 6-moment system. Slices in the P_{xx}^*, q_x^*, σ space for different values of q_x^* . Symbol \star identifies thermodynamic equilibrium.

The range for the training data is chosen to be

$$P_{xx}^* \in [10^{-3}, 1] , \quad q_x^* \in [-70, 70] \quad \text{and} \quad \sigma \in [10^{-5}, 1]. \quad (\text{C.9})$$

The choice $P_{xx}^* = 10^{-3}$ implies a rather high degree of pressures anisotropy, $P_{rr}^*/P_{xx}^* \approx 1000$, which we repute to be enough for the purpose of the present work.

The training data for the 5-10-5 and 5-5-5-5-5 ANNs was generated as follows. As a first step, 2 000 000 points were randomly seeded into the whole 3D domain. Then, 1.5 million additional points were seeded on two slices of the 3D domain, as to provide additional importance to the equilibrium. A schematic is shown in Fig. C.8. On such planes, the seeding is performed by patches, in an analogous manner to the 5-moment case. This proved enough for converging the smaller nets, while for more data is needed for the 15-20-15-10 ANN: for such case we keep the same seeding strategy, but increase the total number of points to 8.5 millions.

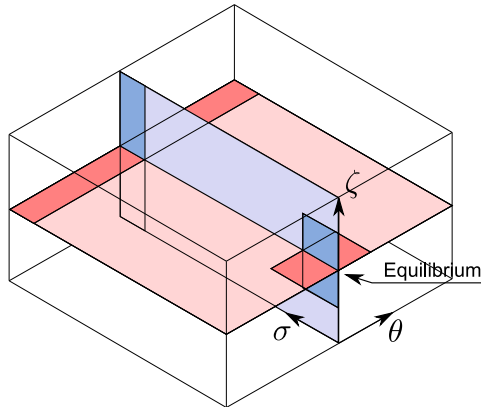


Figure C.8: Slices of the $\theta - \sigma - \xi$ space for the selection of training points, and patches for refined seeding.

Estimating the accuracy of the ANN fits is not trivial, due to the three dimensions involved, and since different regions of moment space bear different importance. For example, it is desirable to obtain good accuracy in the equilibrium plane, while a somewhat higher error could be accepted for extreme conditions of non-equilibrium. We report in Table C.3 an indication of the average error and its 95th percentile, obtained from Eq. (C.6), computed on 50 000 random points. The error is shown both for the whole moment space, by sampling points randomly in the whole domain, and also for equilibrium values of the pressure components, $P_{xx}^* = 1/3$, by probing the error on the $q_x - \sigma$ plane only. For all cases, the choice of seeding ad-

Appendix C. Wave speeds approximation via Artificial Neural Networks

ditional training points on the plane $P_{xx}^* = 1/3$ has the desirable effect of reducing the error in such region.

The error introduced by the simplest ANNs appears rather large, especially out of the equilibrium planes, where as indicated by the 95th percentile, one easily has oscillations of 100% roughly. Yet, this is a strong gain over the simplified expression “ $w = u \pm ka$ ”, where the error could reach some orders of magnitude. By analysis of the results, it appears that the maximum errors arise for situations of extremely high non-equilibrium, often for very low pressures $P_{xx}^* \approx 0.001$. It is possible to alleviate this error by seeding additional data specifically in such region of low P_{xx}^* , or to attempt different weightings of the seeding space. However, this goes beyond the scope of the present work. Also notice that special attention should be payed to the high- q_x^* region for low values of σ , as the numerical computation of eigenvalues gets stiffer and could fail certain algorithms.

Architecture	$\mu(E)$	$P_{95\%}(E)$	$\mu(E); \text{Peq}$	$P_{95\%}(E); \text{Peq}$	N_p
5-10-5	26.27 %	111.8 %	6.043 %	17.70 %	3.5×10^6
5-5-5-5-5	36.71 %	175.6 %	2.615 %	8.847 %	3.5×10^6
15-20-15-10	15.83 %	71.60 %	0.421 %	1.350 %	8.5×10^6

Table C.3: Error for different tested neural network architectures. $\mu(|E|)$ and $P_{95\%}(|E|)$ indicate the average of the absolute error and the 95th percentile. Symbol Peq indicates that the error is computed on a slice of moment space where the pressure tensor is isotropic. N_p is the approximated number of training points.

A further representation is given in Fig. C.9, where we show the errors of some nets, on a slice of the 3D moment space, with $P_{xx}^* = 1/3$. For rough estimations, the 5-10-5 ANN still provides a viable option, if one can accept a solution which is reasonable near equilibrium, but can introduce some error far from it (still reproducing the correct order of magnitude). The 5-5-5-5-5 ANN has the same total number of nodes as the 5-10-5, but is split in more stages. The training shows a better performance on the equilibrium plane, but a worse performance overall. The 15-20-15-10 ANN provides a much better accuracy, if the additional computational cost can be afforded.

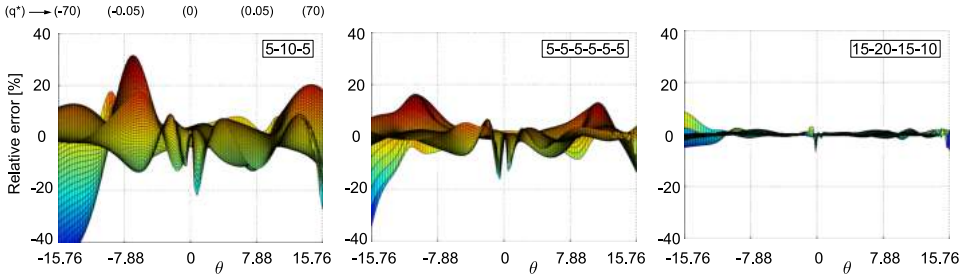


Figure C.9: Error in the predicted maximum wave speed for some ANN architectures, on the plane $P_{xx}^* = 1/3$, for different values of σ .

Concluding notes

To conclude, we resume here the procedure for applying the trained ANNs. For the 5-moment system:

$$\begin{pmatrix} \rho \\ u \\ P \\ q \\ r \end{pmatrix} \rightarrow \begin{pmatrix} q^* \\ \sigma \end{pmatrix} \rightarrow \begin{pmatrix} \theta^s \\ \xi^s \end{pmatrix} \rightarrow \text{ANN}(\theta^s, \xi^s) \rightarrow \begin{pmatrix} \log_{10}(w_{\max}^* + 1) \\ -\log_{10}(-w_{\min}^* + 1) \end{pmatrix} \rightarrow \begin{pmatrix} w_{\min} \\ w_{\max} \end{pmatrix}. \quad (\text{C.10})$$

The computational efficiency of employing the proposed ANNs architectures, in place of computing the eigenvalues numerically appears evident from the numerical simulations. The results are given in Fig. C.10, that compares the computational times of the 6-moment system in three cases: a) computing the eigenvalues from a finite-difference approximation of the Jacobian; b) computing the eigenvalues from the analytical Jacobian (that is available for the 6-moment system); and c) computing the wave speeds using the 5-10-5 ANN.



Figure C.10: Computational efficiency of the whole finite volume program (ms per time step) for 5000 grid cells: a) eigenvalues of numerical finite-difference Jacobian; b) eigenvalues of analytical Jacobian; c) neural nets approximation.

The analysis reported in this appendix can be extended to further moment systems, at the price of including additional unknowns. Regarding order-4 maximum-entropy systems, we suggest that a scaling based on σ^{-1}

Appendix C. Wave speeds approximation via Artificial Neural Networks

is employed in further simulations, as this would most likely improve the accuracy of the ANN training.

\mathcal{D}

APPENDIX

Implementation of the 14-moment wave speeds

We provide here an Octave/MATLAB script for the approximation of the wave speeds of the 14-moment system, as described in Section 4.2.3.

```
function [ws_max, ws_min] = ws_max_min_14mom(s, qx, qy_tilde, Pxx)

% s = sigma is a SCALAR.
% qx:          (array of) DIMENSIONLESS heat fluxes along the considered direction
% qy_tilde:    (array of) DIMENSIONLESS transversal heat flux
% Pxx:          (SCALAR)   DIMENSIONLESS pressure, Pxx/P

% Rename for convenience:
qy = qy_tilde;

% Approximated wave speeds
E = 8/10*sqrt((3 - 3*s)*Pxx);
C = sqrt((3 - 3*s)*Pxx);
B = 5 - 4*sqrt(s) + sqrt(10 - 16*sqrt(s) + 6*s);
Y = B + E^2 - 2*sqrt(B)*E;

a = 1.4*(Pxx^1.1)*exp(-Pxx^2);
b = 0.9*Pxx*exp(-1/2*Pxx^1.4);

% MAXIMUM WAVE SPEED
a_2 = 0.6;
a_1 = -0.38;
```

Appendix D. Implementation of the 14-moment wave speeds

```
a_0 = 0.35;
qx_hat = qx + sqrt(qy.^2)*(a_2*Pxx^2 + a_1*Pxx + a_0);
ws_max = (a*s + b)/(2*s)*(qx_hat + sqrt(qx_hat.^2 ...
-4/5*qx_hat*s*C + 4*s^2*Y + qy.^2/10)) + E;

% MINIMUM WAVE SPEED
qx_hat = -qx_hat;
ws_min = -( (a*s + b)/(2*s)*(qx_hat + sqrt(qx_hat.^2 ...
-4/5*qx_hat*s*C + 4*s^2*Y + qy.^2/10)) + E );
```

Bibliography

- [1] Hendrik Johannes Van der Bijl. *The thermionic vacuum tube and its applications*. McGraw-Hill book Company, Incorporated, 1920.
- [2] Michael A Lieberman and Alan J Lichtenberg. *Principles of plasma discharges and materials processing*. John Wiley & Sons, 2005.
- [3] A Haga, S Senda, Y Sakai, Y Mizuta, S Kita, and F Okuyama. A miniature x-ray tube. *Applied physics letters*, 84(12):2208–2210, 2004.
- [4] Victor Malka, S Fritzler, E Lefebvre, M-M Aleonard, F Burgy, J-P Chambaret, J-F Chemin, K Krushelnick, G Malka, SPD Mangles, et al. Electron acceleration by a wake field forced by an intense ultrashort laser pulse. *Science*, 298(5598):1596–1600, 2002.
- [5] Francis F Chen et al. *Introduction to plasma physics and controlled fusion*, volume 1. Springer, 1984.
- [6] Rudolf A Treumann and Wolfgang Baumjohann. *Advanced space plasma physics*, volume 30. Imperial College Press London, 1997.
- [7] Ernst Stuhlinger. *Ion propulsion for space flight*. McGraw-Hill New York, 1964.
- [8] Edgar Y Choueiri. A critical history of electric propulsion: The first 50 years (1906-1956). *Journal of Propulsion and Power*, 20(2):193–203, 2004.
- [9] Harold R Kaufman and Raymond S Robinson. Electric thruster performance for orbit raising and maneuvering. *Journal of Spacecraft and Rockets*, 21(2):180–186, 1984.
- [10] Robert J Vondra and Keith I Thomassen. Flight qualified pulsed electric thruster for satellite control. *Journal of Spacecraft and Rockets*, 11(9):613–617, 1974.
- [11] George P Sutton and Oscar Biblarz. *Rocket propulsion elements*. John Wiley & Sons, 2016.
- [12] Yves Langevin. Chemical and solar electric propulsion options for a cornerstone mission to mercury. *acta astronautica*, 47(2-9):443–452, 2000.
- [13] Giuseppe D Racca. Capability of solar electric propulsion for planetary missions. *Planetary and Space Science*, 49(14-15):1437–1444, 2001.
- [14] Kybeom Kwon, Gregory Lantoine, Ryan P Russell, and Dimitri N Mavris. A study on simultaneous design of a Hall Effect Thruster and its low-thrust trajectory. *Acta Astronautica*, 119:34–47, 2016.

Bibliography

- [15] K Mani, Stefano Boccelli, Francesco Topputo, Angelo Cervone, et al. Electric propulsion characterization for a stand-alone Mars CubeSat. In *36th International Electric Propulsion Conference*, pages 1–15, 2019.
- [16] Robert G Jahn. *Physics of electric propulsion*. Courier Corporation, 2006.
- [17] Eduardo Ahedo. Plasmas for space propulsion. *Plasma Physics and Controlled Fusion*, 53(12):124037, 2011.
- [18] Rodney L Burton. Pulsed plasma thrusters. *Encyclopedia of Aerospace Engineering*, 2010.
- [19] Derrek Russell, C Dailey, Wayne Goldstein, Ralph Lovberg, James Poylio, and Bernard Jackson. The PIT mark VI pulsed inductive thruster. In *Space 2004 Conference and Exhibit*, page 6054, 2004.
- [20] ROGER MYERS, MICHAEL LAPOINTE, and MARIS MANTENIEKS. MPD thruster technology. In *Conference on Advanced SEI Technologies*, page 3568, 1991.
- [21] Timothy Ziomba, John Carscadden, John Slough, James Prager, and Robert Winglee. High power helicon thruster. In *41st AIAA/ASME/SAE/ASEE Joint Propulsion Conference & Exhibit*, page 4119, 2005.
- [22] Edward Teller, Alexander J Glass, T Kenneth Fowler, Akira Hasegawa, and John F Santarius. Space propulsion by fusion in a magnetic dipole. *Fusion Technology*, 22(1):82–97, 1992.
- [23] Yosef S Razin, Gary Pajer, Mary Breton, Eric Ham, Joseph Mueller, Michael Paluszak, Alan H Glasser, and Samuel A Cohen. A direct fusion drive for rocket propulsion. *Acta Astronautica*, 105(1):145–155, 2014.
- [24] Dan M Goebel and Ira Katz. *Fundamentals of electric propulsion: ion and Hall thrusters*, volume 1. John Wiley & Sons, 2008.
- [25] AI Morozov and VV Savel'Ev. Fundamentals of stationary plasma thruster theory. *Reviews of plasma physics*, pages 203–391, 2000.
- [26] Viacheslav V Zhurin, Harold R Kaufman, and Raymond S Robinson. Physics of closed drift thrusters. *Plasma Sources Science and Technology*, 8(1):R1, 1999.
- [27] C Boniface, GJM Hagelaar, L Garrigues, JP Boeuf, and M Prioul. Modeling of double stage Hall effect thruster. *IEEE Transactions on Plasma Science*, 33(2):522–523, 2005.
- [28] D Pérez-Grande, P Fajardo, and E Ahedo. Evaluation of erosion reduction mechanisms in Hall effect thrusters. In *International Electric Propulsion Conference, Hyogo-Kobe*, 2015.
- [29] Ryan W Conversano, Dan M Goebel, Ioannis G Mikellides, Richard R Hofer, and Richard E Wirz. Performance analysis of a low-power magnetically shielded Hall thruster: computational modeling. *Journal of Propulsion and Power*, 33(4):992–1001, 2017.
- [30] Lou Grimaud and Stéphane Mazouffre. Conducting wall Hall thrusters in magnetic shielding and standard configurations. *Journal of Applied Physics*, 122(3):033305, 2017.
- [31] AI Morozov and VV Savel'Ev. Theory of the near-wall conductivity. *Plasma Physics Reports*, 27(7):570–575, 2001.
- [32] Dan M Goebel, Richard R Hofer, Ioannis G Mikellides, Ira Katz, James E Polk, and Brandon N Dotson. Conducting wall Hall thrusters. *IEEE Transactions on Plasma Science*, 43(1):118–126, 2014.
- [33] S Mazouffre, J Vaudolon, S Tsikata, C Henaux, D Harribey, and A Rossi. Optimization of the design of a wall-less Hall thruster. *Joint 30th ISTS, 34th IEPC and 6th*, 2703, 2015.
- [34] Mario Capitelli, Gianpiero Colonna, and Antonio D'Angola. *Fundamental aspects of plasma chemical physics*, volume 66. Springer, 2012.

- [35] Donald B Melrose. *Instabilities in space and laboratory plasmas*. 1986.
- [36] Sergey T Surzhikov. *Computational physics of electric discharges in gas flows*, volume 7. Walter de Gruyter, 2012.
- [37] Charles Hirsch. *Numerical computation of internal and external flows*. Wiley, 1997.
- [38] Nicolaas G van Kampen and Barend Ubbo Felderhof. Theoretical methods in plasma physics. *Amsterdam: North Holland Publication Co*, 1967.
- [39] JH Ferziger and HG Kaper. Mathematical theory of transport processes in gases. *American Journal of Physics*, 41(4):601–603, 1973.
- [40] Viktor Mikhaĭ Zhdanov. Transport processes in multicomponent plasma.
- [41] Francesco Taccogna and Giorgio Dilecce. Non-equilibrium in low-temperature plasmas. *The European Physical Journal D*, 70(11):1–37, 2016.
- [42] Jean-Pierre Boeuf. Tutorial: Physics and modeling of Hall thrusters. *Journal of Applied Physics*, 121(1):011101, 2017.
- [43] JC Adam, JP Boeuf, N Dubuit, M Dudeck, L Garrigues, D Gresillon, A Heron, GJM Hagelaar, V Kulaev, N Lemoine, et al. Physics, simulation and diagnostics of Hall effect thrusters. *Plasma Physics and Controlled Fusion*, 50(12):124041, 2008.
- [44] Andrey Shagayda. Stationary electron velocity distribution function in crossed electric and magnetic fields with collisions. *Physics of Plasmas*, 19(8):083503, 2012.
- [45] CH Shon and JK Lee. Modeling of magnetron sputtering plasmas. *Applied Surface Science*, 192(1-4):258–269, 2002.
- [46] Igor D Kaganovich, Andrei Smolyakov, Yevgeny Raitses, Eduardo Ahedo, Ioannis G Mikel-lides, Benjamin Jorns, Francesco Taccogna, Renaud Gueroult, Sedina Tsikata, Anne Bourdon, et al. Physics of $E \times B$ discharges relevant to plasma propulsion and similar technologies. *Physics of Plasmas*, 27(12):120601, 2020.
- [47] Kentaro Hara and Sedina Tsikata. Cross-field electron diffusion due to the coupling of drift-driven microinstabilities. *Physical Review E*, 102(2):023202, 2020.
- [48] Trevor Lafleur, SD Baalrud, and Pascal Chabert. Theory for the anomalous electron transport in Hall effect thrusters. II. kinetic model. *Physics of Plasmas*, 23(5):053503, 2016.
- [49] Jean-Pierre Boeuf and Laurent Garrigues. $E \times B$ electron drift instability in Hall thrusters: Particle-in-cell simulations vs. theory. *Physics of Plasmas*, 25(6):061204, 2018.
- [50] Thomas Charoy, Jean-Pierre Boeuf, Anne Bourdon, Johan A Carlsson, Pascal Chabert, B Cuenot, Denis Eremin, Laurent Garrigues, Kentaro Hara, Igor D Kaganovich, et al. 2D axial-azimuthal particle-in-cell benchmark for low-temperature partially magnetized plasmas. *Plasma Sources Science and Technology*, 28(10):105010, 2019.
- [51] Luc Mieussens. Discrete velocity model and implicit scheme for the BGK equation of rarefied gas dynamics. *Mathematical Models and Methods in Applied Sciences*, 10(08):1121–1149, 2000.
- [52] RJ Kingham and AR Bell. An implicit vlasov–fokker–planck code to model non-local electron transport in 2-d with magnetic fields. *Journal of Computational Physics*, 194(1):1–34, 2004.
- [53] Charles K Birdsall and A Bruce Langdon. *Plasma physics via computer simulation*. CRC press, 2004.
- [54] Francesco Taccogna, Savino Longo, Mario Capitelli, and Ralf Schneider. Self-similarity in Hall plasma discharges: Applications to particle models. *Physics of Plasmas*, 12(5):053502, 2005.

Bibliography

- [55] K Matyash, R Schneider, S Mazouffre, S Tsikata, Y Raitses, and A Diallo. 3D simulation of the rotating spoke in a Hall thruster. In *Proceedings of the 33rd International Electric Propulsion Conference*, volume 32, 2013.
- [56] James Joseph Szabo. *Fully kinetic numerical modeling of a plasma thruster*. PhD thesis, Massachusetts Institute of Technology, 2001.
- [57] D Sydorenko, A Smolyakov, I Kaganovich, and Y Raitses. Kinetic simulation of secondary electron emission effects in Hall thrusters. *Physics of Plasmas*, 13(1):014501, 2006.
- [58] Trevor Lafleur, SD Baalrud, and Pascal Chabert. Theory for the anomalous electron transport in Hall effect thrusters. I. insights from particle-in-cell simulations. *Physics of Plasmas*, 23(5):053502, 2016.
- [59] Zahra Asadi, Francesco Taccogna, and Mehdi Sharifian. Numerical study of electron cyclotron drift instability: Application to Hall thruster. *Frontiers in Physics*, 7:140, 2019.
- [60] FI Parra, E Ahedo, JM Fife, and M Martinez-Sanchez. A two-dimensional hybrid model of the Hall thruster discharge. *Journal of Applied Physics*, 100(2):023304, 2006.
- [61] Andrey Shashkov, Alexander Lovtsov, and Dmitry Tomilin. A one-dimensional with three-dimensional velocity space hybrid-PIC model of the discharge plasma in a Hall thruster. *Physics of Plasmas*, 24(4):043501, 2017.
- [62] Henning Struchtrup. Macroscopic transport equations for rarefied gas flows. In *Macroscopic transport equations for rarefied gas flows*, pages 145–160. Springer, 2005.
- [63] Harold Grad. On the kinetic theory of rarefied gases. *Communications on pure and applied mathematics*, 2(4):331–407, 1949.
- [64] C David Levermore. Moment closure hierarchies for kinetic theories. *Journal of statistical Physics*, 83(5):1021–1065, 1996.
- [65] Ingo Müller and Tommaso Ruggeri. *Rational extended thermodynamics*, volume 37. Springer Science & Business Media, 2013.
- [66] Michael Junk. Domain of definition of Levermore’s five-moment system. *Journal of Statistical Physics*, 93(5):1143–1167, 1998.
- [67] James McDonald and Manuel Torrilhon. Affordable robust moment closures for CFD based on the maximum-entropy hierarchy. *Journal of Computational Physics*, 251:500–523, 2013.
- [68] Sean T Miller and Uri Shumlak. A multi-species 13-moment model for moderately collisional plasmas. *Physics of Plasmas*, 23(8):082303, 2016.
- [69] Shaun Gilliam. *A 13-moment two-fluid plasma physics model based on a Pearson type-IV distribution function*. PhD thesis, University of Washington, 2011.
- [70] Andrew Ho, Iman Anwar Michael Datta, and Uri Shumlak. Physics-based-adaptive plasma model for high-fidelity numerical simulations. *Frontiers in Physics*, 6:105, 2018.
- [71] David J Larson. Kinetic plasma simulation using a quadrature-based moment method. *Bulletin of the American Physical Society*, 53, 2008.
- [72] Javier Martines Martinez, Dmytro Rafalskyi, and Ane Aanesland. Development and testing of the NPT30-I2 iodine ion thruster. In *36th International Electric Propulsion Conference*, number 15-20, 2019.
- [73] Mikhail Naumovich Kogan. *Rarefied Gas Dynamics*. Plenum Press, New York, 1969.
- [74] Richard L Liboff. *Kinetic theory: classical, quantum, and relativistic descriptions*. Springer Science & Business Media, 2003.

- [75] Yu L Klimontovich. The statistical theory of non-equilibrium processes in a plasma. *Journal of Plasma Physics*, 3:148, 1969.
- [76] Iu I Klimontovich. Kinetic theory of nonideal gas and nonideal plasma. *Moscow Izdatel Nauka*, 1975.
- [77] Dwight Roy Nicholson and Dwight R Nicholson. *Introduction to plasma theory*. Wiley New York, 1983.
- [78] Vincent Giovangigli. Multicomponent flow modeling. *Science China Mathematics*, 55(2):285–308, 2012.
- [79] Yuri N Dnestrovskii and Dimitri P Kostomarov. *Numerical simulation of plasmas*. Springer Science & Business Media, 2012.
- [80] Prabhu Lal Bhatnagar, Eugene P Gross, and Max Krook. A model for collision processes in gases. I. small amplitude processes in charged and neutral one-component systems. *Physical review*, 94(3):511, 1954.
- [81] Carlo Cercignani. The Boltzmann equation and its applications. pages 40–103. Springer, 1988.
- [82] Luc Mieussens and Henning Struchtrup. Numerical comparison of Bhatnagar–Gross–Krook models with proper prandtl number. *Physics of Fluids*, 16(8):2797–2813, 2004.
- [83] Johannes Martinus Burgers. *Flow equations for composite gases*. Maryland University College Park Institute for Fluid Dynamics and Applied Mathematics, 1969.
- [84] Marzia Bisi and Maria José Cáceres. A BGK relaxation model for polyatomic gas mixtures. *Communications in Mathematical Sciences*, 14(2):297–325, 2016.
- [85] Florian Bernard, Angelo Iollo, and Gabriella Puppo. BGK polyatomic model for rarefied flows. *Journal of Scientific Computing*, 78(3):1893–1916, 2019.
- [86] Henning Struchtrup. The BGK-model with velocity-dependent collision frequency. *Continuum Mechanics and Thermodynamics*, 9(1):23–31, 1997.
- [87] Fran ois Bouchut and Beno t Perthame. A BGK model for small Prandtl number in the Navier-Stokes approximation. *Journal of statistical physics*, 71(1):191–207, 1993.
- [88] John M Sankovic, John A Hamley, and Thomas W Haag. Performance evaluation of the russian SPT-100 thruster at NASA LeRC. 1993.
- [89] OA Mitrofanova, R Yu Gnizdor, VM Murashko, AI Koryakin, and AN Nesterenko. New generation of SPT-100. In *32nd International Electric Propulsion Conference*, pages 2011–041, 2011.
- [90] E Ahedo, P Mart nez-Cerezo, and M Mart nez-S nchez. One-dimensional model of the plasma flow in a Hall thruster. *Physics of Plasmas*, 8(6):3058–3068, 2001.
- [91] Vanessa Vial, A Lazurenko, D Pagnon, and A Bouchoule. Measurement of absolute xenon density and gas injection impact in Hall thrusters. In *4th International Spacecraft Propulsion Conference*, volume 555, 2004.
- [92] John David Jackson. Classical electrodynamics, 1999.
- [93] Biagi database. www.lxcat.net. retrieved on February 22, 2021.
- [94] Leanne C Pitchford, Luis L Alves, Klaus Bartschat, Stephen F Biagi, Marie-Claude Bordage, Igor Bray, Chris E Brion, Michael J Brunger, Laurence Campbell, Alise Chachereau, et al. Lxcat: An open-access, web-based platform for data needed for modeling low temperature plasmas. *Plasma Processes and Polymers*, 14(1-2):1600098, 2017.

Bibliography

- [95] Richard Fitzpatrick. Introduction to plasma physics. *The University of Texas at Austin: sn*, page 242, 2008.
- [96] RJ Goldston, PH Rutherford, and J Wesson. Introduction to plasma physics. *Plasma Physics and Controlled Fusion*, 38(1):103, 1996.
- [97] S Barral, N Gascon, K Makowski, Z Peradzyński, and M Dudeck. Numerical study of the current-voltage characteristic of Hall thrusters. In *27th International Electric Propulsion Conference, IEPC*, pages 01–27, 2001.
- [98] Serge Barral, Karol Makowski, Zbigniew Peradzyński, and Michel Dudeck. Transit-time instability in Hall thrusters. *Physics of Plasmas*, 12(7):073504, 2005.
- [99] J Pérez-Luna, GJM Hagelaar, L Garrigues, and JP Boeuf. Method to obtain the electric field and the ionization frequency from laser induced fluorescence measurements. *Plasma Sources Science and Technology*, 18(3):034008, 2009.
- [100] GJM Hagelaar, J Bareilles, LBJP Garrigues, and J-P Boeuf. Two-dimensional model of a stationary plasma thruster. *Journal of Applied Physics*, 91(9):5592–5598, 2002.
- [101] Sydney Chapman, Thomas George Cowling, and David Burnett. *The mathematical theory of non-uniform gases: an account of the kinetic theory of viscosity, thermal conduction and diffusion in gases*. Cambridge university press, 1990.
- [102] David Burnett. The distribution of velocities in a slightly non-uniform gas. *Proceedings of the London Mathematical Society*, 2(1):385–430, 1935.
- [103] Keith Comeaux, Dean Chapman, Ma, and Robert Cormack. An analysis of the burnett equations based on the second law of thermodynamics. In *33rd Aerospace sciences meeting and exhibit*, page 415, 1995.
- [104] Xiaolin Zhong. Development and computation of continuum higher order constitutive relations for high-altitude hypersonic flow. 1992.
- [105] Benjamin Graille, Thierry E Magin, and Marc Massot. Kinetic theory of plasmas: translational energy. *Mathematical Models and Methods in Applied Sciences*, 19(04):527–599, 2009.
- [106] Radu Balescu. Transport processes in plasmas. 1988.
- [107] SI Braginskii. Transport processes in a plasma. *Reviews of Plasma Physics*, 1:205, 1963.
- [108] Manuel Torrilhon. Convergence study of moment approximations for boundary value problems of the Boltzmann-BGK equation. *Communications in Computational Physics*, 18(3):529–557, 2015.
- [109] George V Khazanov. *Kinetic theory of the inner magnetospheric plasma*, volume 372. Springer Science & Business Media, 2010.
- [110] M Torrilhon. Characteristic waves and dissipation in the 13-moment-case. *Continuum Mechanics and Thermodynamics*, 12(5):289–301, 2000.
- [111] Henning Struchtrup and Manuel Torrilhon. Regularization of Grad’s 13 moment equations: Derivation and linear analysis. *Physics of Fluids*, 15(9):2668–2680, 2003.
- [112] M Torrilhon and Henning Struchtrup. Regularized 13-moment equations: shock structure calculations and comparison to Burnett models. *Journal of Fluid Mechanics*, 513:171, 2004.
- [113] Olivier Desjardins, Rodney O Fox, and Philippe Villedieu. A quadrature-based moment method for dilute fluid-particle flows. *Journal of Computational Physics*, 227(4):2514–2539, 2008.
- [114] Rodney O Fox. Higher-order quadrature-based moment methods for kinetic equations. *Journal of Computational Physics*, 228(20):7771–7791, 2009.

- [115] Manuel Torrilhon. Hyperbolic moment equations in kinetic gas theory based on multi-variate Pearson-IV-distributions. *Communications in Computational Physics*, 7(4):639, 2010.
- [116] GM8807460618 Kremer. Extended thermodynamics of ideal gases with 14 fields. In *Annales de l'IHP Physique théorique*, volume 45, pages 419–440, 1986.
- [117] Boone R Tensuda, James G McDonald, and Clinton PT Groth. Multi-dimensional validation of a maximum-entropy-based interpolative moment closure. In *AIP Conference Proceedings*, volume 1786, page 140008. AIP Publishing LLC, 2016.
- [118] JG McDonald, JS Sachdev, and CPT Groth. Use of the gaussian moment closure for the modelling of continuum and micron-scale flows with moving boundaries. In *Computational Fluid Dynamics 2006*, pages 783–788. Springer, 2009.
- [119] James G McDonald. *Extended fluid-dynamic modelling for numerical solution of micro-scale flows*. University of Toronto, 2011.
- [120] François Forges and James G McDonald. Higher-order moment models for laminar multiphase flows with accurate particle-stream crossing. *International Journal of Multiphase Flow*, 114:28–38, 2019.
- [121] Joachim AR Sarr and Clinton PT Groth. A second-order maximum-entropy inspired interpolative closure for radiative heat transfer in gray participating media. *Journal of Quantitative Spectroscopy and Radiative Transfer*, 255:107238, 2020.
- [122] Vittorio Romano. 2D simulation of a silicon MESFET with a nonparabolic hydrodynamical model based on the maximum entropy principle. *Journal of Computational Physics*, 176(1):70–92, 2002.
- [123] Michael Junk and Andreas Unterreiter. Maximum entropy moment systems and Galilean invariance. *Continuum Mechanics and Thermodynamics*, 14(6):563–576, 2002.
- [124] Hans Ludwig Hamburger. Hermitian transformations of deficiency-index (1, 1), Jacobi matrices and undetermined moment problems. *American Journal of Mathematics*, 66(4):489–522, 1944.
- [125] MJ Druyvesteyn and Fi M Penning. The mechanism of electrical discharges in gases of low pressure. *Reviews of Modern Physics*, 12(2):87, 1940.
- [126] James G McDonald and Clinton PT Groth. Towards realizable hyperbolic moment closures for viscous heat-conducting gas flows based on a maximum-entropy distribution. *Continuum Mechanics and Thermodynamics*, 25(5):573–603, 2013.
- [127] James G McDonald. Approximate maximum-entropy moment closures for gas dynamics. In *AIP Conference Proceedings*, volume 1786, page 140001. AIP Publishing LLC, 2016.
- [128] Reinhard Illner and Helmut Neunzert. On simulation methods for the Boltzmann equation. *Transport Theory and Statistical Physics*, 16(2-3):141–154, 1987.
- [129] Graeme A Bird. Molecular gas dynamics and the direct simulation of gas flows. *Molecular gas dynamics and the direct simulation of gas flows*, 1994.
- [130] Roger W Hockney and James W Eastwood. *Computer simulation using particles*. crc Press, 1988.
- [131] Jay P Boris. Acceleration calculation from a scalar potential. Technical report, Princeton Univ., NJ Plasma Physics Lab., 1970.
- [132] Giovanni Lapenta. Particle in cell methods. In *With Application to Simulations in Space Weather*. Citeseer, 2016.
- [133] Vahid Vahedi and Maheswaran Surendra. A Monte Carlo collision model for the particle-in-cell method: applications to argon and oxygen discharges. *Computer Physics Communications*, 87(1-2):179–198, 1995.

Bibliography

- [134] GA Bird. Approach to translational equilibrium in a rigid sphere gas. *The Physics of Fluids*, 6(10):1518–1519, 1963.
- [135] Iain D Boyd and Thomas E Schwartzentruber. *Nonequilibrium Gas Dynamics and Molecular Simulation*, volume 42. Cambridge University Press, 2017.
- [136] Felix Sharipov. *Rarefied gas dynamics: fundamentals for research and practice*. John Wiley & Sons, 2015.
- [137] Carlo Cercignani and Maria Lampis. Kinetic models for gas-surface interactions. *transport theory and statistical physics*, 1(2):101–114, 1971.
- [138] RG Lord. Some extensions to the Cercignani–Lampis gas–surface scattering kernel. *Physics of Fluids A: Fluid Dynamics*, 3(4):706–710, 1991.
- [139] RG Lord. Some further extensions of the Cercignani–Lampis gas–surface interaction model. *Physics of Fluids*, 7(5):1159–1161, 1995.
- [140] Randall J LeVeque and Randall J Leveque. *Numerical methods for conservation laws*, volume 132. Springer, 1992.
- [141] Randall J LeVeque et al. *Finite volume methods for hyperbolic problems*, volume 31. Cambridge university press, 2002.
- [142] Eleuterio F Toro. *Riemann solvers and numerical methods for fluid dynamics: a practical introduction*. Springer Science & Business Media, 2013.
- [143] Philip L Roe. Characteristic-based schemes for the Euler equations. *Annual review of fluid mechanics*, 18(1):337–365, 1986.
- [144] Meng-Sing Liou. The evolution of AUSM schemes. *Defence Science Journal*, 60(6), 2010.
- [145] DI Pullin. Direct simulation methods for compressible inviscid ideal-gas flow. *Journal of Computational Physics*, 34(2):231–244, 1980.
- [146] Benoit Perthame. Second-order Boltzmann schemes for compressible Euler equations in one and two space dimensions. *SIAM Journal on Numerical Analysis*, 29(1):1–19, 1992.
- [147] Haim Nessyahu and Eitan Tadmor. Non-oscillatory central differencing for hyperbolic conservation laws. *Journal of computational physics*, 87(2):408–463, 1990.
- [148] Alexander Kurganov and Eitan Tadmor. New high-resolution central schemes for nonlinear conservation laws and convection–diffusion equations. *Journal of Computational Physics*, 160(1):241–282, 2000.
- [149] Amiram Harten, Peter D Lax, and Bram van Leer. On upstream differencing and Godunov-type schemes for hyperbolic conservation laws. *SIAM review*, 25(1):35–61, 1983.
- [150] Roman Pascal Schaefer, Pratyuksh Bansal, and Manuel Torrilhon. Efficient algorithms and implementations of entropy-based moment closures for rarefied gases. *Journal of Computational Physics*, 340:138–159, 2017.
- [151] C Kristopher Garrett, Cory Hauck, and Judith Hill. Optimization and large scale computation of an entropy-based moment closure. *Journal of Computational Physics*, 302:573–590, 2015.
- [152] Bram Van Leer. Towards the ultimate conservative difference scheme. II. monotonicity and conservation combined in a second-order scheme. *Journal of computational physics*, 14(4):361–370, 1974.
- [153] Miroslav Čada and Manuel Torrilhon. Compact third-order limiter functions for finite volume methods. *Journal of Computational Physics*, 228(11):4118–4145, 2009.
- [154] Boone R Tensuda, James McDonald, and Clinton P Groth. Application of a maximum-entropy-based 14-moment closure for multi-dimensional non-equilibrium flows. In *22nd AIAA Computational Fluid Dynamics Conference*, page 3420, 2015.

- [155] Alessandro Munafò, Jeffrey R Haack, Irene M Gamba, and Thierry E Magin. A spectral-Lagrangian Boltzmann solver for a multi-energy level gas. *Journal of Computational Physics*, 264:152–176, 2014.
- [156] José A Morales Escalante, Irene M Gamba, Eirik Endeve, and Cory Hauck. Positivity preserving DG schemes for a Boltzmann-Poisson model of electrons in semiconductors in curvilinear momentum coordinates. *arXiv preprint arXiv:1711.03949*, 2017.
- [157] Aldo Frezzotti, Gian Pietro Ghioldi, and Livio Gibelli. Solving the Boltzmann equation on GPUs. *Computer Physics Communications*, 182(12):2445–2453, 2011.
- [158] Stefano Boccelli. FVkin. <https://github.com/sboccce/fvkin>, 2019.
- [159] Roman Pascal Schaerer and Manuel Torrilhon. On singular closures for the 5-moment system in kinetic gas theory. *Communications in Computational Physics*, 17(2):371–400, 2015.
- [160] Gary A Sod. A survey of several finite difference methods for systems of nonlinear hyperbolic conservation laws. *Journal of computational physics*, 27(1):1–31, 1978.
- [161] Ya B Zeldovich, Yuri Petrovich Raizer, WD Hayes, and RF Probstein. *Physics of shock waves and high-temperature hydrodynamic phenomena*. Vol. 2. Academic Press New York, 1967.
- [162] Hans Wolfgang Liepmann and Anatol Roshko. *Elements of gasdynamics*. Courier Corporation, 2001.
- [163] Joe D Hoffman and Maurice Joseph Zucrow. *Gas dynamics*. Wiley, 1976.
- [164] JM Picone, AE Hedin, D Pj Drob, and AC Aikin. NRLMSISE-00 empirical model of the atmosphere: Statistical comparisons and scientific issues. *Journal of Geophysical Research: Space Physics*, 107(A12):SIA–15, 2002.
- [165] Eswar Josyula and Jonathan Burt. Review of rarefied gas effects in hypersonic applications. Technical report, AIR FORCE RESEARCH LAB WRIGHT-PATTERSON AFB OH, 2011.
- [166] Harold Meade Mott-Smith. The solution of the Boltzmann equation for a shock wave. *Physical Review*, 82(6):885, 1951.
- [167] Aldo Frezzotti, Gian Pietro Ghioldi, and Livio Gibelli. Solving model kinetic equations on GPUs. *Computers & fluids*, 50(1):136–146, 2011.
- [168] Alessandro Munafò. *Multi-Scale models and computational methods for aerothermodynamics*. PhD thesis, Ecole Centrale Paris, 2014.
- [169] S Venkateswaran and Charles Merkle. Dual time-stepping and preconditioning for unsteady computations. In *33rd Aerospace Sciences Meeting and Exhibit*, page 78, 1995.
- [170] H Martin Bücker, Bernhard Pollul, and Arno Rasch. On CFL evolution strategies for implicit upwind methods in linearized Euler equations. *International journal for numerical methods in fluids*, 59(1):1–18, 2009.
- [171] Ken Miura. *Development of a Multifluid Magnetohydrodynamic Model for Anisotropic, Partially Ionized Plasmas*. PhD thesis, 2019.
- [172] Amir R Baradaran. *Development and implementation of a preconditioner for a five-moment one-dimensional moment closure*. PhD thesis, Université d’Ottawa/University of Ottawa, 2015.
- [173] PQ Elias, J Jarrige, E Cucchetti, F Cannat, and D Packan. 3D ion velocity distribution function measurement in an electric thruster using laser induced fluorescence tomography. *Review of Scientific Instruments*, 88(9):093511, 2017.
- [174] Bernard B Hamel and D Roger Willis. Kinetic theory of source flow expansion with application to the free jet. *The physics of Fluids*, 9(5):829–841, 1966.

Bibliography

- [175] Susmita Sarkar, Samit Paul, and Raicharan Denra. Bump-on-tail instability in space plasmas. *Physics of Plasmas*, 22(10):102109, 2015.
- [176] Stefano Boccelli, T Charoy, Alejandro Alvarez Laguna, Pascal Chabert, Anne Bourdon, and Thierry E Magin. Collisionless ion modeling in Hall thrusters: Analytical axial velocity distribution function and heat flux closures. *Physics of Plasmas*, 27(7):073506, 2020.
- [177] Vernon H Chaplin, Benjamin A Jorns, Alejandro Lopez Ortega, Ioannis G Mikellides, Ryan W Conversano, Robert B Lobbia, and Richard R Hofer. Laser-induced fluorescence measurements of acceleration zone scaling in the 12.5 kW HERMeS Hall thruster. *Journal of Applied Physics*, 124(18):183302, 2018.
- [178] S Mazouffre and G Bourgeois. Spatio-temporal characteristics of ion velocity in a Hall thruster discharge. *Plasma Sources Science and Technology*, 19(6):065018, 2010.
- [179] Kentaro Hara, Iain D Boyd, and Vladimir I Kolobov. One-dimensional hybrid-direct kinetic simulation of the discharge plasma in a Hall thruster. *Physics of Plasmas*, 19(11):113508, 2012.
- [180] Lyon B King and Alec D Gallimore. Ion-energy diagnostics in an SPT-100 plume from thrust axis to backflow. *Journal of propulsion and power*, 20(2):228–242, 2004.
- [181] Ioannis G Mikellides, Ira Katz, Robert A Kuharski, and Myron J Mandell. Elastic scattering of ions in electrostatic thruster plumes. *Journal of propulsion and power*, 21(1):111–118, 2005.
- [182] JP Boeuf and L Garrigues. Low frequency oscillations in a stationary plasma thruster. *Journal of Applied Physics*, 84(7):3541–3554, 1998.
- [183] Lewi Tonks and Irving Langmuir. A general theory of the plasma of an arc. *Physical review*, 34(6):876, 1929.
- [184] ER Harrison and WB Thompson. The low pressure plane symmetric discharge. *Proceedings of the Physical Society (1958-1967)*, 74(2):145, 1959.
- [185] SG Ingram and N St J Braithwaite. Ion and electron energy analysis at a surface in an RF discharge. *Journal of Physics D: Applied Physics*, 21(10):1496, 1988.
- [186] Thomas Charoy. *Numerical study of electron transport in Hall thrusters*. PhD thesis, Institut Polytechnique de Paris, 2020.
- [187] L Garrigues, S Mazouffre, and G Bourgeois. Computed versus measured ion velocity distribution functions in a Hall effect thruster. *Journal of Applied Physics*, 111(11):113301, 2012.
- [188] D Gawron, S Mazouffre, N Sadeghi, and A Héron. Influence of magnetic field and discharge voltage on the acceleration layer features in a Hall effect thruster. *Plasma Sources Science and Technology*, 17(2):025001, 2008.
- [189] B Graille, TE Magin, and M Massot. Modeling of reactive plasmas for atmospheric entry flows based on kinetic theory. In *Proceedings of the Summer Program*, page 17, 2008.
- [190] Pascal Chabert and Nicholas Braithwaite. *Physics of radio-frequency plasmas*. Cambridge University Press, 2011.
- [191] MV Berry and DHJ O'Dell. Ergodicity in wave-wave diffraction. *Journal of Physics A: Mathematical and General*, 32(19):3571, 1999.
- [192] Denis A Silantyev, Pavel M Lushnikov, and Harvey A Rose. Langmuir wave filamentation in the kinetic regime. I. filamentation instability of Bernstein-Greene-Kruskal modes in multidimensional Vlasov simulations. *Physics of Plasmas*, 24(4):042104, 2017.
- [193] Gui-Qiang Chen and Hailiang Liu. Formation of δ -shocks and vacuum states in the vanishing pressure limit of solutions to the Euler equations for isentropic fluids. *SIAM journal on mathematical analysis*, 34(4):925–938, 2003.

- [194] E Ahedo, JM Gallardo, and M Martínez-Sánchez. Model of the plasma discharge in a Hall thruster with heat conduction. *Physics of Plasmas*, 9(9):4061–4070, 2002.
- [195] John Tamin Yim. *Computational Modeling of Hall Thruster Channel Wall Erosion*. PhD thesis, 2008.
- [196] Yongjun Choi. *Modeling an Anode Layer Hall Thruster and its Plume*. PhD thesis, 2008.
- [197] A De Marco Enrico and Andrenucci Mariano. 3D transient modeling of Hall thrusters: a fully fluid approach. 2009.
- [198] François Bouchut, Shi Jin, and Xiantao Li. Numerical approximations of pressureless and isothermal gas dynamics. *SIAM Journal on Numerical Analysis*, 41(1):135–158, 2003.
- [199] Naveen Kumar Garg, Michael Junk, SV Rao, and M Sekhar. An upwind method for genuine weakly hyperbolic systems. *arXiv preprint arXiv:1703.08751*, 2017.
- [200] S Boccelli, F Giroux, TE Magin, CPT Groth, and JG McDonald. A 14-moment maximum-entropy description of electrons in crossed electric and magnetic fields. *Physics of Plasmas*, 27(12):123506, 2020.
- [201] Stefano Boccelli, Pietro Parodi, Lorenzo Vallisa, Willem Kaufmann, Paolo Barbante, James G McDonald, and Thierry E Magin. Maximum-entropy 14 moments description of non-equilibrium electrons in crossed electric and magnetic fields. *Bulletin of the American Physical Society*, 2020.
- [202] TE Sheridan, MJ Goeckner, and J Goree. Electron velocity distribution functions in a sputtering magnetron discharge for the $E \times B$ direction. *Journal of Vacuum Science & Technology A: Vacuum, Surfaces, and Films*, 16(4):2173–2176, 1998.
- [203] G Guerrini, C Michaut, M Dudeck, AN Vesselovzorov, and M Bacal. Characterization of plasma inside the SPT-50 channel by electrostatic probes. In *25th International Electric Propulsion Conference*, pages 97–053, 1997.
- [204] V Lago, M de Graaf, and M Dudeck. Electron energy distribution function in a stationary plasma thruster plume. *AIAA Paper*, (97-3049), 1997.
- [205] Naohiko Shimura and Toshiaki Makabe. Electron velocity distribution function in a gas in $E \times B$ fields. *Applied physics letters*, 62(7):678–680, 1993.
- [206] V Yu Fedotov, AA Ivanov, G Guerrini, AN Vesselovzorov, and M Bacal. On the electron energy distribution function in a Hall-type thruster. *Physics of Plasmas*, 6(11):4360–4365, 1999.
- [207] S Barral, Z Peradzynski, K Makowski, and M Dudeck. About the double-humped electron distribution function in Hall thrusters. In *Proceedings of the 27th International Electric Propulsion Conference*, 2000.
- [208] AA Shagayda, SA Stepin, and AG Tarasov. Electron velocity distribution moments for collisional inhomogeneous plasma in crossed electric and magnetic fields. *Russian Journal of Mathematical Physics*, 22(4):532–545, 2015.
- [209] Andrey Shagayda, Aleksey Tarasov, and Dmitry Tomilin. Analytical and numerical study of electron velocity distribution function in a Hall discharge. In *The 35th International Electric Propulsion Conference*, 2017.
- [210] ID Kaganovich, Yevgeny Raitses, Dmytro Sydorenko, and Andrei Smolyakov. Kinetic effects in a Hall thruster discharge. *Physics of Plasmas*, 14(5):057104, 2007.
- [211] Yevgeny Raitses, Igor D Kaganovich, Alexander Khrabrov, Dmytro Sydorenko, Nathaniel J Fisch, and Andrei Smolyakov. Effect of secondary electron emission on electron cross-field current in ExB discharges. *IEEE Transactions on Plasma Science*, 39(4):995–1006, 2011.

Bibliography

- [212] John R Lamarsh. *Introduction to nuclear reactor theory*. Addison-Wesley, 1966.
- [213] M Surendra, DB Graves, and GM Jellum. Self-consistent model of a direct-current glow discharge: Treatment of fast electrons. *Physical Review A*, 41(2):1112, 1990.
- [214] David Stirzaker. *Elementary probability*. Cambridge University Press, 2003.
- [215] Pierre Andries, Kazuo Aoki, and Benoit Perthame. A consistent BGK-type model for gas mixtures. *Journal of Statistical Physics*, 106(5):993–1018, 2002.
- [216] George W Sutton and Arthur Sherman. *Engineering magnetohydrodynamics*. Courier Dover Publications, 2006.
- [217] Stefano Boccelli, Thierry E Magin, and Aldo Frezzotti. Numerical investigation of reversed gas feed configurations for Hall thrusters. *Under Review*.
- [218] Samuel J Araki. Radiosity view factor model for sources with general distribution. *Journal of Computational Physics*, 406:109146, 2020.
- [219] G Guerrini, C Michaut, M Dudeck, and M Bacal. Parameter analysis of three ion thrusters (SPT-20, SPT-50 and A-3). In *European Spacecraft Propulsion Conference*, volume 398, page 441, 1997.
- [220] Daniel L Brown, C William Larson, Brian E Beal, and Alec D Gallimore. Methodology and historical perspective of a Hall thruster efficiency analysis. *Journal of Propulsion and Power*, 25(6):1163–1177, 2009.
- [221] Y Raitses, J Ashkenazy, and M Guelman. Propellant utilization in Hall thrusters. *Journal of Propulsion and Power*, 14(2):247–253, 1998.
- [222] Kimitomo Komurasaki and Yoshihiro Arakawa. Performance calculation of Hall thrusters. *Acta astronautica*, 38(3):185–192, 1996.
- [223] Bryan M Reid and Alec D Gallimore. Review of Hall thruster neutral flow dynamics. In *30th International Electric Propulsion Conference*, pages 2007–038, 2007.
- [224] L Garrigues, GJM Hagelaar, C Boniface, and JP Boeuf. Optimized atom injection in a Hall effect thruster. *Applied physics letters*, 85(22):5460–5462, 2004.
- [225] SJ Plimpton, SG Moore, A Borner, AK Stagg, TP Koehler, JR Torczynski, and MA Gallis. Direct simulation Monte Carlo on petaflop supercomputers and beyond. *Physics of Fluids*, 31(8):086101, 2019.
- [226] Carl F Book and Mitchell LR Walker. Effect of anode temperature on Hall thruster performance. *Journal of Propulsion and Power*, 26(5):1036–1044, 2010.
- [227] Rafael A Martinez and Mitchell LR Walker. Propellant thermal management effect on neutral residence time in low-voltage Hall thrusters. *Journal of Propulsion and Power*, 29(3):528–539, 2013.
- [228] Wensheng Huang, Alec D Gallimore, and Richard R Hofer. Neutral flow evolution in a six-kilowatt Hall thruster. *Journal of Propulsion and Power*, 27(3):553–563, 2011.
- [229] S Mazouffre, P Echegut, and M Dudeck. A calibrated infrared imaging study on the steady state thermal behaviour of Hall effect thrusters. *Plasma Sources Science and Technology*, 16(1):13, 2006.
- [230] Felix Sharipov. Numerical simulation of rarefied gas flow through a thin orifice. *Journal of Fluid Mechanics*, 518:35, 2004.
- [231] Thomas W Tuer and George S Springer. A test particle Monte Carlo method. *Computers & Fluids*, 1(4):399–417, 1973.

- [232] Kenichi Nanbu. Direct simulation scheme derived from the Boltzmann equation. I. mono-component gases. *Journal of the Physical Society of Japan*, 49(5):2042–2049, 1980.
- [233] Alejandro L Garcia. *Numerical methods for physics*. Prentice Hall Englewood Cliffs, NJ, 2000.
- [234] Stefano Boccelli. Tpmc-2d. https://github.com/sbocce/TPMC_2D, 2020.
- [235] S Venkateswaran and L Merkle. Analysis of preconditioning methods for the Euler and Navier-Stokes equations. *Lecture series-van Karman Institute for fluid dynamics*, 3:B1–B155, 1999.
- [236] Tommaso Andreussi, Eugenio Ferrato, Vittorio Giannetti, Antonio Piragino, Christopher A Paissoni, Gianluca Cifali, and Mariano Andrenucci. Development status and way forward of SITAEI’s air-breathing electric propulsion engine. In *AIAA Propulsion and Energy 2019 Forum*, page 3995, 2019.
- [237] Francesco Romano, Y-A Chan, Georg Herdrich, C Traub, S Fasoulas, PCE Roberts, K Smith, S Edmondson, S Haigh, NH Crisp, et al. Rf helicon-based inductive plasma thruster (IPT) design for an atmosphere-breathing electric propulsion system (ABEP). *Acta Astronautica*, 176:476–483, 2020.
- [238] Pietro Parodi, Damien Le Quang, Federico Bariselli, Stefano Boccelli, Zuhayr Alsalihi, and Thierry Magin. Study of a collector-intake system for VLEO air-breathing platforms. In *FAR - International Conference on Flight Vehicles, Aerothermodynamics and Re-entry Missions and Engineering*, 2019.
- [239] Gregory Ruetsch and Massimiliano Fatica. *CUDA Fortran for scientists and engineers: best practices for efficient CUDA Fortran programming*. Elsevier, 2013.
- [240] M Aissa. *GPU-accelerated CFD simulations for turbomachinery design optimization*. PhD thesis, Doctoral thesis, Delft University of Technology, 2017.
- [241] Daniel Molinero, Sergio Galván, Jesús Pacheco, and Nicolás Herrera. Multi GPU implementation to accelerate the CFD simulation of a 3D turbo-machinery benchmark using the RapidCFD library. In *International Conference on Supercomputing in Mexico*, pages 173–187. Springer, 2019.
- [242] Martín Abadi, Ashish Agarwal, Paul Barham, Eugene Brevdo, Zhifeng Chen, Craig Citro, Greg S. Corrado, Andy Davis, Jeffrey Dean, Matthieu Devin, Sanjay Ghemawat, Ian Goodfellow, Andrew Harp, Geoffrey Irving, Michael Isard, Yangqing Jia, Rafal Jozefowicz, Lukasz Kaiser, Manjunath Kudlur, Josh Levenberg, Dandelion Mané, Rajat Monga, Sherry Moore, Derek Murray, Chris Olah, Mike Schuster, Jonathon Shlens, Benoit Steiner, Ilya Sutskever, Kunal Talwar, Paul Tucker, Vincent Vanhoucke, Vijay Vasudevan, Fernanda Viégas, Oriol Vinyals, Pete Warden, Martin Wattenberg, Martin Wicke, Yuan Yu, and Xiaoqiang Zheng. TensorFlow: Large-scale machine learning on heterogeneous systems, 2015. Software available from tensorflow.org.org.
- [243] Rami Al-Rfou, Guillaume Alain, Amjad Almahairi, Christof Angermueller, Dzmitry Bahdanau, Nicolas Ballas, Frédéric Bastien, Justin Bayer, Anatoly Belikov, Alexander Belopolsky, et al. Theano: A Python framework for fast computation of mathematical expressions. *arXiv*, pages arXiv–1605, 2016.
- [244] François Chollet et al. Keras. <https://keras.io>, 2015.
- [245] Ian Goodfellow, Yoshua Bengio, and Aaron Courville. *Deep Learning*. MIT Press, 2016. <http://www.deeplearningbook.org>.
- [246] Hessam Mirgolbabaei and Tarek Echekki. Nonlinear reduction of combustion composition space with kernel principal component analysis. *Combustion and flame*, 161(1):118–126, 2014.

List of publications

This section collects the author's scientific contributions, prepared while carrying out the research presented in this work.

Journal articles

1. S. Boccelli, T.E. Magin, A. Frezzotti, *Numerical investigation of reversed gas feed configurations for Hall thrusters*, Under Review.
2. S. Boccelli, F. Giroux, T.E. Magin, C.P.T. Groth, J.G. McDonald, *A 14-moment maximum-entropy description of electrons in crossed electric and magnetic fields*, Physics of Plasmas 27 (12), 123506, 2020.
3. S. Boccelli, T. Charoi, A. Alvarez Laguna, P. Chabert, A. Bourdon, T.E. Magin, *Collisionless ion modeling in Hall thrusters: analytical axial velocity distribution function and heat flux closures*, Physics of Plasmas 27 (7), 073506, 2020.
4. S. Ramjatan, A. Lani, S. Boccelli, B. Van Hove, Ö. Karatekin, T. Magin, J. Thoemel, *Blackout analysis of Mars entry missions*, Journal of Fluid Mechanics 904, 2020.
5. F. Bariselli, S. Boccelli, B. Dias, A. Hubin, T.E. Magin, *A self-consistent method for the simulation of meteor trails with an application to radio observations*, Astronomy & Astrophysics 641, A100, 2020.
6. M. Babaiasl, S. Boccelli, Y. Chen, F. Yang, J.L. Ding, J.P. Swensen, *Predictive mechanics-based model for depth of cut (DOC) of waterjet in soft tissue for waterjet-assisted medical applications*, Medical & Biological Engineering & Computing 58, 1845-1872, 2020.
7. S. Boccelli, F. Bariselli, B. Dias, T.E. Magin, *Lagrangian diffusive reactor for detailed thermochemical computations of plasma flows*, Plasma Sources Science and Technology 28 (6), 065002, 2019.

Conference proceedings and presentations

1. S. Boccelli, P. Parodi, L. Vallisa, W. Kaufmann, P. Barbante, J.G. McDonald, T.E. Magin, *Maximum-entropy 14 moments description of non-equilibrium electrons in crossed electric and magnetic fields*, 73rd Gaseous Electronics Conference, 2020.

Bibliography

2. M. Babaiasl, F. Yang, S. Boccelli, J.P. Swensen, *Fracture-directed waterjet needle steering: design, modeling, and path planning*, 2020 8th IEEE RAS/EMBS International Conference for Biomedical Robotics and Biomechatronics (BioRob), 2020.
3. K. Mani, S. Boccelli, F. Topputo, A. Cervone, *Electric propulsion characterization for a stand-alone Mars CubeSat*, 36th International Electric Propulsion Conference, 1-15, 2019.
4. F. Bariselli, S. Boccelli, B. Dias, A. Hubin, T.E. Magin. *Detailed Simulations of Meteor Trails with Application to Radio Observations*, FAR - International Conference on Flight vehicles, Aerothermodynamics and Re-entry Missions and Engineering, 2019.
5. P. Parodi, D. Le Quang, F. Bariselli, S. Boccelli, Z. Alsalihi, T.E. Magin, *Study of a Collector-Intake System for VLEO Air-Breathing Platforms*, FAR - International Conference on Flight vehicles, Aerothermodynamics and Re-entry Missions and Engineering, 2019.
6. J. Amorosetti, A. Bultel, S. Boccelli, T.E. Magin, J. Annaloro, *Simulation of electronic excitation in transitional atmospheric entry flows*, Radiation of High Temperature Gas - RHTG Workshop, 2019.
7. S. Boccelli, F. Bariselli, B. Dias, T.E. Magin, *Lagrangian diffusive reactor for detailed thermochemical computations of plasma flows*, Radiation of High Temperature Gas - RHTG Workshop, 2019 (presented by T. Magin).
8. F. Bariselli, S. Boccelli, T. Magin, A. Frezzotti, A. Hubin, *Aerothermodynamic modelling of meteor entry flows in the rarefied regime*, 2018 Joint Thermophysics and Heat Transfer Conference, 4180, 2018.